# Experimental Vibration Analysis in the Knowledge Process of a Historic Confined Masonry Building

Concetta Tripepi, Fernando Saitta, Paolo Clemente, Giacomo Buffarini, Giovanni Bongiovanni

buildings

MDPI

*Article*

# Experimental Vibration Analysis in the Knowledge Process of a Historic Confined Masonry Building

**Concetta Tripepi [1], Fernando Saitta [2], Paolo Clemente [2,*], Giacomo Buffarini [2] and Giovanni Bongiovanni [2]**

[1] Italian National Agency for New Technologies, Energy and Sustainable Economic Development, Bologna Research Centre, 40129 Bologna, Italy; concetta.tripepi@enea.it
[2] Italian National Agency for New Technologies, Energy and Sustainable Economic Development, Casaccia Research Centre, 00123 Rome, Italy; fernando.saitta@enea.it (F.S.); giacomo.buffarini@enea.it (G.B.); giovanni.bongiovldi8@alice.it (G.B.)
* Correspondence: paolo.clemente@enea.it

**Abstract:** Experimental vibrational analysis is used in the knowledge process of a historic building, made of confined masonry, a construction system suggested in the reconstruction after the 1915 earthquake at Avezzano, Italy. The building was the primary subject of the usual experimental campaign to verify the structural geometry, the characteristics of the materials and the permanent loads. Then, a detailed experimental vibration analysis was carried out. Data were analysed both in the frequency and in the time domains. This combined approach allowed us to point out the importance of the floor deformability on the dynamic behaviour of the structure. A finite element model was set up using the equivalent frame method and calibrated on the basis of the experimental vibrational analysis results. The constitutive law of the confined masonry was fine-tuned, following the literature and present standard suggestions. The pushover analyses allowed us to uncover the behaviour factor of the structure and the seismic safety index, which was found to be quite low and very similar to that obtained via a response spectrum analysis.

**Keywords:** historic buildings; masonry buildings; confined masonry; experimental vibration analysis; pushover analysis



**Citation:** Tripepi, C.; Saitta, F.; Clemente, P.; Buffarini, G.; Bongiovanni, G. Experimental Vibration Analysis in the Knowledge Process of a Historic Confined Masonry Building. *Buildings* **2023**, *13*, 2560. https://doi.org/10.3390/buildings13102560

Academic Editor: Francisco López-Almansa

Received: 10 September 2023
Revised: 3 October 2023
Accepted: 6 October 2023
Published: 10 October 2023



## 1. Introduction

The knowledge of static and dynamic properties is essential to understand the structural behaviour of complex buildings or buildings whose materials have mechanical characteristics that are difficult to evaluate. Knowledge makes it possible to develop reliable models, calibrated on the real response, which can be used to evaluate behavioural scenarios that are also in the presence of different types of actions. Obviously, the experimental data are not easy to interpret, especially for the complex buildings mentioned above, such as the historical masonry ones. Moreover, the application of monitoring techniques to the field of cultural heritage is challenging due to the need of respecting its architectural and historical value [1]. However, all this information is essential for a correct assessment of the structural health status of a building and the definition of an effective retrofit intervention. You cannot decide how to intervene if you do not know the structure very well.

Experimental vibration analysis is undoubtedly a technique to use to understand the behaviour of a structure in a seismic area. It is cheap, minimally invasive, fast and reliable. It is useful for finding out the actual vibration modes to consider in a dynamic response spectrum analysis or for establishing the most appropriate force system in a push-over analysis. Recently, the application of wireless sensor networks (WSNs) as a new kind of monitoring system architecture, flexible and with minor costs, has been explored [2].

The convenience is, above all, in the exploitation of the environmental vibrations to excite the structure. These are present everywhere at no cost and, in general, offer a natural excitation with a broad spectrum in frequency. The downside is that they have low energy.

Therefore, they almost never succeed in triggering a non-linear response. On the other hand, for the same reason, they provide useful indications of the dynamic behaviour at the onset of motion and can allow for the identification of the most vulnerable elements of a building, whereby the first exceeding instances of the elastic limits presumably occur.

The analysis of the obtained recordings can be performed in the time domain and/or in the frequency domain. The study in the frequency domain is usually carried out by analysing the auto-spectra of the recordings obtained at various locations on the structure and the cross-spectra of significant pairs of the recordings themselves and allows for identifying the resonance frequencies and the mode shapes, obviously in the case of linear behaviour. The analysis in the time domain makes it possible to identify the maximum values of the vibration amplitudes and also to have an immediate vision of the prevailing movement of the structure, if any.

Relevant previous applications concerned structures of historical and artistic interest. Among these, the Coclid columns [3,4], the Colosseum [5] and the Egyptian obelisks in Rome [6]. In the first case, the synergistic use of the analysis in the time and frequency domains allowed for the highlighting of peculiar aspects of the behaviour of each column. In the second one, the study was conducted by considering multiple configurations for the sensors and reconstructing the movement in the space of the remaining portion of the north wall. In the third case, an accurate analysis of the materials was carried out in parallel with the dynamic analysis, through non-destructive tests, and was able to develop an effective numerical finite elements model. Recently, particular attention has been paid to the possibility of using historical structures to host social events, such as pop music concerts [7].

The long-term monitoring allowed for the underscoring of the environmental parameters' influence (particularly thermal variations) on the modal characteristics of ancient masonry constructions [8]. Environmental conditions evolving over time can hide variations in the dynamic properties due to structural damaging, leading to an incorrect health status assessment. For this reason, the influence of environmental conditions on modal parameters has to be quantified and eliminated [9].

Among the tower structures, the San Frediano bell tower in Lucca (Italy) was instrumented along its height with triaxial seismometric stations for about one year, and the dependence of the tower's frequencies on the ambient temperature was investigated [10]. Correlation studies between modal frequencies and temperature were the result of a one-year dynamic monitoring performed on the tower of the historic complex of "Santa Maria del Carrobiolo" in Monza (Italy) [11]. The feasibility of damage detection methods based on natural frequency shifts was demonstrated through the 15-month dynamic monitoring of the tallest historic tower in Mantua (Italy) by means of low-cost monitoring systems (consisting of a few accelerometers and temperature sensors) [12].

The environmental effects on the dynamic response were investigated also with reference to two complex case studies of the modal and structural identification of monuments in Portugal: the Clock Tower of Mogadouro and the Church of Jerónimos Monastery in Lisbon, monitored by University of Minho through vibration, temperature and relative air humidity sensors [13].

It must also be considered that the phenomenon of Soil Structure Interaction (SSI), acting on the static and dynamic response of buildings, can affect the dynamic identification process. The issue was addressed by considering the bell tower of Santa Sofia in Benevento (Italy), as a case study which attempted to unravel the influence of the ground on the structural response [14].

A large number of case studies in Italy are reported in [15]. The viability of ambient vibration testing for complex masonry structures is demonstrated in [16] for the relevant case study of the Sanctuary of Vicoforte (Italy). Finally, in [17], a collection of interesting works on the subject is presented.

Experimental tests on shaking tables are useful when the aim of the study is to analyse the response of the structure under established inputs. In [18], interesting applications on

models of masonry buildings before and after the retrofit intervention are shown. Shaking table tests were also used for damage detection via a modal analysis of confined masonry structures [19].

Furthermore, a recent study has highlighted the structural behaviour of a masonry building, subject to a push-over performed in reality, i.e., an experimental push-over [20].

Previous experiences in the field of buildings have also pointed out the difficulty in interpreting experimental data, but above all, the difficulty lies in structural modelling [21], especially when the structure is significantly damaged [22]. In some cases, the modulus of elasticity of the masonry was adjusted so that the numerical model achieved the experimental results [23]. In other cases, vibration measurements were used for the numerical model calibration of a multi-leaf stone masonry wall [24] or to validate the rigid diaphragm assumption in the seismic assessment [25]. Moreover, the tuning of the numerical model can include, as calibration parameters, boundary conditions in addition to mechanical quantities [2].

Also the choice of the modelling method is relevant. In fact, besides the Finite Element Method (FEM), the Discrete Element Method (DEM) proved to be particularly successful in analysing masonry structures. This discontinuous approach, where the masonry is represented as a system of interacting distinct blocks, is especially suited when the interest is in the prediction of collapse mechanisms. A method for simulating the seismic response of masonry structures based on DEM, taking into account for sliding, separation and impact among blocks, is proposed in [26]. In [27], a review of the main models based on DEM and related numerical techniques is presented, whereas in [28], DEM is implemented to capture all commonly noted failure mechanisms through a novel computational modelling strategy. Recently, an interesting application of DEM for structural collapse simulation, with as case study on the Great Wall of China, was published [29].

In [30,31], the general principles for the correct use of the experimental vibrational analysis were analysed, while in [32], an analytical comparison between techniques for the identification of modal properties through ambient vibrations was performed. As far as the issues faced by the authors of [33], the aim was to check if the dynamic identification procedures, usually applied to reinforced concrete or steel buildings, could provide useful information in the estimation of the dynamic characteristics of existing masonry buildings as well. In [34], statistical models and data processing algorithms were developed and applied in order to address the problem of uncertainty quantification in the structural health monitoring of cultural heritage buildings. Moreover, in [35], a design methodology of sensor networks based on Optimal Sensor Placement (OSP) techniques suitable for historical structures was proposed. The OPC techniques represent a tool of designing of the sensor layout to achieve an effective modal identification with a reduced number of sensors.

In the present paper, the experimental vibrational analysis is used in the knowledge process of a historic building made of confined masonry [36] in Avezzano, Italy. It was built during the reconstruction after the earthquake that destroyed the city of Avezzano entirely on 15 January 1915 ($Mw = 7.0$); therefore, it represents a very common typology used in that period in most buildings, also in other Italian regions, and still used in other countries. After undergoing an identification process through an analysis in the frequency domain of the obtained recordings, the main resonance frequencies of the building and the corresponding vibration modes, an accurate analysis was performed in the time domain. The combined use of frequency and time domain analyses allowed us to highlight important features of the dynamic behaviour, which are very common in historic buildings. In the analysed structure, these characteristics are related to the deformability of the floors in their own plane and to the non-rigid connection with the load-bearing walls. The results of the experimental analysis were used to set up a finite element model. Finally, a push-over analysis was performed, highlighting how the choice of the reference node for the target displacement is delicate and important for such buildings.

## 2. Torlonia Building: Description and Traditional Tests

The Torlonia Building, which the herein reported analysis will refer to, dates back to the 1920s and was constructed according to the provisions of the Italian Royal Decree 573, issued on 29 April 1915, just after the Avezzano earthquake. Consequently, it shows some early anti-seismic design features. Particularly, according to the regulations at the time, concerning the number of floors and heights, the building was developed on two levels above the ground (two storeys), with an unusable garret. In Figure 1, a longitudinal vertical section of the building's original conceptual design is reported. Even if it is not evident in the figure, a gap is present between the foundation and the planking level, which is therefore a slab, with two practicable spaces at basement level. The building is of a C shape (Figure 2), which makes it intrinsically vulnerable.

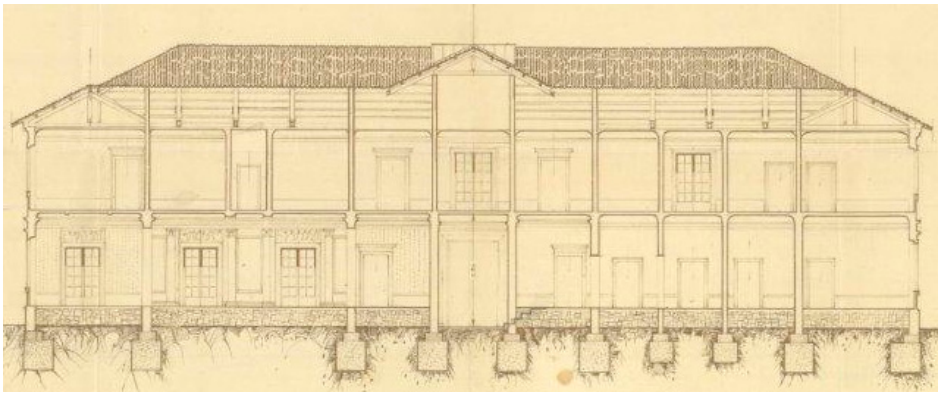

**Figure 1.** Vertical section from the original drawings.

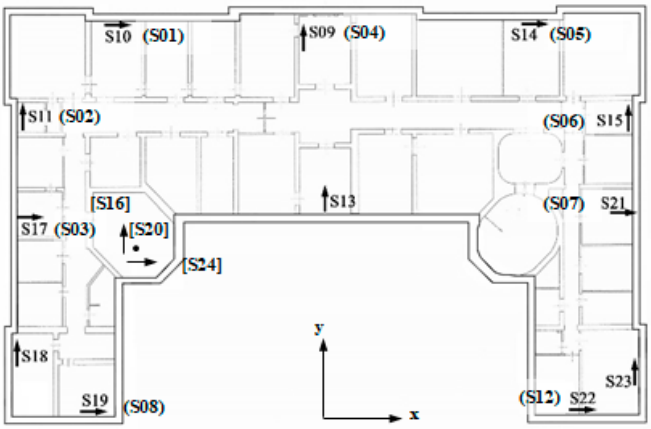


**Figure 2.** Plan of the building with sensors layout. Sensor in () are on the first floor; sensors in [] are in the basement; the other sensors are at the top.

The Royal Decree 573 also established specific regulations about the types of materials to use and the construction typology to be observed. In compliance, the load-carrying structure of the building comprises clay brick masonry walls confined with lightly reinforced concrete (r.c.) elements, both horizontally and vertically arranged, which also surround the openings and extend in height until the floor is reached. This kind of masonry is generally known as confined masonry.

Furthermore, visual inspections revealed some internal r.c. columns, collaborating with wood trusses to sustain the pavilion roofing, and floor slabs made of mixed concrete and hollow clay blocks, with a total height of 23 cm. In contrast, based on in situ inspections as well as the design tables, it was found that the foundations, placed almost 80 cm under the ground level, consisted of reinforced curbs, realized under the load-carrying walls, and in turn rested on reinforced concrete beams no less than 1.10 m wide.

The available original documentation provided sufficient information on the building geometry, but extensive in situ investigations on both materials and structural details were nevertheless necessary. These included: visual inspections and endoscopic inspections, as well as single and double jack tests on masonry; penetration tests on mortars; cover meter inspections to check number, position and diameters of reinforcing bars; concrete core extraction and related compression tests; resistograph, sonic and sclerometer tests on wooden elements; endoscopic inspection on slabs; and visual inspection, by means of shaft sinking, to check base level and geometrical characteristics of foundations.

From the investigations above, it was found that the masonry structure is made up of bricks and cement mortar with an average compression strength $f_m$ = 2.76 N/mm$^2$, an average shear strength $\tau_0$ = 0.067 N/mm$^2$, a Young's and a shear modulus equal to $E$ = 1246 N/mm$^2$ and $G$ = 415 N/mm$^2$, respectively, and a weight per unit volume $w$ = 18 kN/m$^3$.

As far as the concrete is concerned, from the compression tests on the extracted cores, the value of the average experimental cube strength $R_{cm}$ = 13.14 N/mm$^2$ was derived.

With regard to the ground, the available information established that the building was founded on a layer of sandy-gravel, sand, silty-sand and sandy-silt, with a thickness of 20–40 m, below which the sediments become increasingly pelitic. Silt and clay can be observed, up to a depth of 100–200 m, over the lapid sublayer. Dynamic Probing Super Heavy conducted on two layers (marked with the subscripts a and b in the following) presented the following geotechnical factors: weights per unit volume $\gamma_a$= 19.1 kN/m$^3$ and $\gamma_b$= 18.4 kN/m$^3$; internal friction angles $\varphi_a$ = 24° and $\varphi_b$ = 23°; cohesions $c_a$ = 0.006 N/mm$^2$ and $c_b$ = 0.004 N/mm$^2$; and undrained cohesions $c_{ua}$ = 0.07 N/mm$^2$ and $c_{ub}$ = 0.05 N/mm$^2$. From a seismic point of view, the subsoil can be classified as type C, with a seismic wave velocity $V_{s30}$ between 280 and 315 m/s.

## 3. Experimental Vibrational Analysis

The experimental vibration analysis was performed by using 24 Kinemetrics SS-1 seismometers (period = 1 s) connected to a Kinemetrics Granite acquisition system (with a 24-bit A/D converter able to simultaneously convert the 24 channels). In order to capture the global and the local structure behaviour, the sensors were arranged as follows (Figure 2):

- Three seismometers (S24, S16 and S20) were deployed at the basement, in x, y and z directions, respectively.
- Nine seismometers were deployed at the first floor, six of them in x direction, three in y direction.
- Twelve seismometers were deployed at the second floor, six of them in x direction, six in y direction.

Ambient vibrations were recorded. Velocity time histories lasting 1 h were acquired with a sampling ratio of 0.005 s.

### *3.1. Analysis in the Frequency Domain*

In Figure 3, the power spectral densities (PSDs) of the recordings obtained at the second floor are plotted. Because of many not well separated peaks in the spectra, a clear identification of frequencies and modal shapes is not possible. However, a stronger energy content of modes related with the motion of the two wings (i.e., lateral blocks) suggests a prevalent non-global behaviour of the building. Considering also the cross-spectral densities (CSDs) (Figure 4), the following significant resonance frequencies were individualized.

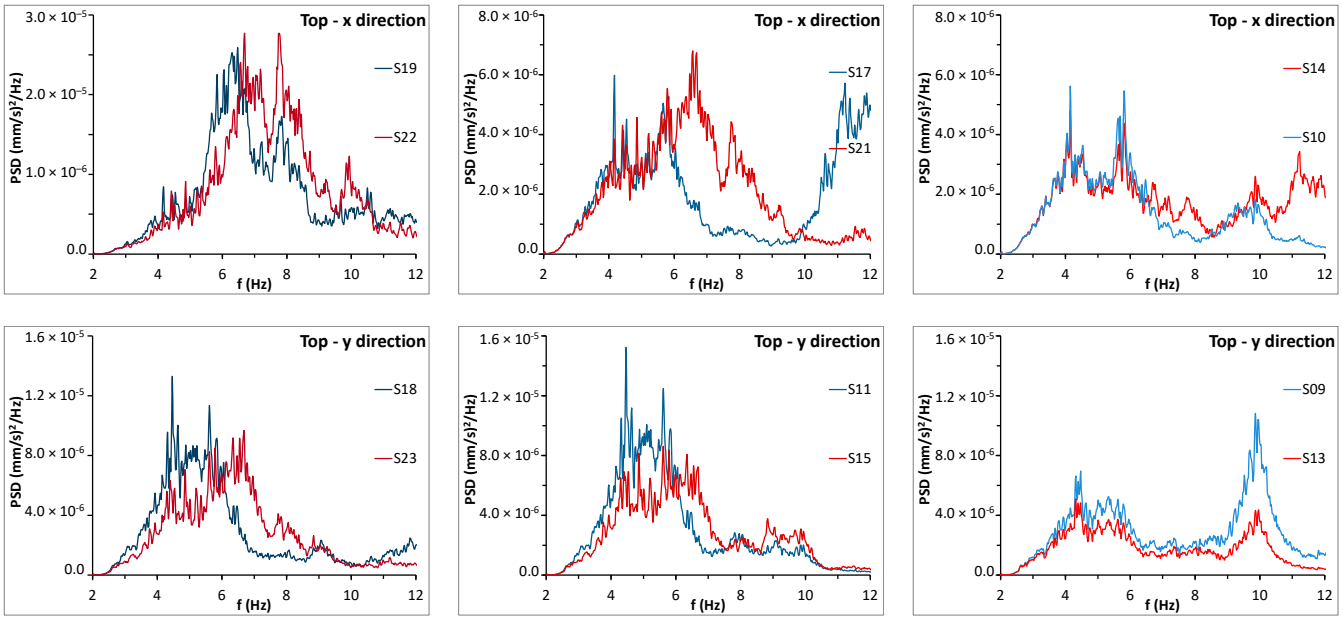


**Figure 3.** Power spectral densities at the second floor.

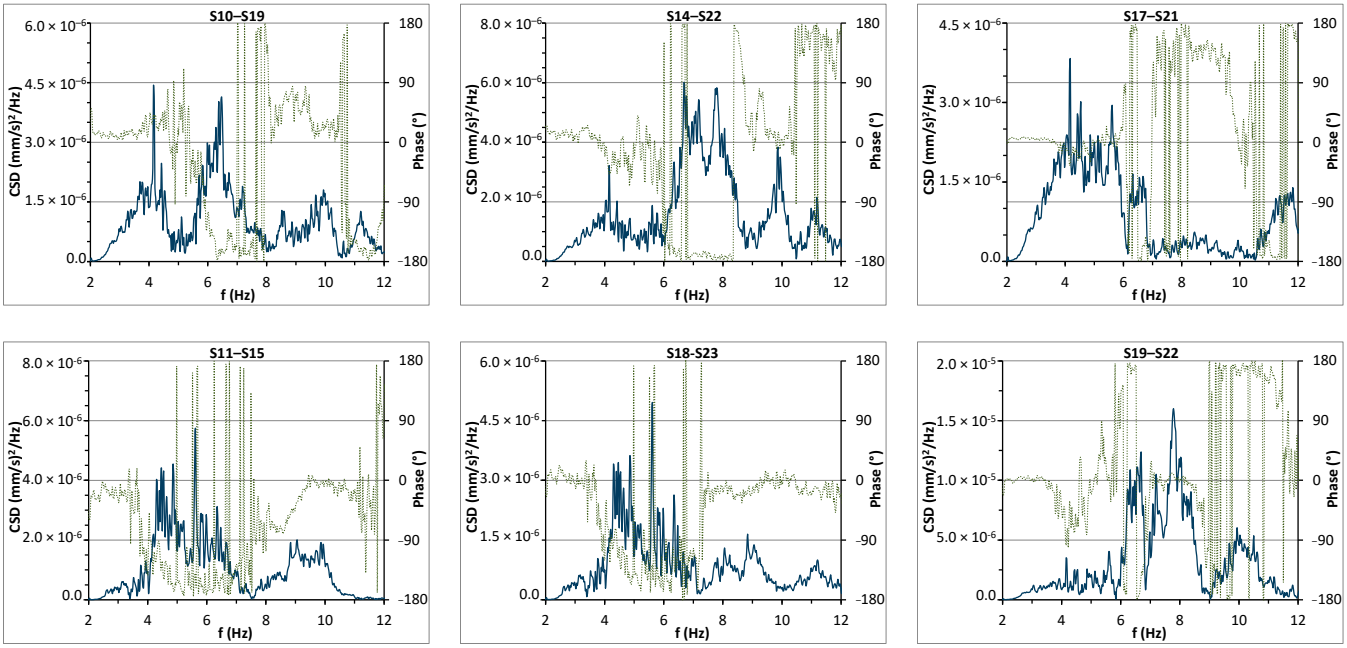


**Figure 4.** Cross-spectral densities at the second floor (phase factor in green lines).

- A first resonance frequency at 4.15 Hz involves the entire building in the x direction, with displacements of the same order for all the sensor locations.
- The first resonance frequency of 4.47 Hz in the y direction, like the previous one, involves the entire building; however, in this case, the modal components at the external walls are about double of those at S09 and S13.
- The third resonance frequency, equal to 5.62 Hz, is still in the y direction; it also involves the entire building and, as above, the modal components at the external walls are about twice as those at S09 and S13.
- The resonance frequency of 5.81 Hz is likely to correspond with a mode of the whole building in the x direction; in this case, the modal components of the main body are similar to each other, while those of the wing (S19 and S22) are much higher.

- The resonance frequency of 6.69 Hz refers to the right wing, both in the x and y directions.
- Analogously, the resonance frequency of 7.84 Hz refers to the right wing, both in x and y directions.
- The resonance frequency of 9.86 Hz, which, once again, concerns the main block in the y direction, involves different signal amplitudes for the sensors of the second floor (S09 and S13) and highlights a certain deformability of that floor in its plane.
- Finally, the resonance frequency of 11.2 Hz corresponds to a mode engaging the two lateral blocks in the x direction.

In Figure 5, the PSDs of all the recordings at the first floor and those at the basement are plotted. As can be seen, the same resonance frequencies highlighted in the recordings of the second floor are also present for the first floor, with low energy. The spectra of the recordings at the basement also contain other lower frequency components.

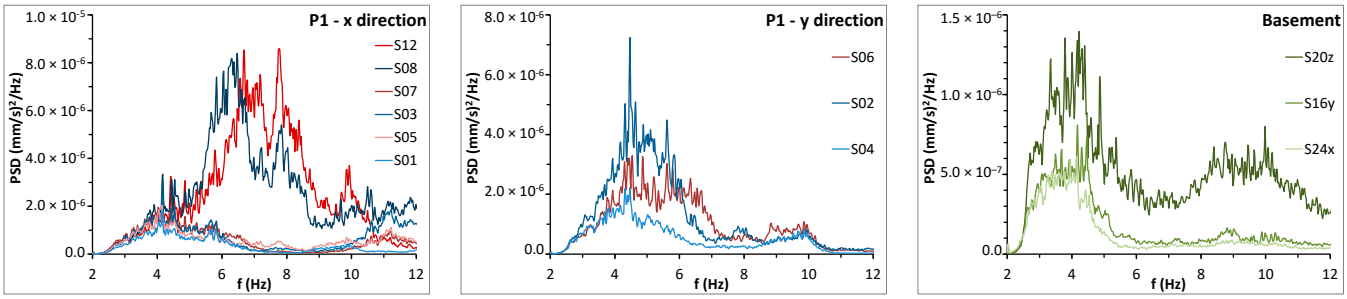


**Figure 5.** Power spectral densities at the first floor (P1) and the basement.

### *3.2. Time Domain Analysis*

In order to analyse the dynamic behaviour of the building in depth, signals were also studied in the time domain.

As pointed out by the frequency domain analysis, the flexibility of the horizontal slabs should be analysed in more detail so as to investigate how it is likely to assume that floors are rigid in their plane. Furthermore, if a pushover analysis is intended to be performed, information is needed to establish whether it is legitimate to assume the centre of mass of the top floor as the control node. According to current Italian Code [37,38], in the case of a floor having finite stiffness, the displacement to be used into the capacity plot should be a weighted average among the displacements at the top of the vertical walls.

If an adequate number of experimental recordings are available, a way to check if a system behaves like a rigid body is to try to find a unique centre of rotation by intersecting the straight lines perpendicular to the motion direction at the measurement points. In Figure 6a,b, the particle motions at the main corners of the building and at the intermediate points of the façades were superimposed onto the second-floor plan. The two figures differ because at each intermediate point, the sensor orthogonal to the façade was coupled with the two different sensors parallel to the same façade, which means to translate each sensor parallel to a façade along its axis up to the sensor at its right angle. This way of proceeding implies neglecting the floor deformation, which is a plausible assumption when the start and end points of translation are close to each other and lined up along the perimeter of the building.

It is immediately evident that the prevalent directions of motion of the building do not correspond to the two main horizontal axes. This occurrence is related to the irregular C-shape of the building in plane. Moreover, whereas a certain behavioural symmetry with respect to the y axis is found for the main body, the same is not true for the two wings (sectors C and D in the following), because the right wing moves much more than the left one.

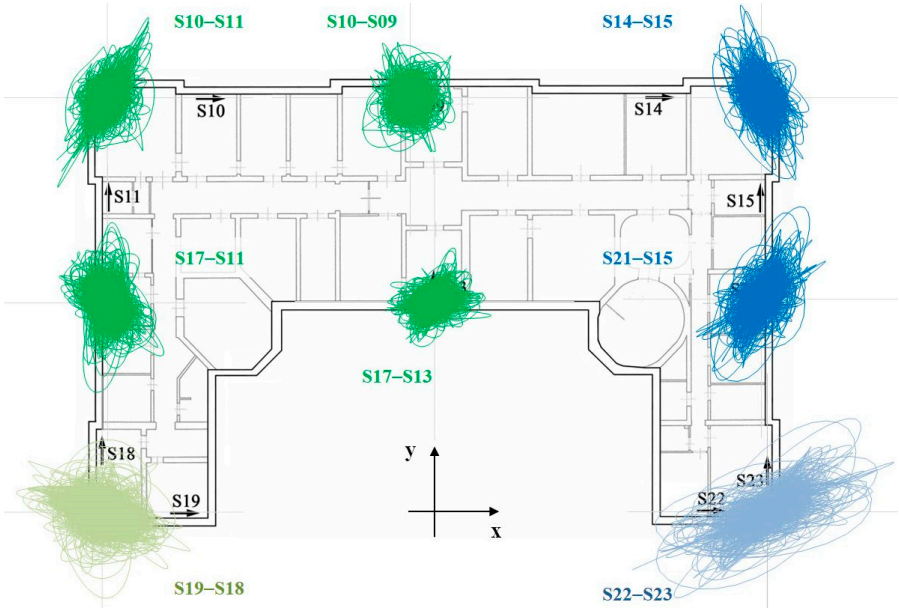


(**a**)

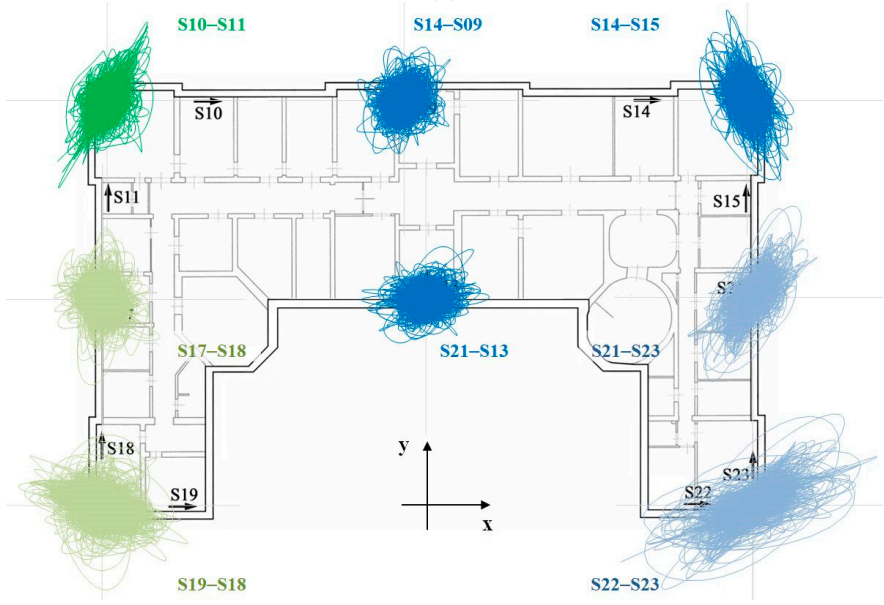


(**b**)

**Figure 6.** Particle motions pairing the sensors in different ways: (**a**) S17 and S21 are paring with S11 and S15, respectively, while S09 and S13 are paring with S11 and S15, respectively; (**b**) S17 and S21 are paring with S18 and S23, respectively, while S09 and S13 are paring with S14 and S13, respectively.

A more detailed representation of motion direction at each measurement point can be obtained through angle distributions, which report the number of times a particle motion is oriented in a certain direction with an approximation of a one-degree angle (Figure 7a,b). The tangles we obtained have quite a regular shape, approximating an ellipse. Then, from each angle distribution, the prevailing direction of motion can be made to coincide with the major axis of this ellipse, whereas the minor one can be assumed as a measure of the dispersion. In other words, the more the approximation ellipse will be elongated and narrowed, the more the movement of the point will keep a constant inclination over time. In contrast, the more the approximation ellipse will be rounded, the more the movement of the point will change direction over time. From the figures, it can be seen that corners have a behaviour closer to the first category, whereas intermediate points fall into the second one, exhibiting a more significant dispersion of the direction of motion. Moreover, the tangles at

intermediate points S09 and S13 differ depending on whether they are coupled with the sensor to their right or with the one to their left.

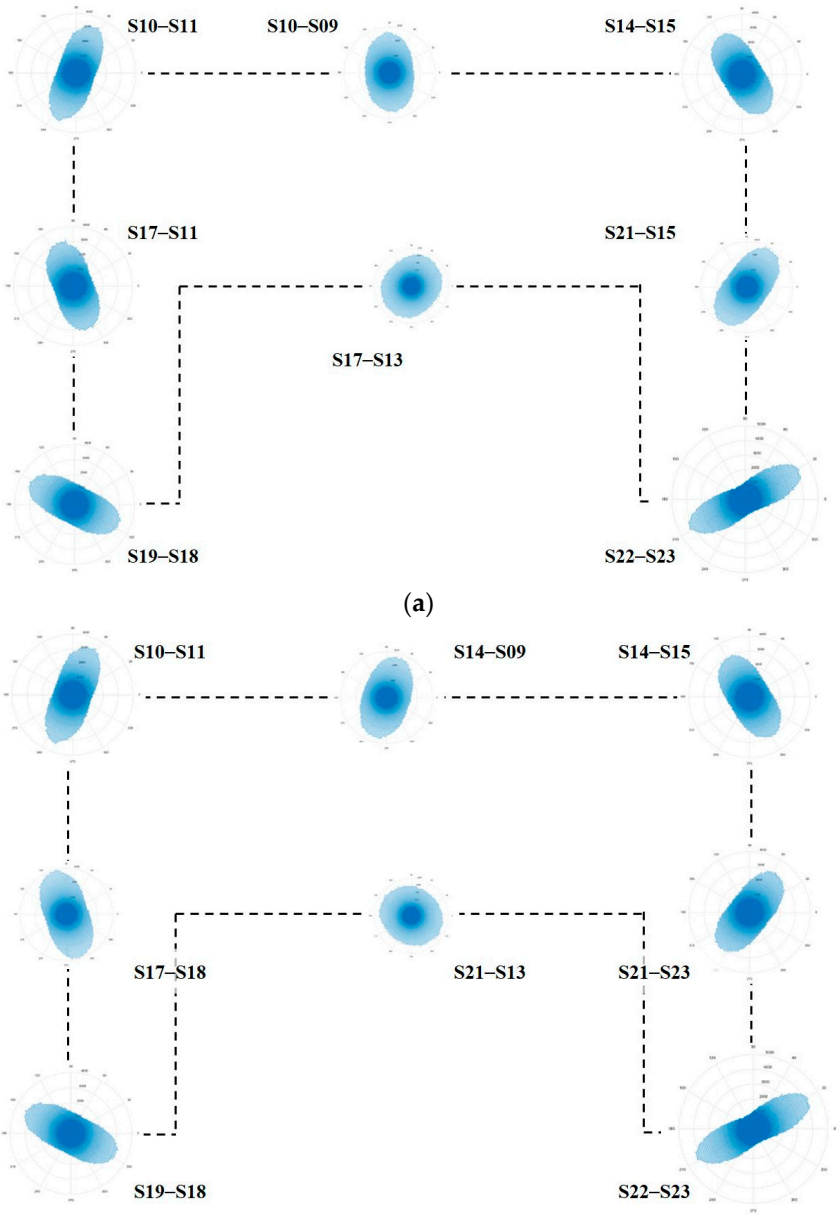


**Figure 7.** Angle distributions corresponding to particle motions of (**a**) Figure 6a and (**b**) Figure 6b.

What has been performed at intermediate points—assuming that along the translation path of sensors, the floor is rigid—likely seems to be the reality in the cases of points S17 and S21, but not in the case of S09 and S13. This is also confirmed by semi-sum and semi-difference time histories between the corresponding translated sensors (Figures 8 and 9). Indeed, while it appears that sensors S18−S11 move mainly in phase, as well as sensors S15–S23, this conclusion is weaker for sensors S14−S10 and far from reality for sensors S17–S21.

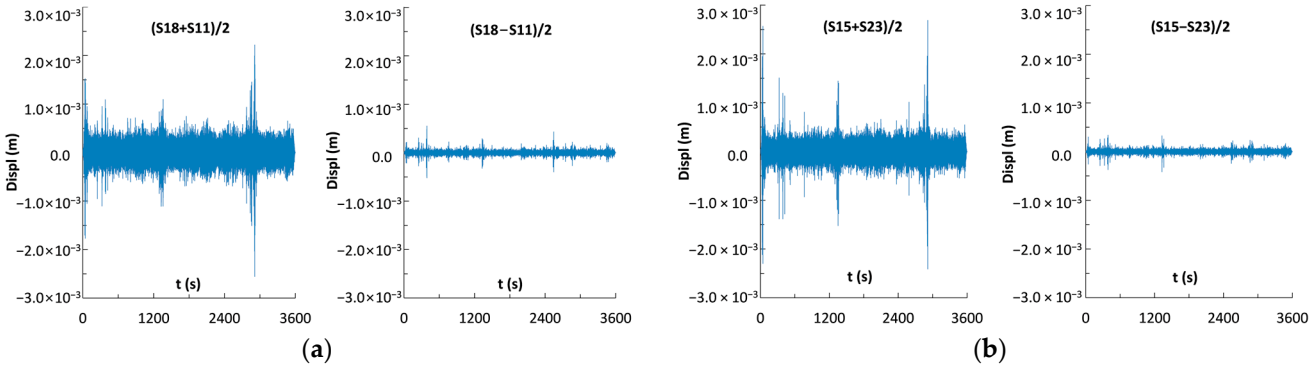


**Figure 8.** Semi-sum and semi-difference time histories of a couple of sensors: (**a**) S18−S11 and (**b**) S15–S23.

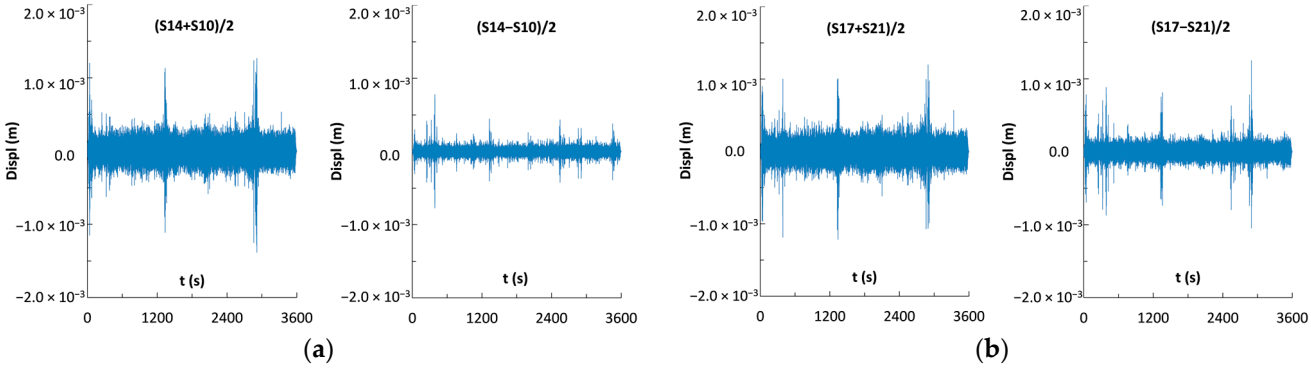


**Figure 9.** Semi-sum and semi-difference time histories of a couple of sensors: (**a**) S14−S10 and (**b**) S17–S21.

Neglecting the dispersion of motion, we will assume that the centre of rotation compatible with the movement of a point is located along the minor axis of the approximation ellipse centred at that point. By applying this rule for each angle distribution in Figure 7, the lines shown in Figure 10 were obtained. It is worth noting that both the contributions of sensors S09 and S13 were excluded from this procedure, as we believe that inferring a prevalent motion direction from their angle distributions is relatively unreliable. On the other hand, the analysis of the frequency domain (see Figure 3) highlighted—for these sensors and unlike the others—the most significant peak on the PSD, at around 9.86 Hz.

If the floor were perfectly rigid, all lines would intersect at a unique point, which would be the floor's exact centre of rotation. This is not the case, and, even if we excluded the two wings, a unique centre of rotation for the main body would not be evident. However, important information on the behaviour of the building may be inferred. For ease of reading, the plan was divided into four sectors: sectors A and B include the left side and right side of main body, respectively, whereas sectors C and D are the left wing and the right wing, respectively. What is immediately noticeable is that the direction of the centre of rotation for S17–S11 is almost coincident with the direction of S17–S18; and the direction of S21–S15 is almost coincident with the direction of S21–S23. This circumstance can be considered representative of the fact that, near the two secondary façades, the floor is quite rigid. However, keeping into account all the directions we deduced, four different centres of rotation were obtained (one for each sector: $C_A$, $C_B$, $C_C$ and $C_D$ in Figure 10). It is interesting to observe that $C_A$ and $C_B$ are aligned along x at about half the height of the main body, whereas the positions of $C_C$ and $C_D$ confirm that the two wings do not have symmetrical behaviour. Moreover, the distances of these two centres from the corresponding wings are compatible with the greater displacements recorded on the right corner (see Figure 6) with respect to the left one.

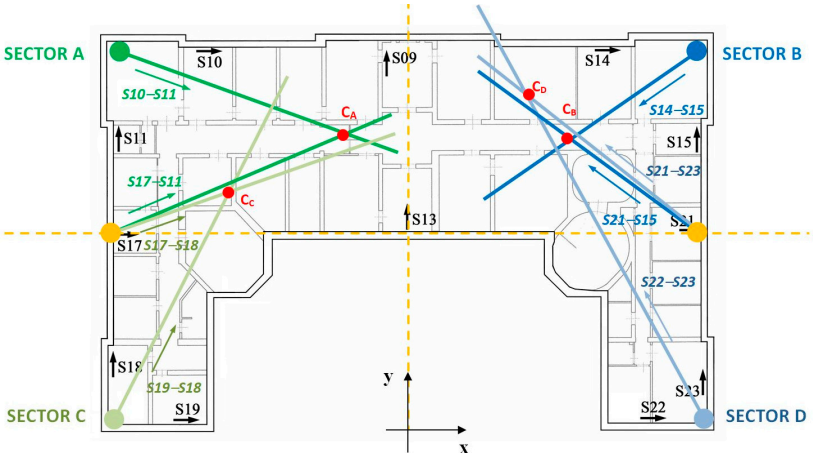


**Figure 10.** Directions that locate the centres of rotation.

## 4. Finite Element Model

### *4.1. Confined Masonry Walls Model*

The confined masonry buildings, even now largely widespread in Latin American countries such as Chile and Mexico, most likely appeared in the Italian overview after the Reggio Calabria and Messina earthquake of 28 December 1908, and the already mentioned Avezzano earthquake of 1915. Therefore, they are likely to be found among the historical or merely old buildings. The construction technique is based on masonry provided with reinforced concrete or reinforced masonry confining elements in the vertical and horizontal directions.

In the recent Italian Technical Code [37,38], some prescriptions are given for the design of new constructions with confined masonry, concerning the geometrical characteristics (e.g., minimum thickness, slenderness), the positioning of the reinforced concrete's vertical and horizontal elements, as well as their spacing, the minimum quantities of the reinforcing bars and stirrups and the construction phases (e.g., the concrete of the confining elements must be cast after the masonry realization). Furthermore, confined masonry is considered more reliable than ordinary masonry and higher values of the behaviour factor are allowed. The Italian Code refers to the European Standards [39] for the check. According to these, the shear resistance of a confined masonry member should be taken as the sum of the shear resistance of the masonry and that of the concrete of the confining elements.

In the following, the mathematical model proposed by Tomazevic and Klemenc [40], and agreed by Ahmad et al. [41], is used. It considers the shear resistance $V$ of the confined masonry as the sum of the contribution of the masonry $V_m$ (for diagonal shear damage mechanism) and of the reinforced concrete elements $V_S$ (due to the dowel action of reinforcing steel), whose expressions are given below:

$$V_m = \frac{\tau_0 l t}{C_i b}\left(1 + \sqrt{C_i^2\left(1 + \frac{\sigma_0}{\tau_0}\right) + 1}\right) \quad (1)$$

$$V_S = 0.8059 \cdot n \cdot \phi^2 \sqrt{f_C f_S} \quad (2)$$

where:

$C_i = 2\alpha b \cdot l/h$ is the interaction coefficient ($\alpha$ = 1.25);
$\tau_0$ = Shear strength of masonry without compression;
$l$ = Wall base width;
$t$ = Thickness;
$h$ = Height;
$b = h/l$, but $1.0 \leq b \leq 1.5$;
$\sigma_0$ = Vertical stress on the wall;

$n$ = Number of reinforcing bars;
$\phi$ = Diameter of reinforcing bar;
$f_c$ = Compressive strength of concrete;
$f_y$ = Yield stress of reinforcing steel.

This model is derived from experimental analyses on specimens of confined and not confined masonry walls tested under a constant vertical load and a programmed pattern of cyclically acting horizontal displacements, while keeping the lower and upper boundaries of the specimen parallel to each other. From the tests conducted, the authors found that lateral resistance and deformation capacity both improve in the confined masonry in comparison with the non-confined one. They attributed the improvement of shear resistance to the additional compression stresses, derived from interaction forces developed between the confining elements and masonry at the contact zones, and to the dowel action of reinforcing bars once the masonry panel is cracked. These two phenomena involve, on the one hand, a modification into the expression of the shear resistance of plain masonry walls, which lead us to obtain Equation (1), and on the other hand, the addition of the contribution of Equation (2) to the total shear resistance of confined masonry.

Nevertheless, with reference to the confined masonry, but as far as bending and/or axial loading are concerned, Eurocode 6 establishes that "in determining the design value of the moment of resistance of a section, a rectangular stress distribution may be assumed, based on the strength of the masonry, only. Reinforcement in compression should also be ignored". It follows that the resistance moment can be computed according to the expression provided by the Italian National Technical Code for unreinforced masonry:

$$M_{Rd} = l^2 t \frac{\sigma_0}{2} \left(1 - \frac{\sigma_0}{0.85 f_d}\right) \quad (3)$$

In Equation (3), $f_d$ is the design compression strength of the masonry, whereas the other symbols are as previously defined above.

### *4.2. Model of the Building*

A finite element model of the structure (Figure 11) was set up by resorting to the equivalent frame method [42]. The above results of experimental analysis provided relevant information and support in realizing a model, which was reliable and close to reality. For its calibration, not only the mechanical parameters, determined on the basis of traditional tests, but also the findings of experimental vibration analysis were used. The latter highlighted, in particular, the need to take into account the floors' deformability. Assuming that the floor diaphragms were planar rigid bodies, as is usually the case, it would have been an oversimplification in this case.

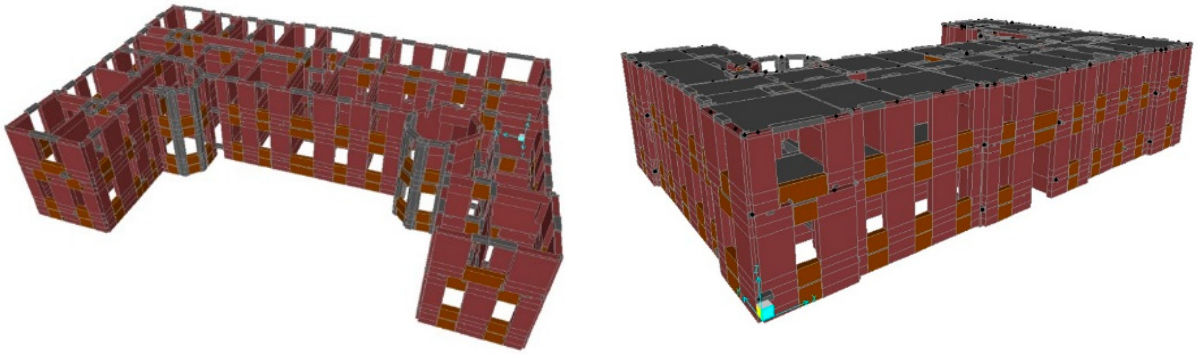

**Figure 11.** Extruded views of the finite element model.

For simulations, the computer code SAP2000 was used. The walls and the masonry spandrels were modelled by means of equivalent "beam" elements with rigid zones at their ends. Floors were modelled by means of "shell" elements having membrane behaviour only, in order to simulate their in-plane response with the effective stiffness, and rigidly connected to the masonry walls.

As for the materials' properties, the experimental results given in Section 2 were elaborated, according to the Italian Technical Code, as summarized below.

The experimental strength values of masonry were multiplied for a factor equal to 1.3 to account for the presence of effective transversal connections in the walls. These strength values must be further divided by a partial safety factor $\gamma_M$ (= 2 for seismic load combination, and = 3 for vertical load combination) when linear analyses are performed.

Regarding the concrete, from the average experimental cube strength, the corresponding average experimental cylindrical strength $f_{cm}$ = 10.9 N/mm$^2$ and the Young's modulus $E_{cm}$ = 22,579 N/mm$^2$ were derived. Having no experimental tests for steel bars, the yield strength was assumed equal to $f_y$ = 350 N/mm$^2$, consistent with the characteristics of the steel used at the time of construction.

Finally, a reduction factor equal to 1.2 was applied to the material strengths based on the knowledge level (LC) reached. It was classified as level 2 (LC2), which is an intermediate level between the lowest (LC1) and the highest (LC3). As a consequence, the concrete's reduced cylindrical strengths $f_{cd}$ = 9.05 N/mm$^2$, for ductile mechanisms, and $f_{cd,f}$ = 6.03 N/mm$^2$, for brittle mechanisms, were obtained. Similarly, $f_{yd}$ = 253.27 N/mm$^2$ represents the steel yield strength for brittle mechanisms.

### *4.3. Modal Analysis*

Results of modal analysis in terms of frequencies are summarized in Table 1, the first five modal shapes are reported in Figure 12. The correspondence with the experimental resonance frequencies is quite good, except for the first two, and in general, modal shapes agree sufficiently well with experimental findings. In detail, the first mode shows prevalent displacements in the x direction for the whole building. The second mode is instead mainly based on an x-directed movement of sector D; for this latter mode, the motion of the points experimentally investigated has outstanding similarities with those observed in the particle motion. The third mode is related to the x-motion of sectors C and D, 180° out of phase, and flexural y-motion of portion A + B. The fourth mode is mainly y-directed for the whole building with an x-component of sector C. Finally, mode 5 is related to the in-phase motion of the flanges in the x direction and the two-wave flexural motion of portion A + B in the y direction.

The modal analysis underscored the importance of multimodal approaches in a seismic nonlinear static analysis, and the selection of different control nodes for the target displacement to obtain a reliable displacement–base shear capacity curve of the structure.

**Table 1.** Numerical resonance frequencies.

| Mode | Numerical Frequencies (Hz) |
|---|---|
| 1 | 5.22 |
| 2 | 5.41 |
| 3 | 5.60 |
| 4 | 5.83 |
| 5 | 6.37 |
| 6 | 7.70 |
| 7 | 8.60 |
| 8 | 9.15 |
| 9 | 9.73 |

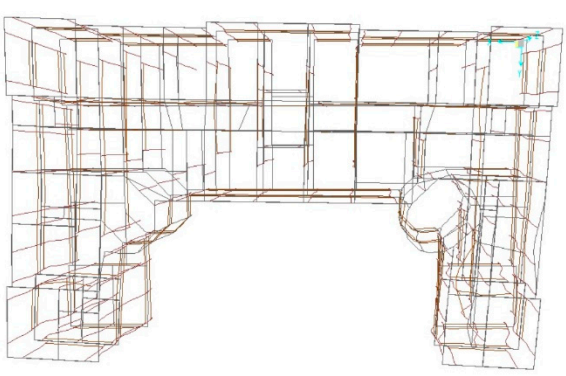

Mode 1

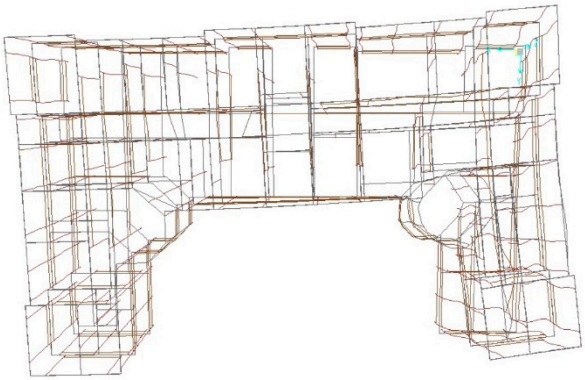

Mode 2

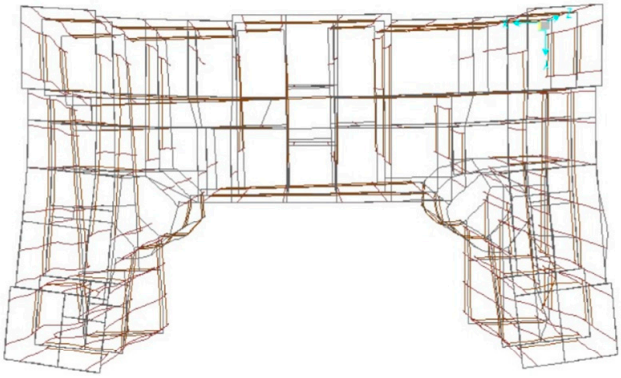

Mode 3

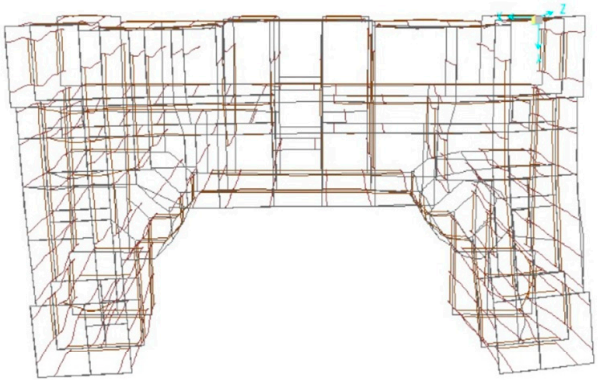

Mode 4

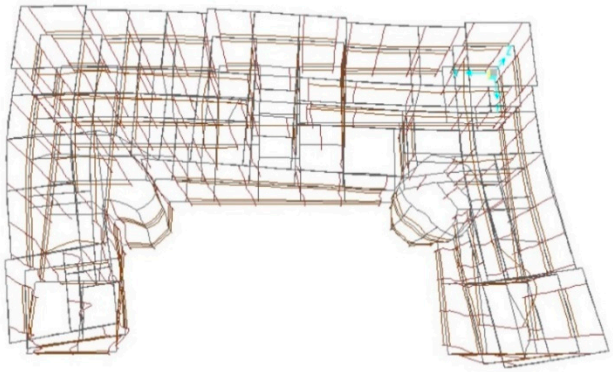

Mode 5

**Figure 12.** First five modal shapes.

## 5. Push-Over and Response Spectrum Analyses

As is well known, the pushover analysis consists of applying different distributions of monotonically increasing horizontal forces at the floors of the building. When the forces are increased, a target displacement of a control node is observed to obtain a force–displacement capacity curve. The force is the base total shear resultant, while the centre of the mass of the top level of the building is usually chosen as control node. However, if a significant torsional–translation coupling is present, as in our case, extreme points of the top level should also be considered. This was also performed.

Material nonlinearities were taken into account, in terms of shear and bending or combined axial-bending behaviours, by modelling the walls and masonry spandrels as elastic beam elements with elasto–perfect plastic behaviour at the two ends. As limit values of the shear and moment, those evaluated by Equations (1)–(3) were assumed, from which the corresponding deformation parameter values can be deduced. The collapse

displacement capacity was assumed equal to $d_u = 0.006 \cdot h$ (where $h$ is the equivalent height of the wall) for the shear mechanism, whereas the ultimate limit of 0.008 was established for the rotation for the axial-bending mechanism.

Two different kinds of forces distributions were applied:

- Main distribution, where forces are proportional to one of the main modal shapes in x or y direction, respectively.
- Secondary distribution, in which forces are proportional to the masses.

The two horizontal components of the forces were applied separately, and the effects obtained in the worst case were assumed as the maximum ones.

With reference to the main distribution, the analyses were performed considering in sequence the modes with a significant participating mass. In Figure 13, the two collapse mechanisms, obtained in the case of the first (x direction) and the fourth (y direction) modal shapes, respectively, are shown for comparison. The corresponding force–displacement curves of the structure (Figure 14) were drawn, assuming as control node, in each case, the node that has the largest modal displacement in each case. The curves were bi-linearized through the criterion of energy equality and scaled by means of the participation factors of the considered modes to obtain the capacity curves, which refer to the equivalent one-degree-of-freedom system.

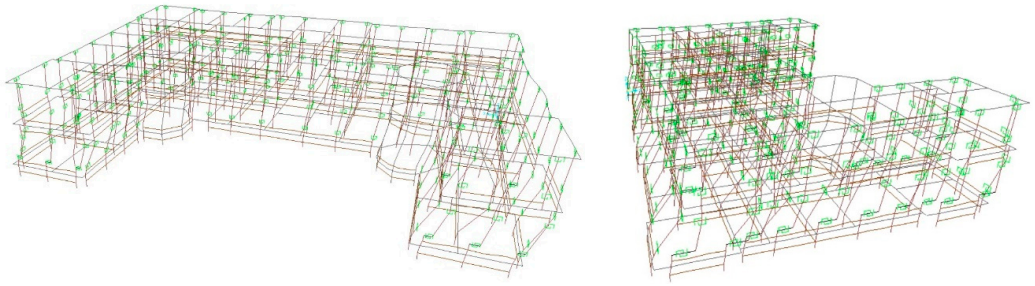

(**a**) (**b**)

**Figure 13.** Collapse mechanisms when force distributions are proportional to (**a**) the first mode and (**b**) the fourth mode (in green are the elasto–perfect plastic elements).

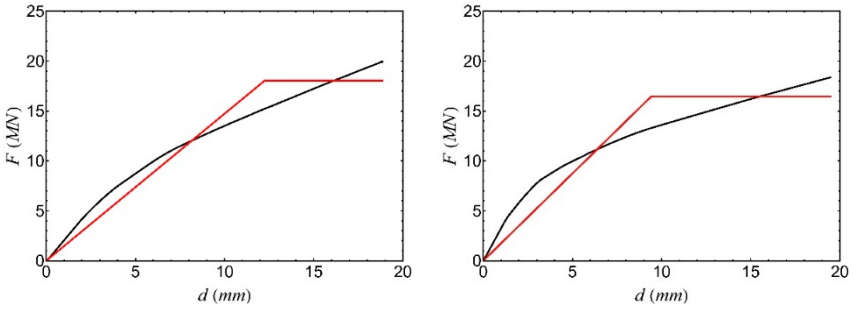


(**a**) (**b**)

**Figure 14.** Force–displacement curves and corresponding bi-linearized curves (red lines) relative to a force distribution proportional to (**a**) the first mode and (**b**) the fourth mode.

As it is evident from the figures, the worst (lower) capacity value corresponds to the fourth mode distribution. The analyses carried out with the secondary distribution of forces showed a higher capacity than those performed by means of the main ones and, therefore, the results herein have been omitted.

The aim of performing a nonlinear static analysis was dual: on the one hand, it was to check the structural seismic capacity $a_{gc}$ (by comparing the capacity curves with the demand requested from the spectrum of the site), and on the other hand, to determine the behaviour factor $q$ (to use in a response spectrum analysis).

- The minimum value of the capacity peak ground acceleration, with reference to the rigid soil, was found to be equal to $a_{gc}$ = 0.151 g and was achieved, as mentioned above, in the case of a force distribution proportional to the fourth mode in y direction. It corresponds to a return period $T_{RC}$ = 139 years.
- According to the Italian Technical Code, the behaviour factor for confined masonry buildings is $q = 2 \cdot \alpha_u/\alpha_1$ . These values must be multiplied by 0.8 if the building is irregular in height. The ratio $\alpha_u/\alpha_1$ , between the 90% of the seismic action at which the structure reaches its maximum strength and the seismic action at which the first masonry panel reaches its ultimate strength, can be evaluated by means of a nonlinear static analysis (but, in any case, it must be $\alpha_u/\alpha_1 \leq 2.5$). In our case study, based on the results of pushover analysis, we computed the value $q$ = 2.5.

However, it should be noted that, in the absence of a nonlinear static analysis, the value of $\alpha_u/\alpha_1$ = 1.6 is suggested by the Italian Technical Code and can be assumed as a reference value. Moreover, for the structural typology under examination, the experimental results on models are also available in the literature. In [43], the authors found a behaviour factor $q$ = 2.9 for the models tested on the shaking table. However, they recommended a value $q$ = 2 for confined masonry to account for any irregularity of the building and the succession and localization of the plasticization that led to the collapse.

Given the uncertainties in modelling this structural typology, the vulnerability was also evaluated by means of a linear response spectrum analysis, reducing the elastic response spectrum with the behaviour factor $q$ = 2.5 previously evaluated from the push-over analysis.

Figure 15a–d show the elements with a capacity/demand ratio (i.e., seismic the safety index) lower than 1 ($T_R$ = 475 years), whereas in Figure 16a,b, the few elements unable to support the demand for $T_R$ = 140 years are highlighted. It is therefore evident that the capacity peak ground acceleration obtained with the response spectrum analysis is very close to that obtained with the nonlinear static analysis.

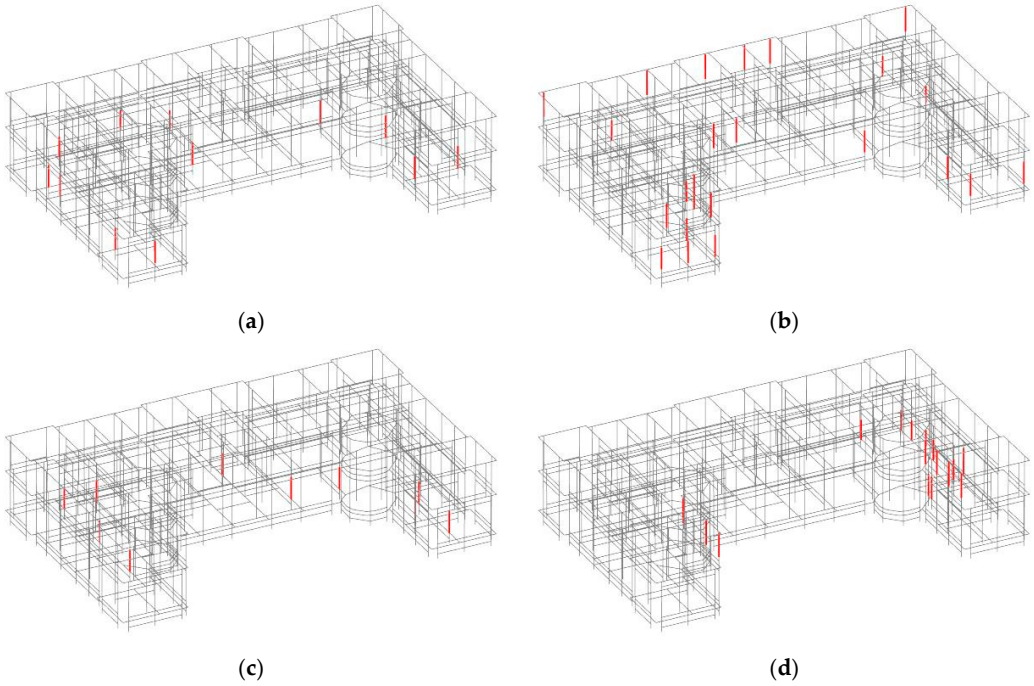


**Figure 15.** Elements (in red) exceeding seismic demand at SLV ($T_R$ = 475 years) for linear analysis: (**a**) shear for prevalent seismic action along x; (**b**) axial and flexural forces for prevalent seismic action along x; (**c**) shear for prevalent seismic action along y; (**d**) axial and flexural forces for prevalent seismic action along y.

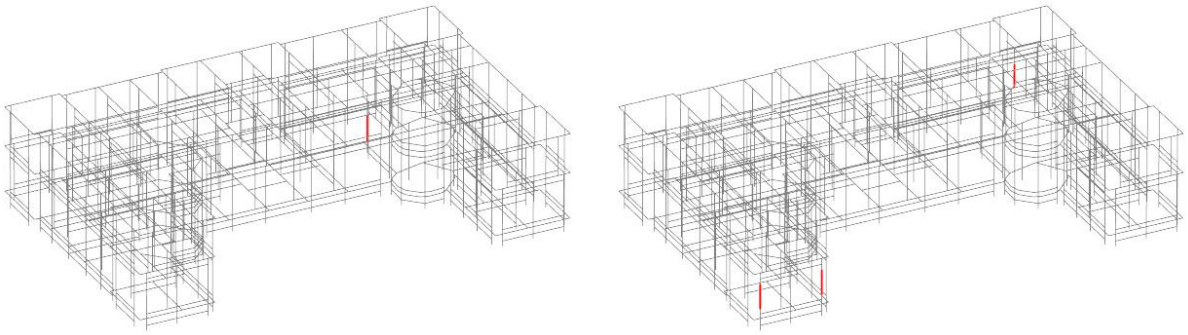

(**a**) (**b**)

**Figure 16.** Elements (in red) exceeding seismic demand when the spectrum corresponding to $T_R$ = 140 years is used, for linear analysis: (**a**) shear; (**b**) axial and flexural forces for x-directed main seismic component.

## 6. Conclusions

The knowledge of an old masonry building is quite a hard task. Information about the material characteristics and structural details, such as the connections between the vertical walls and between these and the floors, are often missing and a reliable evaluation is impossible in practice. The experimental analysis represents the best and at times the only way to obtain reliable data. In particular, the experimental vibration analysis allows for analysing the actual behaviour in a dynamic condition and provides precious information for setting up a suitable numerical model to simulate the behaviour under seismic actions.

Keeping in mind these considerations, the knowledge process of a historic building has been presented in this paper. It represents a typical building realized during the reconstruction after the 1915 Avezzano earthquake, made of confined masonry and with deformable floors. The effects of these characteristics were pointed out by the analyses of the data obtained from an accurate experimental vibration campaign, both in time and frequency domains. The combined use of frequency and time domain analyses, in fact, allowed for highlighting the important features of the structural behaviour, mainly related to the deformability of the floors in their own plane. Resonance frequencies, modal shapes and the preferred movements of significant points of the floors were found.

The knowledge of these features allowed for the setting up of a finite element model. Confined masonry walls were modelled as elastic beam elements with elasto–perfect plastic behaviour at their ends, which takes into account both the contribution of the masonry and the reinforced concrete elements. Material characteristics were defined on the basis of the experimental results and following the literature on the subject. The better performance of the confined masonry was accounted for in terms of strength, by introducing appropriate factors, and behaviour factor of the building.

The numerical model reproduced quite well the actual modal shapes of the building and was used to evaluate its seismic capacity. Both nonlinear static and linear dynamic analyses were performed, which presented similar results in terms of structural capacity. The analysis also highlighted the weakest elements for shear and axial-bending mechanisms, which is useful information for any retrofit intervention.

A comparison with the corresponding rigid floor building and a proposal for the seismic improvement are the main steps for future developments.

**Author Contributions:** Conceptualization, C.T., F.S., P.C., G.B. (Giacomo Buffarini) and G.B. (Giovanni Bongiovanni); methodology, C.T., F.S., P.C., G.B. (Giacomo Buffarini) and G.B. (Giovanni Bongiovanni); software, C.T., F.S., P.C., G.B. (Giacomo Buffarini) and G.B. (Giovanni Bongiovanni); validation, C.T., F.S., P.C., G.B. (Giacomo Buffarini) and G.B. (Giovanni Bongiovanni); formal analysis, C.T., F.S., P.C., G.B. (Giacomo Buffarini) and G.B. (Giovanni Bongiovanni); investigation, C.T., F.S., P.C., G.B. (Giacomo Buffarini) and G.B. (Giovanni Bongiovanni); resources, C.T., F.S., P.C., G.B. (Giacomo Buffarini) and G.B. (Giovanni Bongiovanni); data curation, C.T., F.S., P.C., G.B. (Giacomo Buffarini)

and G.B. (Giovanni Bongiovanni); writing—original draft preparation, C.T., F.S., P.C., G.B. (Giacomo Buffarini) and G.B. (Giovanni Bongiovanni); writing—review and editing, C.T., F.S., P.C., G.B. (Giacomo Buffarini) and G.B. (Giovanni Bongiovanni); visualization, C.T., F.S., P.C., G.B. (Giacomo Buffarini) and G.B. (Giovanni Bongiovanni); supervision, C.T., F.S., P.C., G.B. (Giacomo Buffarini) and G.B. (Giovanni Bongiovanni); project administration, P.C. and G.B. (Giacomo Buffarini); funding acquisition, P.C. and G.B. (Giacomo Buffarini) All authors have read and agreed to the published version of the manuscript.

**Funding:** This research received no external funding.

**Data Availability Statement:** Not applicable.

**Acknowledgments:** The research work leading to this paper has been the result of a joint effort between ENEA and the Municipality of Avezzano, Italy, for the evaluation and structural health monitoring of strategic historic buildings in the city of Avezzano.

**Conflicts of Interest:** The authors declare no conflict of interest.

## References

1. Rossi, M.; Bournas, D. Structural Health Monitoring and Management of Cultural Heritage Structures: A State-of-the-Art Review. *Appl. Sci.* **2023**, *13*, 6450. [CrossRef]
2. Pierdicca, A.; Clementi, F.; Isidori, D.; Concettoni, E.; Cristalli, C.; Lenci, S. Numerical model upgrading of a historical masonry palace monitored with a wireless sensor network. *Int. J. Mason. Res. Innov.* **2016**, *1*, 74. [CrossRef]
3. Bongiovanni, G.; Buffarini, G.; Clemente, P.; Rinaldis, D.; Saitta, F. Experimental vibration analyses of a historic tower structure. *J. Civ. Struct. Health Monit.* **2017**, *7*, 601–613. [CrossRef]
4. Bongiovanni, G.; Buffarini, G.; Clemente, P.; Saitta, F. Time and Frequency Domain Analyses in the Experimental Dynamic Behaviour of the Marcus Aurelius' Column. *Int. J. Arch. Heritage* **2019**, *15*, 64–78. [CrossRef]
5. Bongiovanni, G.; Buffarini, G.; Clemente, P.; Rinaldis, D.; Saitta, F. Dynamic Characteristics of the Amphitheatrum Flavium northern wall from traffic-induced vibrations. *Ann. Geophys.* **2017**, *60*, S0439. [CrossRef]
6. Bongiovanni, G.; Çelebi, M.; Clemente, P. The flaminio obelisk in Rome: Vibrational characteristics as part of preservation efforts. *Earthq. Eng. Struct. Dyn.* **1990**, *19*, 107–118. [CrossRef]
7. Puzzilli, L.M.; Bongiovanni, G.; Clemente, P.; Di Fiore, V.; Verrubbi, V. Effects of Anthropic and Ambient Vibrations on Archaeological Sites: The Case of the Circus Maximus in Rome. *Geosciences* **2021**, *11*, 463. [CrossRef]
8. Pellegrini, D.; Barontini, A.; Girardi, M.; Lourenço, P.; Masciotta, M.; Mendes, N.; Padovani, C.; Ramos, L. Effects of temperature variations on the modal properties of masonry structures: An experimental-based numerical modelling approach. *Structures* **2023**, *53*, 595–613. [CrossRef]
9. Zonno, G.; Aguilar, R.; Boroschek, R.; Lourenço, P.B. Experimental analysis of the thermohygrometric effects on the dynamic behavior of adobe systems. *Constr. Build. Mater.* **2019**, *208*, 158–174. [CrossRef]
10. Azzara, R.M.; De Roeck, G.; Girardi, M.; Padovani, C.; Pellegrini, D.; Reynders, E. The influence of environmental parameters on the dynamic behaviour of the San Frediano bell tower in Lucca. *Eng. Struct.* **2018**, *156*, 175–187. [CrossRef]
11. Saisi, A.; Gentile, C.; Ruccolo, A. Continuous monitoring of a challenging heritage tower in Monza, Italy. *J. Civ. Struct. Health Monit.* **2017**, *8*, 77–90. [CrossRef]
12. Gentile, C.; Guidobaldi, M.; Saisi, A. One-year dynamic monitoring of a historic tower: Damage detection under changing environment. *Meccanica* **2016**, *51*, 2873–2889. [CrossRef]
13. Ramos, L.F.; Marques, L.; Lourenço, P.B.; De Roeck, G.; Campos-Costa, A.; Roque, J. Monitoring historical masonry structures with operational modal analysis: Two case studies. *Mech. Syst. Signal Process.* **2010**, *24*, 1291–1305. [CrossRef]
14. De Angelis, A.; Lourenço, P.B.; Sica, S.; Pecce, M.R. Influence of the ground on the structural identification of a bell-tower by ambient vibration testing. *Soil Dyn. Earthq. Eng.* **2022**, *155*, 107102. [CrossRef]
15. De Stefano, A.; Matta, E.; Clemente, P. Structural health monitoring of historical heritage in Italy: Some relevant experiences. *J. Civ. Struct. Health Monit.* **2016**, *6*, 83–106. [CrossRef]
16. Chiorino, M.A.; Ceravolo, R.; Spadafor, A.; Fragonara, L.Z.; Abbiati, G. Dynamic Characterization of Complex Masonry Structures: The Sanctuary of Vicoforte. *Int. J. Arch. Heritage* **2011**, *5*, 296–314. [CrossRef]
17. Clemente, P. Extending the life-span of cultural heritage structures. *J. Civ. Struct. Health Monit.* **2018**, *8*, 171–179. [CrossRef]
18. De Canio, G.; Muscolino, G.; Palmeri, A.; Poggi, M.; Clemente, P. Shaking Table Tests Validating Two Strengthening Interventions on Masonry Buildings. In Proceedings of the AIP Conference Proceedings, 2008 Seismic Engineering International Conference commemorating the 1908 Messina and Reggio Calabria Earthquake, MERCEA'08, Reggio Calabria, Italy, 24–27 June 2008; American Institute of Physics: Melville, NY, USA; Volume 1020, pp. 896–903. [CrossRef]
19. Pepi, C.; Cavalagli, N.; Gusella, V.; Gioffrè, M. Damage detection via modal analysis of masonry structures using shaking table tests. *Earthq. Eng. Struct. Dyn.* **2021**, *50*, 2077–2097. [CrossRef]

20. Boccamazzo, A.; Di Emidio, G.; Diotaiuti, G.; Dudine, A.; Asta, A.D.; Micozzi, F.; Morici, M.; Liberatore, D.; Addessi, D.; Buffarini, G.; et al. Push 'o ver: A pushover test program on an existing brickwork construction. *Procedia Struct. Integr.* **2023**, *44*, 51–58. [CrossRef]
21. Clemente, P.; Rinaldis, D.; Buffarini, G. Experimental Seismic Analysis of a Historical Building. *J. Intell. Mater. Syst. Struct.* **2007**, *18*, 777–784. [CrossRef]
22. Clemente, P.; Delmonaco, G.; Puzzilli, L.M.; Saitta, F. Stability and seismic vulnerability of the stylite tower at umm ar-rasas. *Ann. Geophys.* **2019**, *61*, 49. [CrossRef]
23. Aras, F.; Krstevska, L.; Altay, G.; Tashkov, L. Experimental and numerical modal analyses of a historical masonry palace. *Constr. Build. Mater.* **2011**, *25*, 81–91. [CrossRef]
24. Misir, I.S.; Yucel, G. Numerical Model Calibration and a Parametric Study Based on the Out-Of-Plane Drift Capacity of Stone Masonry Walls. *Buildings* **2023**, *13*, 437. [CrossRef]
25. Sivori, D.; Lepidi, M.; Cattari, S. Ambient vibration tools to validate the rigid diaphragm assumption in the seismic assessment of buildings. *Earthq. Eng. Struct. Dyn.* **2019**, *49*, 194–211. [CrossRef]
26. Pagnoni, T. Seismic analysis of masonry and block structures with the discrete element method. In Proceedings of the 10th European Conference on Earthquake Engineering, Vienna, Austria, 28 August–2 September 1994; Volume 3, pp. 1669–1674.
27. Lemos, J.V. Discrete Element Modeling of Masonry Structures. *Int. J. Arch. Heritage* **2007**, *1*, 190–213. [CrossRef]
28. Pulatsu, B.; Erdogmus, E.; Lourenço, P.B.; Lemos, J.V.; Tuncay, K. Simulation of the in-plane structural behavior of unreinforced masonry walls and buildings using DEM. *Structures* **2020**, *27*, 2274–2287. [CrossRef]
29. Du, H.; Yu, J.; Wang, Y.; Zhu, Y.; Tang, Y.; Wang, H. Visualized Failure Prediction for the Masonry Great Wall. *Buildings* **2022**, *12*, 2224. [CrossRef]
30. Clemente, P.; Buffarini, G. Dynamic Response of Buildings of the Cultural Heritage. In *Enciclopedia of Structural Health Monitoring*; Boller, C., Chang, F.K., Fujino, Y., Eds.; John Wiley & Sons Ltd.: Chichester, UK, 2009; pp. 2243–2252. ISBN 978-0-470-05822-0. [CrossRef]
31. De Stefano, A.; Clemente, P. Structural health monitoring of historical structures. In *Structural Health Monitoring of Civil Infrastructure Systems*; Karbhari, V.M., Ansari, F., Eds.; Woodhead Publishing Ltd.: Cambridge, UK, 2009; Chapter 13; pp. 412–434. [CrossRef]
32. Giraldo, D.F.; Song, W.; Dyke, S.J.; Caicedo, J.M. Modal Identification through Ambient Vibration: Comparative Study. *J. Eng. Mech.* **2009**, *135*, 759–770. [CrossRef]
33. De Sortis, A.; Antonacci, E.; Vestroni, F. Dynamic identification of a masonry building using forced vibration tests. *Eng. Struct.* **2005**, *27*, 155–165. [CrossRef]
34. Lorenzoni, F.; Casarin, F.; Caldon, M.; Islami, K.; Modena, C. Uncertainty quantification in structural health monitoring: Applications on cultural heritage buildings. *Mech. Syst. Signal Process.* **2016**, *66–67*, 268–281. [CrossRef]
35. Pachón, P.; Infantes, M.; Cámara, M.; Compán, V.; García-Macías, E.; Friswell, M.I.; Castro-Triguero, R. Evaluation of optimal sensor placement algorithms for the Structural Health Monitoring of architectural heritage. Application to the Monastery of San Jerónimo de Buenavista (Seville, Spain). *Eng. Struct.* **2019**, *202*, 109843. [CrossRef]
36. Bongiovanni, G.; Buffarini, G.; Clemente, P.; Saitta, F.; Tripepi, C. Experimental analysis of the Torlonia Building in Avezzano, Italy. In Proceedings of the 7th International Conference on Advances in Experimental Structural Engineering, Pavia, Italy, 6–8 September 2017; EUCENTRE Foundation, Pavia, Italy: 2017. 2017; pp. 841–853. [CrossRef]
37. NTC 2018. Aggiornamento delle Norme Tecniche per le Costruzioni. DM MIT 17 January 2018, Supplemento Ordinario n. 8 alla Gazzetta Ufficiale, 2018, Serie Generale n. 42 of 20 February 2018. Available online: https://www.gazzettaufficiale.it/eli/gu/2018/02/20/42/so/8/sg/pdf (accessed on 5 May 2023).
38. Circ. MIT 7/2019. Istruzioni per l'applicazione dell'«Aggiornamento delle "Norme tecniche per le costruzioni"» di cui al DM 17 gennaio 2018, Circolare C.S.LL.PP. n. 7, 21 gennaio 2019, Gazzetta Ufficiale n. 35/2019. Available online: https://www.gazzettaufficiale.it/eli/gu/2019/02/11/35/so/5/sg/pdf (accessed on 5 May 2023).
39. EN 1996. Design of Masonry Structures. Eurocode 6, CEN 2022. Available online: https://eurocodes.jrc.ec.europa.eu/EN-Eurocodes/eurocode-6-design-masonry-structures (accessed on 5 May 2023).
40. Tomaževič, M.; Klemenc, I. Seismic behaviour of confined masonry walls. *Earthq. Eng. Struct. Dyn.* **1997**, *26*, 1059–1071. [CrossRef]
41. Ahmad, N.; Ali, Z.; Ashraf, M.; Alam, B. Performance assessment of low–rise confined masonry structures for Earthquake induced ground motions. *Int. J. Civ. Struct. Eng.* **2012**, *2*, 842–859. [CrossRef]
42. Magenes, G.; Della Fontana, A. Simplified non-linear seismic analysis of masonry buildings. In Proceedings of the British Masonry Society, London, UK, 13–15 October 1998.
43. Tomaževič, M.; Bosiljkov, V.; Weiss, P. Structural Behaviour Factor for Masonry Structures. In Proceedings of the 13th World Conference on Earthquake Engineering (13WCEE), Vancouver, BC, Canada, 1–6 August 2004.

*buildings*

MDPI

*Article*

# An Open Database to Evaluate the Fundamental Frequency of Historical Masonry Towers through Empirical and Physics-Based Formulations

**Arnaud Montabert [1,*,†], Cédric Giry [1,*,†], Claire Limoge Schraen [2], Jade Lépine [3], Clarisse Choueiri [3], E. Diego Mercerat [4] and Philippe Guéguen [5]**

[1] Université Paris-Saclay, ENS Paris-Saclay, CentraleSupélec, CNRS, LMPS—Laboratoire de Mécanique Paris-Saclay, 91190 Gif-sur-Yvette, France
[2] Equilibre Structures, 10 Rue Saint Nicolas, 75012 Paris, France; c.schraen@unanimesentier.onmicrosoft.com
[3] Université Paris-Saclay, ENS Paris-Saclay, Department of Civil and Environmental Engineering, 91190 Gif-sur-Yvette, France; jade.lepine@ens-paris-saclay.fr (J.L.); clarisse.choueiri@ens-paris-saclay.fr (C.C.)
[4] Equipe REPSODY, CEREMA Méditerranée, 500 Route des Lucioles, 06903 Sophia Antipolis, France; diego.mercerat@cerema.fr
[5] ISTerre, Université Grenoble Alpes, CNRS, IRD, Université Savoie Mont-Blanc, Université Gustave Eiffel, 38058 Grenoble, France; philippe.gueguen@univ-grenoble-alpes.fr
* Correspondence: arnaud.montabert@ens-paris-saclay.fr (A.M.); cedric.giry@ens-paris-saclay.fr (C.G.)
† These authors contributed equally to this work.

**Abstract:** The fundamental frequency plays a primary role in the dynamic assessment of Cultural Heritage towers. Local and global features may impact its value: geometric, material features, interaction with the soil and adjacent buildings, aging, the construction phase, and repairs. A database is assembled to study the relationship between the fundamental frequency and the slender masonry structure features. Empirical and physics-based approaches were developed to assess the fundamental frequency from different sources of information. A Rayleigh–Ritz approach is proposed and compared with a 3D finite element model. A sensitivity analysis is then performed to quantify the contribution of each feature. As expected, it is shown that the height of the tower contributes the most to the fundamental frequency. The other tower features have a second-order impact on both the fundamental frequency and the mode shape. A comparison between the different approaches shows that the Rayleigh–Ritz drastically minimizes the difference between numerical and experimental frequencies when all information is available. Empirical relations are a good compromise when less information is available.

**Keywords:** slender structures; historical structures; masonry; operational modal analysis; Rayleigh–Ritz; database; sensitivity analysis



**Citation:** Montabert, A.; Giry, C.; Limoge Schraen, C.; Lépine, J.; Choueiri, C.; Mercerat, E.D.; Guéguen, P. An Open Database to Evaluate the Fundamental Frequency of Historical Masonry Towers through Empirical and Physics-Based Formulations. *Buildings* **2023**, *13*, 2168. https://doi.org/10.3390/buildings13092168

Academic Editor: Bartolomeo Pantò

Received: 25 July 2023
Revised: 19 August 2023
Accepted: 22 August 2023
Published: 26 August 2023



## 1. Introduction

Masonry towers belong to a peculiar structural typology in Cultural Heritage buildings. They are mainly diffused in the form of defensive towers, bell towers, clock towers, watch towers, etc., and can be found in every place in the world. Because they bear witness to a history spanning several centuries, they are a capital of irreplaceable cultural, social, environmental, and economic values. However, science can play a fundamental role in increasing and disseminating knowledge about heritage towers' history, composition, and behavior. This work is an opportunity to share with the community a database of historic slender heritage structures, as well as tools to help protect them, following on from previous pioneering works, e.g., [1–3].

The historical structures were mainly designed to withstand only vertical loads. They are, however, particularly vulnerable to seismic activity. The last Italian earthquakes in

L'Aquila (April 2009), Emilia-Romagna (May 2012), and Amatrice (August 2016), highlighted the high seismic vulnerability of the specific typology of slender masonry structures. The weak mechanical properties, the geometric features of the structure, and the soil–structure interaction generally explain this vulnerability.

Since the first mode of slender structures generally exhibits the highest mass participation, the value of the fundamental frequency plays a prominent role in assessing its dynamic behavior [4]. Its evaluation is suggested in some codes and provisions, such as the Italian guidelines for the assessment and mitigation of the seismic risk to cultural heritage [5], where their dynamic behavior is roughly comparable to either a cantilever equivalent beam or those that can be obtained from trustworthy simplified formulations.

On the other hand, modal parameters may be extracted from vibration measurements through operational modal analysis (see [6] for a review). This non-invasive dynamic identification is particularly suitable for Cultural Heritage structures. In the last decade, databases of the dynamic properties, materials, and geometric features of slender masonry structures have been assembled [1–3,7]. It has opened new opportunities to challenge the classical simple formulations and to design empirical formulations to estimate the fundamental frequency of slender masonry towers. The contribution of other parameters like the interaction with adjacent buildings [8] and the openings have been evaluated [2]. Despite considering many global features, we note the persistent variability of the fundamental frequency, which prompts us to consider more local features. Cultural heritage buildings may be strongly affected by the construction history, aging, repairs, retrofitting actions, bell systems, etc., e.g., [9].

In this work, we propose to quantify the contribution of global and local features when evaluating the fundamental frequency of slender masonry towers. The first step aims to gather existing databases [1–3,7], extended by a survey performed by the authors and isolated studies identified from an exhaustive literature review. Additional features have been added, such as the construction periods, local geometric features (thickness, openings geometry), and details about the measured fundamental frequency, the setup of the vibration analysis survey, and the technique used to identify modal parameters. The Towers featURes & fRequencIes databaSe (TURRIS) database is first described. Descriptive statistics provide information on the parameters well constrained by the data, which is necessary to study their impact on the fundamental frequency using the models proposed in the following section. Instrumentation practices and the extraction of modal characteristics also make it possible to discuss potential sources of uncertainty in fundamental frequency identification. We update empirical and physics-based models derived from existing relations found in the literature [1,10–15] to consider the tower dynamic features. The regression coefficients of the empirical formulations are updated. Empirical and physics-based models are then tested and discussed in light of the collected database. Additional parameters, such as the interaction with the soil, adjacent buildings, and the bells system, are then used in the Euler–Bernoulli beam formulation to test their impact on the dynamic properties. A semi-analytical Rayleigh–Ritz approach is then introduced to evaluate the dynamic properties of slender masonry structures. The formulation is calibrated through a comparison with a 3D finite element model. The results of evaluating the fundamental frequencies using empirical, physics-based, and Rayleigh–Ritz approaches are discussed. A sensitivity analysis based on the Random Balance Design Fourier-Amplitude Sensitivity Test (RBD-FAST) is used to test the sensitivity of the fundamental frequency to the structural features when using the Rayleigh–Ritz approach. The limits of the values of the parameters tested are taken from the descriptive statistical analysis of the database. It allows us to discuss future experimental efforts required to constrain the evaluation of the fundamental frequency. A significant result of this work is sharing a database and codes for evaluating the fundamental frequency of slender structures using empirical, physics-based models and Rayleigh–Ritz formulation. Both are available at the following GitHub link: https://github.com/MArnaud/TURRIS [16].

## 2. Masonry Towers Database

### *2.1. Parameters Describing the Towers*

In the TURRIS database, the towers are described in terms of the associated literature reference; tower location (town, geographic coordinates); tower name; modal, geometric, and material parameters; construction period; details about the instrumental survey; and type of modal parameter identification technique. Modal parameters consist of the measured natural frequencies and the nature of the mode shape described in each reviewed paper. The geometry of each tower is simply described from its total and effective height (i.e., the height of the portion of the tower that is free from the restraint offered by adjacent buildings); the dimension of the ground section (length, width); the minimum and maximum thickness of walls; dimensions of openings (altitude, height, and width); its relation with adjacent buildings (isolated or bounded); and the mass of bells. Material parameters are described with the density, Young modulus, and Poisson's ratio. When available, the year or the century of construction is specified. The instrumental surveys are detailed with the type of instruments, the campaign duration, and the sampling of records.

### *2.2. Compilation of Data Collection*

The data is assembled through an extensive literature review, including previously compiled data collections, isolated studies, and the authors' recent measurements (references, e.g., [1–3,7,8,12,13,17–181]). Values from previous data collection have been cross-checked, and additional information from the original papers has been included. Figure 1 highlights the number of instrumented slender masonry structures through time. The first instrumentation of a masonry tower was performed in 1989 [24]. We note some remarkable data collection. In 1995, Lund et al. [7] reported the vibration results of 19 old masonry towers in the Northeast of England to investigate the impact of the English bells system on the bell towers' behaviors (LU collection). In 2007 and 2009, Schmidt [17,18] presented experimental investigations of 16 twin bell towers in Saxony-Anhalt (Germany) and investigated the relationship between the natural frequencies and the geometric parameters of the towers (SC collection). In 2011, Rainieri and Fabbrocino [19] conducted an output-only modal identification of nine masonry towers (RF collection) in the Molise Region (Southern Italy) and compared the measured fundamental frequencies with the empirical relation provided by the Italian Seismic Code (NTC2008, [182]). In 2016, Limoge [20] reported an extensive dynamic identification survey of 20 baroque churches in French Savoy (France) to conduct a large-scale vibration-based model updating process (LI collection). In 2017, the Ziegler consultant group [21] published a report for the dynamic assessment of 18 masonry towers in Switzerland (Z collection). In 2020, Ruiz-Jaramillo et al. [22] conducted a large-scale survey of 21 watchtowers along the Southeast Spanish coast, providing valuable data for low-rise masonry towers (RJ collection). As part of the ACROSS ANR project, Mercerat et al. [23] identify the modal parameters of six medieval bell towers in the Mugello area (Tuscany, Italy). Some of the collections have been used in the compiled database proposed by Shakya et al. [1], Bartoli et al. [8], and Pallarès et al. [3].

Before 2011, dynamic identification is mainly performed to investigate the structural response of old towers under service loads, such as bell loads (e.g., [7]). However, the Italian earthquakes (L'Aquila and Amatrice) have led to increasing attention to the seismic behavior of historical structures, inducing an increase in dynamic identification studies.

Figure 2 shows the location of the 244 instrumented Cultural Heritage towers. Italy contributes most extensively to the collection of instrumented towers (44% of instrumented towers), resulting from a dense slender heritage, one of Europe's most significant seismic activities, and a preservation policy since the last damaging Italian earthquakes.

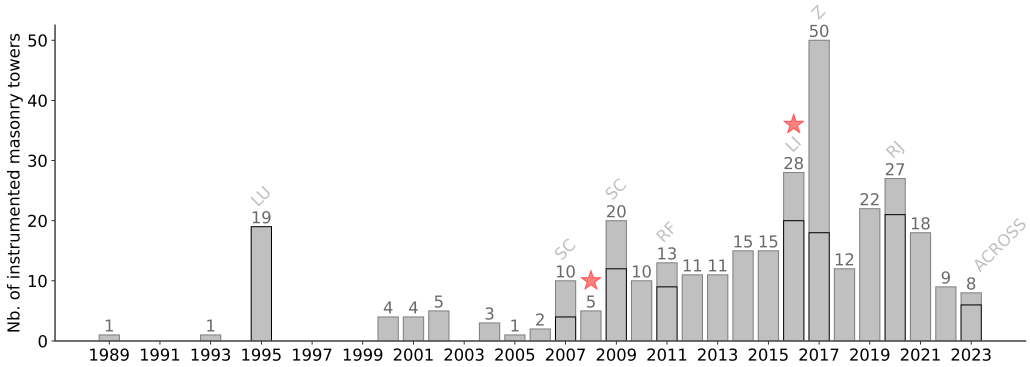


**Figure 1.** Graph of publication year for dynamic identification of slender Cultural Heritage towers in the compiled database for this study. The main previous database collections are indicated with black edge bar: LU [7], SC [17,18], RF [19], LI [20], Z [21], RJ [22], ACROSS [23]. The 2008 L'Aquila and 2016 Amatrice seismic events are reported with a red star.

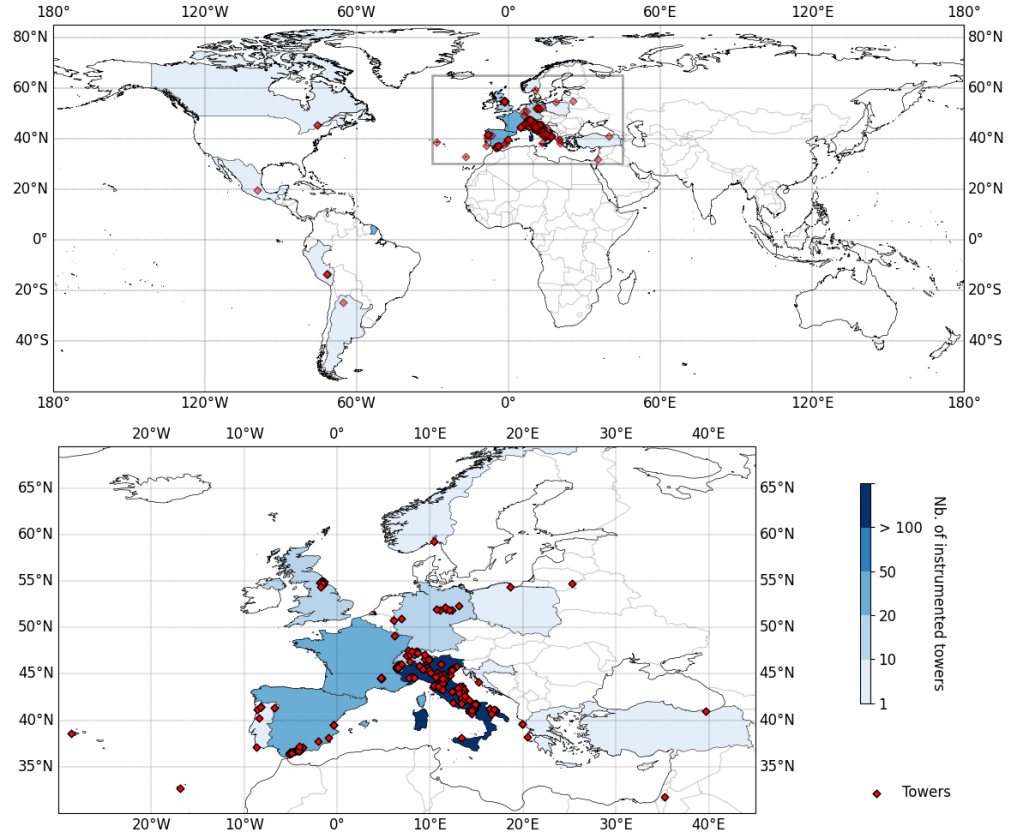


**Figure 2.** Locations of instrumented slender Cultural Heritage towers in the database.

### *2.3. Statistical Description*

Figure 3 depicts the distribution of six geometric parameters of the database: the height $H$, the effective height $H_{eff}$ (defined by [8] as the difference between the absolute height of the tower and the height of its constrained portion), the length $L_s$, the width $\ell_s$, and the minimum and maximum thickness of walls $t_w$. The dimensions were reported from the articles' descriptions or plans when available. When both pieces of information are available, an error in the order of a decimeter is generally observed, which can impact the dynamic properties and then motivate a sensitivity analysis in the rest of the study.

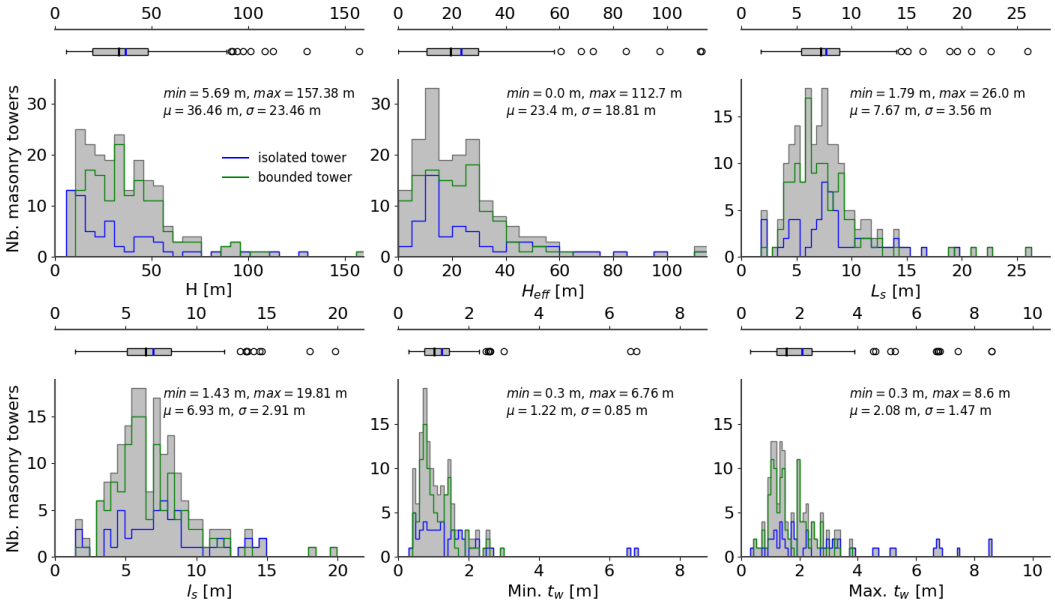


**Figure 3.** Distribution of the geometric parameters of the Cultural Heritage towers assembled in the database: the height $H$, the effective height $H_{eff}$, the length $L_s$, the width $\ell_s$, the minimum and maximum thickness of walls $t_w$. The median and mean values are shown in black and blue, respectively. The distribution of isolated towers is shown in blue. The distribution of the bounded towers is shown in green.

The six parameters highlight a right-skewed bimodal distribution. The bimodal distribution can be explained when distinguishing between isolated and bounded towers. We generally observe small and wide isolated towers but large and narrow linked towers.

The distribution asymmetry reveals only a few historical masonry towers with large dimensions (therefore, insufficient sampling for towers with important geometric characteristics). Indeed, most of the towers (75%) have a height between 5.69 m (water tower number 3 in Pompeii, in [134]) and 48.0 m, an effective height lower than 29.97 m (the database contains 65 isolated towers and 177 bounded towers), a length between 1.79 m and 8.75 m, a width between 1.43 m and 8.2 m, and a wall thickness between 0.3 m and 2.5 m. We note the presence of a few outliers for each parameter. The highest tower (157.38 m) corresponds to the Northern tower of the Cologne cathedral, known as the tallest twin-spired church in the world. The tower of the Universidad Laboral (130.0 m), the Torrazzo di Cremona (112.70 m), the Guglia Maggiore tower of the Duomo (108.50 m), and the twin bell towers of the cathedral in Magdeburg (101.0 m) are among the tallest instrumented towers of this study, and are not representative of the standard dimension of ancient masonry towers. The towers mentioned above also classify as outliers when considering the effective height.

Some remarkable Cultural buildings such as the Tower of Pisa (Italy), the Giotto's bell tower (Italy), the North Tower of the Cologne Cathedral (Germany), the Guglia Maggiore Tower of the Duomo (Italy), the twin bell towers of the Cathedral in Halberstadt (Germany), the Calbe Stephani church (Germany), the Moya tower (Spain), and the Umong pagoda (China) highlight huge section (length and width). The outliers for the wall thickness are mainly composed of the watchtowers along the Spanish coast, since many are filled towers.

Figure 4 shows the material parameter distributions of the masonry towers when available. Most values come from building codes or model updating processes, minimizing the difference between the measured and numerical modal parameters. These values are then indirectly identified. Such an origin should be kept in mind in the rest of the study. Only 42.4% of the reviewed studies provide a value for the Young modulus, 12.5% for the Poisson ratio, and 28% for the density. The Young modulus highlights a right-skewed bimodal distribution. The highest Young modulus values are related to retrofitting actions using concrete that have been considered in the model updating process. They may induce

a bias in the distribution, since they are not masonry. The two modes are observed around 1.52 GPa and 3.96 GPa. Despite the limited number of values, the Poisson ratio and the density have a more symmetric distribution. It is important to note that most studies impose the value of the Poisson ratio.

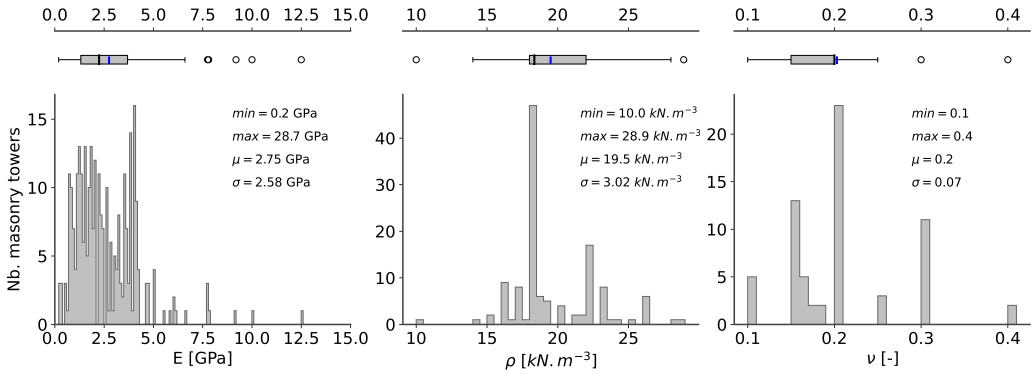


**Figure 4.** Distribution of material parameters of the masonry towers database. The median and mean values are shown in black and blue, respectively.

When the values are available, the mass of the bells is reported in the database. It constitutes an essential mass on top that can impact the modal behavior of the slender structures. The bells are usually located at the top of the tower. Figure 5 again shows an asymmetric distribution of the bell's mass. Among the outliers (over 10,000 kg), there are the church of Nuestra Señora Candelaria de la Viã (Argentina), as well as three bell towers of the French Savoy (LI collection).

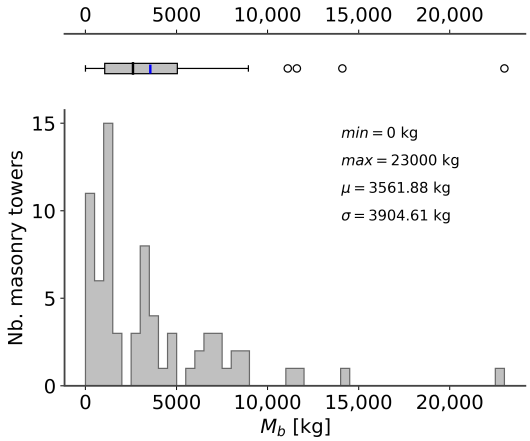


**Figure 5.** Distribution of bell mass of the masonry towers database. The median and mean values are shown in black and blue, respectively.

Figure 6 shows that most of the instrumented towers were built in the medieval period, which induced a potential vulnerability of the structures studied due to the decay of the mechanical properties (mortar and bricks). We note a second group of structures built between the 19th and 20th centuries. The oldest masonry towers are Pompeii's water towers, which date from the 1st century BC.

Figure 7 shows the distribution of the recording times during the OMA survey. Short and long SHM are, respectively, plotted on left and right (long SHM concern surveys lasted more than one day). Most of the studies (83%) consist of a short SHM. The white noise hypothesis in OMA is still debated and may impact dynamic identification. Rodriguez et al. [183] and Cantieni [184] recommended the measurement duration to be at least 2000 times the natural period of interest in the case of slender masonry structures in order to reduce uncertainties. Studies respecting this empirical law are shown in green in Figure 7.

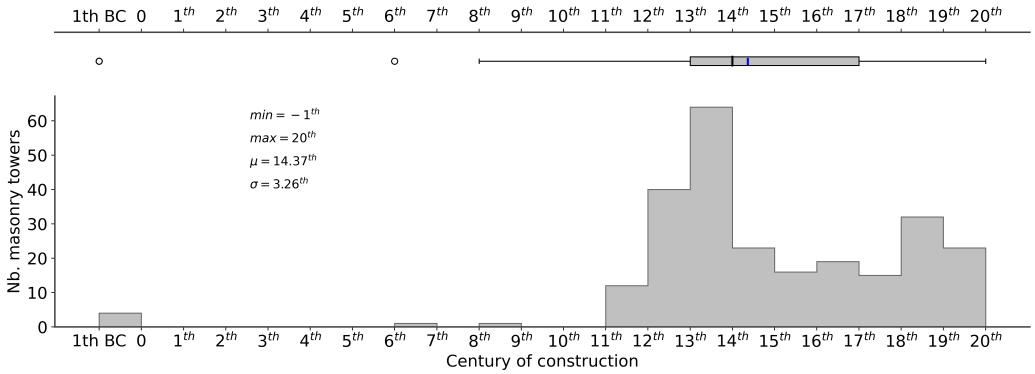


**Figure 6.** Distribution of the century of bell tower construction. The median and mean values are shown in black and blue, respectively.

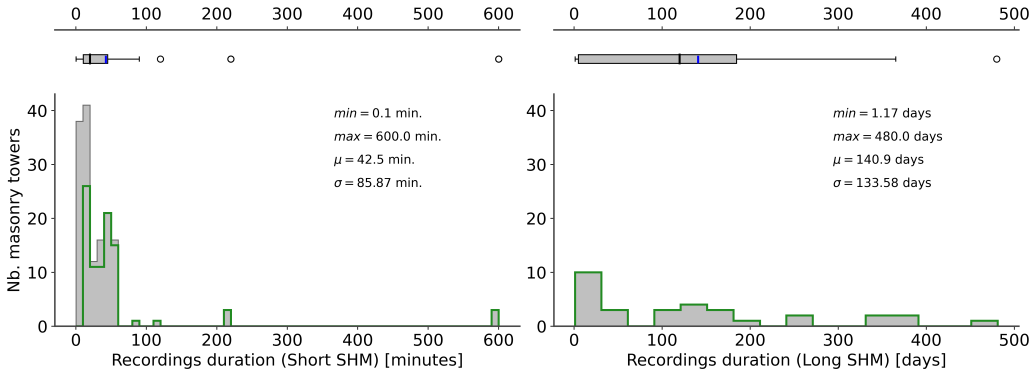


**Figure 7.** Distribution recordings duration during OMA surveys. The median and mean values are shown in black and blue, respectively. Instrumentations respecting a measurement duration longer than 2000 times the natural period of interest established by Rodriguez et al. [183] and Cantieni [184] are shown in green.

Many OMA techniques have been developed in recent decades (Table 1) due to their many advantages: they are a non-invasive, non-destructive method, easy to deploy, and no external source is required. The output-only method is particularly adapted in the context of Cultural Heritage Monitoring since it allows model parameter tracking in a non-invasive way. However, these techniques have different precision to identify natural frequencies. Figure 8 shows the use of the OMA techniques in the dynamic identification of slender masonry structures. Generally, they can be classified into two categories: frequency domain and time domain (in gray and blue, respectively, in Figure 8). Frequency domain techniques have been largely used in masonry towers (69.1%) compared to time domain techniques. The earliest methods are based on a peak-picking algorithm from diverse frequency representations of the record: the power spectral density (PSD), the fast Fourier transform (FFT), the acceleration spectral amplitude (ASA) or displacement (ASD), and the transfer function (TF). The natural frequency is then directly obtained from the choice of the peak. Despite its simplicity, the technique suffers from difficulty in distinguishing close modes, and its limitation of the spectrum frequency resolution contributes to an increase in the uncertainty of the natural frequency identification [185,186]. Peak picking from frequency graphs represents 3% of the data in the masonry tower database. Consequently, the frequency domain decomposition (FDD) was developed to meet the challenge when identifying close modes [187], and is used in 12.5% of the instrumented towers. The structure's response is derived into a set of single-degree-of-freedom systems by introducing a decomposition of the spectral density function matrix. The enhanced FDD (EFDD) has also been introduced to extract the damping ratios, representing 14.23% of the case studies. However, these frequency domain methods are under the assumption that the input signals are stationary Gaussian white noise, and the structure is very lightly damped. At

the same time, methods in the time domain have been developed. Techniques from the experimental modal analysis, such as Random Decrement Technique (RDT) and eigen realization algorithm (ERA), were also successfully extended for the OMA, but have rarely been applied to the dynamic identification of slender masonry towers (one case for the ERA method, and two cases for the RDT technique). Furthermore, much research was spent on subspace identification techniques [188], which constitute 21.5% of the measured frequencies in the masonry towers database. The two primary forms of Stochastic Subspace Identification (SSI) techniques used in the database are Covariance-Driven Stochastic Subspace Identification (COV-SSI) and Data-Driven Stochastic Subspace Identification (DATA-SSI), in 10% and 3%, respectively. A total of 46% of studies using SSI techniques do not specify which method is used (they only mention SSI).

**Table 1.** Acronyms of methods used to extract modal parameters described in this section.

| **Glossary** | |
|---|---|
| TFIE | Time Frequency Instantaneous Estimators |
| PRTD | Polyreference time domain |
| DSPI | Direct system parameter identification |
| SSI | Stochastic Subspace Identification |
| CC-SSI | Crystal Clear Stochastic Subspace Identification method |
| SSI-COV-PC | Principal Component Covariance-Driven Stochastic Subspace Identification |
| SSI-DATA | Data-Driven Stochastic Subspace Identification |
| SSI-DATA-UPC | Unweighted Principal Component Stochastic Subspace Identification |
| SSI-DATA-CVA | Canonical Variate Analysis |
| ASA | Acceleration Spectral Amplitudes |
| ASD | Auto-Spectrum Displacement |
| ERA | Eigensystem realization algorithm |
| SM | stretching method |
| TF | Transfer function |
| SOBI | Second Order Blind Identification |
| PSD | Power Spectral Density |
| SSR | Standard Spectral Ratio |
| SDOF | Single Degree of Freedom technique |
| p-LSCF | Poly-reference Least Squares Complex Frequency-domain |

Figure 9 shows the distribution of the experimental fundamental frequency variation for each instrumented masonry tower. Masonry towers for which there is only a single value of the fundamental frequency are excluded from the figure, as they do not provide any information about the variations in the dynamic properties of the structure studied (83% of the studies). Most of the main frequency variation is between 0.13% and 32.39% (the San Luzi bell tower) and has several origins. Considerable variations in the fundamental frequency are observed before and after restoration works. The SS. Annunziata church bell tower, significantly damaged by an earthquake, shows a fundamental frequency of 1.66 Hz [127] and 1.97 Hz after restoration [32], an increase of 18.7%. In 2005, the Mogadouro Clock Tower was characterized by large cracks, deterioration, and material loss in some parts. Following restoration work in 2005, the fundamental frequency was raised from 2.15 to 2.56 Hz (an increase of 19%). The same phenomenon is observed in the tower of the S. Giorgio church in Trignano. Following the 1996 Reggio Emilia earthquake, restoration works led to the main frequency from 2.43 Hz to 2.7 Hz (an increase of 11% on the fundamental frequency). The bell tower of Sant Andrea Apostolo highlights an increase in its fundamental frequency of 27.08% after retrofitting actions [102,103]. The tower of Notre Dame de l'Assomption, damaged after Le Teil earthquake, highlights a double fundamental frequency peak (Mercerat, personal communication). Structure monitoring over long periods shows significant variations. Monitoring of the San Luzi bell tower over a whole year shows a variation of 32.29% between winter and summer [87]. The bell tower of the church of San Frediano highlights a variation of 14% due to the impact of environmental parameters [67].

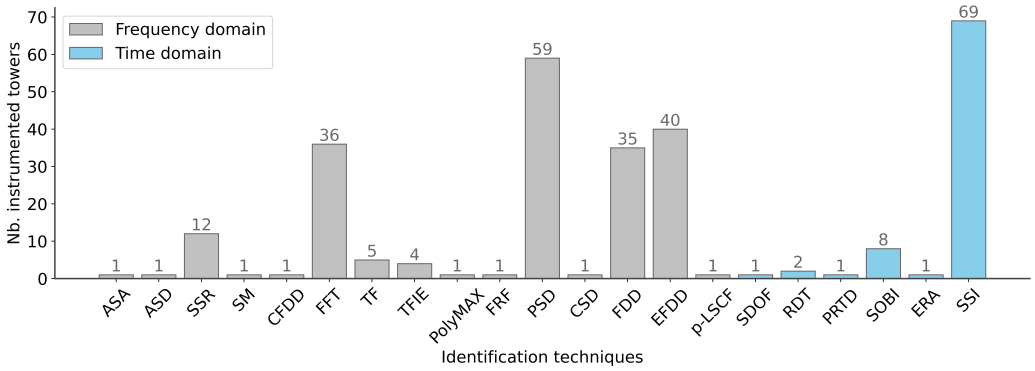


**Figure 8.** Distribution of the identification techniques used in the database. Abbreviations are summarized in the glossary (Table 1).

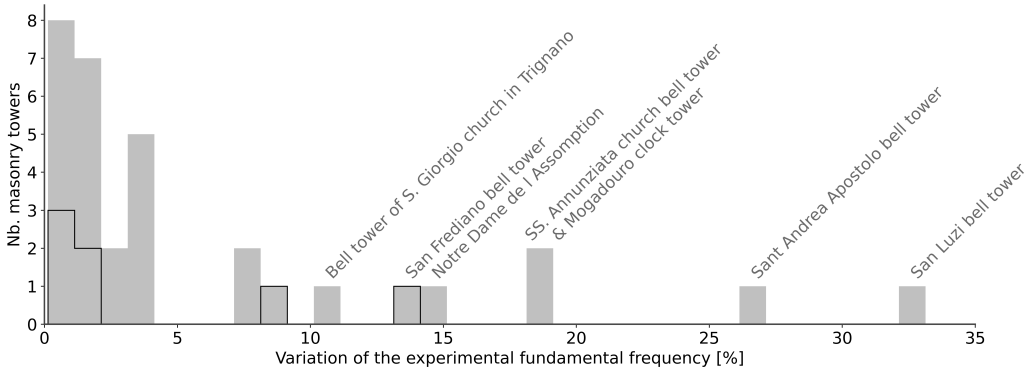


**Figure 9.** Distribution of variation in the measured fundamental frequency expressed as $(f_0^{max} - f_0^{min})/f_0^{min}$, i.e., the maximum difference between the minimum and maximum measured fundamental frequency for each instrumented masonry tower. Long SHM (with measurements duration over one day) are plotted with a dark gray edge.

## 3. Model for the Evaluation of the Fundamental Frequency of the Tower

### *3.1. Empirical Models*

The models exposed here propose to estimate the fundamental frequency of slender masonry structures according to the global geometric parameters expressed in Table 2. To analyze these models, let us define a set of global geometric parameters $\boldsymbol{p}$ that characterize the structures: $\boldsymbol{p} = \{H, \ell_s, h_n\}$. The height of interaction $h_n$ between the tower and any adjacent structures is expressed as $h_n = H - H_{eff}$. Dimensionless parameters are introduced: $\alpha_\ell = \ell_s / H$ and $\alpha_{h_n} = h_n / H$.

In the empirical model's category, we consider models that integrate the main parameters that influence the fundamental frequency of the structures without deriving their expression from mechanical models (e.g., a power law with an exponent identified from a regression process). We introduce the empirical model derived from the reference summarized in Table 3 as follows:

$$f_0(\boldsymbol{p}) = a_1 \cdot H^{b_1} \cdot f_s(\alpha_\ell) \cdot f_e(\alpha_{h_n}) \tag{1}$$

The function associated with the influence of the geometric characteristics of the section $f_s$ is as follows:

$$f_s = (\alpha_\ell)^{b_1^s} \cdot \left(1 + a_1^s \alpha_\ell + a_2^s \alpha_\ell^2 + a_3^s \alpha_\ell^3\right)^{b_2^s} \tag{2}$$

The function associated with the interaction with adjacent structures $f_e$ is as follows:

$$f_e = (1 - \alpha_{h_n})^{b_1^e} \tag{3}$$

**Table 2.** Set of geometric parameters and regression coefficients used in the empirical formulation of geometric models.

| **Nomenclature** | | |
|---|---|---|
| **Symbol** | **Unit** | **Description** |
| Geometric parameters | | |
| $\boldsymbol{p}$ | | Set of global geometric parameters |
| $H$ | [m] | Height of the tower |
| $\ell_s$ | [m] | Width, lowest size of the tower's section |
| $h_n$ | [m] | Height of interaction between the tower and any adjacent structures system |
| $f_0$ | [Hz] | Eigenfrequency |
| Dimensionless parameters | | |
| $\alpha_\ell$ | [-] | Slenderness |
| $\alpha_{h_n}$ | [-] | Interaction factor |
| Regression coefficients | | |
| $b_1$ | [-] | Regression coefficient related to the height |
| $a_1^s$, $b_1^s$, $b_2^s$, $a_2^s$, $a_3^s$ | [-] | Regression coefficient related to the section geometry |
| $b_1^e$ | [-] | Regression coefficient related to lateral interaction |

**Table 3.** Parameters of existing and updated empirical models. Line labeled from Empirical model 1 to 7 correspond to this study.

| **Id. Model** | **Ref.** | $a_1$ | $b_1$ | $a_1^s$ | $b_1^s$ | $b_2^s$ | $a_2^s$ | $a_3^s$ | $b_1^e$ |
|---|---|---|---|---|---|---|---|---|---|
| 1 | [10] | 20 | −3/4 | 0 | 0 | 0 | 0 | 0 | 0 |
| 1 | [11] | 1/0.0187 | −1 | 0 | 0 | 0 | 0 | 0 | 0 |
| 1 | [12] | 1/0.01137 | −1.138 | 0 | 0 | 0 | 0 | 0 | 0 |
| 1 | [1] | 1/0.0151 | −1.08 | 0 | 0 | 0 | 0 | 0 | 0 |
| 1 | [13] [b] | 28.35 | −0.83 | 0 | 0 | 0 | 0 | 0 | 0 |
| 1 | [13] [i] | 135.343 | −1.32 | 0 | 0 | 0 | 0 | 0 | 0 |
| Empirical model 1 | | 22.55 | 2.818 | 0 | 0 | 0 | 0 | 0 | 0 |
| 2 | [1] | 3.58 | 0 | 0 | 0.57 | 0 | 0 | 0 | 0 |
| Empirical model 2 | | 7.608 | 0 | 0 | 0.817 | 0 | 0 | 0 | 0 |
| 3 | [13] [i] | 208.54 | −1.18 | 0 | 0.55 | 0 | 0 | 0 | 0 |
| Empirical model 3 | | 17.113 | −0.369 | 0.538 | 0 | 0 | 0 | 0 | 0 |
| 4 | [14] | 1/0.06 | −0.5 | 2 | 0.5 | 0.5 | 0 | 0 | 0 |
| 4 | [1] | 1/0.03 | −0.83 | 1 | 0.17 | 0.5 | 0 | 0 | 0 |
| Empirical model 4 | | 7.361 | −0.46 | −0.03 | 0 | 3053.821 | 0 | 0 | 0 |
| 5 | [15] | 1/0.0117 | 0 | −9.632 | 3 | −1 | 94.786 | 144.461 | 0 |
| Empirical model 5 | | 0.1 | 0 | −26.78 | 188.47 | 29.40 | −34.47 | 13.93 | 0 |
| 6 | [13] [b] | 12.96 | −0.686 | 0 | 0 | 0 | 0 | 0 | −0.686 |
| Empirical model 6 | | 23.322 | −0.695 | 0 | 0 | 0 | 0 | 0 | −0.028 |
| 7 | [13] [b] | 14.61 | −0.811 | 0 | −0.254 | 0 | 0 | 0 | −0.341 |
| Empirical model 7 | | 17.619 | −0.365 | 0.616 | 0 | 0 | 0 | 0 | −0.171 |

[b] Bounded tower. [i] Isolated tower.

Table 3 lists the coefficient of Equation (1) obtained through regression in the dedicated studies. Empirical models may be separated into seven models based on the parameters used and the power of the monomials. Each model is updated based on the assembled database. The results of the seven regression models (labeled from Empirical model 1 to Empirical model 7 in Table 3) are shown in Figure 10 with their associated coefficient of determination. They range from 0.48 (Empirical model 1) to 0.67 (Empirical model 7). The best prediction is obtained for model 7, taking into account the height of interaction $h_n$. However, this model depicts a coefficient of determination very close to the empirical model 4 that considered only $H$ and $l_s$.

### *3.2. Physics Based Models*

The models exposed here propose to estimate the fundamental frequency of slender masonry structures according to global geometric parameters, geometric section, and mate-

rial characteristics. Table 4 summarizes the parameters considered in these models. The set of global parameters is defined as $\boldsymbol{p} = \{H, \ell_s, h_n, t_w, L_s, E, \rho\}$. Additional dimensionless parameter are introduced: $\alpha_t = \frac{t_w}{\ell_s}$ and $\alpha_L = \frac{L_s}{\ell_s}$.

**Table 4.** Set of geometric and material parameters and regression coefficients used for the physics-based approach.

| **Nomenclature** | | |
|---|---|---|
| **Symbol** | **Unit** | **Description** |
| Geometrical and material parameters | | |
| $\boldsymbol{p}$ | | Set of global geometric parameters |
| $H$ | [m] | Height of the tower |
| $\ell_s$ | [m] | Width, lowest size of the tower's section |
| $h_n$ | [m] | Height of interaction between the tower and any adjacent structures |
| $f_0$ | [Hz] | Fundamental frequency |
| $L_s$ | [m] | Length, largest size of the tower's section |
| $t_w$ | [m] | Wall thickness |
| $h_b$ | [m] | Altitude of the bell system |
| $S$ | [m$^2$] | Surface area |
| $I_{G_x}$, $I_{G_y}$ | [m$^4$] | Second moment of area |
| $r$ | [m] | Radius of inertia |
| $E$ | [MPa] | Young modulus |
| $\rho$ | [kg·m$^{-3}$] | Volumetric mass density |
| Dimensionless parameters | | |
| $\alpha_\ell$ | [-] | Slenderness |
| $\alpha_{h_n}$ | [-] | Interaction factor |
| $\alpha_t$ | [-] | Thickness factor |
| $\alpha_L$ | [-] | Length factor |
| $\alpha_{sh}$, $\alpha^I_{sh}$, $\alpha_\ell$, | [-] | Section factor |
| $\theta$ | [rad.] | Angle of bending direction with respect to x axis |
| Regression coefficients | | |
| $C_1$, $C_2$, $C_3$ | [-] | Regression coefficient |

This second category of models originates from the dynamic characteristics of an equivalent beam model. For a cantilever Euler–Bernoulli beam with homogeneous geometric and material properties, the fundamental frequency is expressed as:

$$f_0 \sim \frac{1.875^2}{2\pi} \cdot \frac{r}{H^2} \cdot \sqrt{\frac{E}{\rho}} \tag{4}$$

Considering classical shapes for the hollow section of the slender structures (see Figure 11, and Table 5), a generic formula can be derived for the radius of inertia $r$.

$$I_{G_x} = \alpha^I_{sh} \cdot \ell_s^4 \cdot \left(\alpha_L - (1-2\alpha_t)^3 \cdot (\alpha_L - 2\alpha_t)\right) = \ell_s^4 \cdot \alpha_{I_x}\left(\alpha^I_{sh}, \alpha_L, \alpha_t\right) \tag{5}$$

$$I_{G_y} = \alpha^I_{sh} \cdot \ell_s^4 \cdot \left(\alpha_L^3 - (1-2\alpha_t) \cdot (\alpha_L - 2\alpha_t)^3\right) = \ell_s^4 \cdot \alpha_{I_y}\left(\alpha^I_{sh}, \alpha_L, \alpha_t\right) \tag{6}$$

$$S = 2 \cdot \alpha^S_{sh} \cdot \ell_s^2 \cdot \alpha_t \cdot (\alpha_L + 1 - 2\alpha_t) = \ell_s^2 \cdot \alpha_A\left(\alpha^I_{sh}, \alpha_L, \alpha_t\right) \tag{7}$$

**Table 5.** Surface and second moment of area for different classical hollow sections of masonry tower (square (SQ), rectangular (REC), and circular (CIR)).

| **Parameters** | **SQ** | **REC** | **CIR** |
|---|---|---|---|
| $\alpha^S_{sh}$ | 1 | 1 | $\pi/4$ |
| $\alpha^I_{sh}$ | 1/12 | 1/12 | $\pi/64$ |
| $\alpha_\ell$ | 1 | >1 | 1 |

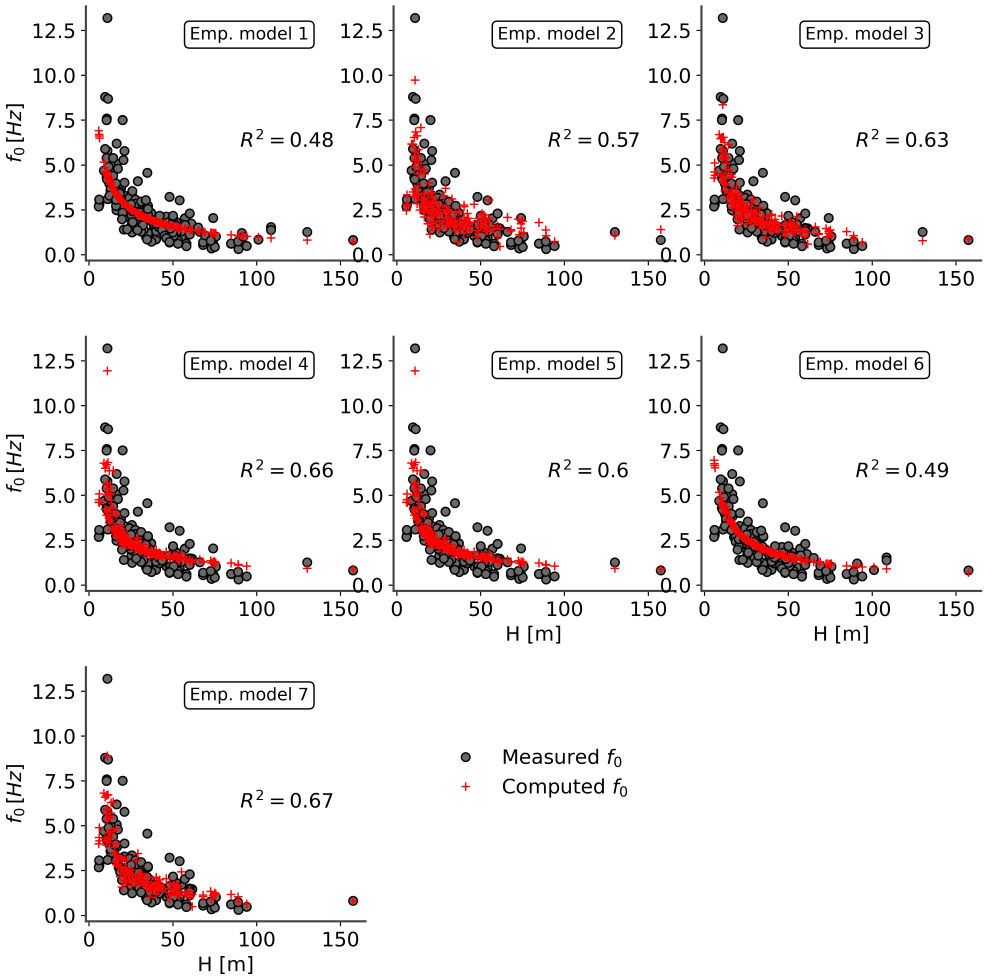


**Figure 10.** Evaluation of the fundamental frequency of towers from experimental natural frequency (gray dot) and empirical models (red cross) (labeled from Empirical model 1 to Empirical model 7 in Table 3) as a function of the tower's height.

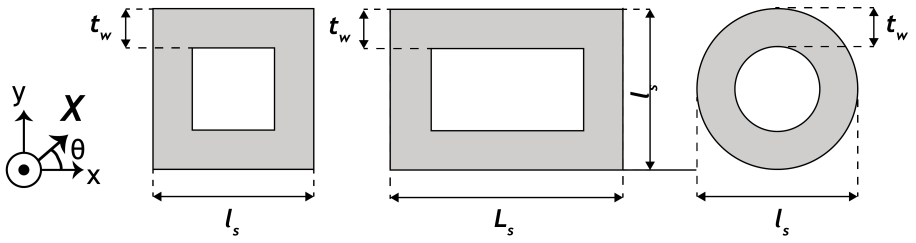


**Figure 11.** Parametric hollow sections: square (SQ), rectangular (REC), and circular (CIR).

The radius of inertia for simple hollow sections is

$$r_{G_X} = \ell_s \cdot \sqrt{\frac{1}{\alpha_A}} \cdot \sqrt{\frac{\alpha_{I_x} + \alpha_{I_y}}{2} + \frac{\alpha_{I_y} - \alpha_{I_y}}{2} \cdot \cos(2\theta)} \quad (8)$$

The models in this category are derived from the formula of the fundamental frequency of a cantilever beam with some simplification regarding the radius of inertia or the influence of the material characteristics. A generic formula for these models is expressed as:

$$f_0 = C_1 \cdot \frac{1.875^2}{2\pi} \cdot \frac{\tilde{r}}{H^2} \cdot \left(\frac{1}{1-\alpha_{h_n}}\right)^{C_2} \cdot \left(\sqrt{\frac{E}{\rho}}\right)^{C_3} \quad (9)$$

With the value of $C_1$, $C_2$, $C_3$, and $\tilde{r}$ summarised in Table 6.

**Table 6.** Parameters of the physics-based models.

| Id Model | Ref. | $C_1$ | $C_2$ | $C_3$ | $\tilde{r}$ |
|---|---|---|---|---|---|
| 1 | [1] | $\sqrt{1.375}$ | 0 | 1 | $r_{G_X}$ |
| 2 | [8] (Equation (22)) | 0.8 | 1 | 1 | $\frac{\ell_s}{\sqrt{12}} \cdot 1.5 \cdot (1-\alpha_t)$ |
| 3 | [8] (Equation (23)) | 0.8 | 0 | 1 | $\frac{\ell_s}{\sqrt{12}} \cdot 1.125$ |
| 4 | [8] (Equation (24)) | 800 | 0 | 0 | $\frac{\ell_s}{\sqrt{12}} \cdot 1.125$ |

The results of evaluating the fundamental frequency using physics-based relation are shown in Figure 12, restrained to the available data. It is important to note that the material properties used (and recorded in the database) are derived from calibrating finite element models based on vibration measurements. The second physics-based model shows the best prediction. The performance of these methods is inferior to that of the empirical formulation. One reason could be the incompatibility of material property values calibrated from more complex models.

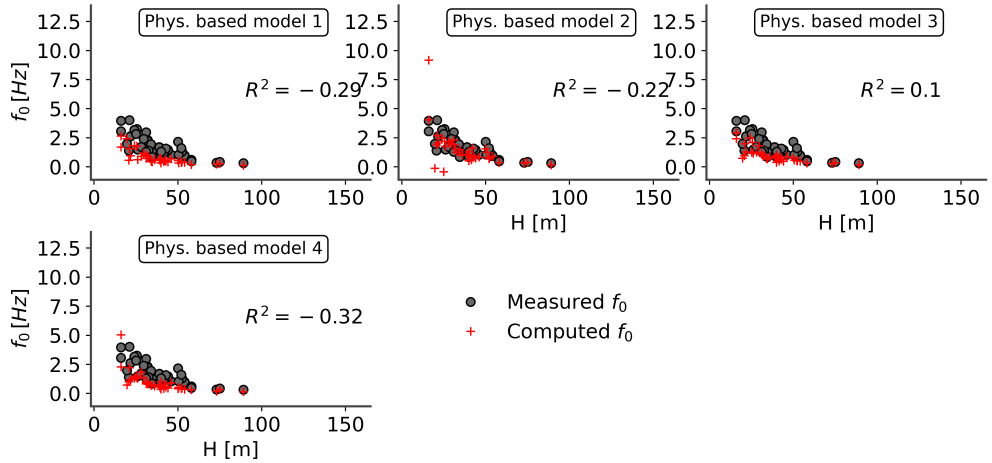


**Figure 12.** Evaluation of the fundamental frequency of towers from physics-based models (red cross) and experimental natural frequency (gray dot) as a function of the tower's height.

### *3.3. Description of the Timoshenko Beam*

In this section, we propose introducing additional parameters to the physics-based models to consider the influence of the environment of the slender structures and the bell system (Table 7). The influence of the soil/structure interaction on the dynamic properties of the tower has been studied, for instance, in [189,190]. Furthermore, this model is used later to evaluate these properties' sensitivity to interactions parameters (soil/tower interaction, nave/tower interaction) and bell system. The model illustrated in Figure 13 is limited to describing flexural bending modes. All parameters are summarized in Table 7.

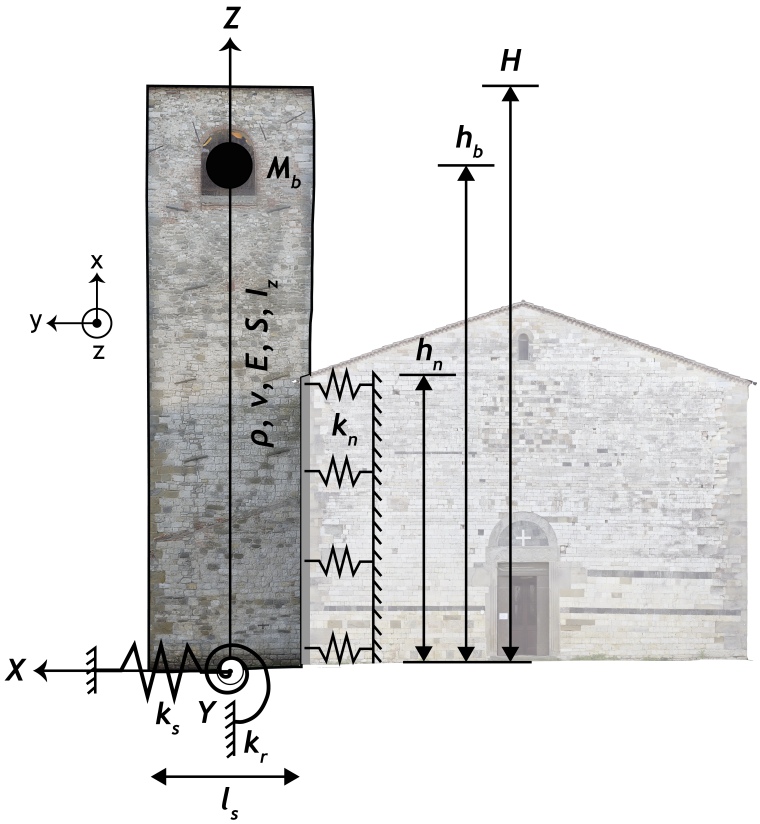


**Figure 13.** Model of the bell tower (Euler–Bernoulli beam model).

**Table 7.** Parameters and symbols used to describe the Rayleigh–Ritz approach.

| **Nomenclature** | | |
|---|---|---|
| **Symbol** | **Unit** | **Description** |
| $\boldsymbol{p}$ | | Set of global geometric parameters |
| $H$ | [m] | Height of the tower |
| $\ell_s$ | [m] | Width, lowest size of the tower's section |
| $h_n$ | [m] | Height of interaction between the tower and any adjacent structures |
| $f_0$ | [Hz] | Eigenfrequency |
| $L_s$ | [m] | Length, largest size of the tower's section |
| $t_w$ | [m] | Wall thickness |
| $h_b$ | [m] | Altitude of the bell system |
| $S$ | [$m^2$] | Surface area |
| $E$ | [MPa] | Young modulus |
| $\rho$ | [$kg \cdot m^{-3}$] | Volumetric mass density |
| $\nu$ | [-] | Poisson ratio |
| $I_z$ | [$m^4$] | Second moment of inertia |
| $k_s$ | [$N \cdot m^{-1}$] | Soil/structure translational stiffness |
| $k_r$ | [N] | Soil/structure rotational stiffness |
| $k_n$ | [$N \cdot m^2$] | Nave/structure translational stiffness |
| $M_b$ | [kg] | Mass of the bell system |
| $G$ | [Pa] | Shear modulus |
| $k$ | [-] | Shear coefficient |
| $v(x,t)$ | [m] | Transversal deflection |
| $\theta(x,t)$ | [rad.] | Normal rotation |
| $\mathcal{V}$ | [J] | Potential energy |
| $\mathcal{T}$ | [J] | Kinetic energy |
| $\mathcal{V}_{beam}$ | [J] | Potential energy associated with the beam system |
| $\mathcal{V}_{SSI}$ | [J] | Potential energy associated with the soil–structure interaction |
| $\mathcal{V}_{TNI}$ | [J] | Potential energy associated with the tower-nave interaction system |
| $\mathcal{T}_{beam}$ | [J] | Kinetic energy associated with the beam system |
| $\boldsymbol{\varphi}(x), \boldsymbol{\vartheta}(x)$ | [-] | Polynomial functions to approximate the displacement and rotation field |
| $\boldsymbol{q}$ | [-] | Generalized coordinates system |
| $\boldsymbol{M}, \boldsymbol{K}$ | | Mass and Stiffness matrix |

The dynamic response of the tower alone is described by a Timoshenko beam model. Indeed, as it has been observed in [191], the Euler–Bernoulli beam model tends to overestimate the eigenfrequency of non-slender structures.

The structural parameters $\boldsymbol{p}$ for the tower of height $H$ are

$$\boldsymbol{p} = \{H, S, I_y, k, E, \nu, \rho, k_s, k_r, k_n, h_n, M_b, h_b\} \tag{10}$$

### *3.4. Rayleigh–Ritz Method*

The Rayleigh–Ritz method has been successfully used to approximate the dynamic characteristics of the Euler–Bernoulli (EB) beam (e.g., [192]) or Timoshenko (TIMO) beam (e.g., [28]) with additional masses or springs.

The potential energy $\mathcal{V}$ and the kinetic energy $\mathcal{T}$ for the model described in Figure 13 are: $\mathcal{V} = \mathcal{V}_{beam} + \mathcal{V}_{SSI} + \mathcal{V}_{TNI}$, $\mathcal{T} = \mathcal{T}_{beam} + \mathcal{T}_{bell}$. The energies associated with the beam $\mathcal{V}_{beam}$ and $\mathcal{T}_{beam}$ are

$$\mathcal{V}_{beam} = \frac{1}{2}\int_0^H \left\{ EI_z \left(\frac{\partial \theta}{\partial x}\right)^2 + kGS\left(\theta - \frac{\partial v}{\partial x}\right)^2 \right\} \mathrm{d}x \tag{11}$$

$$\mathcal{T}_{beam} = \frac{1}{2}\int_0^H \left\{ \rho S \left(\frac{\partial v}{\partial t}\right)^2 + \rho I_z \left(\frac{\partial \theta}{\partial t}\right)^2 \right\} \mathrm{d}x \tag{12}$$

where $v(x,t)$ is the transversal deflection and $\theta(x,t)$ is the normal rotation. For the sake of simplicity, the shear coefficient is estimated with the formulas for thin-walled structures in [193].

The energy for the soil–structure interaction $\mathcal{V}_{SSI}$ is

$$\mathcal{V}_{SSI} = \frac{1}{2}\left( k_r \left( \left.\frac{\partial v}{\partial x}\right|_0 \right)^2 + k_s (v|_0)^2 \right) \tag{13}$$

The energy for the tower-nave interaction $\mathcal{V}_{TNI}$ is

$$\mathcal{V}_{TNI} = \frac{1}{2}\int_0^{h_n} k_n v^2 \mathrm{d}x \tag{14}$$

The energy for the bell system $\mathcal{V}_{bell}$ is

$$\mathcal{T}_{bell} = \frac{1}{2} M_b \left( \left.\frac{\partial v}{\partial t}\right|_{h_b} \right)^2 \tag{15}$$

The displacement $v$ and the rotation $\theta$ fields of the beam are approximated over simple polynomial functions $\boldsymbol{\varphi}(x)$ and $\boldsymbol{\vartheta}(x)$, and their coordinates in the polynomial basis $\boldsymbol{R(t)}$, and $\boldsymbol{V(t)}$,

$$v(x,t) \approx \sum_{i=0}^{n_H} V_i(t)\varphi_i(x), \quad \theta(x,t) \approx \sum_{i=0}^{n_r} R_i(t)\vartheta_i(x) \tag{16}$$

For the sake of simplicity, admissible functions (functions satisfying all the geometric boundary conditions) [194] are considered as the basis. For the cantilever beam, the following functions are used [195]:

$$\varphi_i(x) = \left(\frac{x}{H}\right)^2 \cdot \left(1 - \frac{x}{H}\right)^{i-1}, \quad \vartheta_i(x) = \left(\frac{x}{H}\right) \cdot \left(1 - \frac{x}{H}\right)^{i-1} \tag{17}$$

In the presence of soil–structure interaction, the functions corresponding to free–free boundary conditions are considered [195],

$$\varphi_i(x) = \left(1 - \frac{x}{H}\right)^{i-1}, \quad \vartheta_i(x) = \left(1 - \frac{x}{H}\right)^{i-1} \tag{18}$$

The size of the system for the Rayleigh–Ritz model is equal to $n_H + n_r$.

By considering $\boldsymbol{q}(\boldsymbol{V}, \boldsymbol{R})$ as a generalized coordinates system, the equation of Lagrange is

$$\frac{\mathrm{d}}{\mathrm{d}}\left(\frac{\partial \mathcal{T}}{\partial \dot{\boldsymbol{q}}}\right) + \left(\frac{\partial \mathcal{V}}{\partial \boldsymbol{q}}\right) = \boldsymbol{0} \tag{19}$$

After some mathematical developments, the equation of motion is

$$\boldsymbol{M}.\ddot{\boldsymbol{q}} + \boldsymbol{K}.\boldsymbol{q} = \boldsymbol{0} \tag{20}$$

Finally, the approximation of the eigenfrequencies $f_{mod}^{(i)}$ and the mode shapes $\mathcal{F}_i(\boldsymbol{\phi}^{(i)}, x)$ are obtained by solving the generalized eigenvalues problem,

$$\left(\boldsymbol{K} - \left(2 \cdot \pi \cdot f_{mod}^{(i)}\right)^2 \boldsymbol{M}\right)\boldsymbol{\phi}^{(i)} = \boldsymbol{0} \tag{21}$$

### *3.5. Model Validation*

#### 3.5.1. Characteristics of the Reference Tower

To evaluate the Rayleigh–Ritz model's capacity to estimate the tower's dynamic properties, a referenced case computed with a 3D finite element model is considered. The finite element code Cast3M has been used for this study. The 3D FE model of the tower is composed of 104,400 elements and 122,500 nodes. A total of 700 nodes are involved in the SSI, and 2368 nodes in the interaction with an adjacent structure. Three degrees of freedom per node are used. Additional stiffness and displacement boundary conditions are managed by dual Lagrange multipliers. Figure 14a gives the mesh of the reference computation made with the finite element code Cast3M [196], (see: http://www-cast3m.cea.fr/ accessed on 1 October 2021).

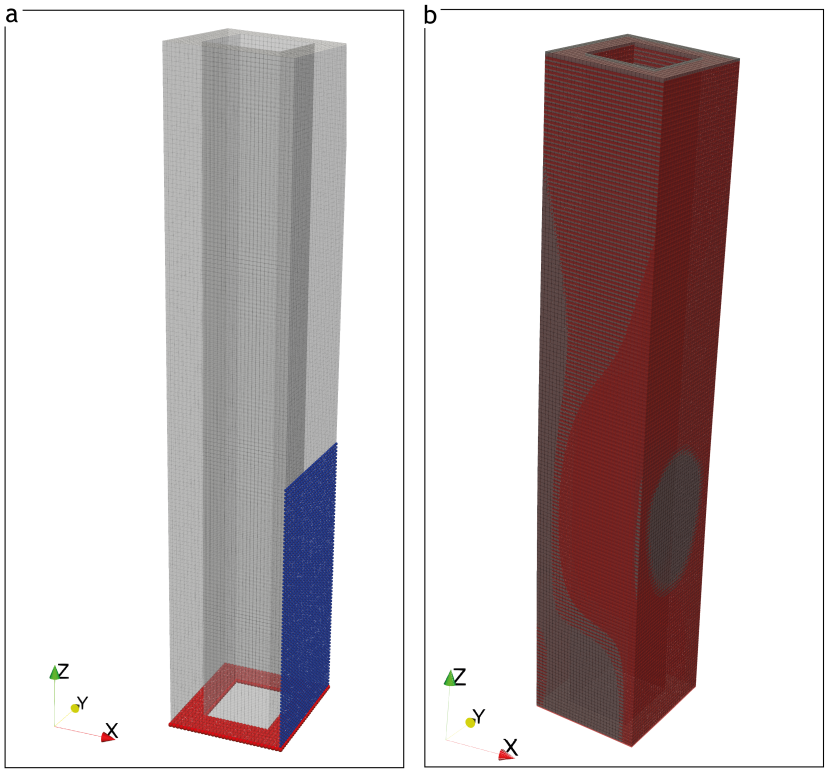


**Figure 14.** (**a**) 3D finite element model of the reference bell tower (red dots—SSI multiaxial springs, blue dots—TNI monoaxial springs along the direction *X*). (**b**) Comparison of the mode shape for the first bending mode between the reference 3D FE model (red) and the Rayleigh–Ritz model (gray).

The geometric and material characteristics considered for the tower are: $H$ = 17.6 m (isolated tower), $H$ = 35 m (bounded tower), $l_s$ = 7.39 m (isolated tower), $l_s$ = 6.17 m (bounded tower), $L_s = 1.01 \cdot \ell_s$, $t_w = 0.2 \cdot \ell_s$, $E$ = 2.2 GPa, $\nu = 0.2$, $\rho = 1800$ kg/m$^3$, $k_s = 10^7$ N/m, $k_r = 10^8$ N·m, $k_n = 10^8$ N/m$^2$, $h_n = 0.42 \cdot H$, $M_b = 2600$ kg, and $h_b = H$. Except for the soil, these values correspond to the median values in the database.

3.5.2. Evaluation of the Error

The consistency can be evaluated by comparing the frequencies:

$$\Delta f\left(f_{mod}^{(i)}, f_{FE}^{(i)}\right) = \frac{f_{FE}^{(i)} - f_{mod}^{(i)}}{f_{FE}^{(i)}} \tag{22}$$

The degree of consistency between the mode shapes of the Rayleigh–Ritz model $f_{mod}^{(i)}$ and the ones of the finite element reference $f_{FE}^{(i)}$ can be measured with the Modal Assurance Criterion (MAC),

$$MAC\left(f_{mod}^{(i)}, f_{FE}^{(j)}\right) = \frac{\left[\boldsymbol{f}_{mod}^{(i)}(\boldsymbol{x}_p)\right]^T \boldsymbol{f}_{FE}^{(j)}(\boldsymbol{x}_p)}{\left(\left[\boldsymbol{f}_{mod}^{(i)}(\boldsymbol{x}_p)\right]^T \boldsymbol{f}_{mod}^{(i)}(\boldsymbol{x}_p)\right)\left(\left[\boldsymbol{f}_{FE}^{(j)}(\boldsymbol{x}_p)\right]^T \boldsymbol{f}_{FE}^{(j)}(\boldsymbol{x}_p)\right)} \tag{23}$$

where $\boldsymbol{x}_p$ is the set of points for which the mode shapes are computed. From the MAC, one can define an error $\Delta_{MAC}$ as

$$\Delta_{MAC} = \frac{1}{N_m} \sum_{i=1}^{N_m} \left[1 - MAC\left(f_{mod}^{(i)}, f_{FE}^{(i)}\right)\right] \tag{24}$$

where $N_m$ is the number of modes considered.

3.5.3. Results

Three cases are considered to evaluate the capacity of the Rayleigh–Ritz model to describe the dynamic properties of slender structures: (1) a fixed base without interaction with the nave, (2) a fixed base with interaction with the nave, and (3) soil–structure interaction and nave interaction.

Table 8 gives the three first eigenfrequencies for global bending modes along the direction $X$ in the three case studies.

**Table 8.** Evaluation of the eigenfrequencies using the Rayleigh–Ritz model. Case 1: fixed base without interaction with the nave. Case 2: fixed base with interaction with the nave. Case 3: soil–structure interaction and nave interaction.

| | **Case 1** | | | **Case 2** | | | **Case 3** | | |
|---|---|---|---|---|---|---|---|---|---|
| **Mode** | $f_{FE}$ **[Hz]** | $f_{mod}$ **[Hz]** | $\Delta f$ **[%]** | $f_{FE}$ **[Hz]** | $f_{mod}$ **[Hz]** | $\Delta f$ **[%]** | $f_{FE}$ **[Hz]** | $f_{mod}$ **[Hz]** | $\Delta f$ **[%]** |
| 1 | 2.40 | 2.39 | 0.42 | 4.88 | 4.87 | 0.2 | 4.49 | 4.40 | 2.00 |
| 2 | 12.26 | 12.27 | 0.08 | 15.83 | 16.00 | 1.07 | 11.77 | 11.74 | 0.25 |
| 3 | 28.27 | 28.34 | 0.02 | 29.76 | 29.92 | 0.54 | 16.80 | 16.31 | 2.92 |

An excellent estimation is obtained for the eigenfrequencies for the three case studies with relative errors lower than 3%.

To compute the MAC between the modal basis of the Rayleigh–Ritz model and the reference with volumic finite element, the mode shapes should be described on the same set

of point $\boldsymbol{x}_p$. The mode shapes obtained with the Rayleigh–Ritz model are thus considered to move the nodes of the 3D finite element mesh by using the beam kinematic,

$$u_X\left(x_p^i\right) = v\left(X\left(x_p^i\right)\right), \quad u_Y\left(x_p^i\right) = 0, \quad u_Z\left(x_p^i\right) = -Z(x_p^i) \cdot \theta\left(X\left(x_p^i\right)\right) \tag{25}$$

Figure 14b compares the mode shape of the first mode for the third case study between the finite Element reference and the Rayleigh–Ritz model. The two mode shapes appeared similar. The non-consideration of the Poisson effect with the beam model can explain the slight discrepancy.

Figure 15 gives the MAC matrix obtained for the three case studies regarding the three first bending modes in the X direction.

The MAC error $\Delta_{MAC}$ between the three first bending modes of the Rayleigh–Ritz model and the reference FE model in the $X$ direction for the three case studies are $\Delta_{MAC}^{(1)} = 13.32\%$, $\Delta_{MAC}^{(2)} = 15.36\%$, $\Delta_{MAC}^{(3)} = 12.93\%$. The slight difference between the two models expressed in terms of eigenfrequency and MAC error highlights the Rayleigh–Ritz model's efficiency in describing the system's main dynamic properties, considering local features and interaction.

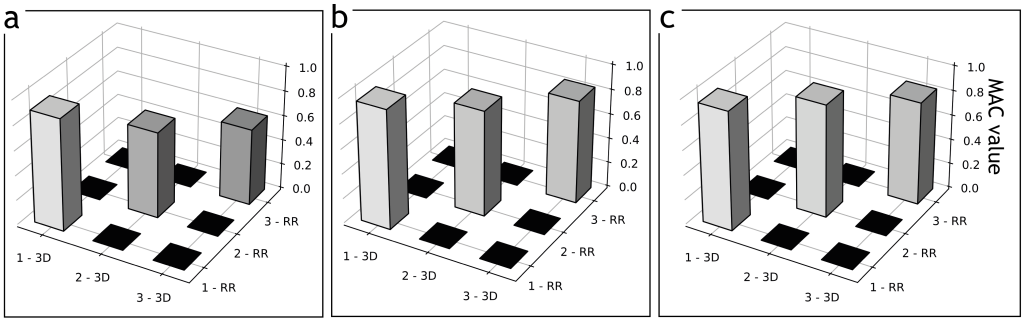


**Figure 15.** Modal Assurance Criterion matrix with the three first modes of the 3D finite element model (3D) and the Rayleigh–Ritz model (RR). (**a**) Case 1: fixed base without interaction with the nave. (**b**) Case 2: fixed base with interaction with the nave. (**c**) Case 3: soil–structure interaction and nave interaction.

### *3.6. Sensitivity Analysis*

In this last part, sensitivity analyses are performed to quantify the contribution of each of the parameters on the dynamic properties of the Rayleigh–Ritz model. This analysis aims to identify the main parameters influencing the fundamental frequency estimation. It aims to help identify the main parameters to measure on an actual structure when characterizing the dynamic properties of the structure with the model.

#### 3.6.1. The FAST Method

Global sensitivity analysis is a method used to decompose the uncertainty in the output of a computational model according to the input sources of uncertainty [197]. In this kind of sensitivity analysis, the space of the input factors is explored within an infinite region [198].

The Fourier amplitude sensitivity test (FAST), [198,199] and the Random balance designs Fourier amplitude sensitivity test (RBD-FAST) [200,201] are some of the most robust global sensitivity analysis techniques, e.g., [201–204]. This last technique sampled all input parameters from a periodic function with a different characteristic frequency. Thus, the output model becomes a periodic function. The Fourier spectrum is then calculated on the model output at specific frequencies to obtain the first-order Sobol sensitivity index ($S_i$) of each $p_i$ parameter.

Let us consider a computer model $Y = \mathcal{M}(p_1, \ldots, p_n)$ treated as a black box, where $n$ is the number of independent input parameters. The parametric curve assigned to each input parameter is defined as:

$$p_i(s) = \frac{1}{2} + \frac{1}{\pi} \arcsin(\sin(w_i \cdot s)) \quad (26)$$

where $p_i(s) \in [0,1]^n$ and $s = 2 \cdot \pi \frac{j-1}{N}$; $\forall j = 1, \ldots, N$. The $Y$ model is then evaluated $N$ times over the sample of size $N$. If the model output $Y$ is expanded with a Fourier series, the marginal variance ($V$) can be obtained as:

$$\mathcal{M}_0 = E[Y] \quad (27)$$

$$\mathcal{M}_0 = \lim_{T \to \infty} \frac{1}{2\pi} \int_{-\pi}^{\pi} f(\mathrm{p(s)}) ds \quad (28)$$

$$V = \frac{1}{2\pi} \int_{-\pi}^{\pi} \mathcal{M}^2(\mathrm{p(s)}) ds - \mathcal{M}_0^2 \quad (29)$$

$$V \simeq 2 \sum_{j=1}^{\infty} (A_j^2 + B_j^2) \quad (30)$$

where $A_j$ and $B_j$ are the Fourier coefficients defined as:

$$A_j = \frac{1}{2\pi} \int_{-\pi}^{\pi} \mathcal{M}(\mathrm{p(s)}) \cos(js) ds \quad (31)$$

$$B_j = \frac{1}{2\pi} \int_{-\pi}^{\pi} \mathcal{M}(\mathrm{p(s)}) \sin(js) ds \quad (32)$$

The marginal partial variance of an individual input parameter ($V_i$) is obtained from the Fourier coefficients $A_{kw_i}$ and $B_{kw_i}$ at the harmonics of $w_i$ as follows:

$$V_i = 2 \sum_{k=1}^{\infty} (A_{kw_i}^2 + B_{kw_i}^2) \quad (33)$$

Finally, the first-order Sobol index ($S_i$) of each $p_i$ parameters is defined as:

$$S_i = \frac{V_i}{V} \quad (34)$$

The number of simulations $N_s$ needed in FAST and the $\omega_i$ values for Equation (26) are provided in Table 9. It is noted that even for a problem with a few numbers of input variables, the minimum number of simulations required to obtain reliable data is high.

The advantage of RBD-FAST is that each random variable may be sampled from a periodic search function considering a single frequency $w_i$ for all input variables, which will reduce the number of simulations $N_s$. However, only the first-order sensitivity index ($S_i$) could be calculated. This is possible thanks to a randomization procedure used in RBD-FAST [201]. The randomization procedure consists of the following:

- Randomly permutes the set of samples for each input variable;
- Run the model using those permuted sets of input variables;
- Reorder the model output according to the input permutation for each input variable.

Then, for each reordered output set, the single frequency $w_i$ is restored, and the sensitivity indices may be evaluated using the same procedure as in FAST. The reader may refer to [198,201,204,205] or [206], among others, for further details about the FAST and RBD-FAST methods.

**Table 9.** Minimum number of model runs required by FAST [198].

| Input Factors | $N_s$ | $\omega_i$ |
|---|---|---|
| 5 | 626 | $\{11, 21, 27, 35, 39\}$ |
| 6 | 786 | $\{1, 21, 31, 37, 45, 49\}$ |
| 7 | 1394 | $\{17, 39, 59, 69, 75, 83, 87\}$ |
| $N_s = (2 \cdot M \cdot \omega_{max} + 1) \cdot 2$ | | |

### 3.6.2. Sensitivity Analysis of the Rayleigh–Ritz Model

The first-order Sobol indices [207] are computed for the case of bounded towers without soil–structure interaction and with a rectangular hollow section. For this computation, a combination of the Random Balance Design (RBD) and the Fourier Amplitude Sensitivity Analysis Test (FAST) [200] is used. The sampling is made by considering Latin Hypercube Sampling (LHS). These analyses have been made with the Python library SALib [208].

Table 10 lists the range of the values for the different parameters. The ranges have been constructed according to the descriptive statistics of the database in the first part of this work.

**Table 10.** Range of values for the parameters of the Rayleigh–Ritz approach for the sensitivity analysis.

| Parameters [Unit] | Range |
|---|---|
| $H$ [m] | 13.1–56.8 |
| $\ell_s$ [m] | 3.2–10.2 |
| $\frac{t_w}{\ell_s}$ [%] | 100–130 |
| $\frac{L_s}{\ell_s}$ [%] | 25–36 |
| $E$ [GPa] | 0.2–5.3 |
| $\nu$ [-] | 0.13–0.27 |
| $\rho$ [kg·m$^{-3}$] | 1500–2100 |
| $\frac{h_n}{H}$ [%] | 25–59 |
| $k_n$ [N·m$^2$] | $10^4$–$10^9$ |
| $M_b$ [kg] | 0–6500 |

The first-order Sobol indices are computed for the fundamental frequency associated with the first bending mode. Figure 16 gives these first-order Sobol indices with a confidence interval.

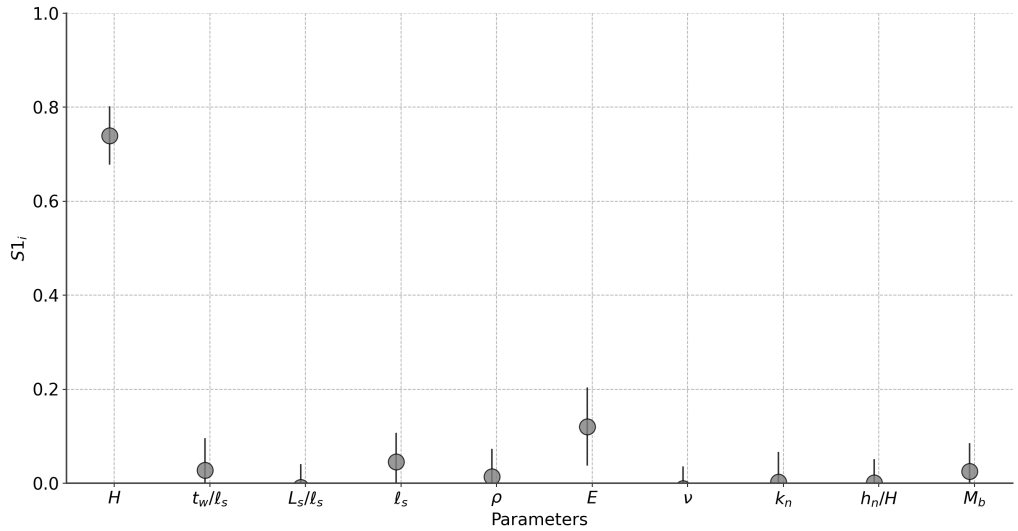


**Figure 16.** First-order Sobol indices for the fundamental frequency associated with bending mode regarding nine parameters for the Rayleigh–Ritz model.

Figure 16 shows that the fundamental frequency is mainly sensitive to the tower's height ($S_1$ = 0.74). This result justifies the choice of $H$ as the single or as one of the parameters for the empirical models. This shows that particular care needs to be taken when evaluating this parameter to minimize the fundamental frequency evaluation error. The modulus of elasticity plays a second-order role ($S_1$ = 0.12). The width and height of the interaction between the bell tower and the nave have a lesser impact, but can be used to refine the evaluation of the fundamental frequency (to a hundredth of a Hz).

However, the impact of characteristics other than height on the fundamental frequency can vary according to the height range of the structure. To assess this, the Sobol index of each parameter is evaluated as a function of the tower's height. The sensitivity analysis was carried out using interval values for the nine parameters as shown in Table 10. Figure 17 (on the left) shows a decreasing contribution of Young's modulus with increasing height. On the contrary, the interaction height between the tower and adjacent buildings increases proportionally with the height. The other parameters have a more constant and minor role in the selected range of values (Figure 17, on the right).

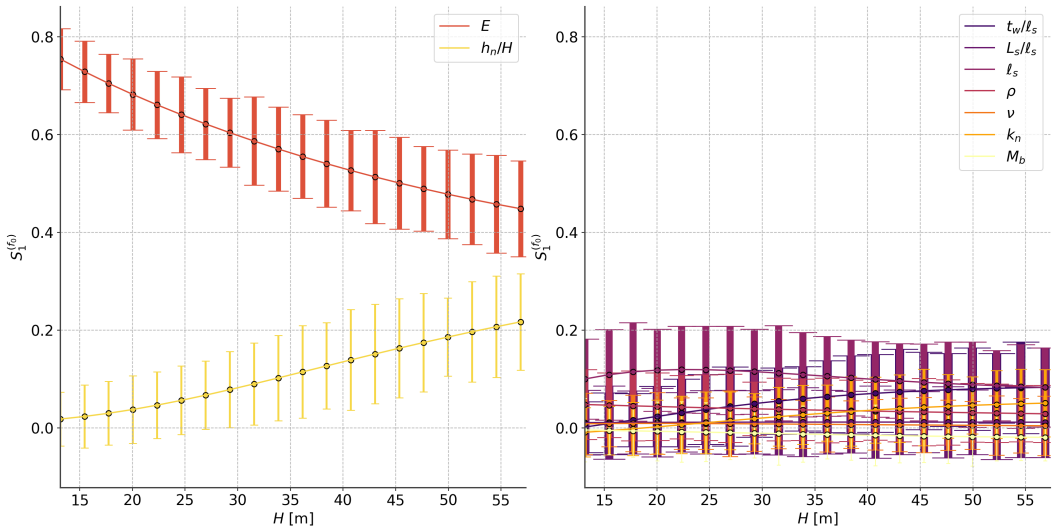


**Figure 17.** Evolution of the first-order Sobol indices of the towers features with respect to the height $H$ of the tower.

### 3.6.3. Sensitivity Analysis for Key Parameter Identification

This section proposes to go a step further and quantify the impact of errors in field measurements of geometric characteristics and material properties on the modal frequencies and strains of the first three bending modes of the tower evaluated using the Rayleigh–Ritz approach. To do this, we use a numerical framework. A 3D Finite Element Model is used as a reference model (Figure 15, on the left). The value of geometric and material characteristics considered are the same as those of the bounded tower discussed in Section 3.5.1 (height, wall thickness, width, length, density, interface stiffness, and height). The Rayleigh–Ritz approach is used to propagate the errors of nine parameters: $t_w$, $\ell_s$, $L_s$, $\rho$, $E$, $\nu$, $k_s$, $h_n$, and $M_b$. The tower's height is kept fixed. To simulate the error, each parameter varies between plus and minus 10 % of the reference value. The consistency between the frequencies and the modes shapes identified with the Rayleigh–Ritz approach and the reference 3D Finite Element Model is evaluated through $\Delta_{f_i}(\boldsymbol{p})$ and $\Delta_{MAC_i}(\boldsymbol{p})$, as defined in Equation (22) and Equation ( 23), respectively. The first-order Sobol indices are computed, and results are shown in Figure 18. The breath measurement error contributes most to the mode shape error of the first three modes. The density and the Young modulus uncertainties impact higher frequencies (the second and third bending modes). The measurement error on the interaction height mainly affects the fundamental frequencies and their associated mode shape.

### *3.7. Comparing Empirical, Physics-Based, and Rayleigh–Ritz Approach for the Evaluation of the Fundamental Frequency*

In this final section, we compare the performance of the empirical, physics-based, and Rayleigh–Ritz approaches for evaluating the fundamental frequency of slender historical structures. The analysis is carried out on a set of towers for which the geometric characteristics, the mass of the bell system, and the material properties are available (31 towers). Figure 19 shows the results expressed in terms of residuals computed as follows: $\frac{f_0^{exp} - f_0^{model}}{f_0^{exp}}$. The physics-based formulations constantly underestimate the experimental frequency. This discrepancy could be related to the value of the selected material parameters found in the literature, primarily identified through the FE model updating processes. The results of the empirical formulation are spread out, and failed to minimize the discrepancy between the estimated and the experimental frequencies. This result is consistent with those shown in Figures 10 and 12. On the contrary, the figure clearly shows that the Rayleigh–Ritz model minimizes the best deviation from the measured frequency. However, this difference does not converge to zero, and this can be explained by several factors. Sensitivity analyses show that the tower's height impacts the fundamental frequency most. This height is often defined with precision about decimeters, or even meters in some cases, and could explain these discrepancies. In addition, the presence of complex and imposing roofs (sometimes made of wood, sometimes of masonry) complicates the definition of the height to be retained. It has been observed that a low value (height at the base of the roof) and a high value (height at the top of the roof) systematically frame the value of the experimental frequency. The presence of an opening in the roof can also have a significant impact by significantly reducing the mass. The material parameters also need to be better known. These are often the result of updating the process with a finite element model that is more complex than the model considered in this study. However, the model proposed here remains a reasonable compromise, given the uncertainties in masonry towers' physical and geometric parameters.

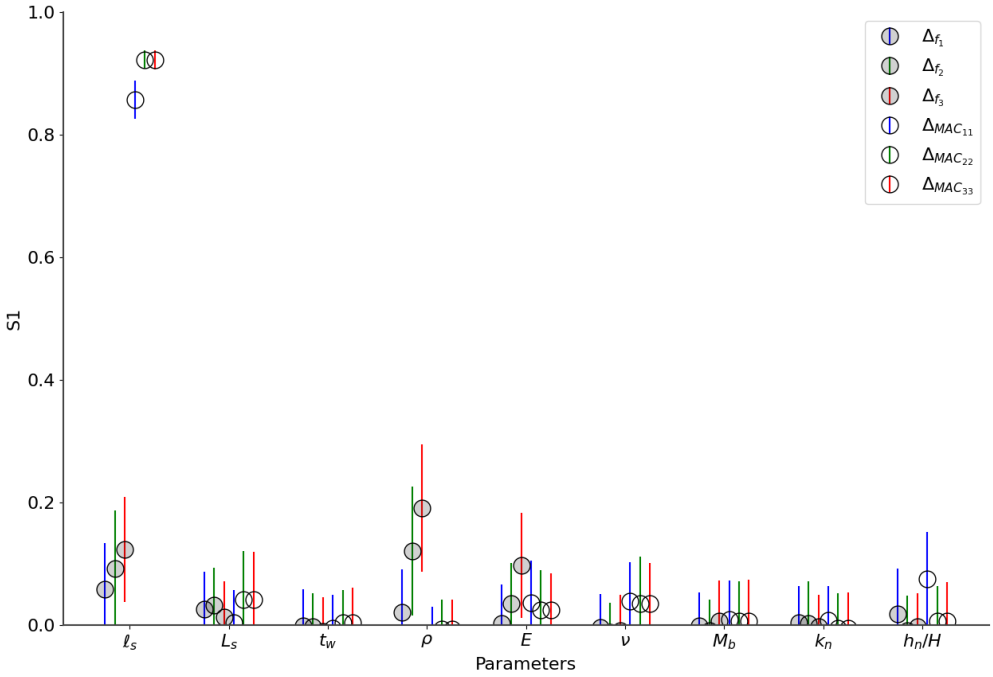


**Figure 18.** Evaluation of the first-order Sobol indices for the errors regarding the dynamic properties.

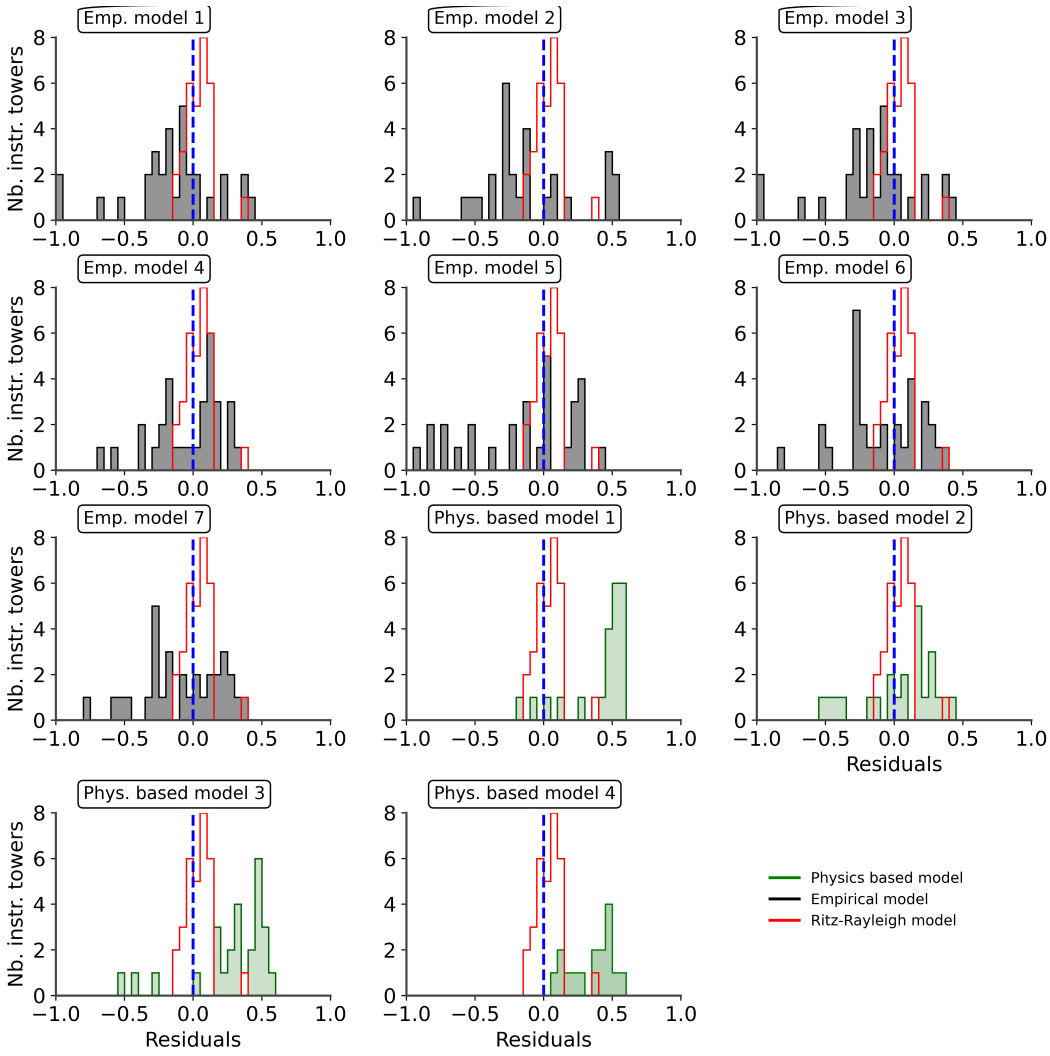


**Figure 19.** Comparison of the fundamental frequency residuals using empirical formulation (gray), physics-based formulation (green), and the Rayleigh–Ritz approach (red).

## 4. Conclusions

The fundamental frequency is crucial in assessing slender masonry structures' dynamic properties. In recent decades, simple formulations have been proposed based on global features avoiding difficult and time-consuming modeling. At the same time, the growing number of OMA campaigns provides information on actual modal characteristics, and this is an opportunity to revisit and investigate the behavior of old masonry structures. This work's contributions are:

- Compiling 244 instrumented masonry towers assembled from an extensive literature review. Worldwide masonry towers are described in terms of geometric, material features, interaction with adjacent buildings, aging, construction phase, repairs, and instrumentation condition;
- Describing the range of each parameter essential for the sensitivity analysis;
- Proposing a generic formulation for empirical and physical models summarizing the ones from the literature (available in the Python script);
- Expressing each feature contribution through a Rayleigh–Ritz formulation (available in the Python script);
- Conducting a sensitivity analysis to quantify how much each feature's tower impacts the fundamental frequency.

The main results of this work show that:

- The variability of the identified experimentally for the same historic tower. When available, most of the repeated OMA surveys highlight a discrepancy of up to 0.05 Hz. This difference is in the range of the contribution of tower features, inviting us to reduce in the uncertainties when evaluating both the fundamental frequency and the tower's features;
- Empirical relations provide a suitable evaluation of the fundamental frequency compared to physics-based formulations regarding a small number of parameters;
- The Rayleigh–Ritz formulation allows the best fit between experimental and computed fundamental frequency when all information about the towers' features are available;
- The height of the tower is the critical parameter to evaluate the fundamental frequency. It invites us to take some precautions when evaluating the height of the building. Moreover, the impact of the interaction between the slender structure and the adjacent structure on the fundamental frequency increase with the tower's height, although as a second-order parameter;
- The width significantly impacts the mode shapes of the three first bending modes. The density and Young modulus impact the frequencies of the second and higher modes. The impact of the height interaction is limited to the first bending modes. The tower's other features play a second-order role. These values are generally taken as known in model updating processes, which prefer to focus on calibrating unknown material properties. They are measured by visual inspection or more advanced techniques (laser measurements, etc.). We recommend particular attention to minimizing the uncertainty associated with measuring these two parameters.

Cultural Heritage buildings are complex, but of inestimable value, which requires our synergy. We believe this work is an initial contribution that invites sharing data relating to OMA (the fundamental frequency in the first instance). The database and the script of this work are available to the community. We encourage the community to send us the characteristics of new instrumented masonry towers so that we can increase our understanding of their behavior and work towards their preservation.

**Author Contributions:** Conceptualization, A.M. and C.G.; Methodology, A.M., C.G., E.D.M. and P.G.; Software, A.M. and C.G.; Validation, A.M. and C.G.; Formal analysis, A.M., C.G., J.L. and C.C.; Investigation, A.M., C.G. and C.L.S.; Resources, C.G.; Data curation, A.M., C.G., C.L.S., J.L. and C.C.; Writing—original draft, A.M. and C.G.; Writing—review & editing, A.M., C.G., C.L.S., E.D.M. and P.G.; Visualization, A.M. and C.G.; Supervision, A.M. and C.G.; Project administration, C.G.; Funding acquisition, C.G. All authors have read and agreed to the published version of the manuscript.

**Funding:** The first, the second, and the sixth author wish to express their most grateful thanks to the French National Research Agency (ANR) for the funding of the ACROSS project (ANR-20-CE03–0003), through which a part of this study has been carried out.

**Data Availability Statement:** The code sources and the TURRIS are provided at the following link: https://github.com/MArnaud/TURRIS [16].

**Acknowledgments:** The authors kindly acknowledge the institutions and researchers who provided additional and helpful information of masonry towers features: the municipality of Montboucher-sur-Jabron. The authors thanks Fernando Lopez-Caballero for the fruitful discussion and the advice regarding the sensitivity analysis, Clotilde Chambreuil and Héloïse Rostagni for their help in completing the database. The authors wish to express their most grateful thanks to the French National Research Agency (ANR) for the funding of the ACROSS project (ANR-20-CE03–0003), through which a part of this study has been carried out.

**Conflicts of Interest:** The authors declare no conflict of interest.

## References


1. Shakya, M.; Varum, H.; Vicente, R.; Costa, A. Empirical formulation for estimating the fundamental frequency of slender masonry structures. *Int. J. Archit. Herit.* **2016**, *10*, 55–66. [CrossRef]
2. Bartoli, G.; Betti, M.; Marra, A.M.; Monchetti, S. On the role played by the openings on the first frequency of historic masonry towers. *Bull. Earthq. Eng.* **2020**, *18*, 427–451. [CrossRef]
3. Pallarés, F.J.; Betti, M.; Bartoli, G.; Pallarés, L. Structural health monitoring (SHM) and Nondestructive testing (NDT) of slender masonry structures: A practical review. *Constr. Build. Mater.* **2021**, *297*, 123768. [CrossRef]
4. Milani, G.; Casolo, S.; Naliato, A.; Tralli, A. Seismic Assessment of a Medieval Masonry Tower in Northern Italy by Limit, Nonlinear Static, and Full Dynamic Analyses. *Int. J. Archit. Herit.* **2012**, *6*, 489–524. [CrossRef]
5. DPCM. *Direttiva del Presidente del Consiglio dei Ministri per Valutazione e Riduzione del Rischio Sismico del Patrimonio Culturale con Riferimento alle Norme Tecniche per le Costruzioni, G.U. n. 47*; DPCM: Roma, Italy, 2011.
6. Brincker, R.; Ventura, C. *Introduction to Operational Modal Analysis*; John Wiley & Sons: Hoboken, NJ, USA, 2015.
7. Lund, J.; Selby, A.; Wilson, J. The dynamics of bell towers—A survey in northeast England. *WIT Trans. Built Environ.* **1995**, *17*, 8.
8. Bartoli, G.; Betti, M.; Marra, A.M.; Monchetti, S. Semiempirical Formulations for Estimating the Main Frequency of Slender Masonry Towers. *J. Perform. Constr. Facil.* **2017**, *31*. [CrossRef]
9. Sanchez-Silva, M.; Klutke, G.A.; Rosowsky, D.V. Life-cycle performance of structures subject to multiple deterioration mechanisms. *Struct. Saf.* **2011**, *33*, 206–217. [CrossRef]
10. Price Code. *Eurocode 8: Design of Structures for Earthquake Resistance—Part 1: General Rules, Seismic Actions and Rules for Buildings*; European Committee for Standardization: Brussels, Belgium, 2005.
11. Faccio, P.; Podestà, S.; Saetta, A. Venezia, Campanile della Chiesa di Sant'Antonin, Esempio 5. In *Linee Guida per la Valutazione e Riduzione del Rischio Sismico del Patrimonio Culturale Allineate alle Nuove Norme Tecniche per le Costruzioni (DM 14/01/2008), Circolare*; Ministero della Cultura: Rome, Italy, 2011; Volume 26.
12. Rainieri, C.; Fabbrocino, G. Estimating the Elastic Period of Masonry Towers. In *Topics in Modal Analysis I*; Springer: New York, NY, USA, 2012; Volume 5, pp. 243–248. [CrossRef]
13. Diaferio, M.; Foti, D.; Potenza, F. Prediction of the fundamental frequencies and modal shapes of historic masonry towers by empirical equations based on experimental data. *Eng. Struct.* **2018**, *156*, 433–442. [CrossRef]
14. Ministerio de Fomento. Real Decreto 997/2002, de 27 de septiembre, por el que se aprueba la norma de construcción sismorresistente: Parte general y edificación (NCSR-02). Boletín Oficial del Estado , 11 October 2002.
15. Formisano, A.; Vituat, R.; Milani, G.; Sarhosis, V. *Parametric Seismic Analysis on Masonry Bell Towers*; Pisa University Press: Pisa, Italy, 2017; pp. 108–116.
16. Montabert, A.; Giry, C.; Limoge Schraen, C.; Lépine, J.; Choueiri, C.; Mercerat, E.D.; Guéguen, P. TURRIS: An open source database and Python tools to compute the fundamental frequency of historic masonry towers. *Zenodo* **2023**. Available online: https://zenodo.org/record/8283641 (accessed on 18 August 2023).
17. Schmidt, T. Dynamic behaviour of twin bell towers. In Proceedings of the 2nd International Operational Modal Analysis Conference, Copenhagen, Denmark, 30 April–2 May 2007.
18. Schmidt, T. FE Comparison of the dynamic behavior of 16 historical twin bell towers. In Proceedings of the 3th International Operational Modal Analysis Conference, Portonovo, Italy, 4–6 May 2009; pp. 483–490.
19. Rainieri, C.; Fabbrocino, G. Output-only modal identification for prediction of the elastic period of masonry towers. In Proceedings of the 4th International Operational Modal Analysis Conference, Istanbul, Turkey, 9–11 May 2011.
20. Limoge, C. Méthode de Diagnostic à Grande Échelle de la Vulnérabilité Sismique des Monuments Historiques: Chapelles et Églises Baroques des Hautes Vallées de Savoie: Large-Scale Seismic Vulnerability Assesment Method for the Masonry Architectural Heritage: Baroque Chapels and Churches of the French Savoye. Ph.D. Thesis, Université Paris-Saclay (ComUE), Paris, France, 2016.
21. Ziegler, A. Dynamik der Glockentürme. In *Bauwerksdynamik und Erschütterungsmessungen*; Springer Fachmedien: Wiesbaden, Germany, 2017; pp. 153–165. [CrossRef]
22. Ruiz-Jaramillo, J.; Montiel-Vega, L.; García-Pulido, L.J.; Muñoz-González, C.; Blanca-Hoyos, Á. Ambient Vibration as a Basis for Determining the Structural Behaviour of Watchtowers against Horizontal Loads in Southeast Spain. *Appl. Sci.* **2020**, *10*, 6114. [CrossRef]
23. Mercerat, D.; Montabert, A.; Giry, C.; Lancieri, M.; Arrighetti, A. Operational Modal Analysis of five historical bell towers in the Mugello basin (Tuscany, Italy). In Proceedings of the 3rd European Conference on Earthquake Engineering & Seismology (3ECEES), Bucharest, Romania, 4–9 September, 2022; pp. 4106–4111.
24. Wimmer, H.; Majer, J. Dynamic behaviour and numerical simulation of old bell towers. In *Structural Repair and Maintenance of Historical Buildings*; Computational Mechanics Publications: Berlin, Germany, 1989; pp. 349–358.
25. Modena, C.; Valluzzi, M.; Folli, R.T.; Binda, L. Design choices and intervention techniques for repairing and strengthening of the Monza cathedral bell-tower. *Constr. Build. Mater.* **2002**, *16*, 385–395. [CrossRef]
26. Ivorra, S.; Foti, D.; Diaferio, M.; Carabellese, I. Preliminary OMA results on a soft calcarenite stone bell-tower in Mola di Bari (Italy). In Proceedings of the 7th International Operational Modal Analysis Conference, IOMAC, Ingolstadt, Germany, 10–12 May 2017.

27. Combey, A.; Mercerat, D.E.; Gueguen, P.; Langlais, M.; Audin, L. Postseismic Survey of a Historic Masonry Tower and Monitoring of Its Dynamic Behavior in the Aftermath of Le Teil Earthquake (Ardèche, France). *Bull. Seismol. Soc. Am.* **2022**, *112*, 1101–1119. [CrossRef]
28. Kohan, P.H.; Nallim, L.G.; Gea, S.B. Dynamic characterization of beam type structures: Analytical, numerical and experimental applications. *Appl. Acoust.* **2011**, *72*, 975–981. [CrossRef]
29. Carone, A.S.; Foti, D.; Giannoccaro, N.I.; Nobile, R. Non-destructive characterization and dynamic identification of an historical bell tower. In Proceedings of the 4th International Conference on Integrity, Reliability and Failure, Funchal, Portugal, 23–27 June 2013; pp. 1–16.
30. Diaferio, M.; Foti, D.; Giannoccaro, N. Modal parameters identification on environmental tests of an ancient tower and validation of its FE model. *Int. J. Mech* **2016**, *10*, 80–89.
31. Mariella, D.; Dora, F.; Gentile, C.; Ivan Giannoccaro, N.; Saisi, A.E. Dynamic testing of a historical slender building using accelerometers and radar. In Proceedings of the 6th International Operational Modal Analysis Conference, Gijón, Spain, 12–14 May 2015; pp. 1–10.
32. Stefano, A.D.; Ceravolo, R. Assessing the Health State of Ancient Structures: The Role of Vibrational Tests. *J. Intell. Mater. Syst. Struct.* **2007**, *18*, 793–807. [CrossRef]
33. Lucidi, A.; Giordano, E.; Clementi, F.; Quattrini, R. Point cloud exploitation for structural modeling and analysis: A reliable workflow. *Int. Arch. Photogramm. Remote Sens. Spat. Inf. Sci.* **2021**, *XLIII-B2-2021*, 891–898. [CrossRef]
34. Gentile, C.; Saisi, A. Operational modal testing of historic structures at different levels of excitation. *Constr. Build. Mater.* **2013**, *48*, 1273–1285. [CrossRef]
35. Gentile, C.; Saisi, A.; Cabboi, A. Structural Identification of a Masonry Tower Based on Operational Modal Analysis. *Int. J. Archit. Herit.* **2014**, *9*, 98–110. [CrossRef]
36. Cabboi, A.; Gentile, C.; Saisi, A. From continuous vibration monitoring to FEM-based damage assessment: Application on a stone-masonry tower. *Constr. Build. Mater.* **2017**, *156*, 252–265. [CrossRef]
37. Ferraioli, M.; Mandara, A.; Abruzzese, D.; Miccoli, L. Dynamic identification and seismic safety of masonry bell towers. In Proceedings of the 14th Conference of Associazione Nazionale Italiana di Ingegneria Sismica (ANIDIS), Bari, Italy, 18–22 September 2011; pp. 18–22.
38. Angelis, A.D.; Lourenço, P.B.; Sica, S.; Pecce, M.R. Influence of the ground on the structural identification of a bell-tower by ambient vibration testing. *Soil Dyn. Earthq. Eng.* **2022**, *155*, 107102. [CrossRef]
39. Pesci, A.; Teza, G.; Bonali, E.; Casula, G.; Boschi, E. A laser scanning-based method for fast estimation of seismic-induced building deformations. *ISPRS J. Photogramm. Remote Sens.* **2013**, *79*, 185–198. [CrossRef]
40. Palermo, M.; Silvestri, S.; Gasparini, G.; Baraccani, S.; Trombetti, T. An approach for the mechanical characterisation of the Asinelli Tower (Bologna) in presence of insufficient experimental data. *J. Cult. Herit.* **2015**, *16*, 536–543. [CrossRef]
41. Carpinteri, A.; Lacidogna, G.; Manuello, A.; Niccolini, G. A study on the structural stability of the Asinelli Tower in Bologna. *Struct. Control. Health Monit.* **2015**, *23*, 659–667. [CrossRef]
42. Invernizzi, S.; Lacidogna, G.; Lozano-Ramírez, N.E.; Carpinteri, A. Structural monitoring and assessment of an ancient masonry tower. *Eng. Fract. Mech.* **2019**, *210*, 429–443. [CrossRef]
43. Milani, G.; Clementi, F. Advanced Seismic Assessment of Four Masonry Bell Towers in Italy after Operational Modal Analysis (OMA) Identification. *Int. J. Archit. Herit.* **2019**, *15*, 157–186. [CrossRef]
44. Standoli, G.; Giordano, E.; Milani, G.; Clementi, F. Model Updating of Historical Belfries Based on Oma Identification Techniques. *Int. J. Archit. Herit.* **2020**, *15*, 132–156. [CrossRef]
45. Colapietro, D.; Fatiguso, F.; Pinto, M.; Bianco, F. Techniques for improving assessment of the seismic vulnerability of a masonry bell tower. *Am. J. Eng. Res. (AJER)* **2017**, *6*, 147–155.
46. Azzara, R.M.; Girardi, M.; Padovani, C.; Pellegrini, D. *Dynamic Behaviour of the Carillon Tower in Castel San Pietro, Italy*; Technical Report; ISTI: Rome, Italy, 2022.
47. Gazzani, V.; Poiani, M.; Clementi, F.; Milani, G.; Lenci, S. Modal parameters identification with environmental tests and advanced numerical analyses for masonry bell towers: A meaningful case study. *Procedia Struct. Integr.* **2018**, *11*, 306–313. [CrossRef]
48. Balduzzi, B.; Mazza, D.; Papis, D.; Rossi, C.; Rossi, P.P. Experimental and numerical analysis for the strengthening intervention of the bell tower of St. Sistós Church in Bergamo. In Proceedings of the 5th International Conference on Structural Analysis of Historical Constructions (SAHC), Delhi, India, 6–8 November 2006; pp. 6–8.
49. Girardi, M.; Padovani, C.; Pellegrini, D.; Robol, L. Model updating procedure to enhance structural analysis in FE code NOSA-ITACA. *J. Perform. Constr. Facil.* **2019**, *33*, 04019041. [CrossRef]
50. Casciati, S.; Al-Saleh, R. Dynamic behavior of a masonry civic belfry under operational conditions. *Acta Mech.* **2010**, *215*, 211–224. [CrossRef]
51. Casciati, S.; Faravelli, L. Vulnerability assessment for medieval civic towers. *Struct. Infrastruct. Eng.* **2010**, *6*, 193–203. [CrossRef]
52. D'Ambrisi, A.; Mariani, V.; Mezzi, M. Seismic assessment of a historical masonry tower with nonlinear static and dynamic analyses tuned on ambient vibration tests. *Eng. Struct.* **2012**, *36*, 210–219. [CrossRef]
53. Casciati, S.; Tento, A.; Marcellini, A.; Daminelli, R. Long run ambient noise recording for a masonry medieval tower. *Smart Struct. Syst.* **2014**, *14*, 367–376. [CrossRef]

54. Bianconi, F.; Salachoris, G.P.; Clementi, F.; Lenci, S. A Genetic Algorithm Procedure for the Automatic Updating of FEM Based on Ambient Vibration Tests. *Sensors* **2020**, *20*, 3315. [CrossRef] [PubMed]
55. Bassoli, E.; Vincenzi, L.; Bovo, M.; Mazzotti, C. Dynamic identification of an ancient masonry bell tower using a MEMS-based acquisition system. In Proceedings of the 2015 IEEE Workshop on Environmental, Energy, and Structural Monitoring Systems (EESMS), Trento, Italy, 9–10 July 2015. [CrossRef]
56. Bru, D.; Ivorra, S.; Betti, M.; Adam, J.M.; Bartoli, G. Parametric dynamic interaction assessment between bells and supporting slender masonry tower. *Mech. Syst. Signal Process.* **2019**, *129*, 235–249. [CrossRef]
57. Pieraccini, M.; Fratini, M.; Dei, D.; Atzeni, C. Structural testing of Historical Heritage Site Towers by microwave remote sensing. *J. Cult. Herit.* **2009**, *10*, 174–182. [CrossRef]
58. Pieraccini, M.; Dei, D.; Mecatti, D.; Parrini, F. Dynamic Testing of Historic Towers Using an Interferometric Radar from an Unstable Measurement Position. *J. Nondestruct. Eval.* **2013**, *32*, 398–404. [CrossRef]
59. Lacanna, G.; Ripepe, M.; Coli, M.; Genco, R.; Marchetti, E. Full structural dynamic response from ambient vibration of Giotto's bell tower in Firenze (Italy), using modal analysis and seismic interferometry. *NDT&E Int.* **2019**, *102*, 9–15. [CrossRef]
60. Ceravolo, R.; Pistone, G.; Fragonara, L.Z.; Massetto, S.; Abbiati, G. Vibration-Based Monitoring and Diagnosis of Cultural Heritage: A Methodological Discussion in Three Examples. *Int. J. Archit. Herit.* **2014**, *10*, 375–395. [CrossRef]
61. Camata, G.; Cifelli, L.; Spacone, E.; Conte, J.; Loi, M.; Torrese, P. Seismic Safety Assessment of the Tower of the S. Maria Maggiore Cathedral in Guardiagrele, Italy. In Proceedings of the Ninth International Conference on Computational Structures Technology, Athens, Greece, 2–5 September 2008. [CrossRef]
62. Capanna, I.; Cirella, R.; Aloisio, A.; Alaggio, R.; Fabio, F.D.; Fragiacomo, M. Operational Modal Analysis, Model Update and Fragility Curves Estimation, through Truncated Incremental Dynamic Analysis, of a Masonry Belfry. *Buildings* **2021**, *11*, 120. [CrossRef]
63. Buffarini, G.P.; Cimellaro, C.G.P.; Stefano, A.D. Experimental dynamic analysis of Palazzo Margherita in L'Aquila after the April 6th, 2009, Earthquake. In Proceedings of the Experimental Vibration Analysis for Civil Engineering Structures (EVACES), Varenna, Italy, 3–5 October 2011; pp. 247–254.
64. Peeters, B.; Sforza, G.; Sbaraglia, L.; Germano, F. Efficient operational modal testing and analysis for design verification and restoration baseline assessment: Italian case studies. In Proceedings of the Experimental Vibration Analysis for Civil Engineering Structures (EVACES), Varenna, Italy, 3–5 October 2011; pp. 3–5.
65. Barsocchi, P.; Bartoli, G.; Betti, M.; Girardi, M.; Mammolito, S.; Pellegrini, D.; Zini, G. Wireless Sensor Networks for Continuous Structural Health Monitoring of Historic Masonry Towers. *Int. J. Archit. Herit.* **2020**, *15*, 22–44. [CrossRef]
66. Zonta, D.; Pozzi, M.; Zanon, P.; Anese, G.; Busetto, A. Real-time probabilistic health monitoring of the Portogruaro Civic Tower. In *Structural Analysis of Historic Construction: Preserving Safety and Significance, Two Volume Set*; CRC Press: Boca Raton, FL, USA, 2008; pp. 743–752.
67. Azzara, R.M.; Roeck, G.D.; Girardi, M.; Padovani, C.; Pellegrini, D.; Reynders, E. The influence of environmental parameters on the dynamic behaviour of the San Frediano bell tower in Lucca. *Eng. Struct.* **2018**, *156*, 175–187. [CrossRef]
68. Barsocchi, P.; Cassara, P.; Mavilia, F.; Pellegrini, D. Sensing a city's state of health: Structural monitoring system by internet-of-things wireless sensing devices. *IEEE Consum. Electron. Mag.* **2018**, *7*, 22–31. [CrossRef]
69. Azzara, R.M.; Girardi, M.; Iafolla, V.; Padovani, C.; Pellegrini, D. Long-Term Dynamic Monitoring of Medieval Masonry Towers. *Front. Built Environ.* **2020**, *6*, 9. [CrossRef]
70. Saisi, A.; Gentile, C.; Guidobaldi, M. Post-earthquake continuous dynamic monitoring of the Gabbia Tower in Mantua, Italy. *Constr. Build. Mater.* **2015**, *81*, 101–112. [CrossRef]
71. Saisi, A.; Gentile, C. Post-earthquake diagnostic investigation of a historic masonry tower. *J. Cult. Herit.* **2015**, *16*, 602–609. [CrossRef]
72. Saisi, A.; Gentile, C.; Ruccolo, A. Pre-diagnostic prompt investigation and static monitoring of a historic bell-tower. *Constr. Build. Mater.* **2016**, *122*, 833–844. [CrossRef]
73. Gentile, C.; Guidobaldi, M.; Saisi, A. One-year dynamic monitoring of a historic tower: Damage detection under changing environment. *Meccanica* **2016**, *51*, 2873–2889. [CrossRef]
74. Cavalagli, N.; Comanducci, G.; Gentile, C.; Guidobaldi, M.; Saisi, A.; Ubertini, F. Detecting earthquake-induced damage in historic masonry towers using continuously monitored dynamic response-only data. *Procedia Eng.* **2017**, *199*, 3416–3421. [CrossRef]
75. Magrinelli, E.; Acito, M.; Bocciarelli, M. Numerical insight on the interaction effects of a confined masonry tower. *Eng. Struct.* **2021**, *237*, 112195. [CrossRef]
76. Gentile, C.; Saisi, A. Dynamic Testing of Masonry Towers Using the Microwave Interferometry. *Key Eng. Mater.* **2014**, *628*, 198–203. [CrossRef]
77. Saisi, A.; Terenzoni, S.; Ruccolo, A.; Gentile, C. Safety of the Architectural Heritage: Structural Assessment of the Zuccaro's Tower in Mantua. In *RILEM Bookseries*; Springer International Publishing: Berlin/Heidelberg, Germany, 2019; pp. 2422–2430. [CrossRef]
78. Fragonara, L.Z.; Boscato, G.; Ceravolo, R.; Russo, S.; Ientile, S.; Pecorelli, M.L.; Quattrone, A. Dynamic investigation on the Mirandola bell tower in post-earthquake scenarios. *Bull. Earthq. Eng.* **2016**, *15*, 313–337. [CrossRef]
79. Lancellotta, R.; Sabia, D. Identification Technique for Soil-Structure Analysis of the Ghirlandina Tower. *Int. J. Archit. Herit.* **2014**, *9*, 391–407. [CrossRef]

80. Foti, D.; Ivorra, S.; Sabbà, M.F. Dynamic Investigation of an Ancient Masonry Bell Tower with Operational Modal Analysis—Non-Destructive Experimental Technique to Obtain the Dynamic Characteristics of a Structure. *Open Constr. Build. Technol. J.* **2012**, *6*, 384–391. [CrossRef]
81. Clementi, F.; Pierdicca, A.; Formisano, A.; Catinari, F.; Lenci, S. Numerical model upgrading of a historical masonry building damaged during the 2016 Italian earthquakes: The case study of the Podestà palace in Montelupone (Italy). *J. Civ. Struct. Health Monit.* **2017**, *7*, 703–717. [CrossRef]
82. Saisi, A.; Gentile, C.; Ruccolo, A. Continuous monitoring of a challenging heritage tower in Monza, Italy. *J. Civ. Struct. Health Monit.* **2017**, *8*, 77–90. [CrossRef]
83. Lorenzoni, F.; Modena, C.; Caldon, M.; Cohen, M.; Kislev, R.; Schaffer, Y. Structural health monitoring of heritage sites: The tower of David in Jerusalem. In *Structural Analysis of Historical Constructions: Anamnesis, Diagnosis, Therapy, Controls*; CRC Press: Boca Raton, FL, USA, 2016; pp. 745–751. [CrossRef]
84. Montabert, A.; Mercerat, E.D.; Clément, J.; Langlaude, P.; Lyon-Caen, H.; Lancieri, M. High resolution operational modal analysis of Sant'Agata del Mugello in light of its building history. *Eng. Struct.* **2022**, *254*, 113767. [CrossRef]
85. Osmancikli, G.; Uçak, Ş.; Turan, F.N.; Türker, T.; Bayraktar, A. Investigation of restoration effects on the dynamic characteristics of the Hagia Sophia bell-tower by ambient vibration test. *Constr. Build. Mater.* **2012**, *29*, 564–572. [CrossRef]
86. Bayraktar, A.; Türker, T.; Sevım, B.; Altunişik, A.C.; Yildirim, F. Modal Parameter Identification of Hagia Sophia Bell-Tower via Ambient Vibration Test. *J. Nondestruct. Eval.* **2009**, *28*, 37–47. [CrossRef]
87. Cantieni, R. One-Year Monitoring of a Historic Bell Tower. *Key Eng. Mater.* **2014**, *628*, 73–78. [CrossRef]
88. Ivorra, S.; Pallarés, F.J.; Adam, J.M. Experimental and Numerical Results from the Seismic Study of a Masonry Bell Tower. *Adv. Struct. Eng.* **2009**, *12*, 287–293. [CrossRef]
89. Ivorra, S.; Pallarés, F.J. Dynamic investigations on a masonry bell tower. *Eng. Struct.* **2006**, *28*, 660–667. [CrossRef]
90. Ivorra, S.; Pallarés, F.J.; Adam, J.M.; Tomás, R. An evaluation of the incidence of soil subsidence on the dynamic behaviour of a Gothic bell tower. *Eng. Struct.* **2010**, *32*, 2318–2325. [CrossRef]
91. Ivorra, S.; Cervera, J.R. Analysis of the dynamic actions when bells are swinging on the bell tower of Bonreposi Mirambell Church (Valencia, Spain). In Proceedings of the 3rd international Seminar of Historical Constructions, Guimarães, Portugal, 7–9 November 2001; Volume 413, p. 19.
92. Cunha, Á.; Ramos, L.F.; Magalhães, F.; Lourenço, P.B. Dynamic identification and modelling of Clérigos Tower: Initial studies. In Proceedings of the EURODYN 2014—9th International Conference on Structural Dynamics, Porto, Portugal, 30 June–2 July 2014.
93. Ramos, L.; Marques, L.; Lourenço, P.; Roeck, G.D.; Campos-Costa, A.; Roque, J. Monitoring historical masonry structures with operational modal analysis: Two case studies. *Mech. Syst. Signal Process.* **2010**, *24*, 1291–1305. [CrossRef]
94. Guerreiro, L.; Azevedo, J. Análise e reforço da torres do relógio da Horta, Faial. In Proceedings of the 5th Encontro National de Sismologia e Engenharia Sismica. In Proceedings of the Encontro National de Sismologia e Engenharia Sismica, Azores, Portugal, 24–27 October 2001; pp. 639–650.
95. Júlio, E.N.B.S.; da Silva Rebelo, C.A.; da Costa, D.A.S.G.D. Structural assessment of the tower of the University of Coimbra by modal identification. *Eng. Struct.* **2008**, *30*, 3468–3477. [CrossRef]
96. Tomaszewska, A. Influence of statistical errors on damage detection based on structural flexibility and mode shape curvature. *Comput. Struct.* **2010**, *88*, 154–164. [CrossRef]
97. Tomaszewska, A.; Szymczak, C. Identification of the Vistula Mounting tower model using measured modal data. *Eng. Struct.* **2012**, *42*, 342–348. [CrossRef]
98. Shabani, A.; Ademi, A.; Kioumarsi, M. Structural Model Updating of a Historical Stone Masonry Tower in Tønsberg, Norway. In *Lecture Notes in Civil Engineering*; Springer International Publishing: Berlin/Heidelberg, Germany, 2021; pp. 576–585. [CrossRef]
99. Jaras, A.; Kliukas, R.; Kačianauskas, R. The dynamic loading of Vilnius archcathedral belfry–Investigation and analysis. In Proceedings of the 10th International Conference Modern Building Materials, Structures and Techniques, Vilnius, Lithuania, 19–21 May 2010.
100. Ribilotta, E.; Giordano, E.; Ferrante, A.; Clementi, F.; Lenci, S. Tracking Modal Parameter Evolution of Different Cultural Heritage Structure Damaged by Central Italy Earthquake of 2016. *Key Eng. Mater.* **2019**, *817*, 334–341. [CrossRef]
101. Pavlovic, M.; Trevisani, S.; Cecchi, A. A Procedure for the Structural Identification of Masonry Towers. *J. Nondestruct. Eval.* **2019**, *38*. [CrossRef]
102. Russo, G.; Bergamo, O.; Damiani, L.; Lugato, D. Experimental analysis of the "Saint Andrea" Masonry Bell Tower in Venice. A new method for the determination of "Tower Global Young's Modulus E". *Eng. Struct.* **2010**, *32*, 353–360. [CrossRef]
103. Bergamo, O.; Campione, G.; Russo, G. Testing of "Global Young's Modulus E" on a rehabilitated masonry bell tower in Venice. *Eng. Fail. Anal.* **2017**, *74*, 202–217. [CrossRef]
104. Rosa Valluzzi, M.; Da Porto, F.; Casarin, F.; Monteforte, N.; Modena, C. A contribution to the characterization of masonry typologies by using sonic waves investigations. *Actes J. Sci. LCPC* **2009**, *1*, 713–718.
105. Colapietro, D.; Fiore, A.; Netti, A.; Fatiguso, F.; Marano, G.; de Fino, M.; Cascella, D.; Ancona, A. Dynamic Identification and evaluation of the seismic safety of a masonry bell tower in the osuth of Italy. In Proceedings of the 4th International Conference on Computational Methods in Structural Dynamics and Earthquake Engineering (COMPDYN 2013), Athens, Greece, 12–14 June 2013. [CrossRef]

106. Bongiovanni, G.; Clemente, P.; Buffarini, G. Analysis of the seismic response of a damaged masonry bell tower. In Proceedings of the 12th World Conference on Earthquake Engineering, Auckland, New Zealand, 30 January–4 February 2000; Volume 30.
107. Ceriotti, M.; Mottola, L.; Picco, G.P.; Murphy, A.L.; Guna, S.; Corra, M.; Pozzi, M.; Zonta, D.; Zanon, P. Monitoring heritage buildings with wireless sensor networks: The Torre Aquila deployment. In Proceedings of the 2009 International Conference on Information Processing in Sensor Networks, San Francisco, CA, USA, 13–16 April 2009; pp. 277–288.
108. Sepe, V.; Speranza, E.; Viskovic, A. A method for large-scale vulnerability assessment of historic towers. *Struct. Control. Health Monit.* **2008**, *15*, 389–415. [CrossRef]
109. Ivorra, S.; Giannoccaro, N.I.; Foti, D. Simple model for predicting the vibration transmission of a squat masonry tower by base forced vibrations. *Struct. Control. Health Monit.* **2019**, *26*, e2360. [CrossRef]
110. Diaferio, M.; Foti, D.; Giannoccaro, N.I.; Ivorra, S. Identification of the modal properties of an historic masonry clock tower. In Proceedings of the SAHC2014—9th International Conference on Structural Analysis of Historical Constructions, Mexico City, Mexico, 14–17 October 2014; Volume 6.
111. Diaferio, M.; Foti, D.; Giannoccaro, N.; Vitti, M. On the use of modal analysis and ground penetrating radar test for the physical parameter identification of an historical bell tower. In Proceedings of the Vienna Congress on Recent Advances in Earthquake Engineering and structural Dynamics, Vienna, Austria, 28–30 August 2013; pp. 28–30.
112. Foti, D.; Diaferio, M.; Venerito, M. Non-Destructive Damage Detection and Retrofitting Techniques on a Historical Masonry Tower. In Proceedings of the 3rd International Balkans Conference on Challenges of Civil Engineering, Epoka, Albania, 19–21 May 2016.
113. Diaferio, M.; Foti, D. Seismic risk assessment of Trani's Cathedral bell tower in Apulia, Italy. *Int. J. Adv. Struct. Eng.* **2017**, *9*, 259–267. [CrossRef]
114. Pieraccini, M.; Dei, D.; Betti, M.; Bartoli, G.; Tucci, G.; Guardini, N. Dynamic identification of historic masonry towers through an expeditious and no-contact approach: Application to the "Torre del Mangia" in Siena (Italy). *J. Cult. Herit.* **2014**, *15*, 275–282. [CrossRef]
115. Pelella, T.; Mannara, G.; Cosenza, E.; Iervolino, I.; Lecce, L. Structural dynamic investigations on the bell tower from the S. Lucia's church–Serra S. Quirico, Ancona. In Proceedings of the 7th International Seminar on Seismic Isolation, Passive Energy Dissipation and Active Control of Vibrations of Structures, Assisi, Italy, 2–5 October 2001; pp. 2–5.
116. Cosenza, E.; Iervolino, I. Case Study: Seismic Retrofitting of a Medieval Bell Tower with FRP. *J. Compos. Constr.* **2007**, *11*, 319–327. [CrossRef]
117. Ferraioli, M.; Miccoli, L.; Abruzzese, D. Dynamic characterisation of a historic bell-tower using a sensitivity-based technique for model tuning. *J. Civ. Struct. Health Monit.* **2018**, *8*, 253–269. [CrossRef]
118. Beconcini, M.L.; Bennati, S.; Salvatore, W. Structural characterisation of a medieval bell tower: First historical, experimental and numerical investigations. *HIstor. Constr.* **2001**, 431–444.
119. Bennati, S.; Nardini, L.; Salvatore, W. Dynamic Behavior of a Medieval Masonry Bell Tower. II: Measurement and Modeling of the Tower Motion. *J. Struct. Eng.* **2005**, *131*, 1656–1664. [CrossRef]
120. Pieraccini, M. Extensive Measurement Campaign Using Interferometric Radar. *J. Perform. Constr. Facil.* **2017**, *31*. [CrossRef]
121. Bartoli, G.; Betti, M.; Giordano, S. In situ static and dynamic investigations on the "Torre Grossa" masonry tower. *Eng. Struct.* **2013**, *52*, 718–733. [CrossRef]
122. Zini, G.; Betti, M.; Bartoli, G.; Chiostrini, S. Frequency vs. time domain identification of heritage structures. *Procedia Struct. Integr.* **2018**, *11*, 460–469. [CrossRef]
123. Bassoli, E.; Vincenzi, L.; Altri, A.M.D.; de Miranda, S.; Forghieri, M.; Castellazzi, G. Ambient vibration-based finite element model updating of an earthquake-damaged masonry tower. *Struct. Control. Health Monit.* **2018**, *25*, e2150. [CrossRef]
124. Castellano, A.; Fraddosio, A.; Martorano, F.; Mininno, G.; Paparella, F.; Piccioni, M.D. Structural health monitoring of a historic masonry bell tower by radar interferometric measurements. In Proceedings of the 2018 IEEE Workshop on Environmental, Energy, and Structural Monitoring Systems (EESMS), Salerno, Italy, 21–21 June 2018. [CrossRef]
125. Clementi, F.; Ferrante, A.; Ribilotta, E.; Milani, G.; Lenci, S. *On the Dynamics of the Civic Clock Tower of Rotella (Ascoli Piceno) Severly Damaged by the Central Italy Seismic Sequence of 2016*; Pisa University Press: Pisa, Italy, 2019; pp. 81–89.
126. Abruzzese, D.; Vari, A. Vulnerabilità sismica di torri medievali in muratura. In Proceedings of the XI ANIDIS Conference, Genova, Italy, 25–29 June 2004.
127. Bonato, P.; Ceravolo, R.; Stephano, A.D.; Molinari, F. Cross-time frequency techniques for the identification of masonry buildings. *Mech. Syst. Signal Process.* **2000**, *14*, 91–109. [CrossRef]
128. Castagnetti, C.; Bassoli, E.; Vincenzi, L.; Mancini, F. Dynamic Assessment of Masonry Towers Based on Terrestrial Radar Interferometer and Accelerometers. *Sensors* **2019**, *19*, 1319. [CrossRef] [PubMed]
129. Vincenzi, L.; Bassoli, E.; Ponsi, F.; Castagnetti, C.; Mancini, F. Dynamic monitoring and evaluation of bell ringing effects for the structural assessment of a masonry bell tower. *J. Civ. Struct. Health Monit.* **2019**, *9*, 439–458. [CrossRef]
130. Pieraccini, M.; Parrini, F.; Dei, D.; Fratini, M.; Atzeni, C.; Spinelli, P. Dynamic characterization of a bell tower by interferometric sensor. *NDT&E Int.* **2007**, *40*, 390–396. [CrossRef]
131. Castellacci, I.; Spinelli, P.; Vignoli, A.; Galano, L. Caratterizzazione dinamica del campanile della pieve di San Cresci a Macioli nei pressi di Pratolino, comune di Vaglia, e progetto di miglioramento sismico. *Boll. Ing.* **2007**, *10*, 21–23.

132. Monchetti, S. On the Role of Uncertainties in the Seismic Risk Assessment of Historic Masonry Towers. Ph.D. Thesis, Technische Universität Braunschweig, Braunschweig, Germany, 2018.
133. Zonta, D.; Pozzi, M. The remarkable story of Portogruaro Civic Tower's probabilistic health monitoring. *Struct. Monit. Maint.* **2015**, *2*, 301–318. [CrossRef]
134. Lorenzoni, F.; Valluzzi, M.; Salvalaggio, M.; Minello, A.; Modena, C. Operational modal analysis for the characterization of ancient water towers in Pompeii. *Procedia Eng.* **2017**, *199*, 3374–3379. [CrossRef]
135. Atzeni, C.; Bicci, A.; Dei, D.; Fratini, M.; Pieraccini, M. Remote Survey of the Leaning Tower of Pisa by Interferometric Sensing. *IEEE Geosci. Remote Sens. Lett.* **2010**, *7*, 185–189. [CrossRef]
136. García-Macías, E.; Ierimonti, L.; Venanzi, I.; Ubertini, F. An Innovative Methodology for Online Surrogate-Based Model Updating of Historic Buildings Using Monitoring Data. *Int. J. Archit. Herit.* **2019**, *15*, 92–112. [CrossRef]
137. García-Macías, E.; Venanzi, I.; Ubertini, F. Metamodel-based pattern recognition approach for real-time identification of earthquake-induced damage in historic masonry structures. *Autom. Constr.* **2020**, *120*, 103389. [CrossRef]
138. García-Macías, E.; Kita, A.; Ubertini, F. Synergistic application of operational modal analysis and ambient noise deconvolution interferometry for structural and damage identification in historic masonry structures: Three case studies of Italian architectural heritage. *Struct. Health Monit.* **2019**, *19*, 1250–1272. [CrossRef]
139. García-Macías, E.; Ubertini, F. Automated operational modal analysis and ambient noise deconvolution interferometry for the full structural identification of historic towers: A case study of the Sciri Tower in Perugia, Italy. *Eng. Struct.* **2020**, *215*, 110615. [CrossRef]
140. Gentile, C.; Ruccolo, A.; Saisi, A. Long-Term Vibration Measurements to Enhance the Knowledge of a Historic Bell-Tower. In *RILEM Bookseries*; Springer International Publishing: Berlin/Heidelberg, Germany, 2019; pp. 2236–2244. [CrossRef]
141. Gentile, C.; Saisi, A. Ambient vibration testing of historic masonry towers for structural identification and damage assessment. *Constr. Build. Mater.* **2007**, *21*, 1311–1321. [CrossRef]
142. Ceroni, F.; Pecce, M.; Manfredi, G. Seismic Assessment of the Bell Tower of Santa Maria Del Carmine: Problems and Solutions. *J. Earthq. Eng.* **2009**, *14*, 30–56. [CrossRef]
143. Cavaleri, L.; Ferrotto, M.F.; Trapani, F.D.; Vicentini, A. Vibration Tests and Structural Identification of the Bell Tower of Palermo Cathedral. *Open Constr. Build. Technol. J.* **2019**, *13*, 319–330. [CrossRef]
144. Ubertini, F.; Comanducci, G.; Cavalagli, N.; Pisello, A.L.; Materazzi, A.L.; Cotana, F. Environmental effects on natural frequencies of the San Pietro bell tower in Perugia, Italy, and their removal for structural performance assessment. *Mech. Syst. Signal Process.* **2017**, *82*, 307–322. [CrossRef]
145. Tsogka, C.; Daskalakis, E.; Comanducci, G.; Ubertini, F. The Stretching Method for Vibration-Based Structural Health Monitoring of Civil Structures. *Comput.-Aided Civ. Infrastruct. Eng.* **2017**, *32*, 288–303. [CrossRef]
146. Hinzen, K.G.; Fleischer, C.; Schock-Werner, B.; Schweppe, G. Seismic Surveillance of Cologne Cathedral. *Seismol. Res. Lett.* **2012**, *83*, 9–22. [CrossRef]
147. Kuhlmann, W.; Butenweg, C.; López, M.; Fernández, S. Seismic Vulnerability Assessment of the Historic Aachen Cathedral Germany. In Proceedings of the 13th World Conference on Earthquake Engineering, Vancouver, BC, Canada, 1–6 August 2004.
148. Uglešić, D.; Uglešić, A. Case Studies of structural natural frequencies assessment and application in SHM and the calibration of FEM models. In Proceedings of the 1st Croatian Conference on Earthquake Engineering, Zagreb, Croatia, 22–24 March 2021. [CrossRef]
149. Gentile, C.; Canali, F. Continuous Monitoring the Cathedral of Milan: Design, Installation and Preliminary Results. In Proceedings of the the 18th International Conference on Experimental Mechanics, Brussels, Belgium, 1–5 June 2018. [CrossRef]
150. Busca, G.; Cappellini, A.; Cigada, A.; Vanali, M. Operational modal Analysis of the "Guglia Maggiore" of the "Duomo" in Milano. In Proceedings of the 4th International Operational Modal Analysis Conference IOMAC 2011, Istanbul, Turkey, 9–11 May 2011; pp. 1–8.
151. Wilson, J.M.; Selby, A.R. Durham Cathedral tower vibrations during bell-ringing. In *Engineering a Cathedral*; Thomas Telford Publishing: London, UK, 1993; pp. 77–100. [CrossRef]
152. Rebelo, C.; Júlio, E.; Costa, D. Modal identification of the Coimbra University tower. In Proceedings of the 2nd International Operational Modal Analysis Conference, Copenhagen, Denmark, 30 April–2 May 2007; pp. 177–184.
153. Foti, D.; Diaferio, M.; Giannoccaro, N.I.; Mongelli, M. Ambient vibration testing, dynamic identification and model updating of a historic tower. *NDT&E Int.* **2012**, *47*, 88–95. [CrossRef]
154. Garcia Garcia, I.; Pardo, A; Pelayo, F.; Martin A.; Aenlle Lopez, M. Modal analysis of the tower of the Laboral City of Culture (Conference Paper). In Proceedings of the 6th International Operational Modal Analysis Conference, Gijon, Spain, 12–14 May 2015.
155. Rainieri, C.; Gargaro, D.; Fabbrocino, G. The role of operational modal analysis in the non-destructive assessment of an Italian Monument. In Proceedings of the 6th International Operational Modal Analysis Conference, Gijon, Spain, 12–14 May 2015.
156. Jardim, C.M.; Mendes, L.A.; Gonçalve, A.M. Dynamic characterization of the Funchal's cathedral bell tower. In Proceedings of the 5th International Operational Modal Analysis Conference, Guimaraes, Portugal, 13–15 May 2013.
157. Salachoris, G.P.; Standoli, G.; Betti, M.; Milani, G.; Clementi, F. Evolutionary numerical model for cultural heritage structures via genetic algorithms: A case study in central Italy. *Bull. Earthq. Eng.* **2023**. [CrossRef]

158. Patron-Solares, A.; Cremona, C.; Bottineau, C.; Leconte, R.; Goepfer, F. Study of bell swinging induced vibrations of bell tower of Metz cathedral (France). *Actes J. Sci. LCPC* **2005**, *1*, 529–536.
159. Ditommaso, R.; Mucciarelli, M.; Parolai, S.; Picozzi, M. Monitoring the structural dynamic response of a masonry tower: Comparing classical and time-frequency analyses. *Bull. Earthq. Eng.* **2012**, *10*, 1221–1235. [CrossRef]
160. Kolaj, M.; Adams, J. Dynamic characteristics of Canada's Parliament Hill towers from ambient vibrations and recorded earthquake data. *Can. J. Civ. Eng.* **2021**, *48*, 16–25. [CrossRef]
161. Peña, F.; Manzano, J. Dynamical Characterization of Typical Mexican Colonial Churches. In *Computational Methods in Applied Sciences*; Springer International Publishing: Berlin/Heidelberg, Germany, 2015; pp. 297–319. [CrossRef]
162. Manos, G.; Kozikopoulos, E. In-situ measured dynamic response of the bell tower of Agios Gerasimos in Lixouri Kefalonia, Greece and its utilization in the numerical predictions of its earthquake response. In Proceedings of the 5th International Conference on Computational Methods in Structural Dynamics and Earthquake Engineering (COMPDYN 2015), Athens, Greece, 25–27 May 2015. [CrossRef]
163. Ubertini, F.; Comanducci, G.; Cavalagli, N. Vibration-based structural health monitoring of a historic bell-tower using output-only measurements and multivariate statistical analysis. *Struct. Health Monit.* **2016**, *15*, 438–457. [CrossRef]
164. Ribilotta, E.; Clementi, F.; Pellegrino, M.; Poiani, M.; Gazzani, V.; Santilli, G.; Lenci, S. Monitoring cultural heritage buildings: The San Ciriaco bell-tower in Ancona. *AIP Conf. Proc.* **2018**, *2040*, 090005 . [CrossRef]
165. Baraccani, S.; Azzara, R.M.; Palermo, M.; Gasparini, G.; Trombetti, T. Long-Term Seismometric Monitoring of the Two Towers of Bologna (Italy): Modal Frequencies Identification and Effects Due to Traffic Induced Vibrations. *Front. Built Environ.* **2020**, *6*, 85. [CrossRef]
166. Sánchez-Aparicio, L.J.; Riveiro, B.; González-Aguilera, D.; Ramos, L.F. The combination of geomatic approaches and operational modal analysis to improve calibration of finite element models: A case of study in Saint Torcato Church (Guimarães, Portugal). *Constr. Build. Mater.* **2014**, *70*, 118–129. [CrossRef]
167. Scamardo, M.; Zucca, M.; Crespi, P.; Longarini, N.; Cattaneo, S. Seismic Vulnerability Evaluation of a Historical Masonry Tower: Comparison between Different Approaches. *Appl. Sci.* **2022**, *12*, 11254. [CrossRef]
168. Casarin, F.; Modena, C. Seismic Assessment of Complex Historical Buildings: Application to Reggio Emilia Cathedral, Italy. *Int. J. Archit. Herit.* **2008**, *2*, 304–327. [CrossRef]
169. Spinelli, P.; Salvatori, L.; Lancellotta, R.; Betti, M. Preliminary Assessment Of The Seismic Behaviour Of Giotto's Bell Tower In Florence. *Int. J. Archit. Herit.* **2022**, *17*, 23–45. [CrossRef]
170. Ramírez, E.; Lourenço, P.B.; D'Amato, M. Seismic Assessment of the Matera Cathedral. In *RILEM Bookseries*; Springer International Publishing: Berlin/Heidelberg, Germany, 2019; pp. 1346–1354. [CrossRef]
171. Mendes, P.; Baptista, M.; Agostinho, L.; Lagomarsino, S.; Costav, J. Structural and dynamic analysis of N. Sra. do Carmo church, Lagos Portugal. In Proceedings of the EURODYN 2005, Structural Dynamics, Paris, France, 4–7 September 2005; pp. 311–318.
172. Baptista, M.; Mendes, P.; Afilhado, A.; Agostinho, L.; Lagomarsino, A.; Victor, L.M. Ambient vibration testing at N. Sra. do Carmo Church, preliminary results. In Proceedings of the 4th International Seminar on Structural analysis of Historical Constructions, Bath, UK, 2–4 July 2004; pp. 483–488.
173. Ramos, L.F.; Aguilar, R.; Lourenço, P.B.; Moreira, S. Dynamic structural health monitoring of Saint Torcato church. *Mech. Syst. Signal Process.* **2013**, *35*, 1–15. [CrossRef]
174. Aguilar, R.; Noel, M.F.; Ramos, L.F. Integration of reverse engineering and non-linear numerical analysis for the seismic assessment of historical adobe buildings. *Autom. Constr.* **2019**, *98*, 1–15. [CrossRef]
175. Ivancic, S.R.; Briceno, C.; Marques, R.; Aguilar, R.; Perucchio, R.; Vargas, J. Seismic assessment of the St. Peter apostle church of Andahuaylillas in Cusco, Peru. In Proceedings of the SAHC2014–9th International Conference on Structural Analysis of Historical Constructions, Mexico City, Mexico, 14–17 October 2014.
176. Zonno, G.; Aguilar, R.; Castañeda, B.; Boroschek, R.; Lourenço, P.B. Environmental and Dynamic Remote Monitoring of Historical Adobe Buildings: The Case Study of the Andahuaylillas Church in Cusco, Peru. In *RILEM Bookseries*; Springer International Publishing: Berlin/Heidelberg, Germany, 2019; pp. 2216–2224. [CrossRef]
177. Peña, F.; Lourenço, P.B.; Mendes, N. Seismic assessment of the Qutb minar in Delhi, India. In Proceedings of the 14th World Conference on Earthquake Engineering, Beijing, China, 12–17 October 2008; pp. 483–488.
178. Masciotta, M.G.; Ramos, L.F. Dynamic identification of historic masonry structures. In *Long-Term Performance and Durability of Masonry Structures*; Elsevier: Amsterdam, The Netherlands, 2019; pp. 241–264.
179. Pineda, P.; Sáez, A. Assessment of ancient masonry slender towers under seismic loading: Dynamic characterization of the Cuatrovitas tower. In *Heritage Masonry*; WIT Press: Billerica, MA, USA, 2013; pp. 143–157. [CrossRef]
180. Buachart, C.; Hansapinyo, C.; Tantisukhuman, N.; Miyamoto, M.; Matsushima, M.; Limkatanyu, S.; Imjai, T.; Zhang, H. Real time vibration measurement and inverse analysis for dynamic properties of an axisymmetric masonry structure. *J. Asian Archit. Build. Eng.* **2022**, 1–10. [CrossRef]
181. Francisca, S.L. Dynamic Characterisation of the Bell Tower of Sant Cugat Monastery. Master's Thesis, Universitat Politècnica de Catalunya, Barcelona, Spain, 2020.
182. Italian Ministry of Infrastructure. *Norme Tecniche per le Costruzioni—DM 14 Gennaio 2008*; Supplemento Ordinario; Italian Ministry of Infrastructure: Rome, Italy, 2008.

183. Rodrigues, J.M.V.B.L. *Identificação modal estocástica: Métodos de análise e aplicações em estruturas de engenharia civil*; FEUP: Porto, Portugal, 2005.
184. Cantieni, R. Experimental methods used in system identification of civil engineering structures. In Proceedings of the International Operational Modal Analysis Conference (IOMAC), Copenhagen, Denmark, 26–27 April 2005; pp. 249–260.
185. Masjedian, M.; Keshmiri, M. A review on operational modal analysis researches: Classification of methods and applications. In Proceedings of the 3rd IOMAC, Portonovo, Italy, 4–6 May 2009; pp. 707–718.
186. Zhang, L.; Wang, T.; Tamura, Y. A frequency–spatial domain decomposition (FSDD) method for operational modal analysis. *Mech. Syst. Signal Process.* **2010**, *24*, 1227–1239. [CrossRef]
187. Brincker, R.; Zhang, L.; Andersen, P. Modal identification from ambient responses using frequency domain decomposition. In Proceedings of the 18th international Modal Analysis Conference (IMAC), San Antonio, TX, USA, 7–10 February 2000; Volume 1, pp. 625–630.
188. Overchee, P.; Moor, B. *Subspace Identification for Linear System*; Atlantis Press: Amsterdam, The Netherlands, 1996.
189. Casolo, S.; Diana, V.; Uva, G. Influence of soil deformability on the seismic response of a masonry tower. *Bull. Earthq. Eng.* **2017**, *15*, 1991–2014. [CrossRef]
190. de Silva, F.; Pitilakis, D.; Ceroni, F.; Sica, S.; Silvestri, F. Experimental and numerical dynamic identification of a historic masonry bell tower accounting for different types of interaction. *Soil Dyn. Earthq. Eng.* **2018**, *109*, 235–250. [CrossRef]
191. Traill-Nash, R.; Collar, A. The effects of shear flexibility and rotatory inertia on the bending vibrations of beams. *Q. J. Mech. Appl. Math.* **1953**, *6*, 186–222. [CrossRef]
192. Nallim, L.G.; Grossi, R.O. A general algorithm for the study of the dynamical behaviour of beams. *Appl. Acoust.* **1999**, *57*, 345–356. [CrossRef]
193. Cowper, G. The shear coefficient in Timoshenko's beam theory. *J. Appl. Mech.* **1966**, *33*, 335–340. [CrossRef]
194. Meirovitch, L. *Analytical Methods in Vibrations*; McMillan: New York, NY, USA, 1967.
195. Mazanoglu, K. Natural frequency analyses of segmented Timoshenko–Euler beams using the Rayleigh–Ritz method. *J. Vib. Control.* **2017**, *23*, 2135–2154. [CrossRef]
196. Combescure, A.; Hoffmann, A.; Pasquet, P. The CASTEM finite element system. In *Finite Element Systems: A Handbook*; Springer: Berlin/Heidelberg, Germany, 1982; pp. 115–125.
197. Gatelli, D.; Kucherenko, S.; Ratto, M.; Tarantola, S. Calculating first-order sensitivity measures: A benchmark of some recent methodologies. *Reliab. Eng. Syst. Saf.* **2009**, *94*, 1212–1219. [CrossRef]
198. Saltelli, A.; Tarantola, S.; Chan, K.S. A quantitative model-independent method for global sensitivity analysis of model output. *Technometrics* **1999**, *41*, 39–56. [CrossRef]
199. Cukier, R.; Fortuin, C.; Shuler, K.E.; Petschek, A.; Schaibly, J.H. Study of the sensitivity of coupled reaction systems to uncertainties in rate coefficients. I Theory. *J. Chem. Phys.* **1973**, *59*, 3873–3878. [CrossRef]
200. Tarantola, S.; Gatelli, D.; Mara, T.A. Random balance designs for the estimation of first order global sensitivity indices. *Reliab. Eng. Syst. Saf.* **2006**, *91*, 717–727. [CrossRef]
201. Mara, T.A. Extension of the RBD-FAST method to the computation of global sensitivity indices. *Reliab. Eng. Syst. Saf.* **2009**, *94*, 1274–1281. [CrossRef]
202. Jacques, J. *Contributions to Sensitivity Analysis and Generalized Discriminant Analysis*; Technical Report; University Joseph Fourier: Grenoble, France, 2005.
203. Helton, J.C.; Johnson, J.D.; Sallaberry, C.J.; Storlie, C.B. Survey of sampling-based methods for uncertainty and sensitivity analysis. *Reliab. Eng. Syst. Saf.* **2006**, *91*, 1175–1209. [CrossRef]
204. Xu, C.; Gertner, G.Z. Uncertainty and sensitivity analysis for models with correlated parameters. *Reliab. Eng. Syst. Saf.* **2008**, *93*, 1563–1573. [CrossRef]
205. Fernandes, V.A.; Lopez-Caballero, F.; d'Aguiar, S.C. Probabilistic analysis of numerical simulated railway track global stiffness. *Comput. Geotech.* **2014**, *55*, 267–276. [CrossRef]
206. Gaspar, A.; Lopez-Caballero, F.; Modaressi-Farahmand-Razavi, A.; Gomes-Correia, A. Methodology for a probabilistic analysis of an RCC gravity dam construction. Modelling of temperature, hydration degree and ageing degree fields. *Eng. Struct.* **2014**, *65*, 99–110. [CrossRef]
207. Sobol, I.M. Global sensitivity indices for nonlinear mathematical models and their Monte Carlo estimates. *Math. Comput. Simul.* **2001**, *55*, 271–280. [CrossRef]
208. Herman, J.; Usher, W. SALib: An open-source Python library for sensitivity analysis. *J. Open Source Softw.* **2017**, *2*, 97. [CrossRef]

*buildings*

MDPI

*Article*

# An Equivalent Frame Digital Twin for the Seismic Monitoring of Historic Structures: A Case Study on the Consoli Palace in Gubbio, Italy

**Daniele Sivori [1,*], Laura Ierimonti [2], Ilaria Venanzi [2], Filippo Ubertini [2] and Serena Cattari [1]**

[1] Department of Civil, Chemical and Environmental Engineering (DICCA), University of Genoa, Via Montallegro 1, 16145 Genoa, Italy; serena.cattari@unige.it
[2] Department of Civil and Environmental Engineering (DICA), University of Perugia, Via G. Duranti 93, 06125 Perugia, Italy; laura.ierimonti@unipg.it (L.I.); ilaria.venanzi@unipg.it (I.V.); filippo.ubertini@unipg.it (F.U.)
* Correspondence: daniele.sivori@unige.it

**Abstract:** Recent advances in computing performance and simulation tools allow today the development of high-fidelity computational models which accurately reproduce the structural behavor of existing structures. At the same time, advancements in sensing technology and data management enable engineers to remotely observe monitored structures in a continuous and comprehensive way. Merging the two approaches is a challenge recently addressed by the engineering research community, which led to the concept of digital twin (DT)—a simulation model continuously fed by sensor data which, throughout the whole lifespan of the structure, stands as its digital proxy. In the seismic field achieving such a task is still problematic, in particular for large and complex structures such as historical masonry palaces. To this aim, the paper proposes the integrated use of DTs and vibration data to support the seismic structural health monitoring of monumental palaces, discussing a practical application to the historical Consoli Palace in Gubbio, Italy. To overcome the computational limitations of classical approaches, an efficient equivalent frame (EF) model of the palace is built and continuously updated in quasi real-time based on modal information identified from vibration data. The performance and accuracy of the Equivalent Frame model are compared with those of a high-fidelity Finite Element representation, highlighting both their feasibility and limitations. Employing modal data recorded across the 15 May 2021 earthquake, the EF model demonstrates the ability to quickly assess the structural integrity of the palace in the post-earthquake scenario, as well as to forecast the residual capacity with respect to future seismic events.

**Keywords:** equivalent frame model; seismic structural health monitoring; model updating; structural damage; historical masonry buildings



**Citation:** Sivori, D.; Ierimonti, L.; Venanzi, I.; Ubertini, F.; Cattari, S. An Equivalent Frame Digital Twin for the Seismic Monitoring of Historic Structures: A Case Study on the Consoli Palace in Gubbio, Italy. *Buildings* **2023**, *13*, 1840. https://doi.org/10.3390/buildings13071840

Academic Editor: Humberto Varum

Received: 13 June 2023
Revised: 6 July 2023
Accepted: 16 July 2023
Published: 20 July 2023



## 1. Introduction

Recent advancements in digital computing, communication technologies, and measurement hardware are driving the digitalization of many engineering fields. The civil engineering sector is gradually adapting to this trend, with digital tools becoming a critical resource for supporting the decision making process in every phase of construction, from design to maintenance and future conservation of built assets.

A key step in this direction has been taken with the development of modern structural health monitoring (SHM) systems, in which different types of sensors are conveniently installed on the structure allowing to extrapolate parameters representative of the system's health in operating conditions, as well as those characterizing the environment and interacting with the system. Such parameters are identified and tracked in real time to detect abnormal states, i.e., states diverging from previous healthy structural conditions. Obtaining accurate and feasible information from monitoring structures, in other words extracting

engineering features from data, is a crucial task to support the structural maintenance and safety. In this regard, several techniques exist in the literature for identifying damage from vibration measurements of existing structures, mainly relying on modal parameters as damage-sensitive features [1]. Data-based approaches [2] are commonly used for early warning systems and damage detection, thanks to their efficiency and ease of implementation, and are today being fuelled by the advancement in machine learning [3]. However, these approaches typically rely on detecting statistically unusual responses with respect to those previously measured, lacking a strong relationship with the physical processes underlying the observed phenomena. This narrows the scope of applications to damage detection and localization, limiting the ability to provide insights about damage severity and predict future unobserved behaviors.

A more comprehensive damage identification framework is achieved by relying on a digital twin (DT) of the structure, a concept that civil engineering has recently inherited [4,5] from the industrial and mechanical fields and that is primarily embodied by the digitalization of the infrastructural management system, i.e., smart infrastructures [6] and smart buildings [7].

DT is a virtual simulation model that continuously acquires information from the physical reality of the structure, information which is encoded in the form of digital data coming from sensors. The model is able to enhance experimental data, providing a deeper understanding of unexpected behaviors or changes (due to aging, degradation, or structural damage) that may have occurred to the system. By incorporating sensors into the so-called "smart building" or "smart infrastructure" and developing a digital model, stakeholders such as concessionaires, managers, and decision makers can make informed decisions based on both data and models to guarantee the longevity and safety of their infrastructure [8]. Although the use of SHM for condition assessment, testing, and monitoring is becoming more and more prevalent, there is still a lack of agreement within the scientific community on its implementation. As a result, these practices are yet to be fully integrated into structural codes and standards, resulting in independent technological interpretations and implementations across different countries.

DTs are becoming essential for the preventive conservation of historical assets, combining building information modeling (BIM) [9] with SHM data and structural models [10,11]. As a cardinal principle of the DT concept [12], the need to continuously calibrate the model in quasi real time, thus solving an inverse optimization problem to minimize the difference between simulated and experimental response, can be exceptionally demanding from a computational viewpoint. This issue is widely testified in the literature, in particular dealing with the analysis of historical masonry structures. The complex architectural shapes arising from the search for beauty in the composition, the heterogeneous distribution of materials, the employment of different building techniques and structural systems, and the mark of historical interventions are all products of the long history of heritage structures, at the same time cultural value to be preserved and engineering challenge to be faced for this purpose.

On the one hand, these issues encourage the research community in integrating experimental data and mechanical models [13] towards the development of DT of historical masonry structures [14,15]. On the other hand, the computational burden of structural simulations is a limiting factor in employing physically based structural models as DT of historical buildings, particularly when dealing with almost real-time SHM.

In this context, the paper discusses the benefits and issues of integrating a structural DT to enhance the seismic structural health monitoring (S2HM, Ref. [16]) of historical masonry palaces, exploring its practical implementation for the dynamically monitored Consoli Palace of Gubbio located in Umbria Region, Central Italy. In particular, as a complementary approach to the commonly used finite element (FE) models, the research highlights the benefits of using a simplified equivalent frame (EF) formulation, which can be efficiently fused with continuous monitoring data using model updating techniques.

Section 2 proposes a general methodology to build and update a digital structural model for masonry palaces, suitable for pairing with a continuous monitoring system within the seismic SHM framework. Particular emphasis is given to the requirement of continuously updating the model with experimental modal data identified from the dynamic monitoring system, and how computational times play a key role in both the pre-earthquake calibration and post-earthquake simulation phases.

Section 3 presents the case study, the Consoli Palace of Gubbio, an ancient monumental masonry building continuously monitored with a mixed static–dynamic system by the University of Perugia. Focus is put on the behavior of the modal properties of the structure identified on a subdaily basis during May 2021, investigating any possible variations caused by a low-intensity earthquake that hit the structure on the 15th of the same month. The data-based analysis points out a slight but permanent reduction in natural frequencies of the structure as well as localized changes in mode shapes, revealing the potential occurrence of structural damage.

Section 4 exemplifies the methodology proposed to enhance the seismic monitoring of the palace, which employs a twinned structural model fuelled by monitoring data. In particular, the paper presents a detailed equivalent frame (EF) model of the structure, which is employed as a physics-based surrogate model. Its computational efficiency compared with the finite element (FE) counterpart allows for the continuous dynamic calibration of the elastic properties, which are directly updated based on daily-identified modal information. Employed a posteriori for the online assessment of seismic damage after the earthquake of 15 May 2021, the EF twin enriches the results of the data-based analysis, providing a model-based quantitative estimation of the reduction in the elastic stiffness of structural elements due to the damage caused by the seismic event.

Finally, in Section 4.3, the nonlinear capabilities of the EF twin are exploited to provide an effective offline tool to forecast the potential reduction in the seismic performance of the building after the earthquake. Based on experimental and numerical results from the literature, the constitutive laws of the masonry structural elements—in particular the parameters governing the secant stiffness and the resistance in the nonlinear phase—are degraded according to the updating of the elastic parameters. This allows for recovering, alongside the earthquake-induced reduction in stiffness identified from model updating, the unknown but complementary drop in masonry strength. The nonlinear static analyses performed on the updated/damaged model give an estimate of the reduction in global stiffness, resistance, and displacement capacity, information that can support the engineering judgement regarding the building safety and usability in the postseismic emergency phase.

## 2. Digital Twins for the Seismic Structural Health Monitoring of Masonry Palaces: Model-Driven and Data-Informed Methods

### *2.1. General Framework*

Integrating a structural DT in common data-based methods for the condition assessment of structures provides a great extension to the capabilities of health monitoring systems, for both the condition assessment during operational conditions and damage evaluation after an extreme event, such as an earthquake [17]. In vibration-based SHM systems, the physical asset is sensed by a set of heterogeneous sensors that extract information about the response of the structure to operational or extreme actions, as well as from the environment. Through data analysis techniques, the feedback loop is closed by a real-time casting of the structural conditions, which can be entirely based on the acquired data. This implies that informed decisions are fully dependent, in this case, on the ability to extract meaningful engineering quantities from the acquired data. Among the other factors, this possibility depends (i) on the quality and amount of available data, which in turn reflects the sensitivity, extension, and denseness of the sensor network, and (ii) on the compliance with the hypothesis underlying the analysis technique, such as the classical requirement of white noise input to perform operational modal analysis. The most evident limitation, however, is the impossibility of making predictions for the long-term behavior

of the structure, in particular for conditions that differ from those measured (for example, the strong nonlinear and inelastic response during the earthquake as opposed to the linear elastic conditions of ambient vibrations).

Employing a physics-based structural DT allows for enriching the information inferred from data with the one provided by the physics of the model (Figure 1). These benefits, among others, include

- virtual sensing, i.e., the possibility to measure locations and phenomena that are difficult or impossible to measure with physical sensors;
- the estimation of uncertainties and model sensitivities;
- the identification of damage, intended as its detection, localization, and quantification;
- the forecasting of linear and nonlinear structural behavior, predicting the response for arbitrary loading and environmental conditions.

Informed decisions are thus driven by the model response, which, in turn, is informed by experimental data. This scheme allows for casting the condition of the structure almost in real time. Moreover, based on the model's computational efficiency, such integration allows for quasi-real-time (online) simulations or, more often, for deferred-time (offline) forecasting of the structural behavior in future unmeasured states. Indeed, this general framework is still heavily case dependent and lacks a general systematic implementation for civil structures.

The following paragraphs discuss different strategies to achieve a model-driven and data-informed seismic health assessment of dynamically monitored masonry palaces, focusing first on the suitable structural modeling approaches (Section 2.2) and, second, on possible data fusion techniques (Section 2.3).

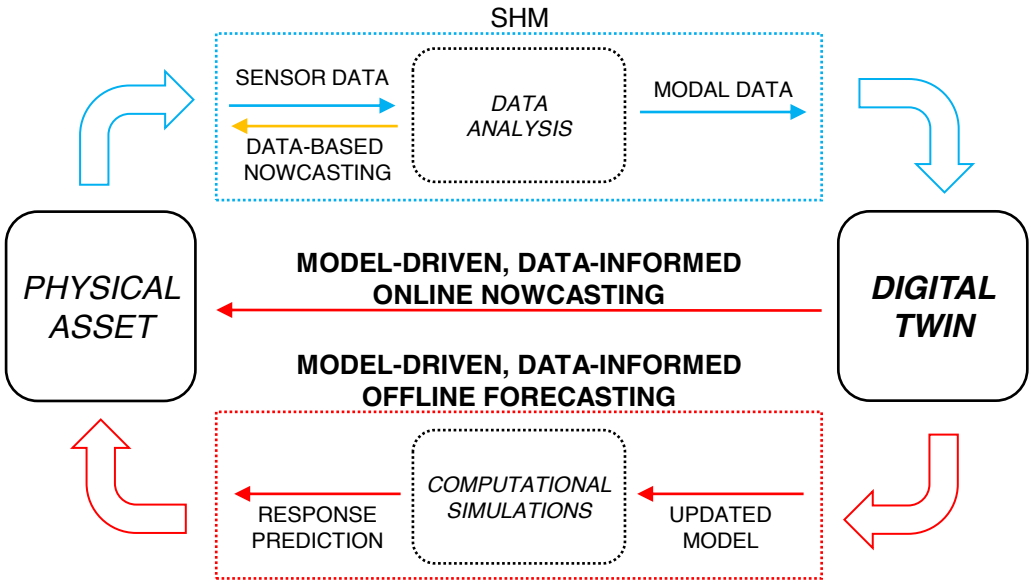


**Figure 1.** Conceptual diagram of the SHM–DT framework for the condition assessment of physical assets.

### *2.2. Structural Modeling*

The conservation and seismic protection of monumental masonry buildings pose significant challenges for the engineering community due to their intrinsic vulnerability to earthquake actions and intricate structural behavior. Heritage buildings are typically large structures that have undergone spontaneous transformations in the past, resulting in a current structural configuration characterized by geometrical irregularities, material heterogeneities, and peculiar structural systems. As a result, assessing the health and safety conditions of these structures presents some critical issues to be solved to achieve a reliable structural analysis.

One of the main challenges is the choice of the modeling strategy. Among the possibilities, deeply reviewed in [18,19] and discussed from a seismic engineering viewpoint in [20,21], finite element (FE) models constitute the most common choice for monumental assets. According to the classification proposed in [20], which refers to the modeling and discretization scales, these models may be classified as CCLM (continuous constitutive law models) in which the behavior of the masonry material is described by homogenized constitutive laws of phenomenological or micromechanical derivation. The literature is rich in examples of FE models built and employed to analyze the structural behavior of historical masonry structures, such as towers [22], churches and monasteries [23–25], fortresses and castles [26,27], and, not least, palaces [28–30].

The FE approach provides a very detailed representation of the structure, which comes at the cost of (i) a large initial effort devoted to the modeling phase (even though, today, automatized modeling strategies based on laser-scanned point clouds are becoming a real possibility [15,31,32]); (ii) dealing with a variety of input parameters to define the material and mechanical behavior in the linear and nonlinear regimes, especially in the calibration phase; and (iii) a significant computational demand in the simulation phase, depending on the complexity of the model and on the phenomena investigated. The second and third points can introduce limitations for the aspired SHM–DT integration in both the model updating and forecasting phases, particularly when dealing with earthquake actions—which imply strong nonlinearities and long computational times.

Focusing on the analysis of the response to seismic actions, in the case of historical masonry palaces, a complementary modeling strategy is provided by the equivalent frame (EF) formulation [33]. This approach falls within the class of SEM (structural elements models), in which macroscopic structural elements governed by a limited number of mechanical parameters discretize the masonry continuum. In the equivalent frame representation, only specific areas of masonry walls are explicitly modeled, the vertical and horizontal portions of masonry between openings exhibiting structural damage due to earthquake actions (namely, piers and spandrels). Deformability is thus narrowed to these elements, whereas the remaining parts of the walls are assumed to behave rigidly (rigid nodes). The three-dimensional model results from the assemblage of vertical frames, which commonly accounts for the sole in-plane stiffness of masonry panels, with horizontal diaphragms of finite stiffness representing the flooring system. An in-depth discussion regarding the EF implementation, which includes algorithms, failure criteria, static and dynamic analysis techniques, is reported in [33].

This approach shares some similarities with classical model reduction techniques, which aim at lowering the computational complexity of mathematical models by reducing their dimension, i.e., their degrees of freedom, accepting an approximation error with respect to the original model. The EF concept intrinsically follows this route, since the discretization condenses all the degrees of freedom of the structure at the scale of structural elements. This strategy strongly reduces the model's complexity and improves its performance, with the main limitations of losing (i) the resolution to describe scales smaller than that of masonry panels—such as the material continuum—and (ii) the possibility to capture unexpected (unmodeled) deformations happening in the rigid parts.

The morphological peculiarities that palaces typically share with ordinary masonry buildings, above all the regularity in the layout of the openings in the facades, suggest the EF modeling approach to be a suitable analysis tool. Indeed, other assumptions of this formulation have to be judged with expert knowledge on a case-by-case basis. A common example is the hypothesis of in-plane behavior of masonry walls, which is satisfied in the case of stiff horizontal diaphragms and by the presence of adequate wall-to-wall and wall-to-diaphragm connections. Due to the complexity and heterogeneity characterizing existing masonry buildings, there are several proposals in the literature to calibrate, adapt, or improve the rules governing the equivalent-frame representation to deal with common issues encountered in the modeling of these structures. Among the others, these issues are posed by an irregular arrangement of the openings [34–36], the presence of deformable

diaphragms [37,38], vaulted floors [39,40] and arch systems [41,42], the quality of the connection between orthogonal walls [43]. Undoubtedly, the relevance of these factors in the simulation of the global behavior of the structure and local behavior of its subsystems can be accurately evaluated from the comparison with experimental measurements [44–46] or with the results of a more detailed FE model, often adopted in the literature as a benchmark reference [47–51].

Following the guidelines provided by the literature, the EF technique can be reliably employed for the structural modeling of masonry palaces. Structural element modeling, even though simplified from the mechanical viewpoint, is still accurately representative of the building's seismic behavior and comes with the main advantage of being extremely computationally efficient when compared with higher-fidelity FE models. In the DT framework, the limited number of elements and degrees of freedom allows the updating phase to be solved in seconds (see the following Section 2.3), whereas prediction of nonlinear behavior can be obtained in a reasonable time ranging from several minutes to a few hours, even for large and complex structures—thanks to the efficient constitutive laws defined at the scale of structural elements.

### *2.3. Continuous Model Updating for Model Calibration and Real-Time Damage Assessment*

In structural engineering, model updating is the process of calibrating a structural model to improve its accuracy in reproducing the actual behavior of the structure subjected to different types of loading [52]. In the framework of a continuous vibration-based SHM, the structure is monitored during its operational conditions. Model updating involves, in this case, a periodic comparison—which can take place daily, hourly, or practically in real time, based on the characteristics of the acquisition and the computational effort required—between the modal parameters predicted by the model (natural frequencies and mode shapes) and the ones identified from ambient vibrations, i.e., from the low-amplitude oscillations generated by an ideal frequency-flat spectral input provided by environmental loading. In this case, among the several parameters involved in the direct eigenvalue problem, the sensitive ones (whose small change significantly influences the modal behavior [53]) can be tuned using an optimization algorithm, with the aim of minimizing the differences between the predicted and measured dynamical responses. These statements still hold true when dealing with the condition assessment of the structure after an extreme event, such as an earthquake, which is typically carried out by comparing the operational states before and after the loading to detect damage [54].

Model updating can be thus formulated as an inverse optimization problem. To approach it, two categories of optimization techniques can be employed: global and local optimization [55]. Global optimization algorithms, either deterministic, stochastic, or heuristic, try to explore the entire search space in order to find the global minimum of the objective function, the function that measures the difference between the predicted and target response. The objective function typically combines, through a tradeoff, the discrepancies between simulated and identified natural frequencies and mode shapes. These algorithms are generally more computationally expensive and thus slower, but are more likely to find the optimal solution, even if the solution space is nonlinear or nonconvex.

In contrast, local optimization algorithms focus on finding the minimum of the objective function within a small region of the space neighboring a known solution. These iterative algorithms are typically faster and more efficient but, at the same time, are more likely to become stuck in a local minimum, which may not be the optimal one.

The choice between global and local optimization techniques for model updating depends on the careful consideration of the complexity of the model, the specific issues to be addressed, and the available computational resources. A combination of both global and local optimization techniques may be used in some cases to achieve a balance between accuracy and efficiency. The ability to thoroughly explore the parameter space makes global optimization algorithms ideal for the first model calibration, a phase potentially dominated by several unknowns and large uncertainties (for example, related to the mechanical

properties of the building materials) but in which computational time is not a primary issue. Local optimization algorithms, instead, fit better the requirements of the continuous model updating, where the starting solution is already known from the first or previous calibrations, and relatively small changes are expected in the target solution (such as those due to changes in environmental conditions, to aging or degradation, to structural damage). Finally, low computational times are mandatory to keep track of real-time data coming from the monitoring system.

Overall, the large number of simulations involved in the model updating phase can become the limiting factor in employing physically based DT for the condition assessment of historical buildings. The calibration of a high-fidelity finite element (FE) model can be reasonably pursued when dealing with simple beamlike structures, such as towers [56–60], in these cases even in quasi real time [61–64]. Depending on the structural complexity and the level of detail of the model, even with modern computing capabilities, this task can become unfeasible due to unsustainable computational times.

One way of alleviating this burden is constructing approximation models, or surrogate models, as closely as possible representative of the original simulation model while being computationally cheaper to evaluate. Surrogate models are black box mathematical representations of a system. These models are typically built using a limited number of simulations and can be used to rapidly predict the behavior of the system under different conditions. The use of surrogate models has several advantages over traditional simulation methods. On the one hand, surrogate models can greatly reduce the computational cost of simulations, while, on the other hand, such models inherently incorporate some degree of uncertainty (due to the limited number of simulations they are based on). There are several types of surrogate models that can be used for structural applications. One popular type is the polynomial chaos expansion, which uses orthogonal polynomials to represent the system's behavior [65]. Another type is the Kriging model [66,67], which uses Gaussian processes to interpolate between the simulated data points. Despite their many advantages, surrogate models do have some limitations. Surrogates may not accurately capture the behavior of the system under new operating conditions. Additionally, the accuracy of the model may degrade over time as the system evolves or as new data become available. Moreover, they may not be appropriate for all types of systems, particularly those with highly nonlinear behavior.

For the seismic monitoring of masonry buildings and palaces, as previously discussed in Section 2.2, a possible alternative approach is to rely on an equivalent frame (EF) representation of the structure. This model can be considered for all purposes a physics-enhanced surrogate, an efficient model that is capable of simulating the global seismic response of the structure based on the underlying mechanics of a limited number of macroelements, the masonry panels. The reliability of this simplified approach in simulating the seismic response of masonry buildings, even in the strongly nonlinear regime, is well documented in the literature. Previous validations include, among the others, the comparison with the results of shaking table tests [68–70], with high-fidelity micro modelling techniques [35], with acceleration measurements acquired on monitored buildings recently hit by earthquakes [44–46,71]. The employment of the EF model in the framework of seismic monitoring is still evolving from an exploratory stage, which nonetheless is following recent satisfactory outcomes obtained from the simulation of the modal dynamic behaviour of existing buildings (see [38,44]) as well as some validations for low-amplitude vibrations [72] and in the weakly nonlinear regime [73].

The EF discretization allows for greatly reducing the complexity of the simulation and, as a consequence, reducing the computational effort paying the cost of spatial resolution (which is limited by the scale of structural elements). As it will be shown in the applications (Section 4), this efficient model can be employed directly in continuous updating procedures, making it effectively a structural DT of the monitored structure—enriching the information extracted from the monitoring system in the immediate aftermath of the earthquake,

evolving data-based damage detection to a more robust model-driven and data-informed damage assessment, which can include also damage localization and quantification.

### *2.4. Model-Driven Data-Informed Forecasting of the Postseismic Structural Behavior*

As discussed in the previous paragraph (Section 2.3), ideal DT models should have capabilities that can be readily employed online in parallel to data acquisition, i.e., in a quasi-real-time framework, to support the structural health monitoring and the condition assessment of monitored buildings after the earthquake, enriching the information provided by vibration data alone. These tasks commonly involve, among others, an initial evaluation of potential damage to the structure, which is usually followed by a more detailed evaluation of the residual structural capacity.

The first task (ideally including all three levels of damage assessment, detection, localization, and quantification) can be achieved through model updating and provides useful information related to the actual damage diffusion and gravity in the real structure, as well as quantitative estimates of the degradation of the mechanical properties of the structural elements.

More accurate evaluations regarding, for example, the structural functionality, are usually carried out offline since they require computationally expensive nonlinear simulations. These analyses are commonly addressed to verify the operativity of the structure (in particular, if the structure holds a strategic function in the management of the seismic emergency of the urban area, as often happens to town hall buildings in Italian municipalities), its usability and safety (to allow the following in situ inspections, the recovering of artistic assets in safety conditions, eventually the return of occupants), and finally, the residual capacity to future seismic actions to ensure the protection of human lives in the case of aftershocks.

In this respect, FE modal surrogates are well suited for quick damage assessment (Section 2.3) but lack the capabilities to forecast the behavior of the structure after the earthquake. EF models, on the other hand, have roughly the same efficiency in the elastic regime and are able, in a few tens of minutes, to simulate the nonlinear response of the structure to known or expected seismic actions. Thus, they can be used to accurately simulate structural damage and the subsequent loss of capacity, making them a valuable tool to assess the response to future shocks.

Simulations regarding the general seismic behavior of the structure can be carried out in advance, by selecting plausible seismic input and simulating and interpreting the expected structural response in a statistical sense. When effectively synthesized, these results become immediately useful once the earthquake strikes. For example, the recently proposed behavioral charts that relate a measured frequency reduction to the expected global damage level reached by the structure [74] allow for a quick model-driven, data-informed evaluation of the damage level expected on the structure. Indeed, a precise evaluation of the effects caused by a specific earthquake that hit the structure can be only carried out only after the event. The seismic input measured at the base or in the proximity of the building is employed directly, when available, to accurately simulate the nonlinear structural response to the earthquake and, in the case of a monitored structure, to compare it with response measurements [45].

Following the methodology outlined, the following paragraphs present the development of an EF digital twin for the historical Consoli Palace of Gubbio, Italy. The DT is employed to support the evaluations of structural integrity after the seismic sequence that hit the building on 15 May 2021, tackling the online damage assessment based on continuous model updating (Section 4.2) and the offline evaluation of the building residual capacity based on nonlinear static analyses (Section 4.3).

## 3. The Consoli Palace of Gubbio, Italy, and the Seismic Sequence of 15 May 2021

### *3.1. The Palace: Dynamic Monitoring System and AVT*

The Consoli Palace, situated in Gubbio, Umbria (Central Italy), is an impressive architectural complex constructed during the 14th century. It stands out as one of the most daring constructions of its time, towering over the town's main square at a height of 60 meters. The palace comprises a central body, a panoramic loggia, and a bell tower, accessible from the rooftop. The load-bearing walls of the Consoli Palace have a thickness of about 1.2 m, measured from in situ inspections, and each floor is characterized by differently oriented and distributed vaulted ceilings. The building is constructed with a homogeneous texture of calcareous stone masonry. The east- and west-side facades of the palace are adorned with round-arched windows and merlons on the rooftop.

As per the seismic regulations outlined in the Italian technical standard NTC2018 [75], the site is characterized by a peak ground acceleration (PGA) of 0.227 g with a 10% probability of exceedance in a 50-year time frame (return period of 475 years). In addition, the city is situated near the Gubbio normal fault, a preorogenic fault that stretches for 22 km [76]. To monitor the high seismicity of the area, a dense network of seismic stations, known as Alto Tiberina Near Fault Observatory—TABOO, was established in 2014 [77].

In 2017, a continuous monitoring system was installed in the palace, which underwent further improvements in July 2020 by increasing the number of sensors (A1–A12 with reference to Figure 2). The Department of Civil and Environmental Engineering at the University of Perugia designed and managed the system within the framework of European and national projects. The acquisition system consists of several components:

- a mixed data acquisition system wired to sensors (NI CompactDAQ-9132 model equipped with NI 9234 acquisition modules for accelerometers with 24-bit resolution, 102-dB dynamic range, and anti-aliasing filters;
- a NI 9219 acquisition module with 24-bit resolution, $\pm$60 V range, 100 S/s for LVDTs and thermocouples);
- a wireless network (LoRaWAN system technology).

The monitoring system comprises twelve unidirectional accelerometers named A1–A12, located and oriented as schematically reported in Figure 2. The accelerometers, model PCB393B12, have the following characteristics: a measurement range of $\pm$0.5 g, a frequency range of 0.15–1000 Hz, a broadband resolution of 8 μg, and a resonant frequency $\geq$ 10 kHz. Additionally, four linear variable transducers (model S-series) with a measurement range of 0–0.5 mm and a resolution of 0.31 m (D1–D4), and six thermocouples (T1–T6, model K-type) are included in the system.

Acceleration data are recorded in files that span a duration of 30 min of measurements with a sampling frequency of 100 Hz, then downsampled to 40 Hz. Measurements of crack amplitudes and temperature values are acquired every half hour. All the data are consistently saved in a cloud-based storage system, conveniently accessible via a web-based platform. The data are constantly post-processed by means of the MOVA integrated software, an automated tool based on the covariance-based stochastic subspace identification (SSI) technique. Environmental effects are removed from original signals through the multiple linear regression (MLR) statistical models after analyzing the time series of ambient and material temperature measurements during the training period of one year. More details on the analyzed case study can be found in [67,78,79].

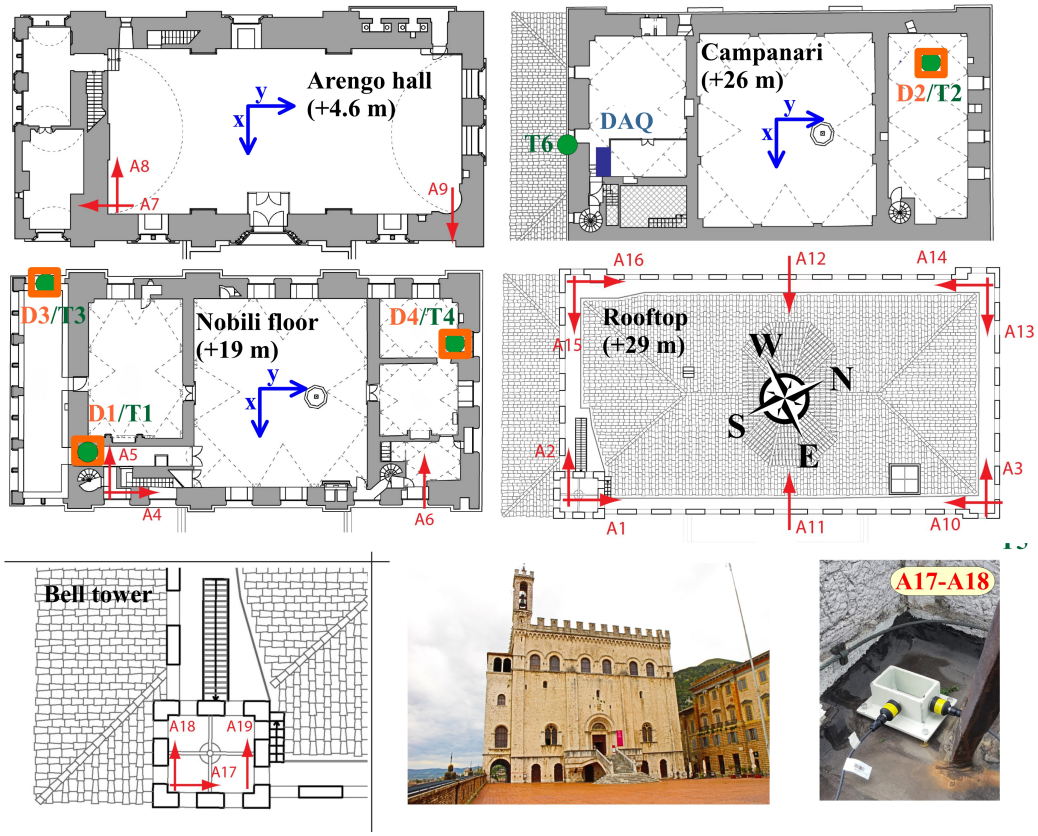


**Figure 2.** A schematic representation of the SHM system of the palace (A1–A12) and of the AVT extended sensors network (A1–A19).

For the purpose of tackling the initial calibration of computational models, an AVT was performed on 7 May 2021 by including channels A13–19 (Figure 2). More in detail, channels A13–A16 allowed for improving the definition of the rooftop's dynamic behavior, whereas channels A17–A19, placed at the top of the bell tower, were included to assess the impact of this slender element on the global dynamics of the palace. The identification results are presented here as a reference for the following discussion. The first five identified modes (Table 1) are found in the frequency range 2.3–4.2 Hz, corresponding to the range of periods 0.24–0.43 s. The labels "G" and "L" indicate, respectively, a global and local mode, with a dominant "F" flexural or "T" torsional component developing along the x, y, or z reference axes (see Figure 2).

**Table 1.** Natural frequency $f$ and damping ratio $\xi$ identified for the first five natural modes of the palace during the AVT performed on 7 May 2021.

| Mode | Type | $f$ (Hz) | $\xi$ (%) |
|---|---|---|---|
| 1 | G-$F_x$ | 2.296 | 1.121 |
| 2 | L-$F_y$ | 2.989 | 0.751 |
| 3 | L-$F_x$ | 3.508 | 0.779 |
| 4 | G-$F_y$ | 3.743 | 2.477 |
| 5 | G-$T_z$ | 4.172 | 1.104 |

### *3.2. Continuous Monitoring across the Seismic Sequence of 15 May 2021*

On 15 May 2021, a minor seismic sequence took place with the epicenter in Gubbio, Italy, characterized by the strongest shock of magnitude Mw 3.9 hitting at 07:56:01 UTC, and other slight shocks occurred in the following days, with a maximum magnitude up to Mw 3.1. Ground accelerations have been recorded by the measurement station "Gubbio Parcheggio Santa Lucia" (GBSL) of the Italian Strong Motion Network (RAN, [80]), a dense

network of seismic stations distributed all over the Italian territory managed by the Italian Department of Civil Protection. The station is lying at a distance of around 700 m from the epicenter (Figure 3a) on a soil of class B according to Eurocode 8 ($V_{S,30}$ = 765 m/s$^2$, quite close to the 800 m/s$^2$ threshold of class A representing the bedrock condition). The waveforms downloaded from the ITACA database [81] show that the peak ground accelerations (PGA) reached 102.38, 77.83, and 47.15 cm/s$^2$ along the HNE, HNN, and HNZ components, respectively (Figure 3b, top). The response spectra show that the energy content of the horizontal components is localized in the range 0.1–0.25 s (Figure 3b).

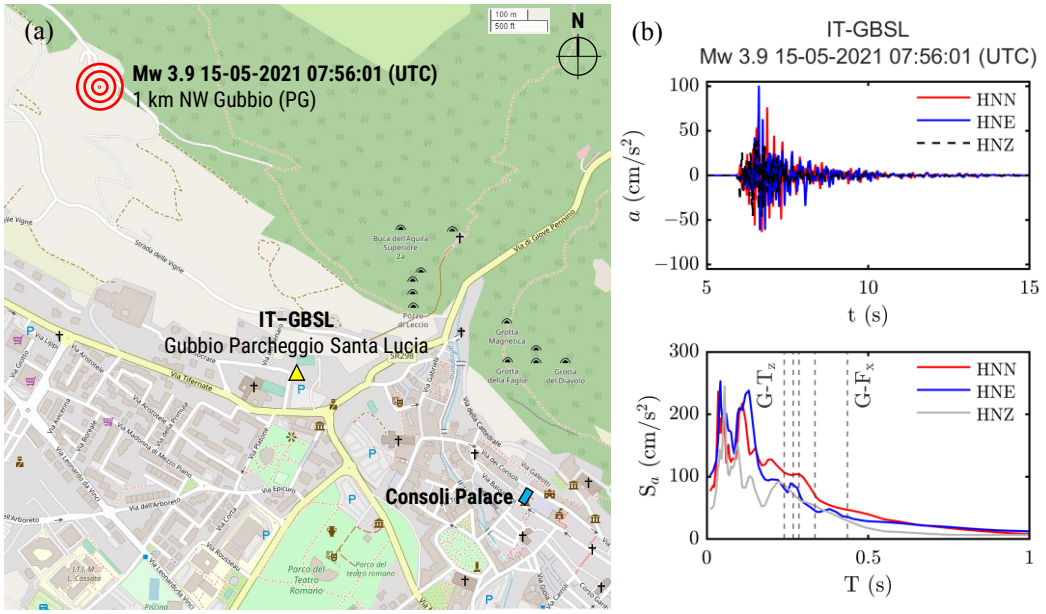


**Figure 3.** Earthquake of 15 May 2021 in Gubbio, Italy. (**a**) Location of the epicenter, of the RAN seismic station GBSL and of the Consoli Palace. (**b**) Accelerations measured by the GBSL station along the HNN, HNE, and HNZ components, and corresponding response spectra (damping 5%).

Because of an electrical interruption affecting the SHM system until around 08:00 UTC, continuous vibration data acquired on the palace are available only before and after the event [82]; nonetheless, they remain extremely valuable for the purposes of this work. To test the reliability of a continuous updating of the structural models of the palace (see Section 4.1) and their ability to support the post-earthquake damage assessment, a month of modal data going from 1 May to 31 May and including the earthquake event is first analyzed and, later in the paper, employed as baseline data set to carry out the model updating and the following damage assessment.

To contain their variability, the natural frequencies and mode shapes of the first five modes of vibrations—which have been identified from the research unit of Perugia from continuous 30 min long acquisitions and depurated from environmental effects—have been averaged over each day. Further information regarding the continuous dynamic identification is provided in [82].

The Consoli Palace, located at a distance of around 1.25 km from the epicenter of the main earthquake, exhibited a mild evolution of the pre-existing damage mechanisms, which are related to some observed cracks affecting the north facade and its connection with the orthogonal west facade. An in-depth assessment of the damage caused by the seismic sequence, endorsed by the fusion of in situ inspections with FE-based computational simulations, is reported in [67]. For the purpose of the following applications, it should be highlighted that, as a consequence of the low intensity of the shock, the mild severity of the damage pattern does not pose a relevant threat to the structural integrity of the palace.

Nonetheless, as reported in [67], a permanent frequency decay has been observed for the first five modes of vibration, ranging from 1.1% to 1.4% for the global modes of the palace, from 2.3% up to 2.7% for the local modes of the bell tower.

This change is already evident by looking at the average daily value of the natural frequencies (referred to as $\hat{f}$ in the following) in the short observing period of the month of May 2021 (Figure 4a). The relative frequency variations with respect to the initial observation $\Delta\hat{f}/\hat{f} = -(\hat{f} - \hat{f}_0)/\hat{f}_0$ (Figure 4b) show permanent reductions in the range 2–4%, whereas those related to the previous day (subscript $d - 1$, Figure 4d) clearly highlight how those reductions are maximum across the day of the main shock. Variations in mode shapes, which are estimated by the modal assurance criterion (MAC) indicator [83], seem to be generally contained (MAC values higher than 0.94, Figure 4c,e). More in detail, the daily natural frequencies across 15 May, their relative reductions, and cross-MAC are reported in Table 2.

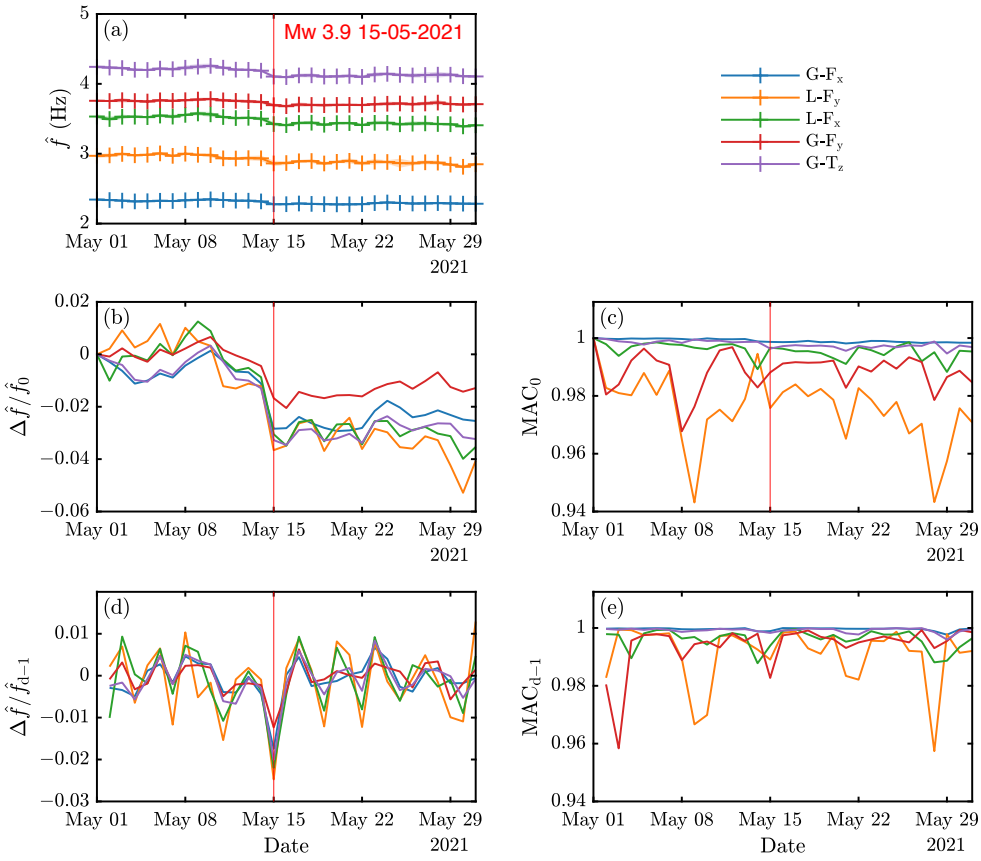


**Figure 4.** First five identified modes of vibrations and their observed variations in May 2021, highlighting the effects of the Mw 3.9 seismic shock of 15 May. (**a**) Daily-averaged frequency $\hat{f}$, (**b**,**d**) relative variations with respect to the first observation $\hat{f}_0$ and previous-day observation $\hat{f}_{d-1}$, (**c**,**e**) MAC values.

For what concerns the long-term behavior, analyzing the average variations—related to the average frequencies $\bar{f}$ and average mode shapes $\bar{\Phi}$ of the pre- and post-event observation periods—confirms the occurrence of permanent changes in mode frequencies, in particular those related to the local modes of the bell tower (right side of Table 2). In general, these changes appear much more limited for mode shapes. Indeed, the average indicator $\overline{\text{MAC}}$ does not suggest a certain mode among those identified to be the most affected by seismic damage.

**Table 2.** Change in natural frequencies caused by the earthquake of 15 May 2021, both with respect to daily-averaged values ($\hat{f}_{14\text{-}05\text{-}21}$, $\hat{f}_{15\text{-}05\text{-}21}$, and relative variations $\Delta\hat{f}/\hat{f}$) and long averages over the whole pre- and post-earthquake observation periods ($\overline{f}_{pre}$, $\overline{f}_{post}$, and relative variations $\overline{\Delta f}/\overline{f}$).

| Mode | Type | $\hat{f}_{14\text{-}05\text{-}21}$ | $\hat{f}_{15\text{-}05\text{-}21}$ | $\Delta\hat{f}/\hat{f}$ | MAC | $\overline{f}_{pre}$ | $\overline{f}_{post}$ | $\Delta\overline{f}/\overline{f}$ | $\overline{MAC}$ |
|---|---|---|---|---|---|---|---|---|---|
| 1 | G-$F_x$ | 2.317 | 2.277 | −0.0174 | 0.9991 | 2.330 | 2.285 | −0.0194 | 0.9993 |
| 2 | L-$F_y$ | 2.934 | 2.861 | −0.0247 | 0.9890 | 2.970 | 2.869 | −0.0340 | 0.9990 |
| 3 | L-$F_x$ | 3.501 | 3.424 | −0.0220 | 0.9931 | 3.531 | 3.425 | −0.0299 | 0.9974 |
| 4 | G-$F_y$ | 3.741 | 3.695 | −0.0123 | 0.9766 | 3.760 | 3.705 | −0.0144 | 0.9928 |
| 5 | G-$T_z$ | 4.188 | 4.104 | −0.0200 | 0.9982 | 4.220 | 4.117 | −0.0244 | 0.9984 |

To achieve a preliminary data-based localization of the occurred damage, a more accurate analysis has been carried out on the whole set of considered modes by estimating different coordinate-based damage indicators, the coordinate MAC (COMAC) in its original [84], scaled ("-s") [85] and enhanced ("-e") [86] versions, as well as the variational MAC ("-var") [87]. The COMAC indicator, intended as the difference from unitary value, is expected to be higher for the coordinate that underwent the most abrupt changes. The variational MAC highlights the coordinates to be subsequently removed from the MAC calculation to maximize its average increase over all modes.

The standard and scaled COMAC indicators evaluated between the mode shapes identified the day of the earthquake and those of the previous day (Figure 5a) suggest sensors A6 and A11, both directed along x (the direction parallel to the short sides of the palace), to be the most affected by earthquake effects. Sensor A6 is located at the Nobili floor close to the northeast corner, whereas sensor A11 is on the rooftop, at the middle of the main facade. The enhanced COMAC points out sensor A2, located on the rooftop and close to the south side, as the most affected sensor, followed in turn by A6 and A11. This result is in better agreement with the MAC-var analysis (Figure 5b). The removal of channel A2, in fact, provides the maximum gain in the average value of the MAC, improving mostly the correlation of the global mode G-$F_y$. This mode develops in the orthogonal direction y (parallel to the long sides of the palace) but includes some torsional effect, which can explain such an outcome.

The same indicators estimated on the averaged mode shapes of the pre- and post-event observation periods seem to be more coherent among themselves. All the COMAC indicators (Figure 5c) agree with the MAC-var analysis (Figure 5d) in identifying locations A2 as the most affected by the long-term effects of the earthquake. The removal of this sensor from the MAC analysis is optimal in an average sense and again is improving mostly the correlation of the global mode G-$F_y$ along the orthogonal direction.

Data-driven results point out, in general, the x direction as the most affected by seismic damage, damage that can be roughly localized—but hardly quantified—in the south perimeter walls of the palace (in accordance with the evolution of the pre-existing crack pattern observed during the in situ inspections, see [67]). These outcomes will be taken as reference in the applications of the proposed model-based data-informed procedures of the following sections.

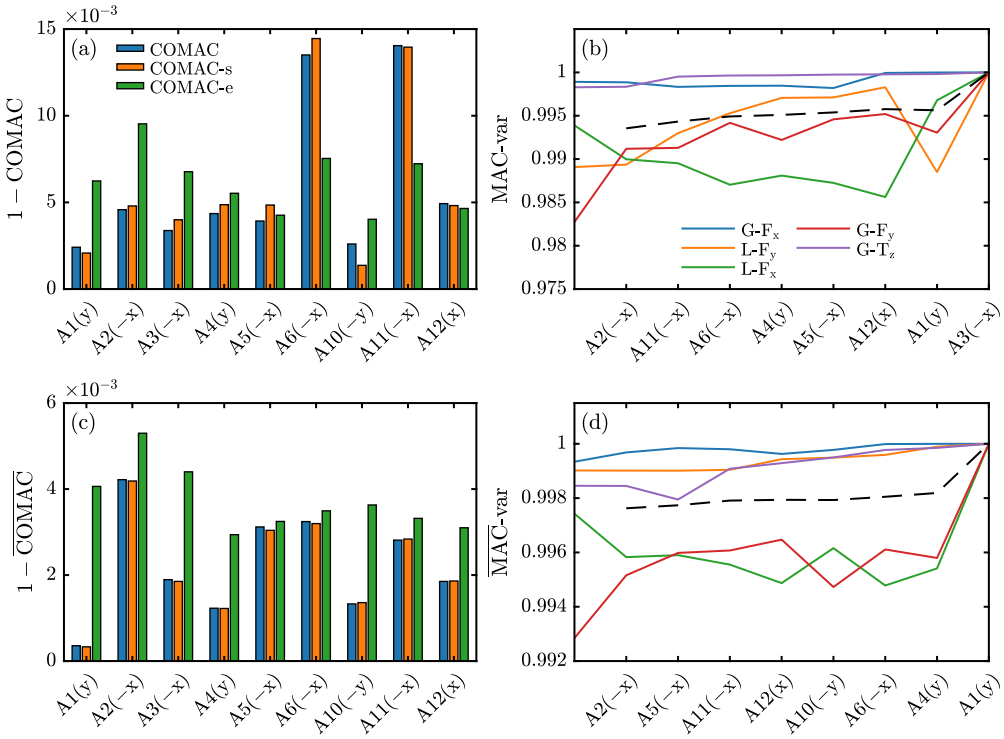


**Figure 5.** COMAC and MAC-var indicators estimated after the earthquake of 15 May 2021, (**a**,**b**) with respect to the previous day, (**c**,**d**) to long averages over the whole pre- and post-earthquake observation periods.

## 4. Continuous Updating of DTs: Applications

### *4.1. Equivalent Frame (EF) and Finite Element (FE) Models of the Palace*

To deepen the analysis regarding the seismic behavior of the palace, keeping in mind the aim of developing a structural DT to support the postseismic evaluations (Section 2), the structure has been modeled according to two different approaches (among those discussed in Section 2.2), the equivalent frame (EF) and finite element (FE) formulations.

The EF model of the structure (Figure 6a) has been built by the research unit of the University of Genoa in the framework of the PRIN research project DETECT-AGING (Degradation Effects on sTructural safEty of Cultural heriTAGe constructions through simulation and health monitorING).

The three-dimensional model has been meshed and assembled employing the commercial software 3Muri (S.T.A. DATA, version 13.9.0.0), whose solver (TREMURI in the following) has been developed at the University of Genoa [33]. Based on the building geometry and openings arrangement and according to the rules commonly employed for ordinary masonry buildings, each masonry wall is automatically subdivided into deformable piers and spandrels, which are connected by rigid nodes. Finally, the three-dimensional model of the structure is built assembling vertical walls and horizontal diaphragms. Manual tweaking of the original mesh has been carried out to improve the EF discretization of the external walls of the Arengo Hall (Section 3.1). This area is characterized, in fact, by a relevant interstorey height—close to 15 m—and relatively small openings. The alteration of the original mesh made the height of the piers more representative of the expected deformable portion of the walls, reducing at the same time the excessive dimensions of rigid nodes, which may otherwise produce an overestimation of the overall stiffness. The development of the model, the optimization of the mesh, and the first dynamic calibration of the model based on the extended AVT campaign of May 2021 (Section 3.1) are described in detail in [88]. The EF model here presented has been recalibrated according to the new updating scheme presented in Section 4.2, which considers just four predefined regions and four updating variables, namely, the regions' Young moduli.

The three-dimensional FE model of the structure (Figure 6b) has been developed by the research unit of the University of Perugia in the framework of previous research [67,89]. To provide more details, the authors reconstructed and calibrated a model using AVT data from May 2017. This model consisted of nine uniaxial high-sensitivity piezoelectric accelerometers, as documented in [89]. Initially, the model was separated into four parts: the Gattapone level (located beneath the square), the Arengo Hall level, the Nobili level (which includes the Campanari level), and the bell tower. To account for possible variations in material properties in these portions of the building, each part was assigned a distinct Young modulus value. Subsequently, in May 2021, a new AVT campaign was conducted (Section 3.1) by means of a dense sensor network (A1–A19 with reference to Figure 2). The model was then recalibrated, whereby the elastic modulus of nine predefined regions was adjusted (for further information, refer to [67]). These regions include the Arengo floor and the Gattapone level, the Nobili arched ceiling, the rooftop and its annexes, the loggia, the bell tower, the potential cracking patterns that can be activated by an earthquake evaluated as reported in [79] through nonlinear static analysis, the vertical walls along the x direction, and the vertical walls along the y direction.

Table 3 reports a general comparison between the two structural models in terms of number of nodes, elements, degrees of freedom (DOFs) resulting from the two discretizations, and the average elapsed time for the execution of different types of analysis (e.g., modal analysis (MA) and nonlinear static analysis (NLSA)) on a modern quad-core CPU. The difference in sophistication emerges immediately. The FE model has a number of DOFs three orders of magnitude greater than that of the EF companion. This huge increase in complexity grants the FE model unparalleled fidelity, at the cost of a dramatic increase in computational times—which are around 200 times longer for a modal analysis and in the order of ten thousand times longer for a nonlinear seismic analysis, such as NLSA.

**Table 3.** Comparison between the EF and FE models of the Consoli Palace.

| | **Equivalent Frame (EF)** | **Finite Element (FE)** |
|---|---|---|
| Nodes | 166 (2-D), 144 (3-D), | 89 976 (3-D) |
| Elements | 203 piers, 102 spandrels, 244 elastic beams, 15 4-nodes, and 95 3-nodes diaphragms | 3 531 140 4-nodes tetrahedral solid elements |
| Free DOFs | 969 | 3 418 097 |
| Restrained DOFs | 243 | 113 043 |
| Total mass | 28 383.666 ton | 29 209.57 ton |
| Elapsed time for MA | ≈4 s | ≈1081.9 s |
| Elapsed time for NLSA | ≈120 s | ≈$2.11 \times 10^6$ s |

Figure 7 summarizes the outcomes of the EF/FEM calibrations with respect to AVT experimental data, in terms of both mode shape correlation (MAC value) and relative difference $\Delta f/f$ between numerical and experimental frequencies. In addition, a schematic depiction of the EF/FEM global mode shapes is illustrated. The EF calibration process (see Section 4.2), which is involving just four parameters, takes around 5 iterations (each with 4 parallel function evaluations to build the parameter sensitivity matrix) and 4 subiterations, for a total of 29 function evaluations completed in less than 1 min. Despite a rougher discretization, the EF model 7 is able to achieve a very good agreement with experimental identification, comparable with the results obtained by the FE model calibration. For both models, the percentage differences in frequency are lower than 4% for all the modes, and the MAC values always exceed 0.7. This result points out the possibility to reproduce the elastic behavior of the masonry palaces by means of a simplified EF formulation. It is important to emphasize that low values of the MAC indicator observed in the EF model for the local modes of the bell tower (modes L-$F_y$ and L-$F_x$) are the result of updating choices. As explained later in the paper (Section 4.2), to ensure a robust continuous updating of the EF digital twin, the updating favors the optimization of frequency and mode shapes for the

global modes (those well captured by the permanent SHM system, which lacks sensors on the top of the bell tower), giving up some correlation for the local ones.

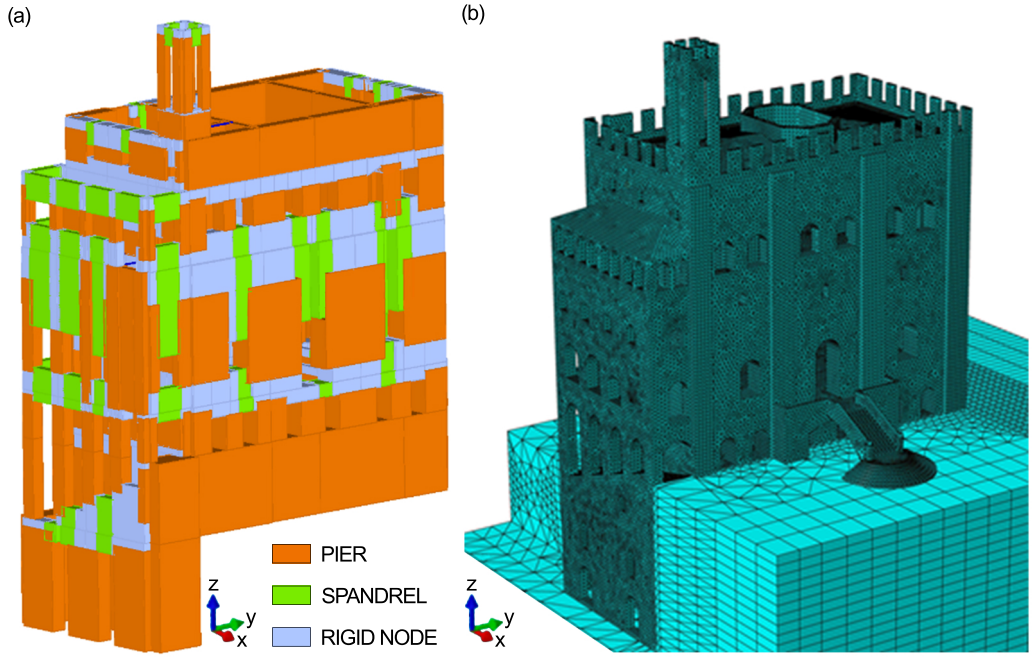


**Figure 6.** Structural models of the Consoli Palace: (**a**) EF model based on a structural element discretization and (**b**) high-fidelity FE model with a refined mesh.

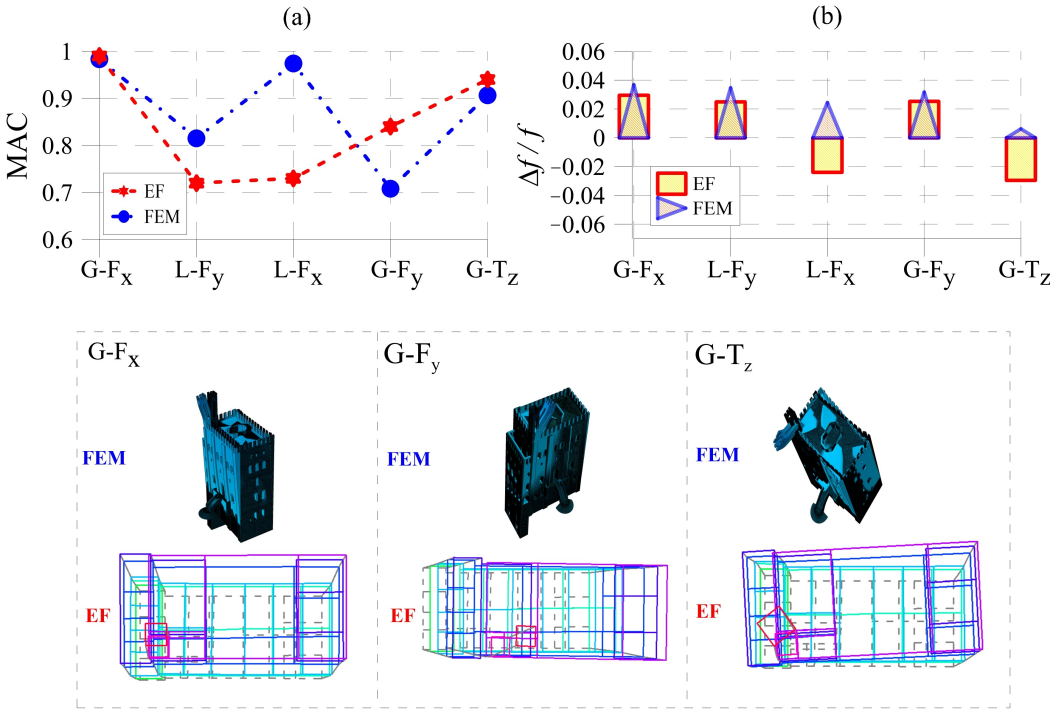


**Figure 7.** Comparison between FEM and EF calibration. (**a**) MAC values and (**b**) relative frequency difference $\Delta f / f$ .

*4.2. EF Model Continuous Updating: Model-Driven Online Damage Assessment*

In the following section, the EF structural model of the palace developed in Section 4.1 is combined, according to the proposal of Section 2.1, with the continuous flux of modal information identified from the dynamic monitoring system. The model is updated continuously based on daily-averaged identified natural frequencies and mode shapes, becoming a dynamically calibrated DT of the real structure. To give an exemplifying overview of the strengths and limitations of this strategy and, in particular, of its usefulness in the postseismic emergency, the updating procedure is carried out over a month of data, which includes the seismic sequence of 15 May 2021 (Section 3.2).

Thanks to its computational efficiency (see Table 3), the EF model of the structure is directly updated employing the well-known sensitivity method [53]. Out of the various techniques for updating structural models of engineering structures based on ambient vibration data [90] and for their optimization under different types of uncertainties [91], this approach has been one of the most successful and appears to be ideally suited for the framework of continuous model updating (in which, as discussed in Section 2.3, small perturbations are applied to the sensible parameters of the computational model which has been previously calibrated).

The optimization problem follows a weighted and regularized Levenberg–Marquardt scheme [92]

$$\left[\mathbf{J}^T\mathbf{W}\mathbf{J} + \lambda\ \mathrm{diag}(\mathbf{J}^T\mathbf{W}\mathbf{J})\right]\delta = \mathbf{J}^T\mathbf{W}(\mathbf{y} - \hat{\mathbf{y}}(\mathbf{p})), \quad \mathbf{J} = \left[\frac{\partial\hat{\mathbf{y}}(\mathbf{p})}{\partial\mathbf{p}}\right] \tag{1}$$

where $\mathbf{y}$ and $\hat{\mathbf{y}}$ are the target and model outputs, $\mathbf{p}$ are the model parameters being updated, $\mathbf{J}$ is the Jacobian matrix representing the local sensitivity of the model output $\hat{\mathbf{y}}$ to variations in the parameters $\mathbf{p}$, $\mathbf{W}$ is a weighting matrix, and $\lambda$ is the Levenberg–Marquardt damping parameter—steering the update between the Gauss–Newton (small $\lambda$) and the gradient descent (large $\lambda$) methods. Solving Equation (1) for $\delta$ gives, at each iteration, the perturbation that minimizes the sum of the (weighted) squared errors, i.e., the function $\chi^2$

$$\chi^2(\mathbf{p} + \delta) = \sum[\mathbf{y} - \hat{\mathbf{y}}(\mathbf{p} + \delta)]^2 \tag{2}$$

In accordance with the satisfying results previously obtained in the dynamic calibration of the EF model of the palace [88,93], only a few parameters are chosen for the continuous updating, in particular, those governing the stiffness of the palace and of the bell tower along each of the two main structural directions x and y. It is assumed that structural masses are quantified up to a satisfactory level of accuracy, whereas the elastic properties of the building material remain affected by a higher degree of uncertainty—no experimental test is available to characterize precisely the mechanical properties of masonry panels. Thus, the four sensible parameters undergoing the update are the Young moduli of the masonry of the palace walls directed along x and y, $E_{p,x}$ and $E_{p,y}$ respectively, the same for the bell tower walls governed by the moduli $E_{t,x}$ and $E_{t,y}$. These are the parameters to which the model's natural frequencies exhibit the most relevant sensitivity. The updating is carried out by normalizing all the moduli with respect to a reference value equal to $p_{ref}$ equal to 4752 MPa, which is representative of a good-quality stone masonry.

Keeping the two directions independent from each other has a twofold objective, aimed at achieving a successful updating phase and a reliable damage localization. First, as discussed in [88], this expedient overcomes some limitations in the modeling of the out-of-plane stiffness of masonry elements in the assumed EF formulation, whose effect is significant due to the large thickness of the palace masonry walls. Second, from the point of view of structural analysis and seismic damage assessment, the choice of analyzing independently the two main directions is a common choice for masonry buildings—in which directional earthquake-resistant systems are easily identified from the architectonic configuration—allowing a more accurate interpretation of the response to earthquake actions and damage proneness of each resisting subsystem. Other uncertain parameters,

such as masonry mass density and the in-plane shear stiffness of vaults, are fixed according to the results obtained in previous calibrations (see [88]).

The Levenberg–Marquardt updating algorithm has been implemented in MATLAB (Mathworks, Inc., Natick, MA, USA, version R2023a) code, whereas TREMURI is handling the solution of the eigenvalue problems, for both the computation of the Jacobian sensitivity matrix **J** by means of finite differences and the updating step. The target output **y** is composed of the frequency of vibration of the first five modes and their mode shapes in all the locations sensed by the dynamic monitoring system (Section 3.2), excluding the out-of-plane measurements A11 and A12 (due to the absence of the corresponding degree-of-freedoms in the EF model; see Section 4.1). The weighting matrix **W** is assigning (i) a double relative weight to global modes with respect to local modes (given the absence of a dedicated SHM sensor at the top of the bell tower, Section 3.1) and (ii) the same relative weight to frequencies and mode shapes. The damping parameter $\lambda$ is initialized to a value of $1 \times 10^{-3}$ and updated according to [92]. Convergence is achieved if, at the end of a subiteration, the relative change in gradient or parameters **p** is less than one part per cent or the relative change in the error function $\chi^2$ is less than one part per thousand.

The results of the updating procedure are graphically summarized in Figure 8. The metrics used to evaluate the quality of the fit (the same employed first in Section 3.2 to assess damage from experimental measurements and later in Section 4.1 to compare the calibrated EF and FE models) are those typical of ambient vibration-based model updating procedures, i.e., (i) a global frequency-based metric aimed at parameter calibration, which is based on the relative difference in modal frequencies $\Delta f/f$ and (ii) a spatial-based metric expressed through the MAC index, which ensures the one-to-one correspondence between experimental and numerical modes. The most interesting steps, in particular, the starting recalibration based on AVT, the first-day calibration on SHM data, and the updates across the day of the 15 May 2021 earthquake event, are reported in Tables 4 and 5 in terms of updated parameters (multiplicative coefficients $cE_{p,x}$, $cE_{p,y}$, $cE_{t,x}$, $cE_{t,y}$) and model output, respectively.

The starting recalibration based on AVT including the bell tower sensors (Section 3.1) is achieved in around four iterations and less than a minute of computation time (Table 4). The reasoning behind the overestimation of the Young modulus for the palace walls in the x direction with respect to those oriented in y (Table 5) can be traced back to the unmodeled out-of-plane stiffness, as pointed out in previous research from the authors [88].

Concerning SHM data, the model continuously reproduces the monitored behavior (Figure 8a), with relative frequency errors lower than 5% (Figure 8b) both before and after the day of the earthquake. The low-mode shapes correlation for local modes—MAC values around 0.7 for modes L-$F_y$ and L-$F_x$; Figure 8c—could be easily improved by increasing the mode shape weighting in the objective function, sacrificing some accordance in frequency. However, this choice is not suited for the purposes of this application, with mode shapes being typically less sensitive than frequencies to structural damage (as observed from experimental data; Section 3.2). It should be highlighted, moreover, that the local modes of the bell tower are governed by the atop modal amplification. The bell tower, even if explicitly modeled in the EF model, is not being directly monitored in the current setup of the SHM system (see Section 3.2).

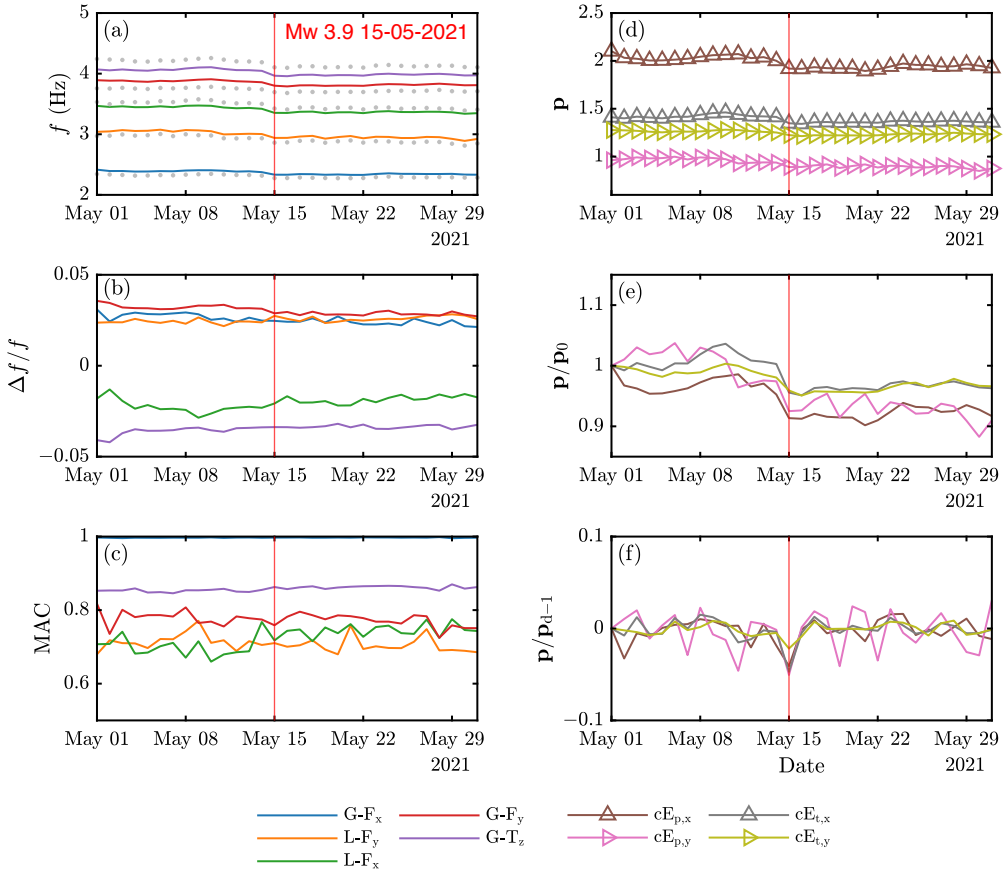


**Figure 8.** Results of the continuous updating of the EF model of the palace over the month of May 2021. (**a**) Model natural frequencies, (**b**) relative difference with respect to experimentally identified ones and (**c**) corresponding MAC, (**d**–**f**) values of the updated parameters **p** and their relative variations with respect to the first calibration $\mathbf{p}_0$ and previous-day calibration $\mathbf{p}_{d-1}$.

The behaviour over time of the updated parameters **p** (Figure 8d) as well as the preliminary comparison with the first-day calibration $\mathbf{p}_0$ highlight the permanent reduction of all the elastic moduli (Figure 8e). As shown by the comparison with the previous-day updating $\mathbf{p}_{d-1}$, such a reduction occurs on the day of the earthquake and with a different significance for each parameter (Figure 8f). Table 4 quantifies the relative change in the updated model parameters across the day of the earthquake, which are obtained with just two iteration and less than 20 s of computation, achieving a significant improvement of the error function $\chi^2$. The variations are clearly reductions—as expected from the lowering of the target frequencies due to structural damage; Section 3.2—and can be defined as mild in absolute terms, being always lower than 10%. In particular, the variations in the elastic moduli **p** are estimated with respect to the reference value $p_{ref}$, to eliminate the influence of unmodeled out-of-plane stiffness from the damage assessment. The reduction across the day of the earthquake is much more significant along the x direction rather than y, affecting primarily the palace walls. This scenario is in agreement with the results of in-situ inspections, at least for what can be deduced from the evolution of pre-existing cracks [67], and shows a good overall agreement with the numerical results obtained from the Bayesian updating of the FE modal surrogate [79] (surrogate which is derived from the same calibrated FE model of the palace previously presented in Section 4.1).

**Table 4.** Updating of the EF model in the initial calibration (01-05-21) and for the days across the earthquake of 15 May 2021 (14-05-21 and 15-05-21). Values of the initial and updated multiplicative coefficient of the Young moduli of the palace masonry along each direction $E_{p,x}$, $E_{p,y}$ and the bell tower $E_{t,x}$, $E_{t,y}$, value of the error function $\chi^2$, number of iterations and processing time.

| | **Initial p** | | | | | **Updated p** | | | | | | |
|---|---|---|---|---|---|---|---|---|---|---|---|---|
| **Date** | $\mathbf{cE_{p,x}}$ | $\mathbf{cE_{p,y}}$ | $\mathbf{cE_{t,x}}$ | $\mathbf{cE_{t,y}}$ | $\chi^2$ | $\mathbf{cE_{p,x}}$ | $\mathbf{cE_{p,y}}$ | $\mathbf{cE_{t,x}}$ | $\mathbf{cE_{t,y}}$ | $\chi^2$ | **Iter.** | **Time (s)** |
| May 2021 (AVT) | 1 | 1 | 1 | 1 | 1.032 | 1.990 | 0.999 | 1.469 | 1.213 | 0.074 | 4 | 35.9 |
| 01-05-21 (SHM) | 1.990 | 0.999 | 1.469 | 1.213 | 0.166 | 2.101 | 0.963 | 1.411 | 1.277 | 0.155 | 3 | 25.3 |
| 14-05-21 | 2.039 | 0.939 | 1.420 | 1.258 | 0.140 | 2.001 | 0.938 | 1.415 | 1.252 | 0.140 | 1 | 12.0 |
| 15-05-21 | 2.001 | 0.938 | 1.415 | 1.252 | 0.162 | 1.919 | 0.891 | 1.348 | 1.225 | 0.141 | 2 | 19.7 |
| | | | | | $\Delta\mathbf{p}/\mathbf{p}_{ref}$ | −0.082 | −0.047 | −0.067 | −0.027 | | | |

A deeper understanding is obtained by looking at the average updated value of the parameters for the whole observation periods before and after the earthquake (Table 6), which should provide a more robust quantification of long-term permanent reductions. The scenario is quite similar to the one previously described, even though, for the palace walls, the differences between the two directions are less evident. This result could be related to an overfitting issue, which can be easily identified by looking at the lowering of the average error function $\overline{\chi^2}$ in the post-earthquake updating, if compared with the pre-event results. In particular, the model reaches a better fit with the frequency of the global mode G-$F_y$, which could explain the significant decrease in the corresponding elastic moduli. Moreover, the fact that the identified frequency reductions following the 15 May earthquake are of the same order of magnitude as the average fitting error further complicates the analysis.

Nonetheless, for what concerns the bell tower, the updating procedure clearly suggests the x direction to be the most affected by seismic damage. This result seems to be in great accordance with the results of data-based damage localization, which highlighted the channel A2—at the rooftop level, in close proximity with the base of the bell tower and orientated along the x direction—as the location most affected by earthquake-induced damage (Section 3.2), confirming the reliability of the proposed model-driven assessment.

**Table 5.** Relative difference in frequency $\Delta f/f$ and values of the MAC coefficient between the EF model and experimental data, for the initial calibration (01-05-21) and for the updating across the earthquake day of 15 May 2021 (14-05-21 and 15-05-21).

| | **May 2021 (AVT)** | | | | **01-05-21 (SHM)** | | **14-05-21** | | **15-05-21** | |
|---|---|---|---|---|---|---|---|---|---|---|
| | **Initial p** | | **Updated p** | | **Updated p** | | **Updated p** | | **Updated p** | |
| **Mode** | $\Delta f/f$ | **MAC** | $\Delta f/f$ | **MAC** | $\Delta f/f$ | **MAC** | $\Delta f/f$ | **MAC** | $\Delta f/f$ | **MAC** |
| G-$F_x$ | −0.177 | 0.961 | 0.029 | 0.990 | 0.0309 | 0.997 | 0.0248 | 0.997 | 0.0247 | 0.997 |
| L-$F_y$ | −0.023 | 0.270 | 0.025 | 0.725 | 0.0237 | 0.680 | 0.0238 | 0.705 | 0.0274 | 0.710 |
| L-$F_x$ | −0.156 | 0.563 | −0.024 | 0.730 | −0.0181 | 0.707 | −0.0231 | 0.768 | −0.0208 | 0.717 |
| G-$F_y$ | −0.093 | 0.825 | 0.025 | 0.842 | 0.0357 | 0.817 | 0.0313 | 0.774 | 0.0288 | 0.759 |
| G-$T_z$ | −0.163 | 0.481 | −0.030 | 0.951 | −0.0409 | 0.853 | −0.0339 | 0.855 | −0.0338 | 0.863 |

**Table 6.** Average value of the updated parameters $\overline{\mathbf{p}}_{\text{pre}}$ and $\overline{\mathbf{p}}_{\text{post}}$ referring to the pre- and post-earthquake updating, their relative change $\Delta\overline{\mathbf{p}}/\mathbf{p}_{\text{ref}}$. On the right side, a detailed comparison between model and target outputs.

| | | | | | $\overline{\chi^2}_{\text{pre}} = 0.149$ | | $\overline{\chi^2}_{\text{post}} = 0.136$ | |
|---|---|---|---|---|---|---|---|---|
| | $\overline{\mathbf{p}}_{\text{pre}}$ | $\overline{\mathbf{p}}_{\text{post}}$ | $\Delta\overline{\mathbf{p}}/\mathbf{p}_{\text{ref}}$ | **Mode** | $\Delta\overline{f}/\overline{f}_{\text{pre}}$ | $\overline{\text{MAC}}_{\text{pre}}$ | $\Delta\overline{f}/\overline{f}_{\text{post}}$ | $\overline{\text{MAC}}_{\text{post}}$ |
| $cE_{p,x}$ | 2.036 | 1.935 | −0.101 | G-$F_x$ | 0.0273 | 0.997 | 0.0238 | 0.997 |
| $cE_{p,y}$ | 0.968 | 0.893 | −0.075 | L-$F_y$ | 0.0241 | 0.715 | 0.0260 | 0.704 |
| $cE_{t,x}$ | 1.423 | 1.361 | −0.062 | L-$F_x$ | −0.0225 | 0.700 | −0.0186 | 0.744 |
| $cE_{t,y}$ | 1.266 | 1.230 | −0.036 | G-$F_y$ | 0.0324 | 0.780 | 0.0285 | 0.771 |
| | | | | G-$T_z$ | −0.0360 | 0.853 | −0.0335 | 0.862 |

### *4.3. Offline Forecasting of the Postseismic Structural Behavior: An EF-Based Perspective*

The computational models of the palace developed in Section 4.1, continuously fed by modal information provided by the dynamic monitoring system (Section 3.2) and updated to match experimental dynamics (Section 4.2), can be effectively employed as structural digital twins of the monitored structure.

The application presented in the following paragraphs should be intended as an exemplification of the proposal of Section 2.3. The EF model of the palace, updated in quasi real time based on vibration data acquired by the monitoring system and already employed online to obtain a quick estimation of the damage gravity (Section 4.2), is now employed in an offline environment to investigate the residual capacity of the building after the earthquake of 15 May 2021 (Section 3.2)—for example, in response to potential aftershocks.

Indeed, the reduction in frequencies experimentally identified on the structure (Section 3.2) is captured by the model updating procedure with respect to variations in the elastic parameters only—in this case, the elastic Young moduli of the masonry for different areas of the palace. It is plausible to assume that, in case of structural damage to the masonry panels, the resistance should be affected as well. As a first assumption, the relative reductions in masonry strength caused by seismic damage can be assumed to be equal to those identified for the elastic moduli by the updating procedure. This statement is supported by recent results of the literature, which investigated, through numerical simulations, the relationship between elastic and resistance parameters in masonry walls and its alteration due to aging and degradation effects [94]. The study results suggest that the respective reductions follow a linear trend with a regression coefficient very close to unity, thus validating the initial assumption.

Table 7 reports, on the left-hand side, the initial values of the parameters governing the strength of masonry panels. In particular, the maximum resistance corresponds to the minimum strength among the considered failure criteria—in this case, diagonal cracking for the shear failure according to the Turnšek and Čačovič criterion, rocking and crushing for the flexural one—and depends on the actual level of axial compression. The updating involves the peak compressive strength $fm$, the peak tensile strength $ft$, and the peak shear strength at zero confining stress $fv0$ (which is governing the equivalent tensile strength of spandrels [95]). As a dual approach to the update of the elastic Young moduli (Section 4.2), the strength parameters of the masonry are individually updated for each of the four areas of the palace previously considered. This implicitly assumes that areas with higher reductions of the elastic moduli, as identified from the optimization, are those more affected by structural damage with respect to not only their stiffness but also their strength. The updated parameters (subscript u) for each area—masonry walls of the palace body in the x and y directions, masonry walls of the bell tower in the x and y directions—are reported on the right-hand side of Table 7.

**Table 7.** Updated values (subscript u) of the masonry resistances, computed according to the results of the online updating (Section 4.2).

| Area | Direction | $fm$ (MPa) | $ft$ (MPa) | $fv0$ (MPa) | 1 + Δp/p | $fm_u$ (MPa) | $ft_u$ (MPa) | $fv0_u$ (MPa) |
|---|---|---|---|---|---|---|---|---|
| Palace | x | 4.0170 | 0.1393 | 0.2320 | 0.9180 | 3.6876 | 0.1279 | 0.2130 |
| Palace | y | | | | 0.9526 | 3.8266 | 0.1327 | 0.2210 |
| Bell tower | x | | | | 0.9335 | 3.7497 | 0.1301 | 0.2166 |
| Bell tower | y | | | | 0.9727 | 3.9074 | 0.1355 | 0.2257 |

By adopting a phenomenological constitutive model that describes the nonlinear response of masonry panels to monotonic and cyclic actions, implemented in the TREMURI research solver with the piecewise linear formulation proposed in [96], the EF model can simulate the nonlinear response of masonry panels until severe damage levels. This provides, in a time frame ranging from a few minutes for NLSA to a few hours for nonlinear dynamic analyses (NLDA) (in the last case, strongly depending on the global damage reached by the structure), a reliable forecast of the future global response of the building to potential aftershocks. In this application, NLSA is selected as the most suited approach to obtain a quick initial estimate of the residual capacity of the building after the earthquake of 15 May. For this purpose, a load pattern of horizontal forces proportional to floor masses is applied on the equivalent frame in the pre-earthquake—i.e., the calibrated model on the 14 May, representative of the reference undamaged state—and post-earthquake conditions—i.e., the calibrated model on the 15th of May, in which the reduced stiffnesses and resistances resulting from the updating procedure reproduce the damaged state caused by the earthquake.

Figure 9 shows a comparison between the pushover curves before and after the earthquake. The curves in the undamaged state exhibit (i) a ductile behavior in the x direction, i.e., along the shorter side, with a gradual drop of resistance starting at around 0.05 m of top displacement and a high displacement capacity, and (ii) a fragile behavior in the y direction, i.e., along the longer side, which is determined, despite the higher maximum resistance (a resistant shear around 50% higher than that of x), by the sudden and huge loss of resistant shear for top displacements of around 0.25 m, rapidly leading to higher damage states. The simulations carried out on the damaged model show a clear picture with respect to the loss of global stiffness. The stiffness reduction reproduces quite accurately the effects of the updating coefficients applied to the palace masonry moduli, with a reduction in the slope of the elastic part of the shear displacement curve equal to 7.1% and 5.0% in x and y direction, respectively. For what concerns resistance, along the y direction, i.e., the long side, only a negligible fraction of the maximum base reacting force, around 1.2%, is lost. On the other hand, the response of the building along the x direction appears to be more significantly affected, with a reduction of the maximum resistance of around 5.4% for forces applied in the positive verse.

Measurements of the palace's dynamic response to the earthquake are not available due to a power outage, which affected the monitoring system (Section 3.2). In this respect, the dynamic response to the earthquake simulated by NLDA on the calibrated EF model cannot be directly compared with experimental measurements. Nonetheless, this application can be extremely valuable to enhance the knowledge regarding damage diffusion and gravity acquired from data processing (Section 3.1) and model updating (Section 4.2). The calibrated EF model in the undamaged state (on 14 May) is thus subjected to the ground acceleration components measured by the close "Gubbio Parcheggio Santa Lucia" (GBSL) seismic station (see Section 3.2). In particular, given the proximity of the station, no attenuation law is applied to the signal. The horizontal components are suitably rotated in order to match the main directions of the palace, x and y, which form an angle with the north and east directions of around −30°(see Figure 2).

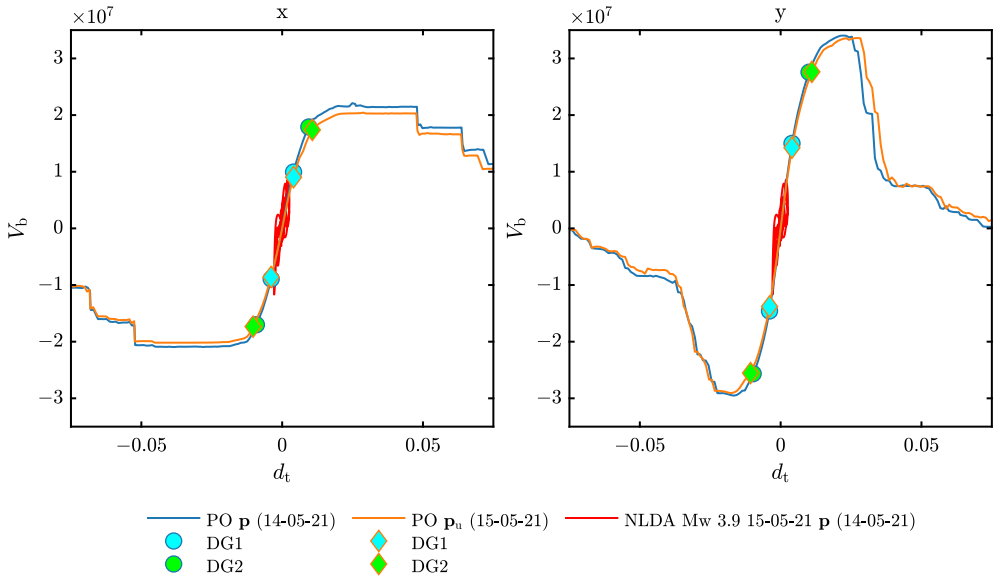


**Figure 9.** Comparison between pushover curves obtained from the continuously updated EF model in the pre-earthquake (14-05-21) and post-earthquake (15-05-21) conditions.

Figure 9 reports, in the base shear displacement plane, the response simulated through NLDA for the 15 May 2021 earthquake compared with that of NLSA. A first comparison with conventional damage thresholds on the pushover curve, respectively assumed for DG1 and DG2 as the attainment of 40% and 80% of the maximum strength in the increasing branch, suggests that the structure reached a global damage grade at least equal to DG1 for the x direction—defined as "negligible to slight damage (no structural damage, slight non-structural damage)" according to the EMS-98 scale. A more in-depth examination of the damage level (DL) reached by masonry walls, which is carried out according to the procedure proposed in [97], highlights how (i), globally, walls directed in the x direction exhibit more diffused damage than those in y but with low severity (Table 8) and (ii), regardless of the direction, a possible concentration of damage can be identified in the upper parts of the palace, at the Nobili level and in the bell tower (Figure 10). Both these results agree with the experimental evidence obtained from the processing of monitoring data and the in-situ inspections which pointed out x as the most affected direction and damage to be localized on the southern side of the palace, mainly in the upper floors (sensor A2; see Section 3.2). It can be concluded that, based on the DT-supported damage assessment, the palace has suffered negligible structural damages, mainly in the x direction, which does not undermine its seismic capacity. In this respect, the event did not increase significantly the building's vulnerability to the possible occurrence of aftershocks.

**Table 8.** Percentage of walls that reached a certain DL for each direction.

| | **Self Weight** | | **NLDA Mw 3.9 15-05-21** | |
|---|---|---|---|---|
| **Wall Damage Level** | **x (%)** | **y (%)** | **x (%)** | **y (%)** |
| DL1 | 15.04 | 2.69 | 27.98 | 4.48 |
| DL2 | 0 | 0.48 | 4.23 | 3.28 |
| DL3 | 0 | 0 | 2.06 | 0.48 |
| DL4 | 0 | 0 | 0 | 0 |

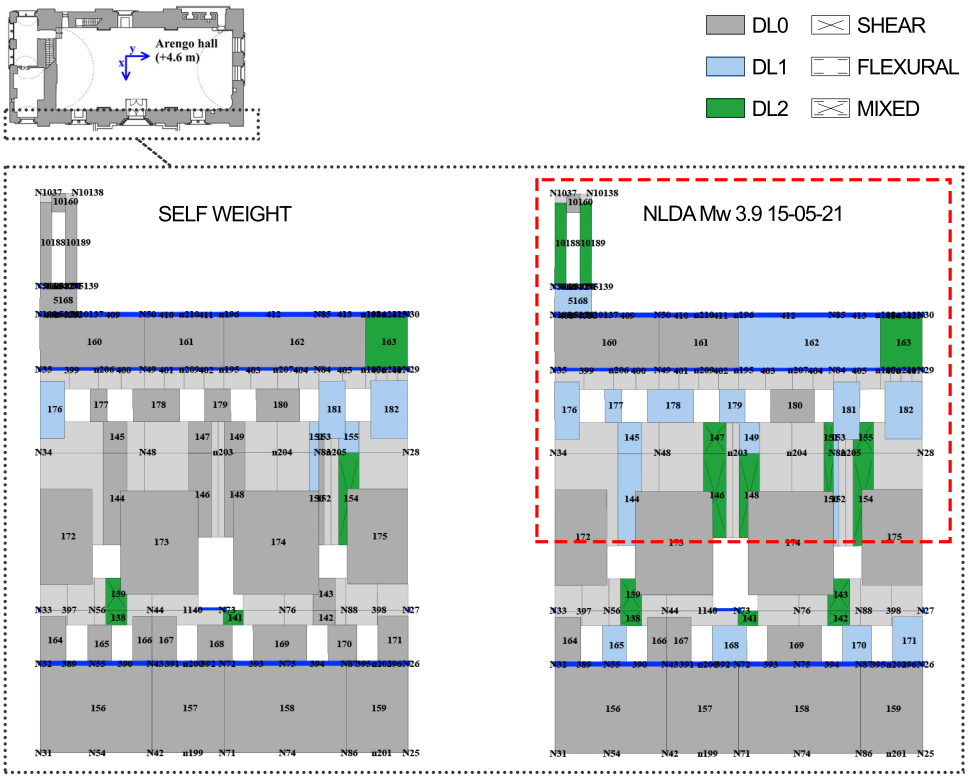


**Figure 10.** Results of NLDA on the EF model of the palace for the 15 May 2021 earthquake. The analysis is performed on the physics-enhanced DT, which is calibrated based on the previous-day modal identification (14-05-21). The model exhibits overall mild damage, which appears more diffused for the x direction (see Table 8). Nonetheless, some damage also occurs in the y direction, as shown in the figure for the facade, which suggests some damage concentration on the Nobili floor and in the bell tower.

## 5. Conclusions

The paper has proposed an innovative model-driven methodology, aimed at developing and continuously updating a physics-enhanced digital twin (DT) for the seismic health monitoring of historical masonry palaces. To illustrate the effectiveness of the proposed methodology, the Consoli Palace of Gubbio (Italy) is used as a compelling case study, a building continuously monitored by the authors since 2017.

A pivotal facet of the proposed methodology resides in the use of a computationally efficient physics-based representation of the monitored structure, the equivalent frame (EF) approach. Thanks to its computational lightness, the EF model of the palace is continuously calibrated based on modal properties identified from monitoring data, ensuring a heightened level of accuracy in capturing the structural behavior of the palace in operational and extreme conditions.

The study demonstrates the physics-based DT's prowess in unravelling the intrinsic physical phenomena and mechanisms governing the system behavior, enabling expeditious real-time localization and quantification of structural damage. By harnessing the dataset derived from a month of daily-identified modal properties in May 2021, the model's iterative enhancement process effectively showcased its prowess in discerning and localizing possible structural damages. The online updating procedure is able to closely reproduce the permanent decrease in natural frequencies identified after a minor seismic event on May 15th, quantifying the corresponding relative reductions in material stiffness from 3% to 8% of the pre-earthquake value for different parts of the building—with maximum reductions along the direction parallel to the short side of the building.

This capability is crucial for assessing the structural integrity of the palace after seismic events, allowing for quick responses in the post-earthquake decision making phase and providing valuable insights for long-term risk assessment and management. Moreover, through offline static and dynamic simulations of the nonlinear response performed after the earthquake, the physics-based DT is able to forecast in a short time frame the potential reduction in strength and capacity caused by seismic damage. Examining the preliminary online evaluations and the accurate offline analyses, it is possible to conclude that the investigated seismic event has not undermined the capacity of the building to resist future seismic actions.

The methodology developed in the paper constitutes a precious tool to support the seismic monitoring and risk assessment of historical masonry palaces, allowing for more effective risk management and preservation efforts and ultimately contributing to the sustainability of cultural heritage structures. The future sheds promising developments of the proposed approach, where the inherent reliance on physics-based principles allows for the application of prior knowledge. This feature enables the seamless adaptation of the model to diverse scenarios, system configurations and operating conditions, thereby enhancing its applicability and versatility.

**Author Contributions:** Conceptualization, D.S.; methodology, D.S. and S.C.; software, S.C.; formal analysis, D.S.; investigation, L.I.; writing—original draft preparation, D.S. and L.I.; writing—review and editing, S.C., F.U., and I.V.; visualization, D.S. and L.I.; supervision, S.C.; funding acquisition, S.C. and F.U. All authors have read and agreed to the published version of the manuscript.

**Funding:** This research was funded by the Italian Ministry of Education, University, and Research (MIUR) within the PRIN project DETECT-AGING "Degradation Effects on Structural Safety of Cultural Heritage constructions through simulation and health monitorING" (Call 2017—Protocol No. 201747Y73L).

**Data Availability Statement:** Not applicable.

**Acknowledgments:** The authors thankfully acknowledge the support of the PRIN project DETECT-AGING "Degradation Effects on Structural Safety of Cultural Heritage constructions through simulation and health monitorING" (Call 2017—Protocol No. 201747Y73L). The authors acknowledge aswell Sara Alfano for contributing to the development and preliminary calibration of the equivalent frame model of the palace.

**Conflicts of Interest:** The authors declare no conflict of interest.

## Abbreviations

The following abbreviations are used in this manuscript:

| | |
|---|---|
| EF | equivalent frame |
| FE | finite element |
| DT | digital twin |
| CCLM | continuous constitutive law models |
| SEM | structural element models |
| SHM | structural health monitoring |
| S2HM | seismic structural health monitoring |
| SSI | stochastic subspace identification |
| MLR | multiple linear regression |
| PGA | peak ground acceleration |
| MAC | modal assurance criterion |
| COMAC | coordinate modal assurance criterion |
| DOF | degree of freedom |
| MA | modal analysis |
| NLSA | nonlinear static analysis |
| NLDA | nonlinear dynamic analysis |
| DG | damage grade (global scale) |
| DL | damage level (element scale) |

## References


1. Avci, O.; Abdeljaber, O.; Kiranyaz, S.; Hussein, M.; Gabbouj, M.; Inman, D.J. A review of vibration-based damage detection in civil structures: From traditional methods to Machine Learning and Deep Learning applications. *Mech. Syst. Signal Process.* **2021**, *147*, 107077. [CrossRef]
2. Quqa, S.; Landi, L.; Diotallevi, P.P. Seismic structural health monitoring using the modal assurance distribution. *Earthq. Eng. Struct. Dyn.* **2021**, *50*, 2379–2397. [CrossRef]
3. Malekloo, A.; Ozer, E.; AlHamaydeh, M.; Girolami, M. Machine learning and structural health monitoring overview with emerging technology and high-dimensional data source highlights. *Struct. Health Monit.* **2022**, *21*, 1906–1955. [CrossRef]
4. Boje, C.; Guerriero, A.; Kubicki, S.; Rezgui, Y. Towards a semantic Construction Digital Twin: Directions for future research. *Autom. Constr.* **2020**, *114*, 103179. [CrossRef]
5. Jiang, F.; Ma, L.; Broyd, T.; Chen, K. Digital twin and its implementations in the civil engineering sector. *Autom. Constr.* **2021**, *130*, 103838. [CrossRef]
6. Callcut, M.; Cerceau Agliozzo, J.P.; Varga, L.; McMillan, L. Digital twins in civil infrastructure systems. *Sustainability* **2021**, *13*, 11549. [CrossRef]
7. Alanne, K.; Sierla, S. An overview of machine learning applications for smart buildings. *Sustain. Cities Soc.* **2022**, *76*, 103445. [CrossRef]
8. Bado, M.F.; Tonelli, D.; Poli, F.; Zonta, D.; Casas, J.R. Digital Twin for Civil Engineering Systems: An Exploratory Review for Distributed Sensing Updating. *Sensors* **2022**, *22*, 3168. [CrossRef]
9. Jouan, P.; Hallot, P. Digital twin: Research framework to support preventive conservation policies. *ISPRS Int. J. Geo-Inf.* **2020**, *9*, 228. [CrossRef]
10. Marra, A.; Trizio, I.; Fabbrocino, G. Digital Tools for the Knowledge and Safeguard of Historical Heritage. *Lect. Notes Civ. Eng.* **2021**, *156*, 645–662. [CrossRef]
11. Rainieri, C.; Rosati, I.; Cieri, L.; Fabbrocino, G. Development of the Digital Twin of a Historical Structure for SHM Purposes. *Lect. Notes Civ. Eng.* **2023**, *254*, 639–646. [CrossRef]
12. Wright, L.; Davidson, S. How to tell the difference between a model and a digital twin. *Adv. Model. Simul. Eng. Sci.* **2020**, *7*, 13. [CrossRef]
13. Degli Abbati, S.; Sivori, D.; Cattari, S.; Lagomarsino, S. Ambient vibrations-supported seismic assessment of the Saint Lawrence Cathedral's bell tower in Genoa, Italy. *J. Civ. Struct. Health Monit.* **2023**, 1–22. . [CrossRef]
14. Angjeliu, G.; Coronelli, D.; Cardani, G. Development of the simulation model for Digital Twin applications in historical masonry buildings: The integration between numerical and experimental reality. *Comput. Struct.* **2020**, *238*, 106282. [CrossRef]
15. Funari, M.F.; Hajjat, A.E.; Masciotta, M.G.; Oliveira, D.V.; Lourenço, P.B. A parametric scan-to-FEM framework for the digital twin generation of historic masonry structures. *Sustainability* **2021**, *13*, 11088. [CrossRef]
16. Limongelli, M.P.; Çelebi, M. *Seismic Structural Health Monitoring: From Theory to Successful Applications*; Springer: Cham, Switzerland, 2019. [CrossRef]
17. Gattulli, V.; Franchi, F.; Graziosi, F.; Marotta, A.; Rinaldi, C.; Potenza, F.; Sabatino, U.D. Design and evaluation of 5G-based architecture supporting data-driven digital twins updating and matching in seismic monitoring. *Bull. Earthq. Eng.* **2022**, *20*, 4345–4365. [CrossRef]
18. Roca, P.; Cervera, M.; Gariup, G.; Pela', L. Structural analysis of masonry historical constructions. Classical and advanced approaches. *Arch. Comput. Methods Eng.* **2010**, *17*, 299–325. [CrossRef]
19. D'Altri, A.M.; Sarhosis, V.; Milani, G.; Rots, J.; Cattari, S.; Lagomarsino, S.; Sacco, E.; Tralli, A.; Castellazzi, G.; de Miranda, S. Modeling Strategies for the Computational Analysis of Unreinforced Masonry Structures: Review and Classification. *Arch. Comput. Methods Eng.* **2020**, *27*, 1153–1185. [CrossRef]
20. Lagomarsino, S.; Cattari, S. PERPETUATE guidelines for seismic performance-based assessment of cultural heritage masonry structures. *Bull. Earthq. Eng.* **2015**, *13*, 13–47. [CrossRef]
21. Cattari, S.; Calderoni, B.; Caliò, I.; Camata, G.; de Miranda, S.; Magenes, G.; Milani, G.; Saetta, A. Nonlinear modeling of the seismic response of masonry structures: Critical review and open issues towards engineering practice. *Bull. Earthq. Eng.* **2022**, *20*, 1939–1997. [CrossRef]
22. Valente, M.; Milani, G. Non-linear dynamic and static analyses on eight historical masonry towers in the North-East of Italy. *Eng. Struct.* **2016**, *114*, 241–270. [CrossRef]
23. Betti, M.; Vignoli, A. Modelling and analysis of a Romanesque church under earthquake loading: Assessment of seismic resistance. *Eng. Struct.* **2008**, *30*, 352–367. [CrossRef]
24. Roca, P.; Cervera, M.; Pelà, L.; Clemente, R.; Chiumenti, M. Continuum FE models for the analysis of Mallorca Cathedral. *Eng. Struct.* **2013**, *46*, 653–670. [CrossRef]
25. Vila-Chã, E.; Barontini, A.; Lourenço, P.B. Implementation of a Condition Monitoring Strategy for the Monastery of Salzedas, Portugal: Challenges and Optimisation. *Buildings* **2023**, *13*, 719. [CrossRef]
26. Tiberti, S.; Acito, M.; Milani, G. Comprehensive FE numerical insight into Finale Emilia Castle behavior under 2012 Emilia Romagna seismic sequence: Damage causes and seismic vulnerability mitigation hypothesis. *Eng. Struct.* **2016**, *117*, 397–421. [CrossRef]

27. Degli Abbati, S.; D'Altri, A.M.; Ottonelli, D.; Castellazzi, G.; Cattari, S.; de Miranda, S.; Lagomarsino, S. Seismic assessment of interacting structural units in complex historic masonry constructions by nonlinear static analyses. *Comput. Struct.* **2019**, *213*, 51–71. [CrossRef]
28. Betti, M.; Galano, L. Seismic analysis of historic masonry buildings: The Vicarious Palace in Pescia (Italy). *Buildings* **2012**, *2*, 63–82. [CrossRef]
29. Clementi, F.; Pierdicca, A.; Formisano, A.; Catinari, F.; Lenci, S. Numerical model upgrading of a historical masonry building damaged during the 2016 Italian earthquakes: The case study of the Podestà palace in Montelupone (Italy). *J. Civ. Struct. Health Monit.* **2017**, *7*, 703–717. [CrossRef]
30. Valente, M. Seismic behavior and damage assessment of two historical fortified masonry palaces with corner towers. *Eng. Fail. Anal.* **2022**, *134*, 106003. [CrossRef]
31. Rolin, R.; Antaluca, E.; Batoz, J.L.; Lamarque, F.; Lejeune, M. From point cloud data to structural analysis through a geometrical hBIM-oriented model. *J. Comput. Cult. Herit.* **2019**, *12*, 1–26. [CrossRef]
32. Castellazzi, G.; Lo Presti, N.; D'Altri, A.M.; de Miranda, S. Cloud2FEM: A finite element mesh generator based on point clouds of existing/historical structures. *SoftwareX* **2022**, *18*, 101099. [CrossRef]
33. Lagomarsino, S.; Penna, A.; Galasco, A.; Cattari, S. TREMURI program: An equivalent frame model for the nonlinear seismic analysis of masonry buildings. *Eng. Struct.* **2013**, *56*, 1787–1799. [CrossRef]
34. Parisi, F.; Augenti, N. Seismic capacity of irregular unreinforced masonry walls with openings. *Earthq. Eng. Struct. Dyn.* **2013**, *42*, 101–121. [CrossRef]
35. Camata, G.; Marano, C.; Sepe, V.; Spacone, E.; Siano, R.; Petracca, M.; Roca, P.; Pelà, L. Validation of non-linear equivalent-frame models for irregular masonry walls. *Eng. Struct.* **2022**, *253*, 113755. [CrossRef]
36. Cattari, S.; D'Altri, A.M.; Camilletti, D.; Lagomarsino, S. Equivalent frame idealization of walls with irregular openings in masonry buildings. *Eng. Struct.* **2022**, *256*, 114055. [CrossRef]
37. Giongo, I.; Dizhur, D.; Tomasi, R.; Ingham, J.M. Field testing of flexible timber diaphragms in an existing vintage URM building. *J. Struct. Eng.* **2015**, *141*, D4014009. [CrossRef]
38. Sivori, D.; Lepidi, M.; Cattari, S. Structural identification of the dynamic behavior of floor diaphragms in existing buildings. *Smart Struct. Syst.* **2021**, *27*, 173–191. [CrossRef]
39. Cattari, S.; Resemini, S.; Lagomarsino, S. Modelling of vaults as equivalent diaphragms in 3D seismic analysis of masonry buildings. In Proceedings of the Structural Analysis of Historic Construction: Preserving Safety and Significance—Proceedings of the 6th International Conference on Structural Analysis of Historic Construction, SAHC08, Bath, UK, 2–4 July 2008; Volume 1, pp. 517–524.
40. Bianchini, N.; Mendes, N.; Calderini, C.; Candeias, P.; Rossi, M.; Lourenço, P. Seismic response of a small-scale masonry groin vault: Experimental investigation by performing quasi-static and shake table tests. *Bull. Earthq. Eng.* **2022**, *20*, 1739–1765. [CrossRef]
41. Lagomarsino, S.; Cattari, S.; Degli Abbati, S.; Ferrero, C. Valutazione della sicurezza statica e sismica del politeama "Giuseppe Verdi" a Carrara. In Proceedings of the IF CRASC 12, Pisa, Italy, 15–17 November 2012. (In Italian)
42. Rossi, M.; Cattari, S.; Lagomarsino, S. Performance-based assessment of the Great Mosque of Algiers. *Bull. Earthq. Eng.* **2015**, *13*, 369–388. [CrossRef]
43. Cattari, S.; Alfano, S.; Lagomarsino, S. A Practice-Oriented Proposal to Consider the Flange Effect in Equivalent Frame Modeling of Masonry Buildings. *Buildings* **2023**, *13*, 462. [CrossRef]
44. Cattari, S.; Degli Abbati, S.; Alfano, S.; Brunelli, A.; Lorenzoni, F.; da Porto, F. Dynamic calibration and seismic validation of numerical models of URM buildings through permanent monitoring data. *Earthq. Eng. Struct. Dyn.* **2021**, *50*, 2690–2711. [CrossRef]
45. Brunelli, A.; de Silva, F.; Piro, A.; Parisi, F.; Sica, S.; Silvestri, F.; Cattari, S. Numerical simulation of the seismic response and soil–structure interaction for a monitored masonry school building damaged by the 2016 Central Italy earthquake. *Bull. Earthq. Eng.* **2021**, *19*, 1181–1211. [CrossRef]
46. Degli Abbati, S.; Morandi, P.; Cattari, S.; Spacone, E. On the reliability of the equivalent frame models: The case study of the permanently monitored Pizzoli's town hall. *Bull. Earthq. Eng.* **2022**, *20*, 2187–2217. [CrossRef]
47. Mallardo, V.; Malvezzi, R.; Milani, E.; Milani, G. Seismic vulnerability of historical masonry buildings: A case study in Ferrara. *Eng. Struct.* **2008**, *30*, 2223–2241. [CrossRef]
48. Clementi, F.; Gazzani, V.; Poiani, M.; Lenci, S. Assessment of seismic behaviour of heritage masonry buildings using numerical modelling. *J. Build. Eng.* **2016**, *8*, 29–47. [CrossRef]
49. Malcata, M.; Ponte, M.; Tiberti, S.; Bento, R.; Milani, G. Failure analysis of a Portuguese cultural heritage masterpiece: Bonet building in Sintra. *Eng. Fail. Anal.* **2020**, *115*, 104636. [CrossRef]
50. Ponte, M.; Bento, R.; Vaz, S.D. A Multi-Disciplinary Approach to the Seismic Assessment of the National Palace of Sintra. *Int. J. Archit. Herit.* **2021**, *15*, 757–778. [CrossRef]
51. Lagomarsino, S.; Degli Abbati, S.; Ottonelli, D.; Cattari, S. Integration of modelling approaches for the seismic assessment of complex urm buildings: The podestà palace in Mantua, Italy. *Buildings* **2021**, *11*, 269. [CrossRef]
52. Jaishi, B.; Ren, W.X. Structural finite element model updating using ambient vibration test results. *J. Struct. Eng.* **2005**, *131*, 617–628. [CrossRef]

53. Mottershead, J.E.; Link, M.; Friswell, M.I. The sensitivity method in finite element model updating: A tutorial. *Mech. Syst. Signal Process.* **2011**, *25*, 2275–2296. [CrossRef]
54. Simoen, E.; De Roeck, G.; Lombaert, G. Dealing with uncertainty in model updating for damage assessment: A review. *Mech. Syst. Signal Process.* **2015**, *56*, 123–149. [CrossRef]
55. Marwala, T. *Finite-Element-Model Updating Using Computional Intelligence Techniques: Applications to Structural Dynamics*; Springer: London, UK, 2010; pp. 1–250. [CrossRef]
56. Bassoli, E.; Vincenzi, L.; D'Altri, A.M.; de Miranda, S.; Forghieri, M.; Castellazzi, G. Ambient vibration-based finite element model updating of an earthquake-damaged masonry tower. *Struct. Control. Health Monit.* **2018**, *25*, e2150. [CrossRef]
57. Bartoli, G.; Betti, M.; Marra, A.M.; Monchetti, S. A Bayesian model updating framework for robust seismic fragility analysis of non-isolated historic masonry towers. *Philos. Trans. R. Soc. A Math. Phys. Eng. Sci.* **2019**, *377*, 20190024. [CrossRef] [PubMed]
58. Pallarés, F.J.; Betti, M.; Bartoli, G.; Pallarés, L. Structural health monitoring (SHM) and Nondestructive testing (NDT) of slender masonry structures: A practical review. *Constr. Build. Mater.* **2021**, *297*, 123768. [CrossRef]
59. Ponsi, F.; Bassoli, E.; Vincenzi, L. Bayesian and deterministic surrogate-assisted approaches for model updating of historical masonry towers. *J. Civ. Struct. Health Monit.* **2022**, *12*, 1469–1492. [CrossRef]
60. Shabani, A.; Feyzabadi, M.; Kioumarsi, M. Model updating of a masonry tower based on operational modal analysis: The role of soil-structure interaction. *Case Stud. Constr. Mater.* **2022**, *16*, e00957. [CrossRef]
61. Cabboi, A.; Gentile, C.; Saisi, A. From continuous vibration monitoring to FEM-based damage assessment: Application on a stone-masonry tower. *Constr. Build. Mater.* **2017**, *156*, 252–265. [CrossRef]
62. Cavalagli, N.; Comanducci, G.; Ubertini, F. Earthquake-Induced Damage Detection in a Monumental Masonry Bell-Tower Using Long-Term Dynamic Monitoring Data. *J. Earthq. Eng.* **2018**, *22*, 96–119. [CrossRef]
63. Kita, A.; Cavalagli, N.; Venanzi, I.; Ubertini, F. On the use of digital twins for seismic structural health monitoring of a monumental masonry tower. In Proceedings of the 8th International Conference on Computational Methods in Structural Dynamics and Earthquake Engineering—COMPDYN 2021, Athens, Greece, 28–30 June 2021; pp. 346–353.
64. Kita, A.; Cavalagli, N.; Venanzi, I.; Ubertini, F. A new method for earthquake-induced damage identification in historic masonry towers combining OMA and IDA. *Bull. Earthq. Eng.* **2021**, *19*, 5307–5337. [CrossRef]
65. Pepi, C.; Gioffre', M.; Grigoriu, M.D. Parameters identification of cable stayed footbridges using Bayesian inference. *Meccanica* **2019**, *54*, 1403–1419. [CrossRef]
66. García-Macías, E.; Ierimonti, L.; Venanzi, I.; Ubertini, F. An Innovative Methodology for Online Surrogate-Based Model Updating of Historic Buildings Using Monitoring Data. *Int. J. Archit. Herit.* **2021**, *15*, 92–112. [CrossRef]
67. Ierimonti, L.; Cavalagli, N.; Venanzi, I.; García-Macías, E.; Ubertini, F. A Bayesian-based inspection-monitoring data fusion approach for historical buildings and its post-earthquake application to a monumental masonry palace. *Bull. Earthq. Eng.* **2023**, *21*, 1139–1172. [CrossRef]
68. Penna, A.; Senaldi, I.E.; Galasco, A.; Magenes, G. Numerical Simulation of Shaking Table Tests on Full-Scale Stone Masonry Buildings. *Int. J. Archit. Herit.* **2016**, *10*, 146–163. [CrossRef]
69. Vanin, F.; Penna, A.; Beyer, K. Equivalent-Frame Modeling of Two Shaking Table Tests of Masonry Buildings Accounting for Their Out-Of-Plane Response. *Front. Built Environ.* **2020**, *6*. [CrossRef]
70. Tomić, I.; Vanin, F.; Božulić, I.; Beyer, K. Numerical simulation of unreinforced masonry buildings with timber diaphragms. *Buildings* **2021**, *11*, 205. [CrossRef]
71. Cattari, S.; Degli Abbati, S.; Ottonelli, D.; Marano, C.; Camata, G.; Spacone, E.; da Porto, F.; Modena, C.; Lorenzoni, F.; Magenes, G.; et al. Discussion on data recorded by the Italian structural seismic monitoring network on three masonry structures hit by the 2016-2017 Central Italy earthquake. In Proceedings of the 7th International Conference on Computational Methods in Structural Dynamics and Earthquake Engineering—COMPDYN 2019, Crete, Greece, 24–26 June 2019; pp. 1889–1906.
72. Martakis, P.; Reuland, Y.; Chatzi, E. Amplitude-dependent model updating of masonry buildings undergoing demolition. *Smart Struct. Syst.* **2021**, *27*, 157–172. [CrossRef]
73. Degli Abbati, S.; Cattari, S.; Lagomarsino, S. Validation of a practice-oriented floor spectra formulation through actual data from the 2016/2017 Central Italy earthquake. *Bull. Earthq. Eng.* **2022**, *20*, 7477–7511. . [CrossRef]
74. Sivori, D.; Cattari, S.; Lepidi, M. A methodological framework to relate the earthquake-induced frequency reduction to structural damage in masonry buildings. *Bull. Earthq. Eng.* **2022**, *20*, 4603–4638. [CrossRef]
75. MIT2018. Decreto Ministeriale del Ministero delle Infrastrutture e dei Trasporti del 17 Gennaio 2018. Aggiornamento delle «Norme Tecniche per le Costruzioni». Gazzetta Ufficiale Serie Generale n. 42 del 20/02/2018, Supplemento Ordinario n. 8. 2018. Available online: https://www.gazzettaufficiale.it/eli/gu/2018/02/20/42/so/8/sg/pdf (accessed on 10 March 2023). (In Italian)
76. Mirabella, F.; Ciaccio, M.; Barchi, M.; Merlini, S. The Gubbio normal fault (Central Italy): Geometry, displacement distribution and tectonic evolution. *J. Struct. Geol.* **2004**, *26*, 2233–2249. [CrossRef]
77. Chiaraluce, L.; Amato, A.; Carannante, S.; Castelli, V.; Cattaneo, M.; Cocco, M.; Collettini, C.; D'Alema, E.; Di Stefano, R.; Latorre, D.; et al. The alto Tiberina near fault observatory (northern Apennines, Italy). *Ann. Geophys.* **2014**, *57*. [CrossRef]
78. García-Macías, E.; Ubertini, F. MOVA/MOSS: Two integrated software solutions for comprehensive Structural Health Monitoring of structures. *Mech. Syst. Signal Process.* **2020**, *143*, 106830. . [CrossRef]

79. Ierimonti, L.; Venanzi, I.; García-Macías, E.; Ubertini, F. A transfer Bayesian learning methodology for structural health monitoring of monumental structures. *Eng. Struct.* **2021**, *247*, 113089. [CrossRef]
80. Gorini, A.; Nicoletti, M.; Marsan, P.; Bianconi, R.; De Nardis, R.; Filippi, L.; Marcucci, S.; Palma, F.; Zambonelli, E. The Italian strong motion network. *Bull. Earthq. Eng.* **2010**, *8*, 1075–1090. [CrossRef]
81. Pacor, F.; Paolucci, R.; Luzi, L.; Sabetta, F.; Spinelli, A.; Gorini, A.; Nicoletti, M.; Marcucci, S.; Filippi, L.; Dolce, M. Overview of the Italian strong motion database ITACA 1.0. *Bull. Earthq. Eng.* **2011**, *9*, 1723–1739. [CrossRef]
82. García-Macías, E.; Ubertini, F. Least Angle Regression for early-stage identification of earthquake-induced damage in a monumental masonry palace: Palazzo dei Consoli. *Eng. Struct.* **2022**, *259*, 114119. [CrossRef]
83. Allemang, R.J. The modal assurance criterion—Twenty years of use and abuse. *Sound Vib.* **2003**, *37*, 14–21.
84. Lieven, N.; Ewins, D. Spatial correlation of mode shapes, the coordinate modal assurance criterion (COMAC). In Proceedings of the 6th International Modal Analysis Conference—IMAC, Kissimmee, FL, USA, 1–4 February 1988; Volume 1, pp. 690–695.
85. Catbas, F.; Aktan, A.; Allemang, R.; Brown, D. Correlation function for spatial locations of scaled mode shapes—(COMEF). In Proceedings of the 16th International Modal Analysis Conference—IMAC, Santa Barabara, CA, USA, 2–5 February 1998; Volume 2, pp. 1550–1555.
86. Hunt, D.L. Application of an enhanced coordinate modal assurance criterion. In Proceedings of the 10th International Modal Analysis Conference—IMAC, San Diego, CA, USA, 3–7 February 1992; Volume 1, pp. 66–71.
87. Brughmans, M.; Leuridan, J.; Blauwkamp, K. The application of FEM-EMA correlation and validation techniques on a body-in-white. In Proceedings of the Measurement Science Conference—MSC, Anaheim, CA, USA, May 1993; p. 646.
88. Cattari, S.; Sivori, D.; Alfano, S.; Ierimonti, L.; Cavalagli, N.; Venanzi, I.; Ubertini, F. Calibration of numerical models to support SHM: The consoli palace of Gubbio, Italy. In Proceedings of the 8th International Conference on Computational Methods in Structural Dynamics and Earthquake Engineering—COMPDYN 2021, Athens, Greece, 28–30 June 2021; pp. 3778–3794.
89. Kita, A.; Cavalagli, N.; Ubertini, F. Temperature effects on static and dynamic behavior of Consoli Palace in Gubbio, Italy. *Mech. Syst. Signal Process.* **2019**, *120*, 180–202. [CrossRef]
90. Girardi, M.; Padovani, C.; Pellegrini, D.; Robol, L. A finite element model updating method based on global optimization. *Mech. Syst. Signal Process.* **2021**, *152*, 107372. [CrossRef]
91. Yang, C.; Yu, Q. Placement and size-oriented heat dissipation optimization for antenna module in space solar power satellite based on interval dimension-wise method. *Aerosp. Sci. Technol.* **2023**, *134*, 108155. [CrossRef]
92. Marquardt, D.W. An algorithm for least-squares estimation of nonlinear parameters. *J. Soc. Ind. Appl. Math.* **1963**, *11*, 431–441. [CrossRef]
93. Sivori, D.; Alfano, S.; Cattari, S.; Ierimonti, L.; Venanzi, I.; Ubertini, F. Nonlinear static analyses to improve the seismic damage assessment of monitored masonry palaces: Application to the Consoli Palace of Gubbio, Italy. XIX ANIDIS Conference, Seismic Engineering in Italy. *Procedia Struct. Integr.* **2023**, *44*, 2090–2097. [CrossRef]
94. Saviano, F.; Parisi, F.; Lignola, G.P. Material aging effects on the in-plane lateral capacity of tuff stone masonry walls: A numerical investigation. *Mater. Struct. Constr.* **2022**, *55*, 198. [CrossRef]
95. Cattari, S.; Lagomarsino, S. A strength criterion for the flexural behaviour of spandrels in un-reinforced masonry walls. In Proceedings of the 14th World Conference on Earthquake Engineering—14WCEE, Beijing, China, 12–17 October 2008.
96. Lagomarsino, S.; Cattari, S. Seismic Performance of Historical Masonry Structures through Pushover and Nonlinear Dynamic Analyses. In *Perspectives on European Earthquake Engineering and Seismology*; Ansal, A., Ed.; Springer International Publishing: Cham, Switzerland, 2015; Volume 2, pp. 265–292. [CrossRef]
97. Cattari, S.; Angiolilli, M. Multiscale procedure to assign structural damage levels in masonry buildings from observed or numerically simulated seismic performance. *Bull. Earthq. Eng.* **2022**, *20*, 7561–7607. [CrossRef]

*buildings*

MDPI

*Article*

# A BIM-Based Model for Structural Health Monitoring of the Central Body of the Monserrate Palace: A First Approach

**Rita Machete, Mariana Neves, Madalena Ponte, Ana Paula Falcão and Rita Bento ***

CERIS, Instituto Superior Técnico, Universidade de Lisboa, 1049-001 Lisbon, Portugal; rita.f.machete@tecnico.ulisboa.pt (R.M.); mariana.vieira.neves@tecnico.ulisboa.pt (M.N.); madalenaponte@tecnico.ulisboa.pt (M.P.); ana.p.falcao@tecnico.ulisboa.pt (A.P.F.)
* Correspondence: rita.bento@tecnico.ulisboa.pt

**Abstract:** The preservation and safeguarding of built cultural heritage is a permanent concern for institutions. These structures were generally poorly prepared for movement triggered by natural disasters, a situation further complicated in the case of earthquakes, as each building has a unique structural dynamic linked to its geometry, materials, method of construction and environmental conditions. The use of structural health monitoring (SHM) systems integrating monitoring techniques as well as inspection and structural analyses has gained great relevance in the appearance of low-cost IoT (Internet of Things) sensors on the market. In this paper, an IoT BIM-based solution is presented for real-time monitoring using low-cost sensors in the scope of building SHM systems. The case study takes place at the central body of the Palace of Monserrate, one of the most distinguished elements of the Cultural Landscape of Sintra. An H-BIM model was created in Autodesk Revit® software (version 2022 and 2023) based on a point cloud, and used as the basis for the numerical model developed in 3MURI. A MeM low-cost sensor was installed on the third floor of the central tower of the Monserrate Palace in Sintra, and the data gathered were recorded in the H-BIM model. The capacity to acquire real-time information on a structure's vibration, both during normal operation and after an extraordinary occurrence, could allow the application of more effective maintenance and repair practices, resulting in lower operating costs and allowing for the best management of built cultural heritage.

**Keywords:** H-BIM; TLS; GPR; structural health monitoring; digital twin; low-cost sensor



**Citation:** Machete, R.; Neves, M.; Ponte, M.; Falcão, A.P.; Bento, R. A BIM-Based Model for Structural Health Monitoring of the Central Body of the Monserrate Palace: A First Approach. *Buildings* **2023**, *13*, 1532. https://doi.org/10.3390/buildings13061532

Academic Editors: Muhammad Shafique and Qian Wang

Received: 3 May 2023
Revised: 29 May 2023
Accepted: 13 June 2023
Published: 15 June 2023



## 1. Introduction

Preserving heritage buildings, such as historical masonry constructions, is relevant to the individual and collective identity of countries, as well as to fuel tourism. In line with the need for the preservation and conservation of historical constructions, the number of designed and applied structural health monitoring (SHM) systems has increased significantly in the last two decades. The final aim is to assess their structural behavior, especially regarding seismic performance, integrating monitoring techniques, inspections and structural analyses.

Historical masonry constructions have been shown to be vulnerable to natural disasters, such as earthquakes, mainly due to their intrinsic fragility. Portugal's seismic hazard puts a high number of historical constructions at risk of damage and collapse, namely, most of the old masonry constructions, which are particularly vulnerable to seismic activities. For the seismic assessment and strengthening of historical constructions, a multi-disciplinary approach is required [1,2]. This approach is a step-by-step procedure, starting with the knowledge process of the historical constructions under study, and should include, among others, the following steps: (i) the research, compilation and analysis of relevant historical data for the generic characterization of the construction and (ii) the definition of a plan for experimental campaigns.

For most historical constructions, it is recommended that the experimental campaigns include: (i) the acquisition of geometry; (ii) static and dynamic monitoring systems; (iii) experimental tests for the mechanical characterization of materials and/or structural elements; and (iv) ambient vibration tests for the dynamic identification of the structure.

According to the characteristics of the building (e.g., the irregularity or dimension of objects), there are many alternatives for the acquisition of geometry using more conventional methods, such as the classical methods of topography [3], photogrammetry [4] or terrestrial laser scanning (TLS) [5], which produce a three-dimensional point cloud. TLS allows for the rapid collection of data from geometry with a high level of detail [6].

The mechanical characterization of materials and/or structural elements can be conducted through different types of tests, taking into account the in situ limitations and available resources. These can be semi-destructive and non-destructive tests, such as the removal of masonry samples, flat-jack tests, ambient vibration tests and ground-penetrating radar (GPR) tests [7].

Experimental dynamic characterization is essential for the obtainment of an accurate portrayal of the current state of structures, the calibration of the numerical models of the constructions to be utilized for seismic structural assessments and the design of retrofitting works [8,9], and the structural health monitoring of the building by observing changes of its dynamic behavior over time [10].

The building information modeling (BIM) approach uses a centralized database that allows access to information in accordance with a users' profile. This brings benefits at each stage of this type of work, namely, due to its adaptability to project modifications or the easiness in communicating between all specialties involved in the design and construction process, reducing the costs and time of planning and construction and, consequently, making the process more efficient. One of the emerging fields of BIM application is in monuments and buildings with heritage value, usually referred to as an H-BIM. According to Biagini et al. [11], the major difference between a BIM model and an H-BIM model is the need to consider not only the information regarding the objects and their properties, but also their history and cultural identity. Additionally, the level of complexity of the representation of elements in an H-BIM needs to consider not only its function, but also future analyses intended for the element; as such, it is important to determine the geometric detail during the modeling and to establish the relevant information associated with the object [12]. As in the case of the Basilica of Collemaggio, reported on by Brumana et al. [12], several configuration levels of detail, geometry, accuracy and information were tested to establish modeling protocols and guidelines to support the BIM-based management. There are other applications and considerations regarding the use of an H-BIM, such as: conducting a structural health assessment through a point cloud BIM-generated element, simplified and meshed, for the creation of a finite element model that fulfills the structural analysis requirements [13]; the creation of a unique model that serves all stakeholders involved in the conservation and rehabilitation of a damaged monument [14]; the uses of an H-BIM model as a digital platform to support tests of construction solutions to achieve the final solution of the rehabilitation process [15]; or the use of an H-BIM as a central database for facility management [6].

One of the great challenges in the implementation of H-BIMs is the non-existence of information (graphical and non-graphical). Heritage buildings are often complex and irregular, with absences of documentation concerning the material (and their properties) when compared to young buildings. Buildings with heritage value do not have monitoring systems installed and follow strict rules concerning their installation, preventing the acquisition of relevant data for SHM systems.

Through the identification of this gap, the main objective of this work is to present a BIM-based solution that enables real-time structural monitoring based on low-cost sensors. The central body of the Monserrate Palace is used as the case study, in which the geometry and description of the materials of the structural elements are defined and stored in an H-BIM model. Thus, this work is divided into the following main parts: (i) data collection

and geometric modeling, (ii) real-time structural monitoring based on low-cost sensors, (iii) numerical modeling and calibration and (iv) the proposal of a SHM for the central body of the Monserrate Palace.

## 2. Literature Review

SHM is a procedure that aims to estimate a structure's condition through the evaluation of measured physical features involving three stages: signal collection, processing and interpretation.

The first stage can utilize a varied range of sensors to measure the physical properties of structures, and is divided into: kinematical (displacement, velocity and acceleration), mechanical (forces, deformations and stress) and ambient (wind and temperature) [16]. Combining various sensing technologies with data acquisition and processing capabilities plays a significant role in assessing the condition of structures [17].

Kinematic sensors in SHM applications measure the motion induced by external forces, ranging from moderate or strong winds to seismic waves, traffic and human-induced vibrations, among others [16]. By measuring the acceleration of the in-test structure through the application of accelerometers, the study of the resulting building vibrations has several fields of application, including the analysis of environmental vibrations and their effects on the comfort and safety of these structures. An accelerometer is an electro-mechanical device that measures the acceleration forces acting on or being exerted onto an object. There are various types of accelerometers that diverge in operation mechanisms, including: piezo-electric, which uses the piezo-electric effect of a specific material and transforms a type of energy into another, which then produces an electrical signal in response to the parameter being measured; force balance, where the relative displacement can be measured with a capacitive gauge or a transducing material (piezo-electric ceramic) fixed onto the compliant element (best for lower frequencies); piezo-resistive, which generates resistance changes in displacement sensors, which are a part of accelerometer systems (best option for measuring the impulse where the amplitude and frequency range are high); and the capacitive micro-electro-mechanical system (MeMs), which works according to capacitance changes in a seismic mass under acceleration [18,19]. With the increasing demand for more efficient and lower-cost sensors for monitoring buildings, coupled with the fast increase in micro-sensor technology and jutting micro-controllers (e.g., Arduino and Raspberry), the increased application of low-cost sensors (encompassed in the MeM category) has been founded in the literature, as reflected in the work of Komarizadehasl et al. [20–22], which demonstrates how to design and set up low-cost sensors of structural vibrations and inclinations. This solution could be the starting point for reducing the uncertainty of building monitoring by increasing the density of measurement points. This new technology, linked with the higher processing power of computers (that allow for the processing of substantial amounts of data) enables the spread of the application of embedded intelligence in buildings, i.e., "smart buildings", through IoT (Internet of Things) solutions. The application of the IoT allows for the permanent monitoring of buildings with real-time readings accessible at a distance. Although the permanent monitoring of buildings for indoor environment data with low-cost sensors can be easily found in the literature, as exemplified in the works applied to historic buildings by Casillo et al. [23], in museums of Chianese et al. [24] and Amato et al. [25] and in the facility management of Valinejadshoubi et al. [26], for dynamic data, permanent readings with the support of the IoT in buildings have been less expressed in research papers; however, there has been an increase in applications, as is the case of Pierleoni et al. [10]. However, in heritage, due to the severe restrictions to which the buildings are subjected to, the application of such monitoring has had minor presence in practice according to Mobaraki et al. [19]. As for applications of wireless sensor networks (WSNs) linked to BIM approaches, such solutions have gained prominence within the management of built environmental assets post-construction, with a focus on environmental data, as described in the work of Mataloto et al. [27,28], applied to energy saving.

Currently, the implementation of IoT solutions for continuous SHM is underway in the scientific community; however, such works have yet to reach significant volume. This direction of research could allow for quick decision making due to real-time data availability in a post-occurrence instance, leading to a shorter time for the recovery of essential utilities, mitigating downtime and associated financial costs. According to Kim and Frangopol [29], continuous monitoring over a long-term period can increase the reliability of the assessment and prediction of structural performance. Gentile et al. [30] described the largest monitoring system in a cultural heritage monument with an implementation of a wired sensor network with a semi-manual data export IoT solution, demonstrating the potential of such surveillance systems during the life cycle of a building. Recently, the work of Li et al. [31] demonstrated the implementation of a multi-sensor solution monitoring structures for guiding maintenance works by measuring safety during the process, demonstrating the importance of surveys with an IoT solution for data management and concluding the importance of a WSN for future works. As such, the apparent future path of research efforts is implementing low-cost MeM WSNs with IoT systems for heritage SHM, notwithstanding monitoring with better-established methods.

Additionally, considering the influx of large quantities of data, methods of monitoring data analysis and structural state assessment have expressed a concern. As Mondal and Jahanshashi [32] stated, the processing of procured data enabling real-time decision making remains an impediment. Therefore, in the literature, some solutions have been proposed to deal with large sets of data, such as the application of machine learning in the interpretation of photographic data [32], with prediction models having been applied through algorithms [29,33,34].

## 3. Materials and Methods

Extensive research of relevant historical data was the first step to better understanding the heritage buildings. In parallel, in situ tests were performed (GPR and ambient vibration tests) for the characterization of the structural elements, together with field surveys to acquire geometric information carried out to obtain the geometry of the buildings using total station and TLS in conjunction with targets that were previously coordinated with the use of a global navigation satellite system (GNSS). The final point cloud was used as the basis for the 3D modeling in the BIM environment, and the database was enriched with information concerning the building materials and their properties. Based on the H-BIM model, a numerical model was developed using 3Muri software (version 13) [35], for which a dynamic modal analysis was conducted; the numerical model was calibrated according to the results of the in situ tests. In complement, static and dynamic monitoring was performed. For the latter, two types of sensors are used, including highly sensitive force balance accelerometer equipment for periodic monitoring, utilized for the structural assessment of the buildings and model calibrations, and a micro-electro-mechanical system (MeM) low-cost sensor was employed for both unique (10 min reading) and continuous (4-month reading) monitoring.

### *3.1. Case Study Description*

The Monserrate Palace belongs to the Cultural Landscape of Sintra (Figure 1), classified as a World Heritage Site by UNESCO since 1995, and is characterized by its unique identity and the progress of architecture and technology in landscape and project planning. These topics alone are an indication of its heritage value, emblematic identity and consequent relevance for the research and preservation of the palace and its surroundings.

Monserrate's history progressed through cycles of greatness and ruin (Figure 2), starting with the chapel devoted to Our Lady of Monserrate, after whom the palace was named, dating back to 1540. In 1718, the property was bought by the Mello e Castro family and administrated through third parties. As the earthquake of 1 November 1755 devastated the area, destroying the houses on the grounds of the current palace, De Visme (tenant) took care of the recovery of Monserrate and built a neo-gothic castle with special attention

to characteristics such as symmetry, proportion and balance. This building followed guidelines quite common in England, and set the tone for what would be the structure of the palace throughout the centuries: three towers, where the central one would have a square base and two floors from which two wings led to each end of the palace with circular towers. De Visme left the property abandoned from 1791 to 1794, after which William Beckford, an English aristocrat and art connoisseur, took the lease and carried out restoration work. Due to the war climate in 1799, he returned to England, and Monserrate was left, once again, to abandonment.


**Figure 1.** Location of the case study: Portugal (**left up**), Lisbon (**center up**), Monserrate Park and palace (**right**), Monserrate Palace (**left down**).

During this cycle, the property was vandalized and received different visitors, one of which was Francis Cook, an English art appreciator, who, during his Grand Tour in 1856, became a tenant, and in 1863 becoming its most notorious owner. It was during Cook's period as an owner that Monserrate came closest to what it is known as today: a palace with gothic, Indian and Moorish influences, with ornaments that extended to the outside of the palace, showing how important it was to be in harmony with the surrounding nature and preserving the memory of the previous owners by preserving the plan of the house, with it later being the scene for large parties, dinners and balls [36].

Due to World War II and the resulting crisis, the Cook family had to sell the palace to Saúl Saragga (an antique dealer), who sold the house to the Portuguese state, after which it was handed over to the management of the park to Parques de Sintra—Monte da Lua S.A. (PSML) in 2007.

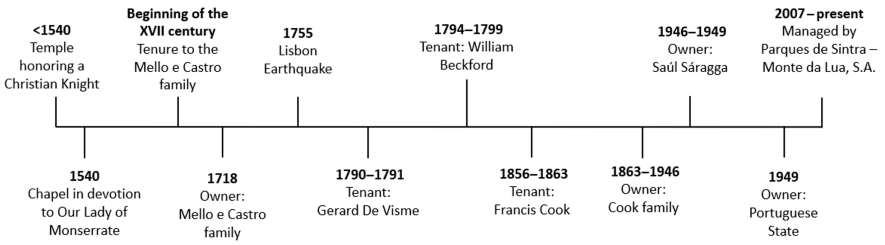


**Figure 2.** Chronogram of Monserrat, showing who it belonged to and the different occupants.

The current iteration of the building rests on a raised platform with a longitudinal symmetrical plan composed of a rectangular central body with two circular plan towers at the ends. The building is 60 m long by 20 m wide, with 5 floors in total. Most of the floors comprise wood flooring supported by wooden beam structures, with a few exceptions of tile flooring over brick vaults supported by steel beams. The exterior (structural) walls of

the building appear to be of rubble stone masonry and air lime mortar, with the interior walls appearing to be "tabique" partition walls. In the central body, the walls that support the interior dome appear to have a mixed structure, being part rubble stone masonry for the first 2 floors and the rest having been built with brick masonry. However, due to the lack of detailed records, the composition of all existing elements is not evident; for the extensive characterization of the monument, it would be necessary to execute non-destructive tests to ascertain particular elements.

For the case of the present work, the central rectangular body was chosen as the focus, due to the symmetrical quality of the building. Specifically, the experimental campaign was started on the third floor of the central body, since this floor was not visitable by the public, allowing the campaign to be performed with reduced external impact (such as uncharacteristic vibrations of the structure due to the walking of visitors) and ease of access to areas for the placement of sensors near the outer walls that define the body. In the future, continuous monitoring should first be extended to the whole central body (Section 4) and then to the entire palace.

### *3.2. Data Collection*

#### 3.2.1. Geometrical Data Acquisition

Regarding the geometric data acquisition, 336 scans were carried out with TLS to obtain geometric information about the Monserrate Palace. Of this total, 205 scans corresponded to the rooms of the central body and side wings, which were the object of the study. These scans were acquired with a Faro Focus S70 laser scanner starting in April 2021. For each scan, a combination of parameters was selected, considering the amount of information that was needed from each room of the palace and finding a balance between collected information and the duration of its acquisition. The detailed point cloud was processed in Autodesk ReCap® [37], and was the basis of the geometric model (Figure 3). To geo-reference the model, a topographic survey was carried out with a GNSS receiver and total station with the support of topographical targets located at strategic points (Figure 4). The coordinates (M, P) are relative to the PTTM06/ETRS89 system, and the H coordinate, orthometric altitude, is in relation to the Cascais tide gauge.

**Figure 3.** Point cloud perspective view.

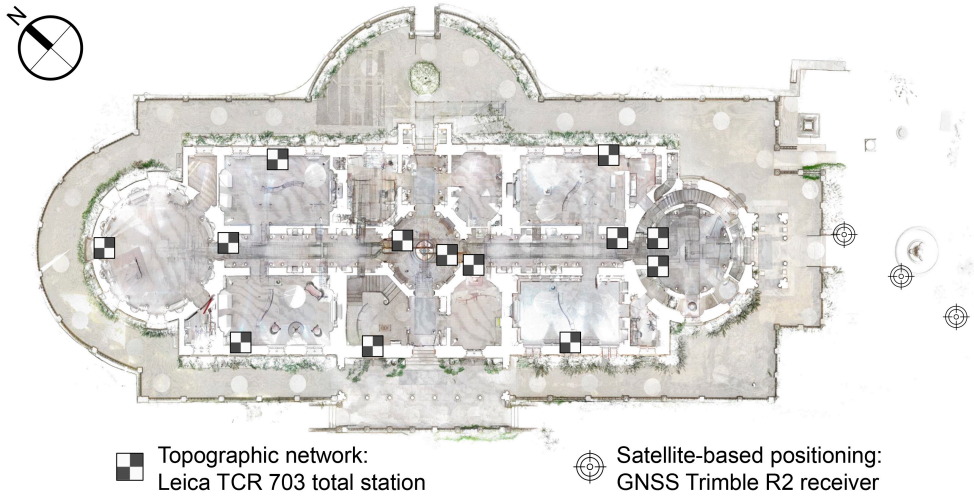


**Figure 4.** Location of the topographic network support targets. Plan view of point cloud in Autodesk ReCap®.

#### 3.2.2. Characterization of the Structural Elements

Due to the scope of the work, a clearer comprehension of structural composition was required whilst maintaining the physical elements of the palace; as such, non-destructive tests were applied. Therefore, in areas where the construction technique applied was unknown, ground-penetrating radar (GPR) surveys were conducted by a team from Morph Geociências Lda [38] and coordinated by the IST team. Through the emission and reception of electro-magnetic waves in the object, it was possible to decipher cavities and alterations in materials, which allowed for a better understanding of the constitution of the elements. In total, we obtained 22 polygons of a 3D inspection with a 1.6 GHz geo-radar, 4 discrete profiles with a 1.6 GHz geo-radar in the columns, 2 discreet profiles with a 500 MHz geo-radar on the pavement and 3 discreet profiles with a 500 MHz geo-radar in the wall. Of which, for the central body, there are 14 polygons of 3D inspection and 2 discrete profiles in the columns. The survey helped to identify the construction apparatus in several walls that were previously mis-categorized, such as the walls on the higher floor in the central tower, which turned out to be composed of masonry instead of brick (Figure 5c) as originally expected, as well as the opposite seen in the ground floor corridor niche (Figure 5a,b). For the remaining elements, the construction technique was inferred from the surveys or exposed elements, such as the walls viewed from the foundation level.

#### 3.2.3. Static Monitoring of the Main Crack

Due to the good conservation of the Monserrate Palace, no cracking state was generally acknowledged. Only one major crack was identified indoors in the west workroom over the window on the third floor of the central body of the palace (Figure 6). As no other cracks or inclinations in the walls were surveyed, it was decided to only place crack meters along this crack to periodically monitor and control any movement that occurred instead of displacement transducers.

#### 3.2.4. Ambient Vibration Tests and Unique Dynamic Monitoring Comparison between Sensors

For the ambient vibration tests, using the unique dynamic monitoring, two types of accelerometers were placed in situ with different typologies and basic characteristics (Table 1 and Figure 7b). The first was a piece of force balance vibration measuring equipment (EpiSensor ES-T triaxial measuring and digital recording unit) from Kinemetrics Inc. (Pasadena, CA, USA) The Etna2 was capable of recording a series of accelerations observed in three orthogonal directions (two horizontal and one vertical). Their communication was performed using a laptop computer connected with a GPS/GNSS antenna (global position system/global

navigation satellite system). The units were configured with the highest available sensitivity of ±1 g at full-scale with a 24-bit resolution (accelerations ranging from $5.96 \times 10^{-8}$ g to 1 g) for a frequency of 200 Hz, and each assay lasted for a duration of 660 s.

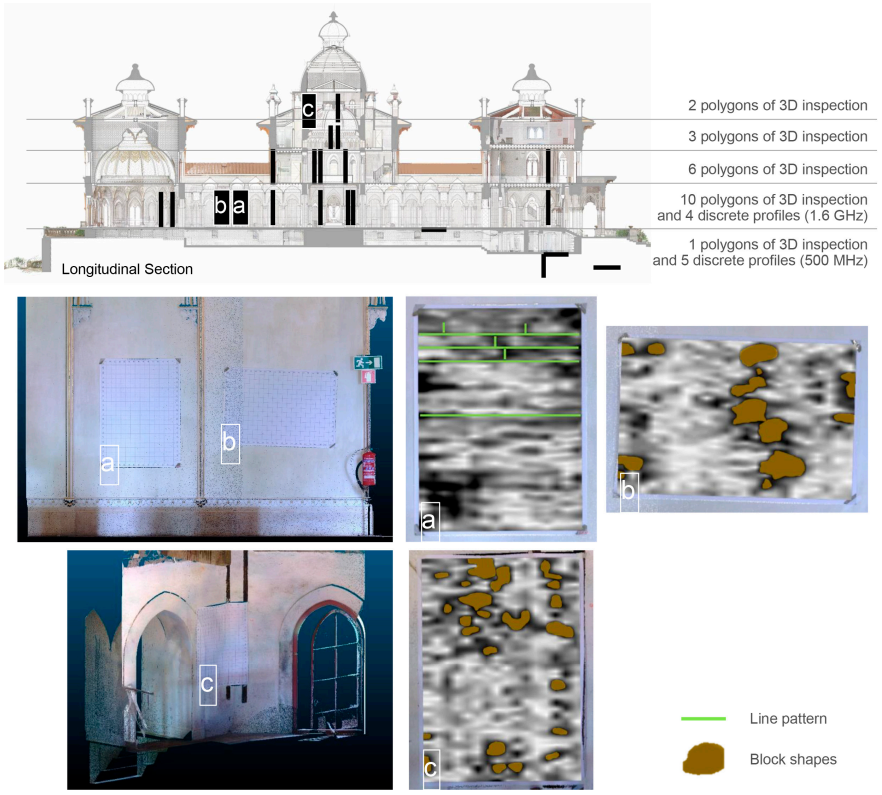


**Figure 5.** Location of GPR windows in longitudinal section of the palace (top) and 3D view (left): (**a**) window at ~0.091 m deep displaying a line pattern consistent with brick masonry; (**b**) window at ~0.17 m deep displaying block shapes consistent with rubble stone masonry; and (**c**) window at ~0.12 m deep displaying block shapes consistent with rubble stone masonry.

**Figure 6.** Location of the cracks in the west workroom over and below the window on the third floor: view of crack meters (**left**); photo of the cracks in relation to the wall (**middle**); location in plan view (**right**).

Alongside the low-cost MeM accelerometer sensor, we also used the Bosch BMA280 sensor (Gerlingen-Schillerhöhe, Germany), encompassed in the Bosch XDK110 kit that

includes environmental and dynamic sensors and a wireless connection. To characterize the low-cost sensor that would be employed for the continuous monitoring, a comparison of accelerations acquired with the MeM device and Etna2, with an equivalent frequency of 0.005 s, was conducted. The available and applied sensitivity was lower than that for the opposing equipment, with a 14-bit resolution at ±2 g full-scale with 4096 LSB/g (accelerations ranging from $2.44 \times 10^{-4}$ g to 2 g). This sensor allowed for the creation of a record log either via a Wi-Fi connection to an online platform (e.g., Microsoft Azure®) or via a USB cable to a laptop computer using the XDK-Workbench program interface to program and record the readings, programmed using the C language. Due to the high frequency of records and low period of time, the USB connection was utilized.

**Table 1.** Characteristics of ETNA2 and Bosch BMA280 sensors.

| | | **ETNA2** | **Bosch BMA280** |
|---|---|---|---|
| Sensor Performance | Typology | Force Balance | MeM |
| | Resolution | 24-bit | 14-bit |
| | Sensitivity | 1 g/2^24 = 1 g/16,777,216 = 59.6 ng<br>2 g/2^24 = 2 g/16,777,216 = 119.2 ng *<br>4 g/2^24 = 4 g/16,777,216 = 238.4 ng * | ±2 g: 4096 LSB/g = 0.244 mg<br>±4 g: 2048 LSB/g = 0.488 mg *<br>±8 g: 1024 LSB/g = 0.977 mg *<br>±16 g: 512 LSB/g = 1.953 mg * |
| | Voltage | 9–28 (VDC) | 1.62–3.6 (VDD) |
| Environmental Restrictions | Temperature and humidity range for correct operation | −20 °C to 70 °C<br>0–100% RH<br>(non-condensing) | −40 °C to +85 °C<br>(0.015%/K sensitivity temperature drift) |
| | Size of sensor | 15 cm × 15 cm × 7.5 cm<br>(1.5 kg)<br>(per unit) | 60 mm × 40 mm × 22 mm<br>(54 g)<br>(XDK110) |
| Economic Issues | Sensor cost | EUR~6300 | EUR~300 (XDK110) |
| | Market availability | Y | N |
| | Easy installation | Y | Y |
| | Need for accessories, such as data acquisition systems, electric current, wiring, etc. | Y<br>(must have electric current and cable connection between units and antenna) | Y<br>(due to limited battery life) |

* Other modes of registration not used in this work.

For this comparison, the accelerometers were placed on the floor in the corners of three of the workrooms on the third floor (Figure 7a,b for the identification of position S1) and leveled with the integrated support system, ensuring that they were in a horizontal plane at points where the largest displacements were expected to occur without the need to fix the accelerometers to the walls, which would damage the property. In total, 4 phases of measurements were performed. In each measurement phase, the accelerations were recorded 2 times for 10 min each to ensure that at least one reliable record was obtained. Four records were obtained with the "master" and two records with each "slave". The in situ testing was conducted on 18 January 2022, and, according to the weather data from "Humberto Delgado" airport, the day temperature varied from 6 to 14 degrees Celsius.

For the comparative test, the rough data from the XDK sensor and treated data from Etna2 were imported into ARTeMIS Modal software (version 7.2.2.3) [39] in an attempt to find the same vibration frequency for both sets. Longitudinal and transverse data for the first "slave" (S1) placement were utilized, ignoring the vertical component. As such, for the XDK dataset, the frequency found for the frequency domain decomposition (FDD) in the X and Y directions was fx = 2.393 Hz and fy = 3.906 Hz, with a complexity of 0.501% and 4.144%, respectively, and a modal assurance criterion (MAC) value of 1. For Etna2,

the single point frequency was set to fx = 2.734 Hz and fy = 3.955 Hz, with a complexity of 0.055% and 17.112%, respectively, and a MAC value of 1 (Figure 8). However, though similar vibration frequencies were found, the data with higher sensitivity had clearer "peaks" that would allow us to easily identify frequencies (or periods) and correspondent modes of vibrations. Something that also became evident during the campaign was the instability of the XDK-Workbench program for data recording, resulting in the loss of data after a forced shutdown of the program due to the computer RAM capacity failures (due to the sheer number of entries kept in temporary memory).

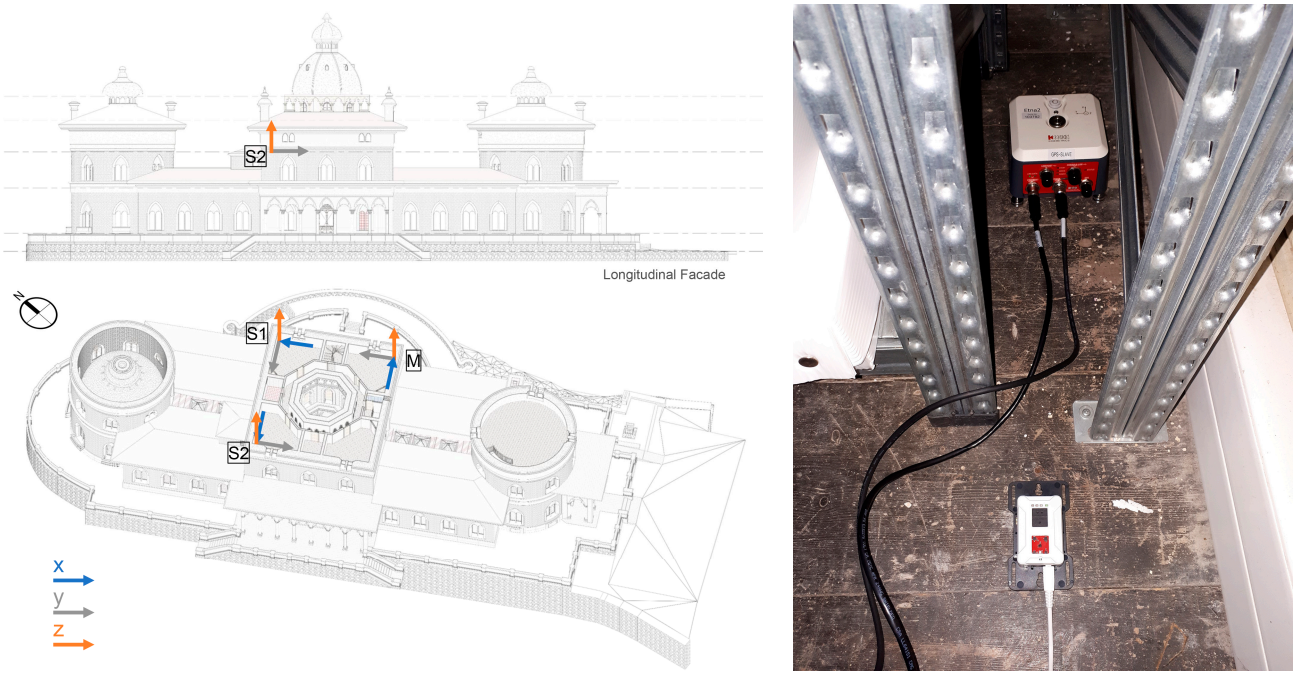


(**a**) (**b**)

**Figure 7.** Equipment in situ survey: (**a**) position and orientation of the accelerometers; (**b**) S1 position: Etna2 (top) and XDK110 (bottom).

Ambient Vibration Tests

With the ambient vibration tests, it was possible to define the main dynamic characteristics of the buildings (frequency/periods and vibration modes), which were then compared with the dynamic characteristics obtained through the numerical model simulation based on the performance of the modal analysis (Section 3.4).

The vibration-measuring equipment used for the ambient vibration tests consisted of two autonomous triaxial Etna2 units, with communication carried out using a laptop computer. In the equipment software, it was possible to configure the type and parameters of the readings and order simultaneous recordings. Two different set-ups were defined; set-up 1 included the master sensor M and slave sensor in position S1, and set-up 2 included the master sensor M and slave sensor in S2 (Figure 7a). For each setup, two different records of 10 min were performed.

Then, the Etna2 records were used and the data were processed with ARTeMIS Modal software, dis-aggregated in the respective orthogonal directions and reduced to 600 s in order to "clean" the signal. From the results, a Fourier spectrum was defined that allowed for the discovery of the frequencies for the X and Y directions, which were fx = 3.95 Hz and fy = 4.065 Hz, respectively. These frequencies and corresponding modes of vibration along the two directions were those expected to govern the seismic response of the central body of the Monserrate Palace; thus, they were of primary interest in the seismic analysis of the central tower.

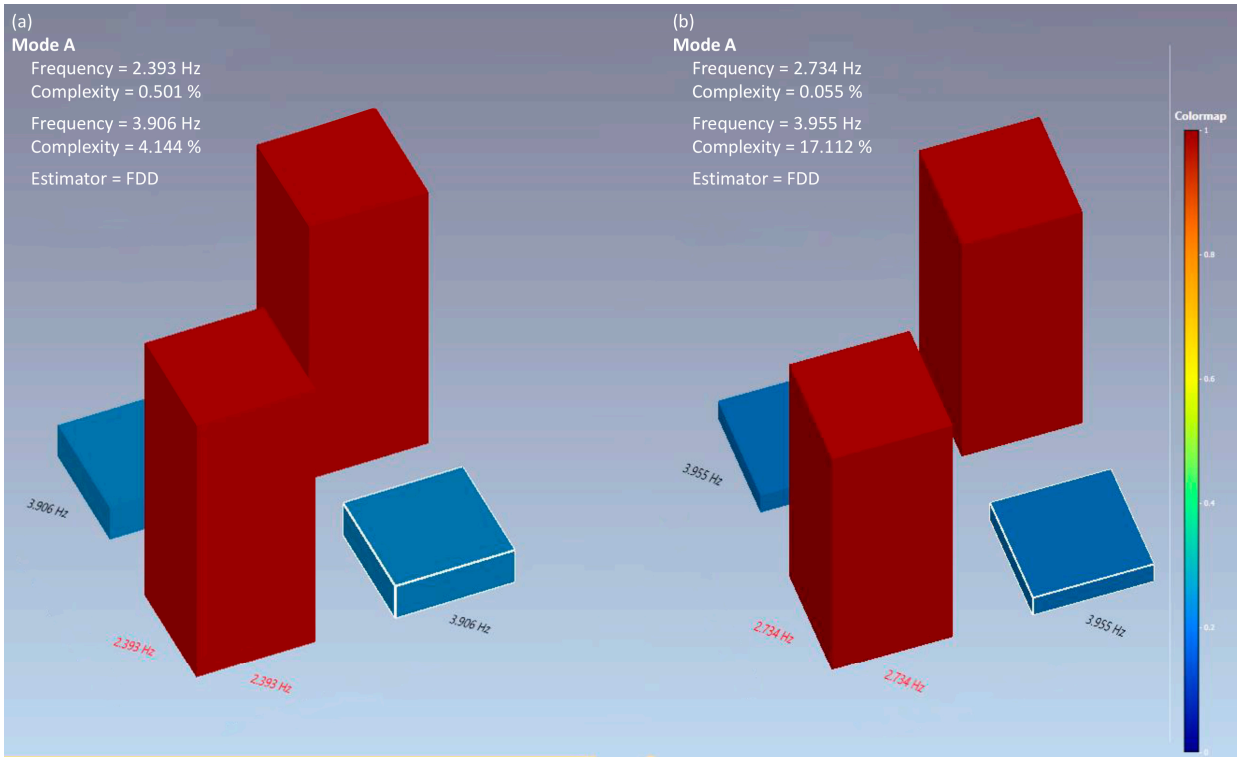


**Figure 8.** ARTeMIS modal assurance criterion, in S1 position, for XDK (**a**) and Etna2 (**b**).

### *3.3. H-BIM Modelling*

The H-BIM model was developed in Autodesk Revit® software [40]. The geometric representation of the building needed to be compatible with its intended use at an adequate detail level. For heritage buildings, in a conservation context, information concerning materials and elements must be registered with a high level of detail, either in attributes or in geometry. For the case of BIM-based management, the level of detail can be simplified, while the attributes should enable operations along a building's life cycle. As for the structural analyses, the structural apparatus elements needed to be properly represented, having a greater value than decorative and simple architectural elements.

Since the present model had more than one intended use, encompassing the future monitoring aspects (pertaining to management), as well as a basis for the structural model, the elements represented were modeled assuming some simplifications while maintaining the overall shape and function, but ignoring the highly decorative elements while maintaining the point cloud alignments and geometric overall shape. During the modeling process, several approaches were considered to find a balance between both intended uses. As such, the structural floor system was based on floorboards laid over beam systems that were possible to observe in the access to the boiler room. Due to the complexity of the domes, the option Model in Place was used to sketch the overall details maintaining the identity, but simplifying the support system, since they did not have structural relevance. For the doorways, simplified families of doors and windows were created to retain the overall atmosphere in conjunction with the desired geometry (as the 3Muri software only required basic opening information), and for the columns, a family was created, allowing for the repletion and tally of elements. The final model is illustrated in Figure 9. To thoroughly utilize the qualities of the H-BIM, information pertaining to the in situ testing was also added to the pertinent elements. To this purpose, new parameters were created in the wall elements, allowing us to identify the areas surveyed and corresponding report information. Information pertaining to the mechanical properties of the walls, described in the following chapter, were also added as attributes to the corresponding family types as new parameters.

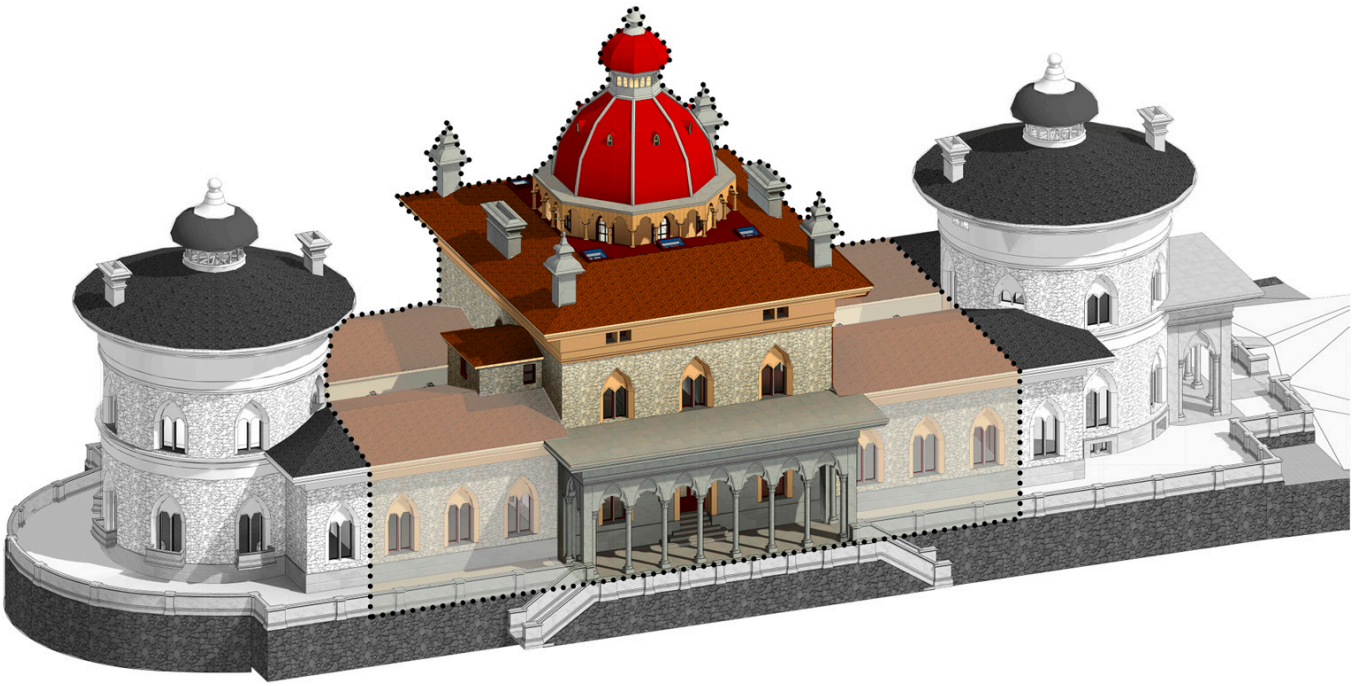

**Figure 9.** H-BIM representation of the palace: area of study in strong color. The light and strong colors identify the parts numerically modeled.

### *3.4. Numerical Modelling and Calibration*

As previously mentioned, based on the BIM model, the numerical model of the central body of the Palace of Monserrate was developed using 3Muri software [35], which uses the equivalent frame method—EFM [41]. The numerical model was calibrated according to the results of the GPR (see Section 3.2.2) and ambient vibration tests (Section 3.2.4).

The inter-operability between Autodesk Revit® and 3Muri was not automatic; therefore, it was necessary to re-model the structural materials and their characteristics for the structural assessment calculation, using the BIM model as a working basis. To facilitate the process of adapting the plans, average thicknesses and the locations of openings, the plans were exported in a .dxf format to Autodesk AutoCAD® [42] and, after making the necessary changes and simplifications (e.g., imposing that nodes were not too close to each other and that the midline of the wall was coincident in height), the plans were imported into 3Muri. The plans used with the assumed simplifications are illustrated in Figure 10a. The simplifications were performed because the structural program could result in conflicts when modeling and predicting the behavior of different macro-elements due to the mesh created.

After this process, the numerical modeling took place by dividing the structure into 6 levels (Figure 10b) to ensure that all structural elements with different characteristics were defined without major approximations. The mechanical properties of the materials, the geometry of the structural elements and the loads applied were defined based on a previous research work by Candeias et al. [43]. These mainly included stone masonry (regular and irregular) and Portuguese pine wood used in the floors, roofs and partition walls, known as "tabique" walls. The mechanical characteristics of the materials were defined after an iteratively processed development based on the results of the calibration using the results from non-destructive experimental in situ tests and the results obtained with the numerical model by performing a dynamic modal analysis (Table 2).

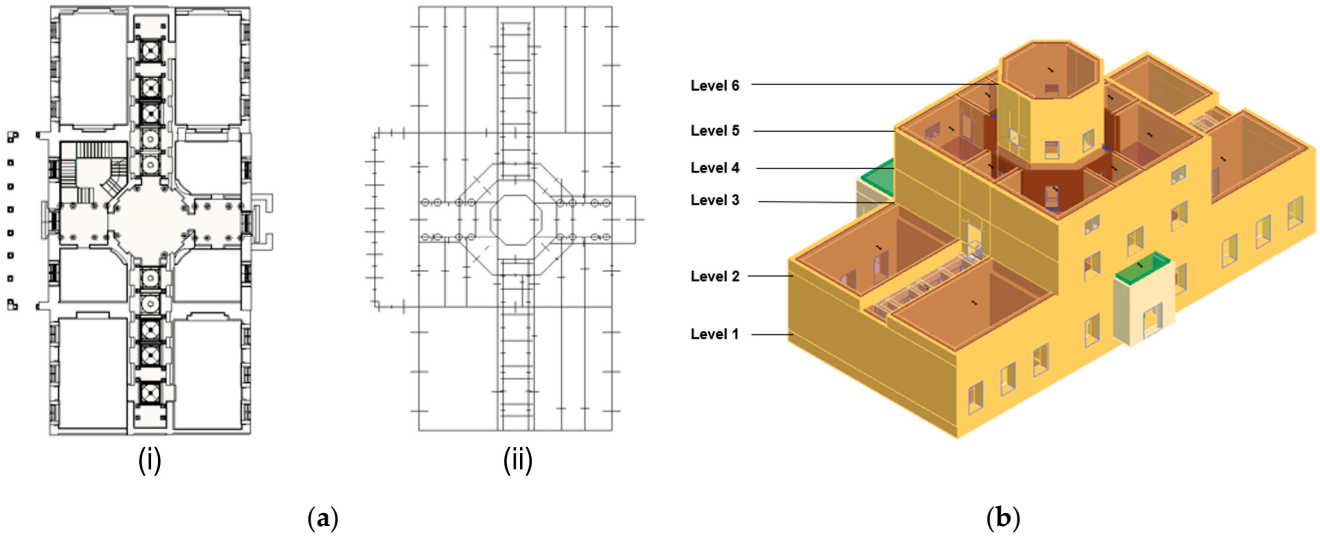


**Figure 10.** From Revit to 3Muri: (**a**) model in Autodesk Revit® (i) and simplified wireframe plan with all structural elements of all floors superimposed (ii); (**b**) identification of levels in 3Muri.

**Table 2.** Mechanical properties of wall materials.

| | Elasticity Modulus E (GPa) | Distortion Modulus G (GPa) | Shear Strength τ (MPa) | Compressive Strength fc (MPa) | Volumetric Weight w (kN/m$^3$) |
|---|---|---|---|---|---|
| Irregular ordinary masonry with good adhesion | 1.70 | 0.60 | 2.60 | 0.08 | 21.00 |
| Regular stone masonry of quality | 2.80 | 0.90 | 6.00 | 0.08 | 22.00 |
| Partition | 0.060 | 0.0035 | 0.075 | 1.000 | 14.000 |

It is worth mentioning that to obtain an adequate numerical model of the central body of the Palace of Monserrate, it was necessary to account for the constraints imposed by adjacent parts of the palace, the ones necessary to obtain the correct dynamic characteristics of the body under analysis. Thus, the numerical model accounted for the central tower and the two wings (Figures 9 and 10b).

In 3Muri, it was possible to perform a modal analysis and obtain the main dynamic characteristics: periods, vibration modes and mass participation factors. After many iterations and changes to the material properties and types of walls in the 3Muri software, the results presented in Table 3 showed the dynamic global response of the calibrated model, and were in accordance with the results obtained in the in situ tests (with an error margin of 9.5% and 6.9% for the fundamental frequencies in the X and Y directions, respectively). The first fundamental vibration mode had a frequency of 3.579 Hz and corresponded to a pure translation in the transverse direction (X direction). The second mode of vibration was a pure fundamental Y-translation mode and corresponded at a frequency of 3.784 Hz in a longitudinal direction. These two fundamental vibration modes can be seen in Figure 11a.

It was noted that the fundamental modes of vibration corresponded to close frequencies, which was a result of the symmetry of the central tower from the first floor up.

The mechanical properties of the wall materials adopted after the calibration are listed in Table 2.

The final numerical calibrated model is depicted in Figure 11b. This model was ready for the seismic structural assessment of the central body of the palace to identify potential vulnerable structural elements and to support the design of retrofitting interventions.

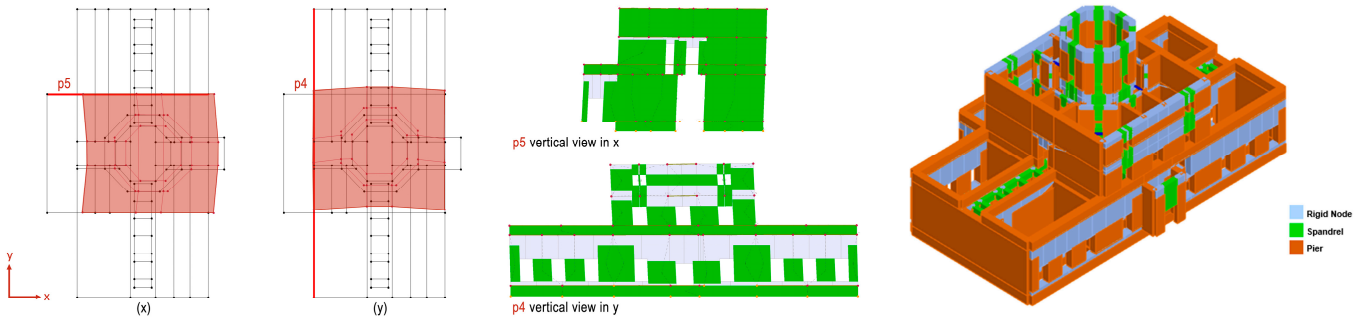


(**a**) (**b**)

**Figure 11.** 3Muri analyses: (**a**) main vibration modes represented in vertical and plan view, (x) pure X-translation with a frequency of 3.579 Hz and (y) pure Y-translation with a frequency of 3.784 Hz; (**b**) final model of 3Muri with rigid nodes, spandrels and piers represented.

**Table 3.** Values of periods, frequencies and mass participation factors for the main vibration modes.

| Modes of Vibration | Numerical | | | Experimental | Error (%) |
|---|---|---|---|---|---|
| | Frequency (Hz) | Mass Participation Factors | | Frequency (Hz) | |
| | | $M_x$ (%) | $M_y$ (%) | | |
| 1 | 3.579 | 35.85 | 0.03 | 3.95 | 9.5 |
| 2 | 3.784 | 0.08 | 17.03 | 4.065 | 6.9 |

### *3.5. Continuous Real-Time Structural Building Monitoring*

Continuous monitoring was implemented to determine its significance for the management and preservation of the palace. As previously mentioned, SHM systems have previously been implemented with success using sensors such as accelerometers to track the structural health of historical masonry structures. These systems have also shown that structures exhibit seasonal variation in response to variations in ambient conditions (temperature and relative humidity) [44]. As such, the Bosch XDK110 kit was programmed to register environmental (Bosch BME280) and dynamic data in a continuous mode, measuring at 1 s intervals while depositing the average data at 3 min spans through a Wi-Fi network using the Microsoft Azure® platform, encompassing the IoT solution. The 3 min span was selected due to limitations of the volume of data available in the Microsoft Azure® platform package. The data were registered and visualized in the Azure platform in real time, allowing for the conductance of a consultation at any point through an internet connection. For the position, as previously determined in Section 3.2.4, the third floor west workroom corner was chosen (Figure 12). The data present in the Azure platform were, subsequently, exported to a Microsoft 365 Excel® spreadsheet, aggregating all the records. For creating an active connection with the Revit model, a generic element representing the sensor format and location was created. In the spreadsheet, a VBA script extracted a series of statistics, e.g., the last value of each parameter or their daily average, storing these values and connecting them to the BIM model (see Section 3.3) through the DiRoots® plug-in for Autodesk Revit®. This allowed for an interpretation of the data connected to its geometric position, as well as all other relevant data pertaining to the affected area stored in the model.

As for data, the sensor collected data from December 2022 (four months of data). Due to the acquisition rate, a detailed modal analysis could not be achieved with these acceleration data due to the low frequency of vibrations in the building (established in Section 3.2.4). Namely, for continuous monitoring, the period of registration was 3 min, in contrast to instant monitoring, which has a period of registration of 0.005 s. As such, the continuous monitoring over the 4 months did not allow us to record the vibrations previously established. However, through the analysis of the vibrations, changes in the

structure of the building could be observed. In Figure 13, for the acceleration data, a shift was detected in the vibrations, which was later established to be due to the roof rehabilitation of the central tower. As such, with the work reaching a higher level of intervention on 23 January, a clear change in transverse vibrations was observed. At this time, most of the work had already been completed. Nevertheless, some interventions were still taking place, and that was reflected in the graph, displaying a slow recovery to the previous vibration period, though not yet stabilized.

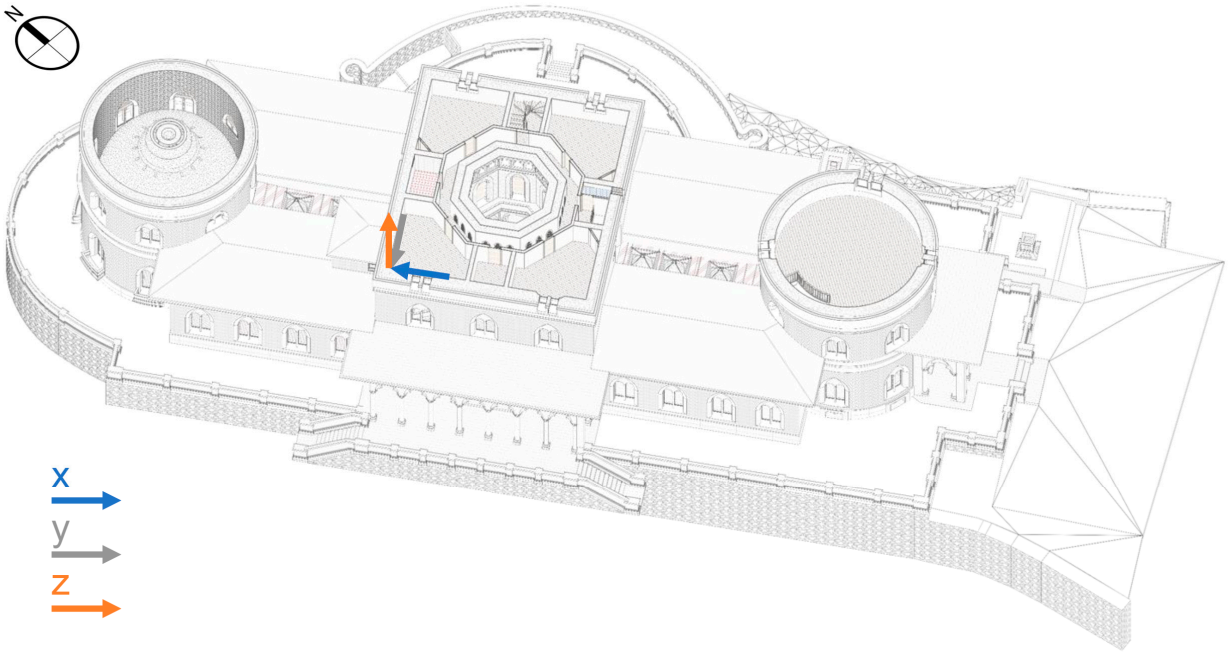


**Figure 12.** XDK sensor for continuous monitoring: position and orientation.

Regarding the temperature data, an impact study of temperature on the structure could not be conducted due to the intervention work that skewed the stated data, as well as the uniform distribution of temperature to the time frame in question. Nonetheless, to determine the importance of in situ temperature measurements, in Figure 14 on the right, temperature data by day were extracted from the closest weather station in Colares, Sintra (4 km distance to the Palace), published by the "Instituto Português do Mar e da Atmosfera" (IPMA), to compare to the collected information inside the building. As was expected, the recorded temperature amplitude varied greatly between the two, as the weather station measured outside at an 11 m elevation, while the palace sensor was inside the building; thus, the weather station values varied between −2 and 31 degrees, while the palace room readings varied from 12 to 22 degrees Celsius.

Figure 15 shows the indoor humidity registered with the same sensor for the same period of time, as well as the rainfall recorded by the IPMA in the closest weather station in Colares, Sintra. The results showed that, for most of the cases, high values of humidity occurred with high values of rainfall. Nevertheless, on some particular days, there were some unexpected high values of amplitude of humidity (difference between maximum and minimum values), which did not correlate with the level of rainfall. However, this may have occurred due to the maintenance works being conducted on the roof in the same period.

In the future, variations in the fundamental frequencies (fx, fy) identified from the periodic ambient vibration recordings should be assessed, and the potential shifts due to the temperature and humidity variations should be analyzed. Based on previous studies [45], the following was expected: (i) a positive correlation between frequencies and temperatures so that an increase in temperature would correspond to an increase in natural frequency; (ii) a weaker correlation with frequency variations and humidity.

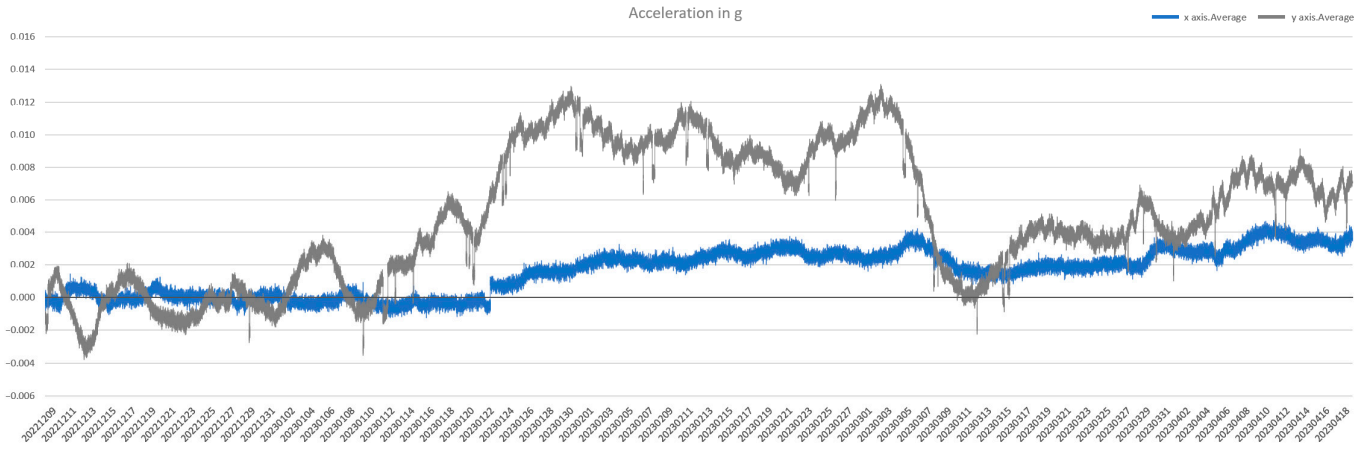


**Figure 13.** Continuous monitoring data (for four months) of acceleration in g for XDK; measurements without detrending and filtering of 3 min average of the 1 s measures.

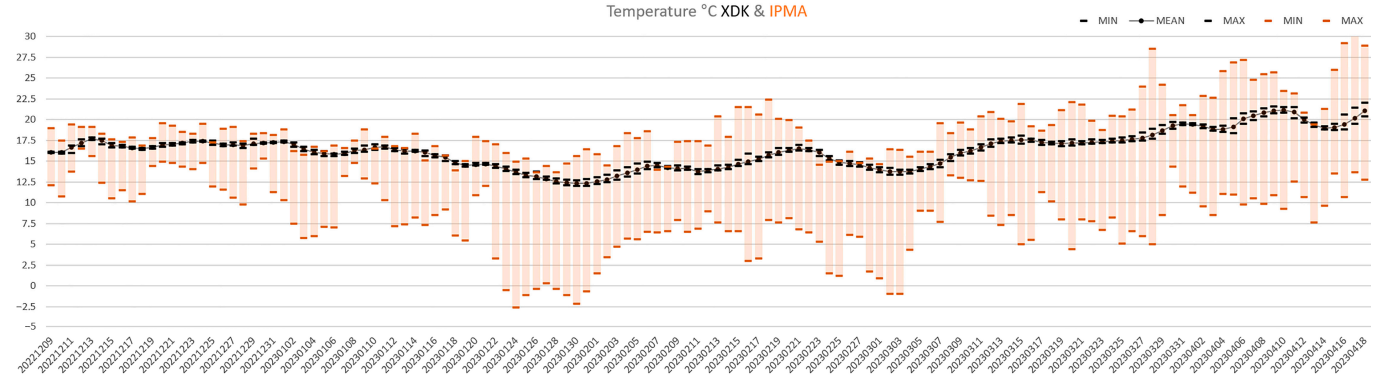


**Figure 14.** Continuous monitoring data (for four months) of temperature in °C XDK in black (mean, max and min by day) and IPMA day temperature in °C max and min values for Sintra.

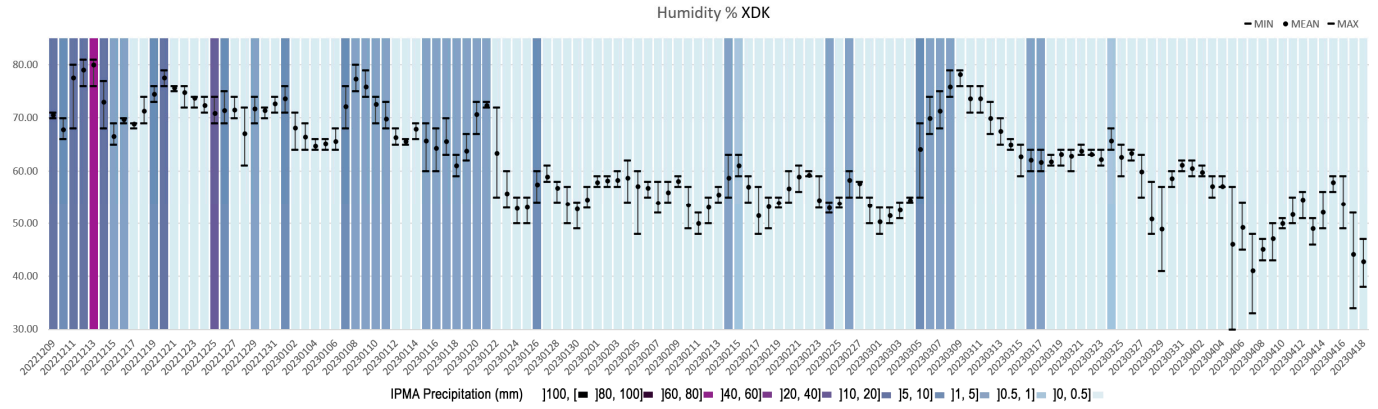


**Figure 15.** Continuous monitoring data (for four months) of humidity in % XDK in black (mean, max and min by day) and rainfall from Sintra IPMA.

## 4. Results and Discussion

In this paper, a first approach for a BIM-based model for structural health monitoring was presented, with the central body of the Palace of Monserrate selected as the case study due to the palace's status as a UNESCO World Heritage building since 1995. To support the definition of a BIM-based solution for real-time structural monitoring of the case study, two models were developed: a geometric one and a numerical one.

Particularly, in the case of old heritage buildings where the lack of geometric and non-geometric information is very frequent, the use of historical data can be a valuable source of information regarding the geometric and constructive changes to which the building was subject throughout its existence.

Concerns relative to an accurate geometric representation led to the acquisition of geometric and physical data relating to the construction system and ambient vibrations. Among them, a topographic survey made it possible to obtain the real coordinates of the palace and a survey using TLS technology, which, after data processing, allowed us to obtain the representative point cloud of the palace that later served as the basis for the H-BIM modeling in Autodesk Revit software. GPR surveys were also conducted to characterize the structure better, as semi-destructive or destructive techniques could not be used due to the historical value of the site.

The capacity to acquire real-time information on a structure's vibrations, both during normal operation and after an extraordinary occurrence, can allow for the application of more effective maintenance and repair practices, resulting in lower operating costs. This paper presented an IoT system for real-time monitoring data shared over the Microsoft Azure® platform. In the future, the suggested system could monitor a structure's health by analyzing, periodically or just after an extraordinary occurrence, its dynamic characteristics, including tracking the evolution of modal characteristics such as fundamental frequencies. During the study, the system worked continuously on the third floor of the central tower of the Monserrate's Palace in Sintra, and the data gathered were recorded in the H-BIM model, which could allow for further studies to best manage the heritage building regarding conservation concerns of the structural health status of the monitored building. It is worth mentioning that the implemented sensor was a low-cost MeM, which, in this work, was proven to be reliable in obtaining the vibrations of the structure and defining its dynamic characteristics when the monitoring period replicated the structure's modal characteristics. Due to limitations with the server platform that hosted the data, 3 min (average of the 1 s measures) was the lowest possible measurement report available. Although the data did not allow for a dynamic characterization, the monitoring was conducted to evaluate if even with this lower sampling any conclusions on the structure could be extracted, which was corroborated when the intervention on the roof for maintenance was noted in the surveyed data.

Despite the challenges in the construction of the H-BIM model, its implementation showed several advantages, such as being a central database on which geometric and non-graphic information regarding each BIM element was stored. As such, generic models representing the used surveyed equipment were added to the corresponding surveyed position on the model and through a new parameter on which the data files could be accessed. For the specific case of the generic model representing continuous monitoring, a parameter was created that connected to the Azure platform's URL for the obtainment of real-time data, another parameter that connected to previously observed values and a third parameter that reported a value in the model that summarized the last day in the records. This last connection was achieved by using the DiRoots® plug-in for Autodesk Revit®, which needed to be selected upon opening the model, through which a VBA script enabled the data stored in an Excel spreadsheet to be called into the H-BIM model. Based on the H-BIM, a numerical model was developed with 3Muri software and calibrated based on the in situ test results.

The H-BIM capacity to store real-time information on a structure's vibration, together with a calibrated numerical model, could be a valuable support for the quick structural health assessment in a general framework of decision-making processes regarding the safety evaluation of the palace post an extraordinary event, such as a post-earthquake emergency scenario. This model was ready to analyze and assess the structural health and damage of the central tower of the palace due to the occurrence of extraordinary events, such as an earthquake. Moreover, it can be easily changed if some structural elements are damaged or collapse due to external actions. In the rigorous context of heritage, a general framework was established (the assessment of the dynamic behavior, details concerning

the installation and configuration of the low-cost sensor and its subsequent calibration) that could be replicated in a similar context.

## 5. Final Comments

In the near future, an extended WSN is intended to be implemented with a permanent sensor layout of the central body of the palace represented in Figure 16; this layout would include a sensor at the base of the building, measuring the ground motion, whereas the other sensors would be fixed directly onto the structure, measuring the continuum of its vibrations, as well as the temperature and humidity. If an earthquake were to occur, the monitoring system would be able to register the seismic action and the seismic response.

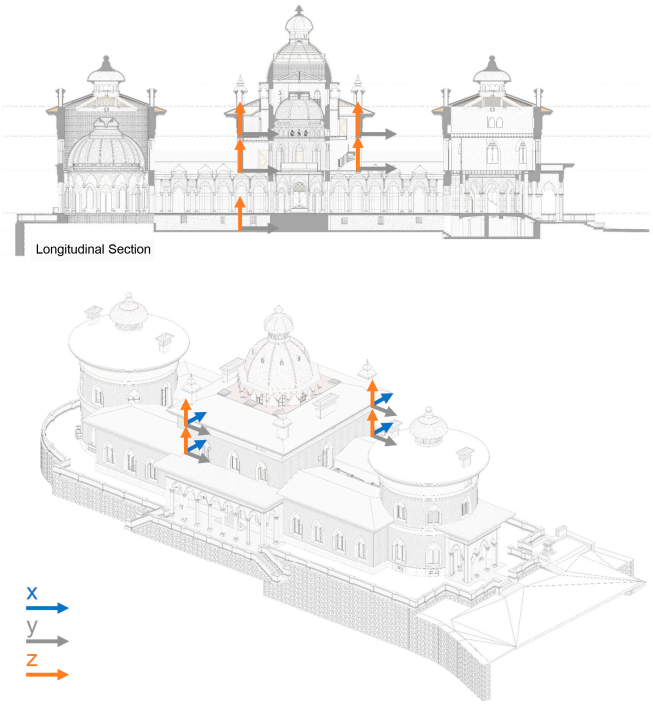


**Figure 16.** Future WSN layout of the central tower.

The final goal of this research work, which started in 2021, was to define a BIM-based solution that enabled real-time structural health monitoring based on a wireless low-cost sensor network of the whole palace.

**Author Contributions:** Conceptualization, A.P.F.; Methodology, R.M. and R.B.; Software, R.M., M.N. and M.P.; Validation, R.M.; Investigation, R.M., M.P. and A.P.F.; Writing—original draft, R.M. and M.N.; Writing—review & editing, A.P.F. and R.B.; Supervision, A.P.F. and R.B. All authors have read and agreed to the published version of the manuscript.

**Funding:** The first and third authors would like to acknowledge the financial support of the Portuguese Foundation for Science and Technology (the Ministry of Science and Technology of the Republic of Portugal) through a PhD scholarship (grant numbers 2020.09705.BD and SFRH/BD/145571/2019).

**Institutional Review Board Statement:** Not applicable.

**Informed Consent Statement:** Not applicable.

**Data Availability Statement:** Data may become available upon substantiated request.

**Acknowledgments:** The authors thank the company Parques de Sintra, Monte da Lua S. A., for supporting this research. We also thank the reviewers for their thorough reviews and comments.

**Conflicts of Interest:** The authors declare no conflict of interest.

## References


1. Bento, R. An Interdisciplinary Approach to the Seismic Assessment of Built Cultural Heritage: Case Studies in Lisbon and Outskirts. In *Structural Analysis of Historical Constructions*; Aguilar, R., Torrealva, D., Moreira, S., Pando, M.A., Ramos, L.F., Eds.; RILEM Bookseries; Springer: Berlin/Heidelberg, Germany, 2019; Volume 18, pp. 3–18. [CrossRef]
2. Masciotta, M.G.; Roque, J.C.A.; Ramos, L.F.; Lourenço, P.B. A multidisciplinary approach to assess the health state of heritage structures: The case study of the Church of Monastery of Jerónimos in Lisbon. *Constr. Build. Mater.* **2016**, *116*, 169–187. [CrossRef]
3. Zrinjski, M.; Tupek, A.; Barković, Đ.; Polović, A. Industrial masonry chimney geometry analysis: A total station based evaluation of the unmanned aerial system photogrammetry approach. *Sensors* **2021**, *21*, 6265. [CrossRef] [PubMed]
4. Lingua, A.; Piumatti, P.; Rinaudo, F. Digital photogrammetry: A standard approach to cultural heritage survey. *Int. Arch. Photogramm. Remote Sens. Spat. Inf. Sci.* **2003**, *34*, 210–215.
5. Silva, A.; Bento, R. Uma abordagem multidisciplinar para a avaliação sísmica do Edifício dos Brasões, Palácio Nacional de Sintra. *Rev. Port. Eng. Estrut.* **2020**, *Série III*, 97–110.
6. Godinho, M.; Machete, R.; Ponte, M.; Falcão, A.P.; Gonçalves, A.B.; Bento, R. BIM as a resource in heritage management: An application for the National Palace of Sintra, Portugal. *J. Cult. Herit* **2020**, *43*, 153–162. [CrossRef]
7. Ponte, M.; Bento, R.; Vaz, S.D. A Multi-Disciplinary Approach to the Seismic Assessment of the National Palace of Sintra. *Int. J. Archit. Herit.* **2021**, *15*, 757–778. [CrossRef]
8. Oliveira, C.S.; Navarro, M. Fundamental periods of vibration of RC buildings in Portugal from in-situ experimental and numerical techniques. *Bull. Earthq. Eng.* **2010**, *8*, 609–642. [CrossRef]
9. Roia, D.; Gara, F.; Balducci, A.; Dezi, L. Ambient vibration tests on a reinforced concrete school building before and after retrofitting works with external steel "dissipative towers". In Proceedings of the 9th International Conference on Structural Dynamics, EURODYN 2014, Porto, Portugal, 30 June–2 July 2014; pp. 2509–2516.
10. Pierleoni, P.; Conti, M.; Belli, A.; Palma, L.; Incipini, L.; Sabbatini, L.; Valenti, S.; Mercuri, M.; Concetti, R. IoT Solution based on MQTT Protocol for Real-Time Building Monitoring. In Proceedings of the IEEE 23rd International Symposium on Consumer Technologies (ISCT), Ancona, Italy, 19–21 June 2019; pp. 57–62.
11. Biagini, C.; Capone, P.; Donato, V.; Facchini, N. Towards the BIM implementation for historical building restoration sites. *Autom Constr* **2016**, *71*, 74–86. [CrossRef]
12. Brumana, R.; Della Torre, S.; Previtali, M.; Barazzetti, L.; Cantini, L.; Oreni, D.; Banfi, F. Generative HBIM modelling to embody complexity (LOD, LOG, LOA, LOI): Surveying, preservation, site intervention—The Basilica di Collemaggio (L'Aquila). *Appl. Geomat.* **2018**, *10*, 545–567. [CrossRef]
13. Barazzetti, L.; Banfi, F.; Brumana, R.; Gusmeroli, G.; Previtali, M.; Schiantarelli, G. Cloud-to-BIM-to-FEM: Structural simulation with accurate historic BIM from laser scans. *Simul Model. Pract. Theory* **2015**, *57*, 71–87. [CrossRef]
14. Brumana, R.; Oreni, D.; Barazzetti, L.; Cuca, B.; Previtali, M.; Banfi, F. Survey and scan to BIM model for the knowledge of built heritage and the management of conservation activities. In *Digital Transformation of the Design, Construction and Management Processes of the Built Environment*; Springer: Berlin/Heidelberg, Germany, 2020; pp. 391–400. [CrossRef]
15. Machete, R.; Silva, J.R.; Bento, R.; Falcão, A.P.; Gonçalves, A.B.; de Carvalho, J.M.L.; Silva, D.V. Information transfer between two heritage BIMs for reconstruction support and facility management: The case study of the Chalet of the Countess of Edla, Sintra, Portugal. *J. Cult. Herit* **2021**, *49*, 94–105. [CrossRef]
16. Moreno-Gomez, A.; Perez-Ramirez, C.A.; Dominguez-Gonzalez, A.; Valtierra-Rodriguez, M.; Chavez-Alegria, O.; Amezquita-Sanchez, J.P. Sensors Used in Structural Health Monitoring. *Arch. Comput. Methods Eng.* **2018**, *25*, 901–918. [CrossRef]
17. Zhu, L.; Fu, Y.; Chow, R.; Spencer, B.F.; Park, J.W.; Mechitov, K. Development of a high-sensitivity wireless accelerometer for structural health monitoring. *Sensors* **2018**, *18*, 262. [CrossRef] [PubMed]
18. Collette, C.; Carmona-Fernandez, P.; Janssens, S.; Artoos, K.; Guinchard, M.; Hauviller, C. *Review of Sensors for Low Frequency Seismic Vibration Measurement*; CERN-ATS-Note-2011-001 TECH 2011; CERN: Geneva, Switzerland, 2011.
19. Mobaraki, B.; Lozano-Galant, F.; Soriano, R.P.; Pascual, F.J.C. Application of low-cost sensors for building monitoring: A systematic literature review. *Buildings* **2021**, *11*, 336. [CrossRef]
20. Komarizadehasl, S.; Mobaraki, B.; Lozano-Galant, J.A.; Turmo, J. Detailed Evaluation of Low-Cost Ranging Sensors for Structural Health Monitoring Applications. In Proceedings of the Recent Trends in Construction Engineering and Education RTCEE International Conference, Online, 10–11 September 2020; pp. 10–11.
21. Komarizadehasl, S.; Mobaraki, B.; Ma, H.; Lozano-Galant, J.A.; Turmo, J. Development of a low-cost system for the accurate measurement of structural vibrations. *Sensors* **2021**, *21*, 6191. [CrossRef] [PubMed]
22. Komarizadehasl, S.; Komary, M.; Alahmad, A.; Lozano-Galant, J.A.; Ramos, G.; Turmo, J. A Novel Wireless Low-Cost Inclinometer Made from Combining the Measurements of Multiple MEMS Gyroscopes and Accelerometers. *Sensors* **2022**, *22*, 5605. [CrossRef]
23. Casillo, M.; Guida, C.G.; Lombardi, M.; Lorusso, A.; Marongiu, F.; Santaniello, D. Predictive preservation of historic buildings through IoT-based system. In Proceedings of the MELECON 2022—IEEE 21st Mediterranean Electrotechnical Conference, Palermo, Italy, 14–16 June 2022; pp. 1194–1198. [CrossRef]
24. Chianese, A.; Piccialli, F. Designing a smart museum: When cultural heritage joins IoT. In Proceedings of the 2014 8th International Conference on Next Generation Mobile Applications, Services and Technologies, NGMAST 2014, Oxford, UK, 10–12 September 2014; pp. 300–306. [CrossRef]

25. Amato, F.; Chianese, A.; Mazzeo, A.; Moscato, V.; Picariello, A.; Piccialli, F. The talking museum project. *Procedia Comput. Sci.* **2013**, *21*, 114–121. [CrossRef]
26. Valinejadshoubi, M.; Moselhi, O.; Bagchi, A. Integrating BIM into sensor-based facilities management operations. *J. Facil. Manag.* **2022**, *20*, 385–400. [CrossRef]
27. Mataloto, B.; Mendes, H.; Ferreira, J.C. Things2people interaction toward energy savings in shared spaces using BIM. *Appl. Sci.* **2020**, *10*, 5709. [CrossRef]
28. Mataloto, B.; Ferreira, J.C.; Resende, R.; Moura, R.; Luís, S. Bim in *people2people* and *things2people* interactive process. *Sensors* **2020**, *20*, 2982. [CrossRef]
29. Kim, S.; Frangopol, D.M. Optimal planning of structural performance monitoring based on reliability importance assessment. *Probabilistic Eng. Mech.* **2010**, *25*, 86–98. [CrossRef]
30. Gentile, C.; Ruccolo, A.; Canali, F. Long-term monitoring for the condition-based structural maintenance of the Milan Cathedral. *Constr Build. Mater.* **2019**, *228*, 117101. [CrossRef]
31. Li, X.; Xie, L.; Lu, W.; Xue, S.; Hong, C.; Lan, W.; Shi, Q. Structural health monitoring of a historic building during uplifting process: System design and data analysis. *Struct. Health Monit.* **2023**. [CrossRef]
32. Mondal, T.G.; Jahanshahi, M.R. Applications of computer vision-based structural health monitoring and condition assessment in future smart cities. In *The Rise of Smart Cities: Advanced Structural Sensing and Monitoring Systems*; Elsevier: Amsterdam, The Netherlands, 2022; pp. 193–221. [CrossRef]
33. Mondal, T.G.; Jahanshahi, M.R. Modelling and forecasting of SHM strain measurement for a large-scale suspension bridge during typhoon events using variational heteroscedastic Gaussian process. *Eng. Struct* **2022**, *251*, 113554. [CrossRef]
34. Wang, Q.-A.; Wang, C.-B.; Ma, Z.-G.; Chen, W.; Ni, Y.-Q.; Wang, C.-F.; Yan, B.G.; Guan, P.X. Bayesian dynamic linear model framework for structural health monitoring data forecasting and missing data imputation during typhoon events. *Struct. Health Monit.* **2022**, *21*, 2933–2950. [CrossRef]
35. S.T.A. DATA. *3Muri*, V13201; S.T.A. DATA: Turin, Italy, 2022.
36. Neto, M.J. *Monserrate A Casa Romântica de Uma Família Inglesa*; Caleidoscópio: Lisboa, Portugal, 2015.
37. Autodesk. *Recap Pro*, V230; Autodesk: San Francisco, CA, USA, 2023.
38. Morph. Campanha de Prospecção Geofísica. 2011. Available online: https://morph.pt/Campanha-de-Prospeccao-Geofisica/ (accessed on 12 June 2023).
39. Structural Vibration Solutions (SVIBS). *ARTeMIS Modal Pro*, Version 7215; SVIBS: Aalborg, Denmark, 2022.
40. Autodesk. *Revit 2023*, Version 2023; Autodesk: San Francisco, CA, USA, 2023.
41. Lagomarsino, S.; Penna, A.; Galasco, A.; Cattari, S. TREMURI program: An equivalent frame model for the nonlinear seismic analysis of masonry buildings. *Eng. Struct* **2013**, *56*, 1787–1799. [CrossRef]
42. Autodesk. *Autocad 2022*, Version 2022; Autodesk: San Francisco, CA, USA, 2022.
43. Candeias, P.; Correia, A.; Costa, A.; Catarino, J.; Pipa, M.; Cruz, H.; Carvalho, E.; Costa, A. Aspetos gerais da aplicação em Portugal do Eurocódigo 8—Parte 3—Anexo C (Informativo)—Edifícios de alvenaria. *Rev. Port. Eng. Estrut.* **2020**, *Série III*, 99–120.
44. Alarcón, M.; Soto, P.; Hernández, F.; Guindos, P. Structural health monitoring of South America's first 6-Story experimental light-frame timber-building by using a low-cost RaspberryShake seismic instrumentation. *Eng. Struct* **2023**, *275*, 115278. [CrossRef]
45. Sivori, D.; Cattari, S.; Lepidi, M. A methodological framework to relate the earthquake-induced frequency reduction to structural damage in masonry buildings. *Bull. Earthq. Eng.* **2022**, *20*, 4603–4638. [CrossRef]

buildings

MDPI

*Article*

# Evaluation of Vibration Detection Using Smartphones in a Two-Story Masonry-Infilled RC Frame Building

**Jae-Do Kang [1,*], Eun-Rim Baek [2] and Sung-Ho Park [1]**

[1] Division of Urban Infrastructure Research, Seoul Institute of Technology, Seoul 03909, Republic of Korea
[2] Seismic Research and Test Center, Pusan National University, Busan 50612, Republic of Korea
* Correspondence: kang@sit.re.kr

**Abstract:** For measuring the structural health of buildings, high-performance vibration detection devices are used in a structural health monitoring (SHM) system, which consists of a sensor and a data logger. Those devices are seismographs or devices with high-performance sensors which are expensive. Recently, smartphones are being used as seismographs to accumulate big data of earthquake wave detection because they have accelerometers of microelectromechanical systems. Since a smartphone has the functions of a detection sensor and a data logger, a low-cost SHM system can be developed by using a low-cost smartphone. In this paper, smartphones were used to confirm the possibility of the development of a low-cost SHM system. To evaluate the vibration detection performance from small displacement and large displacement, smartphones were installed in a specimen of a large shaking table test. The specimen is a scale model of a two-story non-reinforced masonry-filled reinforce concrete (RC) frame building. The natural period and interstory drift ratio were used as the evaluation criteria. The natural period estimated by the smartphone data agreed with that found by the piezoelectric accelerometer data. For estimating the building deformation, which is related to building stability, the measurement performance for large deformation using smartphones was evaluated. The smartphones have 90% or higher accuracies for the estimation of the maximum acceleration and displacement.

**Keywords:** iOS smartphones; i-Jishin; acceleration detection; structural health monitoring; MEMS sensor



**Citation:** Kang, J.-D.; Baek, E.-R.; Park, S.-H. Evaluation of Vibration Detection Using Smartphones in a Two-Story Masonry-Infilled RC Frame Building. *Buildings* **2023**, *13*, 1069. https://doi.org/10.3390/buildings13041069

Academic Editors: Serena Cattari, Ilaria Venanzi and Philippe Gueguen

Received: 13 March 2023
Revised: 3 April 2023
Accepted: 16 April 2023
Published: 18 April 2023



## 1. Introduction

In Japan, with the aim of detecting strong vibrations due to earthquakes, strong-motion accelerographs, termed Strong Motion Acceleration Committee (SMAC) accelerographs, were developed after the 1948 Fukui earthquake. SMAC accelerographs found application in the detection of building vibrations in Japan in the 1950s. The Japan Building Research Institute (BRI) installed SMAC accelerographs in approximately ten buildings [1,2]. In Niigata City, SMAC accelerographs recorded the collapse of a building caused by soil liquefaction during the 1964 Niigata earthquake [2,3]. In 1973, the National Strong Motion Project (NSMP) in the U.S. was absorbed by the U.S. Geological Survey as part of the National Earthquake Hazards Reduction Program for acquiring strong motion records [4]. At this time, the idea was to monitor building vibrations for recordings of damaging earthquakes, which are critical for designing earthquake-resistant structures. The data recorded in the U.S. and Japan were used for evaluations of structural response and correlated performance [5]. In Europe, the earthquake detection network systems have operated to record and analyze earthquake waveforms and to provide high-quality data, for example, ref. [6,7]. Richardson [8] developed technology for damage detection in structures caused by changes in their dynamic (modal) properties. This study focused on structural integrity monitoring for large structures. With the development of devices and technologies, in 1996, Doebling et al. [9] provided a comprehensive review of the technical literature on the detection, location, and characterization of structural damage. The damage caused by

fatigue and external loads (e.g., earthquakes and winds), may progress very slowly [10]. The damage becomes observable only when the structural damage is considerable. Using changes in the measured structural vibration response, the techniques examined in this report [9] estimated the structural damage. This is similar to structural health monitoring (SHM), which aims to estimate the behavior and performance of structures during their life cycle and predict their remaining service life. In SHM, the knowledge and experience in civil, mechanical, electrical, computer, and control engineering are used in assessing the health of structures [11]. In the past three decades, many researchers have worked on SHM [12–16]. Based on the acting load, there are two kinds of SHM methods, static and vibration based [11,17,18]. By measuring the static responses of structures such as strain [19,20] and deflection [21], static-based damage detection methods estimate the health of structures. Vibration-based damage detection methods primarily assess the modal parameters of a structure using system identification methods [22]. In applications using vibration-based damage detection methods, the estimation accuracy depends on the performance of the vibration measurement sensors, the improvement of which requires knowledge and experience in mechanical, electrical, and computer engineering. For detection of earthquake events, some countries have operated seismic stations, for example, [23–26]. Seismographs, which are used as one of the devices at seismic stations, can conduct high-performance vibration measurements. Therefore, seismographs or devices with improved technology [27,28], such as P-wave alert devices (P-Alert) and IT strong-motion accelerographs, are used to detect structural vibrations. P-Alert was developed by a research group at the National Taiwan University for use in earthquake early warning (EEW) systems. P-Alert uses accelerometers of microelectromechanical systems (MEMS). MEMS accelerometers have been tested and applied in detecting vibrations of infrastructure, buildings, and the ground [29–35]. They are also installed in smartphones. Therefore, smartphones have been investigated as a substitute for seismometers [36,37]. The "MyShake" app was developed as an EEW system and uses a classifier algorithm to identify earthquake vibrations on a single phone [36]. Further, the "i-Jishin" app was developed for measuring earthquakes by the National Research Institute for Earth Science and Disaster Resilience of Japan; it makes use of MEMS acceleration sensors incorporated in the mobile information terminals. The measurement settings of the "i-Jishin" app can be modified in terms of the sampling rate, leading allowance time, following allowance time, and trigger to record, and can calculate the velocity and displacement from acceleration [37]. Since a smartphone has the functions of a detection sensor and a data logger, a low-cost SHM system can be developed when using a low-cost smartphone. For developing the low-cost SHM system, the measurement settings of another app, the "accmeasure" app, can also be modified in terms of the sampling rate, leading allowance time, following allowance time, and trigger to record [38]. The two aforementioned apps may be used in SHM because they feature functionalities such as trigger to record and a sampling rate of 100 Hz, setting record time, and time synchronization; their use has been investigated for SHM [38,39]. To estimate the structural health, some researchers used smartphones [40–45]. These can almost estimate the detection performance of the small accretion of small displacement. In architectural engineering, large deformation, such as interstory drift, should be detected. However, the "i-Jishin" app was not evaluated for the estimation of interstory drift. Therefore, the measurement performance of the smartphone for large deformation of a structure close to the full scale should be evaluated.

Given the above, the objective of this study is to evaluate the vibration detection performance of a smartphone with the "i-Jishin" app installed in estimating the large deformation of a building. In addition, the prediction performance of dynamic characteristics, such as the natural period, was also estimated. Those are achieved by comparing the data measured by a reference accelerometer, which is a piezoelectric accelerometer from the PCB Piezotronics Company, wire displacement sensors and a smartphone-installed specimen in shaking table experiments. The specimen is a two-story masonry-infilled RC frame building, which is the standard design of low-story school buildings or residential buildings in

Korea. For estimating large deformation of a building, the displacement calculated from the acceleration measured by the smartphone was compared with displacement of the building measured by the experiment. Additionally, the natural periods estimated by the transfer function of acceleration measured by the reference accelerometer and smartphone were compared.

## 2. Materials and Methods

### *2.1. Specimen Design*

The purpose of the shaking table test is to evaluate the seismic performance of existing buildings. To this end, a masonry-filled RC frame building, which is the standard design of school buildings and other commercial or residential buildings, was selected as a target. In this study, a specimen was designed based on a standard drawing of low-story school buildings or residential buildings in Korea. The specimen, which was an approximately 60% scale model of a school building, was a two-story non-reinforced masonry-filled RC frame building (Figure 1 and Table 1). Figure 1a shows the setup of the shake table test. As shown in Figure 1b, openings were installed at the front and rear of the specimen considering the actual building geometry. The specimen had a 3000 mm × 3000 mm square plane with a floor height of 1830 mm and a total height of 3780 mm (Figure 1c,d). The masonry infill wall on each floor had a length (L) of 2600 mm, height (H) of 1530 mm, an aspect ratio (H/L) of 0.59, and masonry wall thickness of 60 mm. Considering that the specimen was a scale model, the bricks were stacked in an upward direction; nevertheless, the thickness of the masonry infill wall was 57 mm. The concrete used for the frame of the specimen had a nominal compressive strength of 18 MPa, and SD400 (steel deformed bar with yield strength of 400 MPa) was used as a steel reinforcement. The size of the column was 200 × 200 mm. Four D13 (diameter of 13 mm) reinforcing bars were used as the main reinforcement, and the hoop used was a closed hoop with D6 (diameter of 6 mm) at 120 mm spacings. The size of the beam was 200 × 300 mm. Four D13 reinforcing bars were used as the main reinforcement, with two placed in the upper part and two in the lower part. The stirrup was a closed stirrup that used D6 at 120 mm spacings. The thickness of the slab was 120 mm, and D10 (diameter of 10 mm) was placed at 120 mm spacings as horizontal and vertical reinforcements. The first floor formed the shape of a T-beam, whereas the second floor used bolts to connect the slab and beams and facilitate the connection of load blocks on the second floor and roof. In addition, a weight of 96 kN was installed at the upper parts of the first and second floors, respectively, considering the axial load of the column and the upper load.

**Table 1.** Design of specimen.

| Item | Target Building | Specimen | Scaling Factor |
|---|---|---|---|
| Dimension (Depth × Width × Height), (unit: mm) | 7000 × 9000 × 3600 | 2800 × 3600 × 1800 | 0.6 (Height 0.5) |
| Story | 3 | 2 | - |
| Column (unit: mm) | 350 × 400 or 350 × 500 | 200 × 200 | 0.5~0.57 |
| Beam (unit: mm) | 300 × 600 or 300 × 450 | 200 × 300 | 0.33 |
| Shear force in longer direction | 240 kN | 37 kN | 0.15 |
| Shear force in shorter direction | 161 kN | 37 kN | 0.23 |
| Column axial force ratio | 0.13 | 0.17 | |
| Masonry wall thickness | 0.19 (1.0B) | 0.06 | 0.32 |

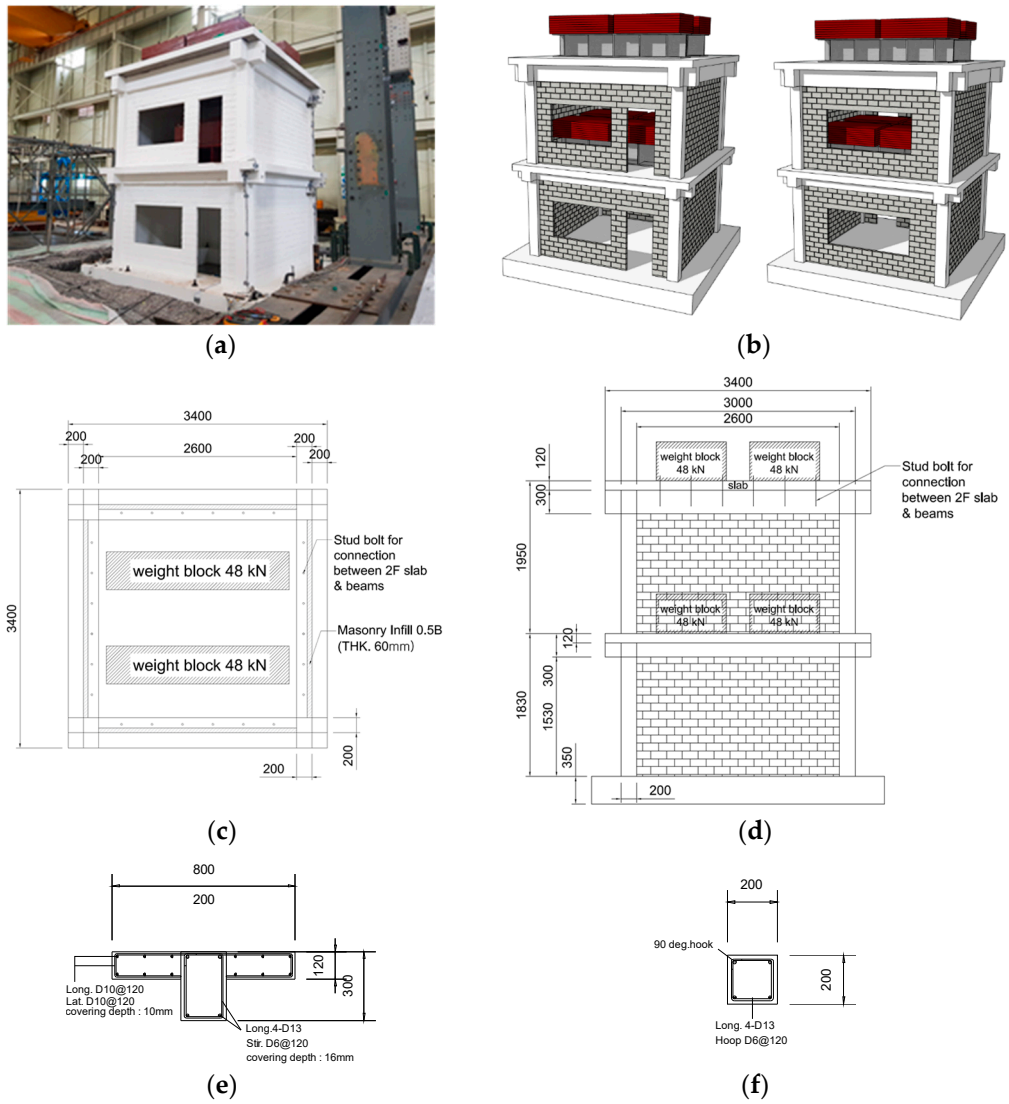


**Figure 1.** Configuration of specimen (unit: mm): (**a**) photo; (**b**) aerial view from the front (left) and the rear (right); (**c**) plan; (**d**) elevation; (**e**) beam and slab; (**f**) column.

### *2.2. Shaking Table Test*

The shaking table used in this study had three degrees of freedom and was installed in the Yangsan campus of Pusan National University. The size and specifications of the shaking table are shown in Table 2.

**Table 2.** Performance of shaking tables.

| Item | Performance |
|---|---|
| Max. loading (kg) | 60,000 |
| Table size (mm) | 5000 × 5000 |
| Control axes | 3 DOF (2 translational axes, 1 rotational axis) |
| Max. displacement (mm) | X-Axis = ±300, Y-Axis = ±200 |
| Max. velocity (m/s) | Hor. (X, Y) = 1.0 |
| Max. acceleration (g) | Hor. (X, Y) = ±3.0 (at bare table) |
| Frequency range (Hz) | (0.1–60.0) |
| Excitation mechanism | Electro-hydraulic Servo, 3-variable control |
| Control software | MTS 469D |
| Feedback data acquisition | 51 channels (Sampling rate = 512 Hz) |

In the resonance frequency search test to evaluate the natural period, which is the dynamic characteristic of a specimen, excitation was performed using white noise vibration waveforms in the forward/backward (Y) and left/right (X) directions. The zero-period acceleration (ZPA) of the excitation wave was set to an RMS average of 0.05 g, and the input frequency was set to range from 0.5 to 50.0 Hz, considering the characteristics of the shaking table and input waveform. The excitation duration was 30 s.

For the earthquake waveform in the shaking table test, an artificial earthquake wave that meets the designed seismic load of South Korea was generated and applied. The design acceleration spectrum used in the test was one that corresponds to seismic zone 1, S3 soil, and a short-period design spectral acceleration (SDS) of 0.54 g, which are suggested in the KDS 41 17 00 building seismic design standards (Figure 2a). For the input seismic wave, an artificial earthquake wave corresponding to a magnitude 7 earthquake, which meets the design acceleration spectrum, was created (Figure 2b). The acceleration and time interval were adjusted according to the similarity law (Table 1) considering that the specimen was a scaled model. The artificial seismic wave was applied after adjusting its scale to 30, 60, 100, and 150%. The detailed procedure of excitation is shown in Table 3.

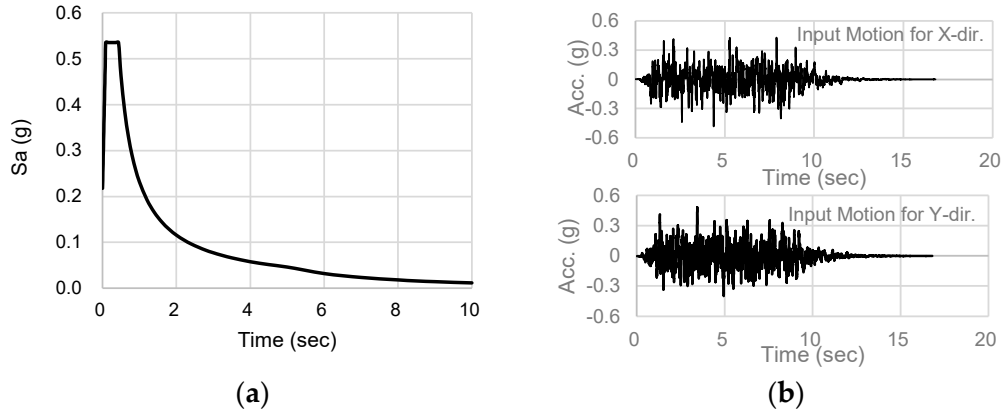


**Figure 2.** Artificial accelerograms: (**a**) design spectrum; (**b**) waveform.

**Table 3.** Test procedure and smartphone measurement.

| Test No. | Excitation | Direction | Scale (%) | Peak acc. (g) | Smartphone Error | | |
|---|---|---|---|---|---|---|---|
| | | | | | First Floor | Second Floor | Roof Floor |
| 1 | Random, 30 s | X | 100 | RMS 0.05 | - | - | - |
| 2 | Random, 30 s | Y | 100 | RMS 0.05 | - | - | - |
| 3 | Artificial accelerograms | XY | 30 | 0.14 | - | - | - |
| 4 | Artificial accelerograms | XY | 60 | 0.29 | - | Error | Error |
| 5 | Artificial accelerograms | XY | 100 | 0.48 | - | Error | Error |
| 6 | Artificial accelerograms | XY | 150 | 0.72 | - | Error | Error |

### *2.3. Measurement System*

To measure the seismic responses of the main parts of the specimen, accelerometers, displacement sensors, and strain gauges were installed at the main positions. A total of six accelerometers were installed at the main positions, including the floor of the shaking table, the base of the second floor, and the base of the roof floor, to measure the acceleration in the forward/backward and left/right directions on each floor. In addition, wire displacement sensors were installed at eight positions on the left and right sides of the first and second floor beams, on the right side and rear of the specimen, to measure the story drift in each direction. Eight displacement sensors were additionally installed in the upper right corner of the masonry infill walls, with no opening on the left and right sides of the specimen, to measure the gap between the frame and masonry infill wall in the horizontal

and vertical directions on each floor. Strain gauges were attached to the lower and upper parts of the first-floor column, the lower part of the second-floor column, and the left/right main reinforcement and stirrups of the first-floor beam before pouring concrete. Figure 3a shows the positions of the accelerometers and displacement sensors used in this study. Data were recorded at 512 Hz. The measured acceleration and displacement data, however, were resampled to 100 Hz for comparison with the smartphone data.

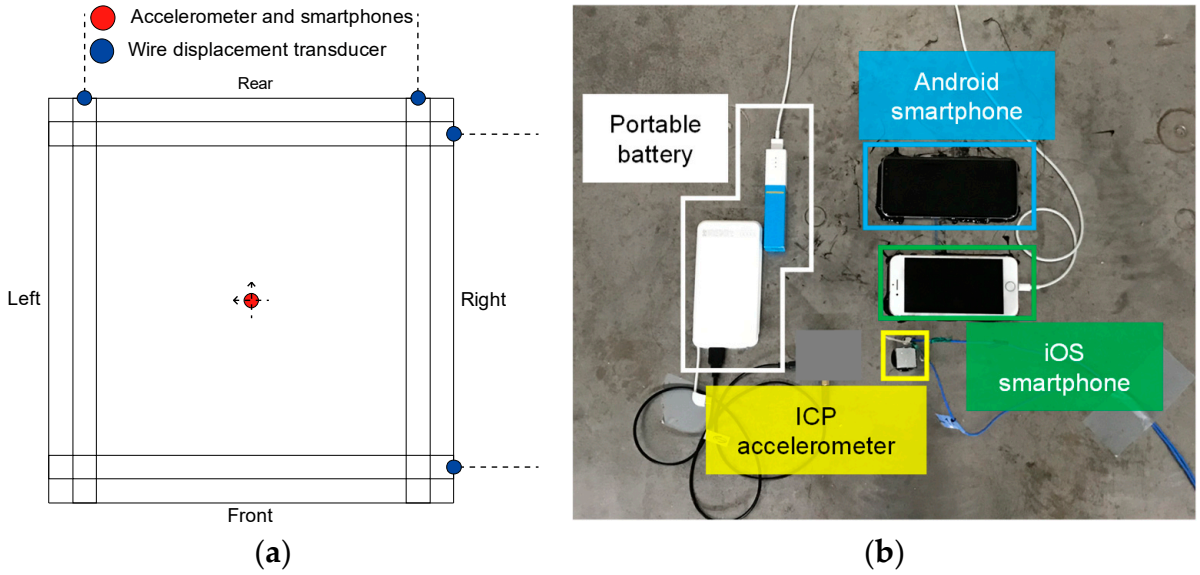


**Figure 3.** Installation of sensors: (**a**) sensor position; (**b**) smartphones.

### *2.4. Smartphone Measurement*

In an additional test, smartphones were installed at the center of the floor on each floor to evaluate their vibration measurement accuracy, and portable batteries were connected to them to prevent them from being turned off during the test (Figure 3b). Three iOS smartphones and three Android smartphones were used in the test. For vibration measurements, the "i-Jishin" app developed by the National Research Institute for Earth Science and Disaster Resilience in Japan [37] was installed in the iOS smartphones. On the other hand, in the Android smartphones, the vibration measurement test application developed by the research team of this study was installed. For the purpose of this study, only the results obtained using the iOS smartphones (iPhone 7, 8, and X) were used. A trigger was set such that vibrations over 10 cm/s$^2$ could be recorded when measured. In addition, the vibration measurement application was running at all times. The sampling rate of the application was set to 100 Hz. Since each smartphone performed measurements independently, all were connected to Wi-Fi for time synchronization with the NTP server. Although the i-Jishin application was equipped with the FFT transmission function, this function could not be used in this study due to the network environment.

## 3. Results and Discussion

### *3.1. Application Measurement Characteristics*

After the vibration test, the data measured by the i-Jishin application used in this study were analyzed. Table 3 shows that there is no measurement error in the data from the smartphone installed on the first floor. However, in the smartphone installed on the roof, the acceleration was not recorded in tests 4 to 6. This is because the smartphone used in these experiments had low battery capacity and the connected portable battery could not fully charge the phone due to its low capacity. This issue needs to be addressed in future tests. In the smartphone installed on the second floor, the acceleration was recorded in tests 4 to 6, but the data could not be used due to errors. It was found that the errors occurred as the brick separated from the wall, which impacted the smartphone during test 4. In future

tests, measures to prevent damage to smartphones are required. Although the smartphones were connected to Wi-Fi installed in the experimental building for time synchronization with the NTP server, synchronization could not be performed well due to the influence of the experimental building environment. Time synchronization was performed using the MATLAB algorithm (finddelay function) to analyze the measurement characteristics. This MATLAB algorithm estimates the normalized cross-correlation between two signals and estimates the lag based on the lag value for which the normalized cross-correlation has the highest absolute value [46]. In evaluating the vibration detection performance using data obtained from the white noise excitation tests, a 0.2–25 Hz band filter was applied to the acceleration measured with the reference accelerometers and smartphones.

### 3.2. Natural Period Evaluation

The natural period was estimated by calculating the transfer function of the acceleration measured at the center of each floor in the specimen and using the curve fitting technique. In this study, five Lorentzian curves (red dotted lines in Figure 4) having a high agreement with the transfer function (black solid lines in Figure 4) between 0 and 10 Hz were extracted. After then, the natural period (blue dotted lines in Figure 4) was estimated from the curve with the maximum value. Analysis of the data obtained from the reference accelerometer revealed that the natural period was 0.25 s in the X direction and 0.14 s in the Y direction (Figure 4). The natural period estimated with the smartphone measurements was identical to that estimated with the reference accelerometers (Figure 4). This implies that the natural period of a building can be evaluated using smartphones if vibration occurs with the same magnitude as in the white noise excitation test.

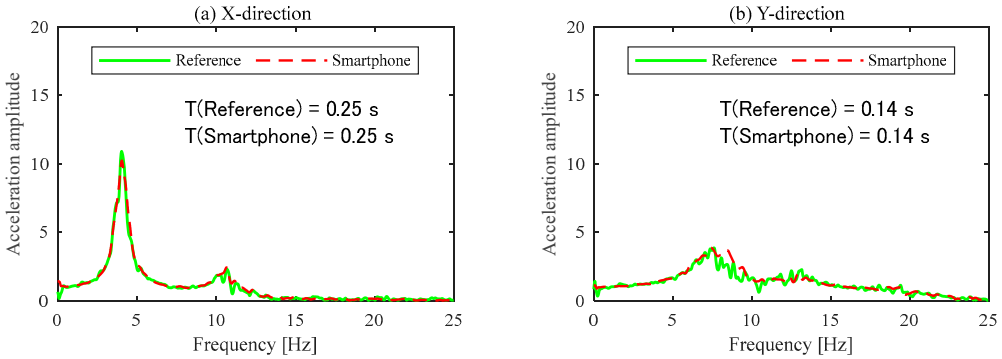


**Figure 4.** Estimated natural period.

### 3.3. Acceleration Measurement Accuracy

To quantitatively evaluate the error of the acceleration waveform measured by the smartphones, the root-mean-square percentage error (RMSPE) values between the measurements obtained with the reference accelerometers and smartphone in the time domain were evaluated using the magnitude-squared coherence function (MSCF) values of the same measurements in the frequency domain. The RMSPE was calculated as follows:

$$\mathrm{RMSPE} = \sqrt{\frac{1}{n}\sum_{k=1}^{n}\left(\frac{x_{smartphone} - x_{icp}}{x_{icp}}\right)^2}, \quad (1)$$

where $x_{icp}$ is the measured acceleration using the reference accelerometers and $x_{smartphone}$ is that using smartphones. For $a$ and $b$ signals, the MSCF [47,48] is defined as follows:

$$C_{ab} = {\gamma_{ab}}^2(f) = \frac{|G_{ab}(f)|^2}{G_{ab}(f)G_{ab}(f)}, \quad (2)$$

where $G_{aa}(f)$ and $G_{bb}(f)$ denote the power spectral density of $a$ and $b$ signals and $G_{ab}(f)$ denotes the cross spectral density of $a$ and $b$ signals. The MSCF is a function of the frequency, with values between 0 and 1. These values indicate how well the two signals correspond to each other at different frequencies. The greater the values, the stronger the correlation. Figures 5 and 6 compare the time series and MSCF between the acceleration measured from the reference accelerometers and smartphones.

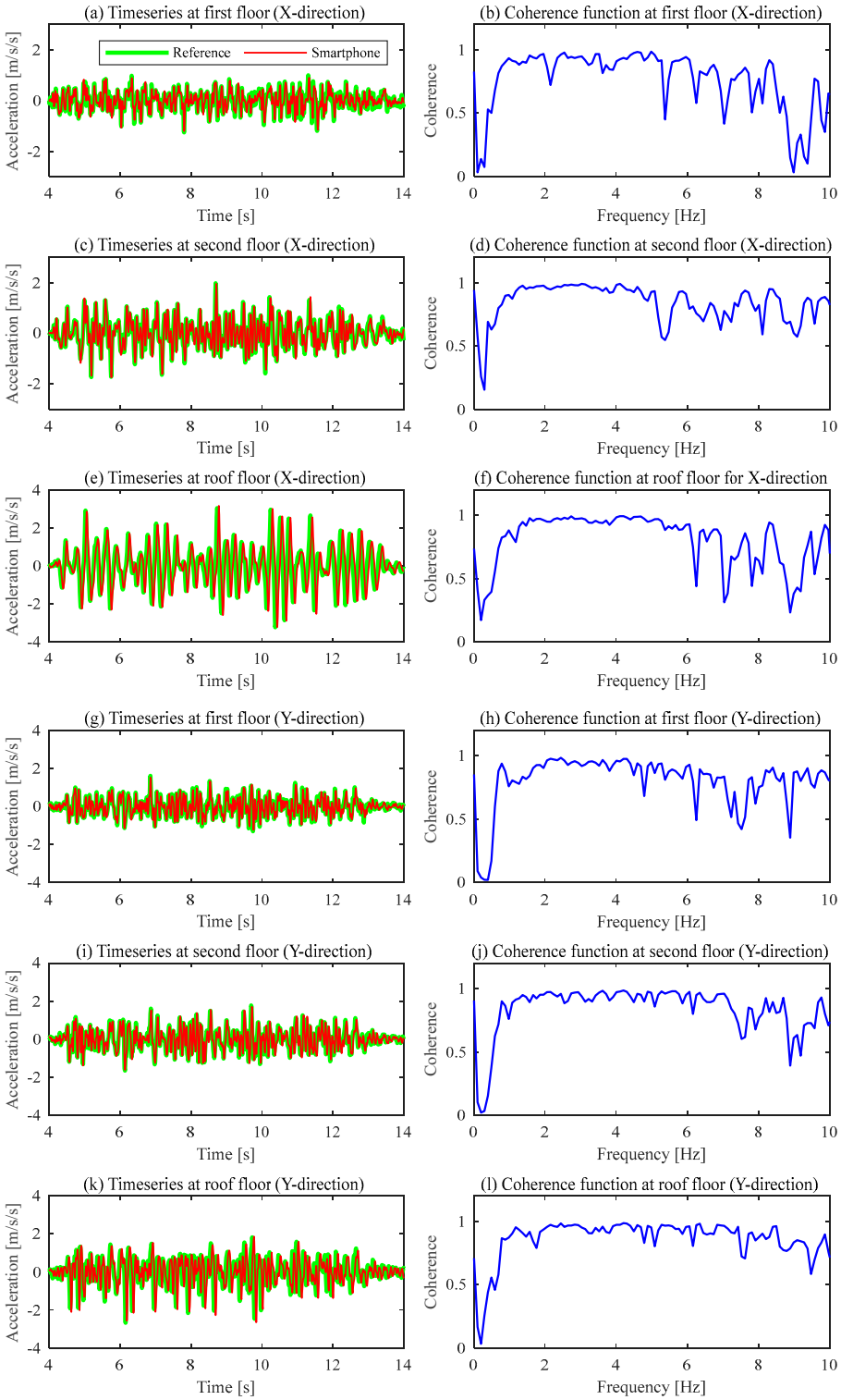


**Figure 5.** Comparison of time series between acceleration obtained from reference accelerometers and smartphones, and coherence for the X and Y directions in test 3.

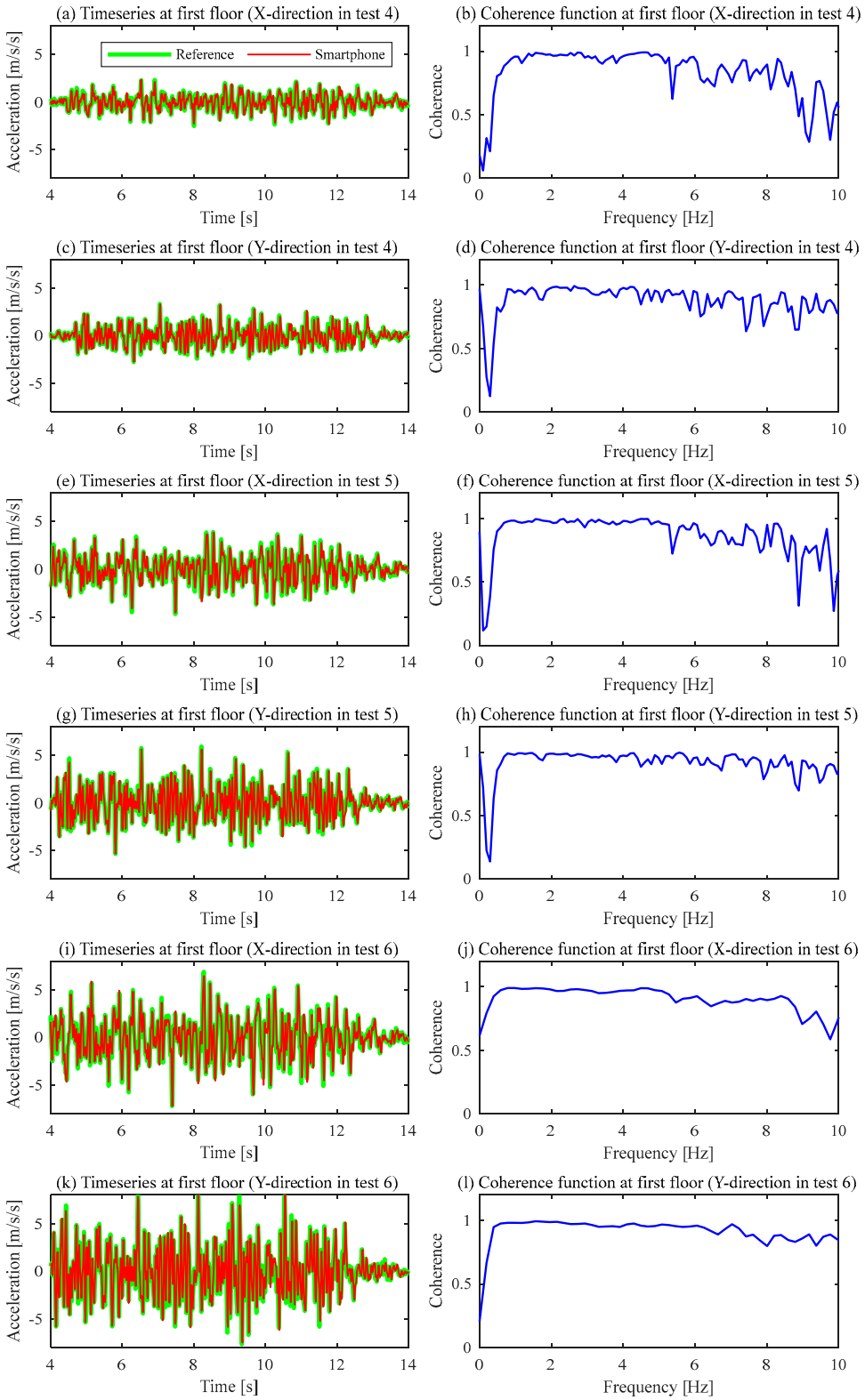


**Figure 6.** Comparison of time series between acceleration obtained from reference accelerometers and smartphones, and coherence for the X and Y directions in tests 4 to 6.

In Figure 5, the acceleration on each floor measured in test 3 was compared. The maximum accelerations measured with the reference accelerometers were 1.61 m/s$^2$ (Y direction) on the first floor, 1.97 cm/s$^2$ (X direction) on the second floor, and 3.22 cm/s$^2$ (X direction) on the third floor. On the other hand, the maximum accelerations measured

with the smartphones were 1.21 cm/s$^2$ (Y direction) on the first floor, 1.95 cm/s$^2$ (X direction) on the second floor, and 3.22 cm/s$^2$ (X direction) on the third floor. The ratio between the maximum acceleration values measured with the smartphones and reference accelerometers ranged from 95.8 to 99.9% in the X direction and from 95.8 to 99.9% in the Y direction. In other words, the maximum acceleration measured with iOS smartphones has an accuracy of 95% or higher. The RMSPE values ranged from 0.16 (X direction) to 0.19 (Y direction) on the first floor, from 0.22 (X direction) to 0.25 (Y direction) on the second floor, and from 0.57 (X direction) to 0.51 (Y direction) on the third floor. In other words, the RMSPE increased as the amplitude increased, but the accuracy can be considered to be high because the RMSPE is small. The MSCF in the X direction showed a tendency to decrease at 6 Hz or higher, but it can be considered that the two waveforms are in good agreement with each other because they are close to 1 and between 1 and 6 Hz. In particular, high agreement was observed in the Y direction on the third floor, where the amplitude was large.

In Figure 6, the acceleration on the first floor measured in tests 4 to 6 was compared. As in test 3 (Figure 5), high agreement was observed in the time series. The MSCF was also high in the Y direction. In test 6, in particular, it can be said that the accuracy is high, because the MSCF is close to 1 under 10 Hz. In tests 4 to 6, the ratio between the maximum acceleration values measured with the smartphones and reference accelerometers ranged from 92.6 to 100.1% in the X direction and from 91.0 to 98.9% in the Y direction, which are lower compared to test 3. The minimum and maximum RMSPE values were 0.23 (test 4) and 0.89 (test 6) in the X direction and 0.41 (test 4) and 1.18 (test 6) in the Y direction. In other words, as the amplitude increased, the RMSPE in the Y direction also increased. It is judged, however, that the smartphones used in this study can be employed for acceleration measurements because the RMSPE is small.

### *3.4. Displacement Estimation Accuracy*

When a structure experiences harmonic motion, the relation $d(t) = \frac{a(t)}{-\omega^2}$ is widely used to determine the displacement, $d(t)$, from the acceleration, $a(t)$. Here, $\omega$ is the angular frequency. The same relation was also used in this study, and the displacement was estimated after converting the acceleration data measured with the smartphones into the frequency domain through FFT. These estimated values were compared with the displacement of each floor obtained from the experiment. The experimental displacements on the second and roof floors were the average values obtained by two wire displacement sensors installed on slabs on these floors. The displacement on the first floor was recorded using the shaking table control system. Figures 7 and 8 compare the total displacement in test 3 and in tests 4 and 5, respectively. In the figures, the displacements are compared only in the time period between 4 and 10 s, when the displacement amplitudes were relatively large. In test 3 (Figure 7), the ratio between the maximum displacements measured with the wire displacement sensors and smartphones ranged from 95.8 to 99.9% in the X direction and from 94.8 to 99.1% in the Y direction. The RMSPE values ranged from 0.16 (X direction) to 0.19 (Y direction) on the first floor, from 0.14 (X direction) to 0.16 (Y direction) on the second floor, and from 0.16 (X direction) to 0.17 (Y direction) on the third floor. In tests 4 to 6 where the amplitude was large (Figure 8), the ratio between the maximum displacement values measured with the wire displacement sensors and smartphones ranged from 92.6% (test 4) to 100.1% (test 6) in the X direction and from 91.0% (test 6) to 98.9% (test 4) in the Y direction. The accuracy showed a tendency to increase as the amplitude increased in the X direction; however, the same tendency was not observed in the Y direction. The minimum and maximum RMSPE values were 0.23 (test 4) and 0.89 (test 6) in the X direction, and 0.41 (test 4) and 1.18 (test 6) in the Y direction, which were the same as the acceleration RMSPE values. In other words, when the displacement is estimated using smartphones, an accuracy of 90% or higher can be obtained, even though the accuracy differs depending on the axial direction of the smartphone.

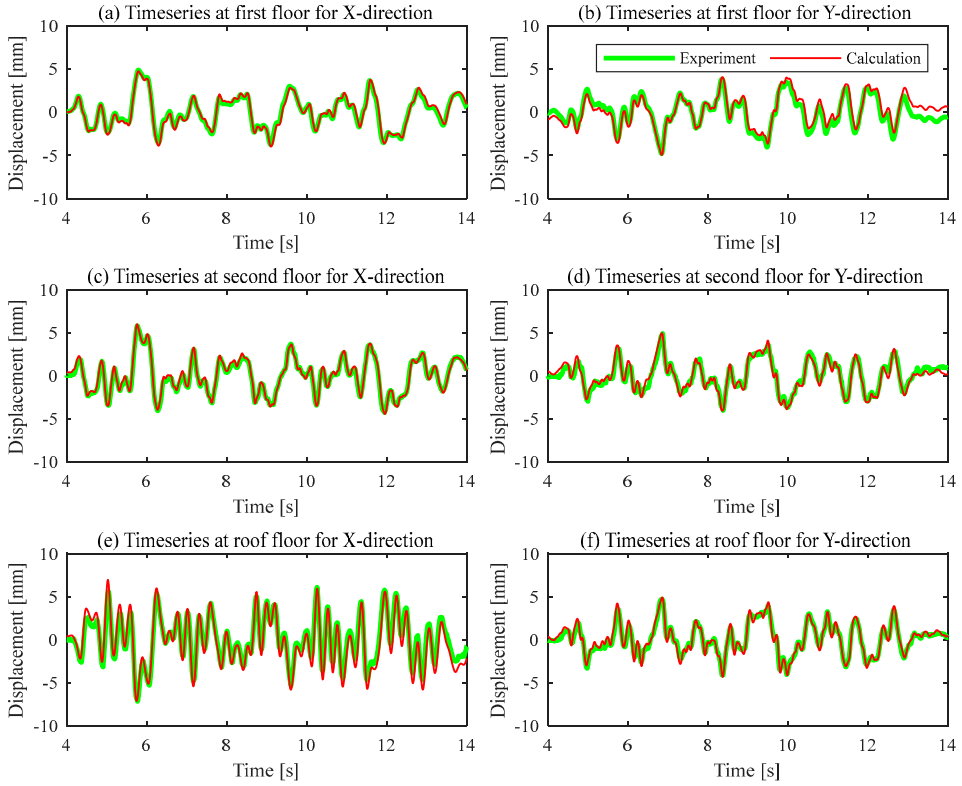


**Figure 7.** Comparison of displacements calculated by acceleration measured from reference accelerometers and smartphones along the X and Y directions in test 3.

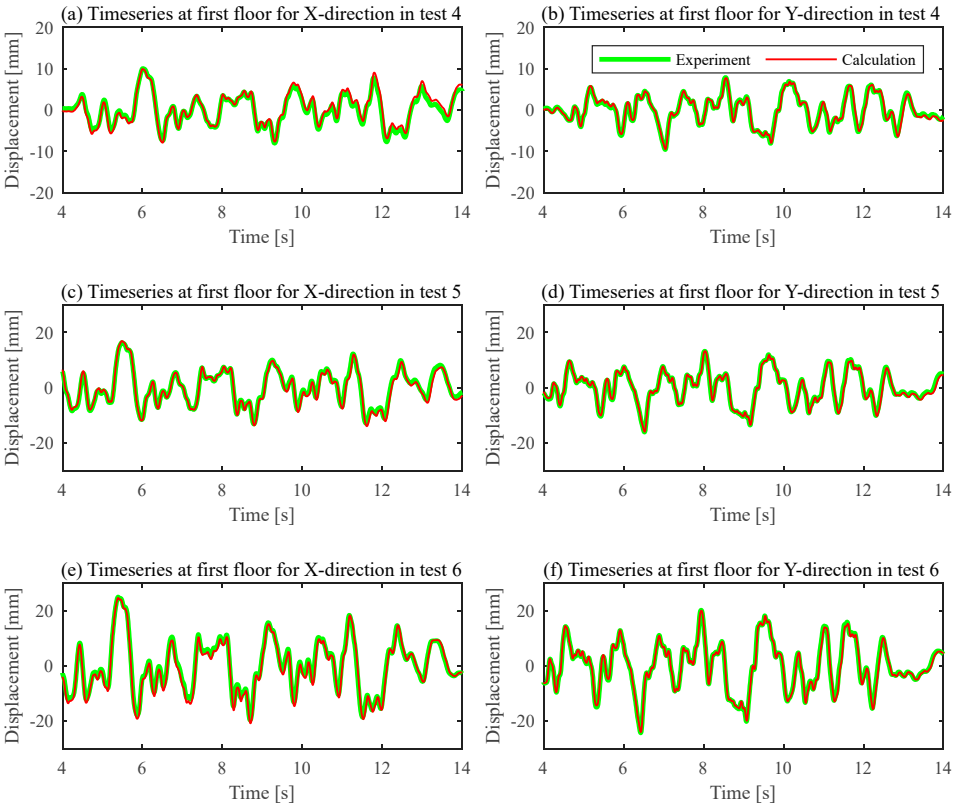


**Figure 8.** Comparison of displacements calculated using acceleration measured by reference accelerometers and smartphones along the X and Y directions in tests 4 to 6.

### *3.5. Estimation Accuracy of Interstory Drift Ratio (IDR)*

When the safety of a building is evaluated after an earthquake, the interstory drift ratio (IDR) is one of the main evaluation indicators. Since the final purpose of this study is to examine the applicability of smartphones in building safety evaluation, this study also compared the IDR estimated from smartphone data with that calculated from the displacement sensors. Figure 9 compares the IDR values for test 3. The ratios between the maximum IDR obtained from the wire displacement sensors and that calculated from the smartphone data ranged from 114% (1 story) to 100% (2 story) in the X direction and from 104% (1 story) to 99% (2 story) in the Y direction. On the first floor in the X direction and the second floor in the Y direction with low IDRs, there is a difference between the IDR obtained from the displacement sensors and that obtained from the smartphone data. On the second floor in the X direction and the first floor in the Y direction, where the IDR was 0.1% or higher, however, that obtained from the smartphone data was similar to that obtained from the displacement sensors. In other words, it is concluded that the accuracy of the IDR estimated from the smartphone data is low when IDR is less than 0.1%, which is considered as the elastic range in building design; nevertheless, the IDR can be sufficiently estimated using smartphones when the IDR is 0.1% or higher.

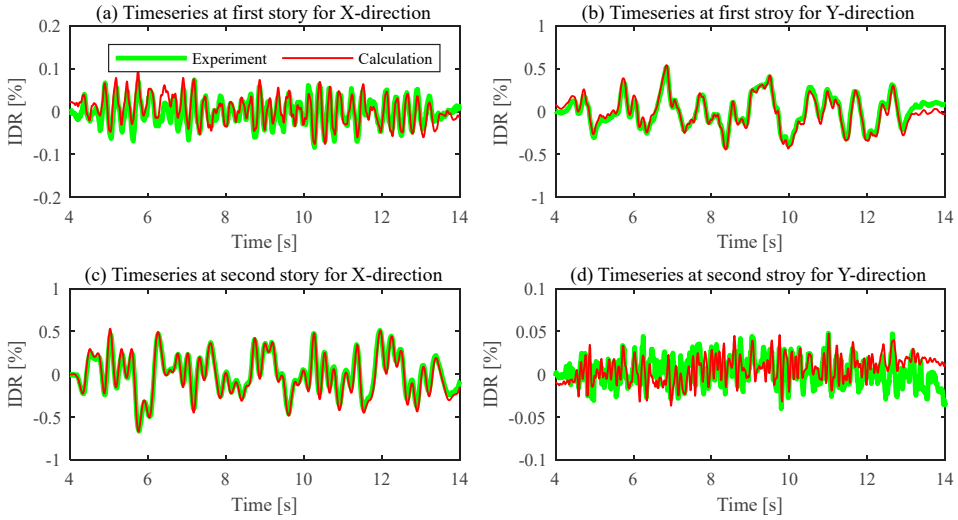


**Figure 9.** Comparison of interstory drift ratios (IDRs) estimated using accelerations measured by reference accelerometers and smartphones along the X and Y directions in test 3.

## 4. Conclusions

In this study, the applicability of smartphones to SHM, the prevalence of which is increasing worldwide, was verified by comparing the data measured using reference accelerometers and wire displacement sensors installed on the specimen through shaking table tests. For estimating the building deformation, which is related to building stability, the measurement performance for large deformation using smartphones was verified. A scale model of a masonry-filled RC frame building was used as the specimen, designed based on standard schematics for school buildings. The results of the shaking table test with smartphones can be summarized as follows.

1. During the shaking table test, some experimental data were lost due to issues with the power supply and the smartphone damage caused by impact; this indicates the need for mitigating measures in SHM use. In addition, there were time synchronization issues for each device when the Wi-Fi communication was incomplete, highlighting the need for continuous time synchronization or time synchronization post data collection. For using smartphones on the SHM in the future, an application, which enables time synchronization between smartphones installed in the same building, recording ambient vibration, and using low power, is necessary.

2. The natural period of the building evaluated using the smartphone coincided with that obtained from the reference accelerometer. This implies that smartphones can be used to measure the natural period of a building if the vibration occurs with the same magnitude as in the white noise excitation test.
3. The ratio between the maximum acceleration values measured with the smartphones and reference accelerometers ranged from 91.0 to 100.1%, and the MSCF ranged from 0.16 to 1.18. Hence, when the maximum acceleration is evaluated with a smartphone, an accuracy of 90% or higher can be expected.
4. The ratio between the displacement estimated from the acceleration data using smartphones and that obtained from the wire displacement sensors ranged from 91.0 to 100.1%, and the MSCF ranged from 0.14 to 0.86, confirming that the smartphone offered a displacement measurement accuracy of 90% or higher.
5. The ratio between the maximum IDR obtained from the wire displacement sensors and that calculated from the smartphone data ranged from 99% (two stories along the Y direction) to 114% (one story along the X direction). On the second floor in the X direction and the first floor in the Y direction, where the IDR was 0.1% or higher, the IDR obtained from the smartphone data was similar to that obtained from the displacement sensors. Thus, the IDR measurement accuracy using smartphones is low for IDRs less than 0.1%, which is considered as the elastic range in building design, but is sufficient when the IDR is 0.1% or higher.

**Author Contributions:** Conceptualization, J.-D.K.; experiment, J.-D.K., E.-R.B. and S.-H.P.; analysis, J.-D.K.; investigation, J.-D.K. and E.-R.B.; data curation, J.-D.K.; writing—original draft preparation, J.-D.K.; writing—review and editing, E.-R.B.; shaking table experimental supervision, E.-R.B.; phone experimental supervision, J.-D.K.; funding acquisition, J.-D.K. All authors have read and agreed to the published version of the manuscript.

**Funding:** This work was supported by Seoul Institute of Technology (SIT) (2021-AF-001 and 2022-AF-003).

**Institutional Review Board Statement:** Not applicable.

**Informed Consent Statement:** Not applicable.

**Data Availability Statement:** The data that support the findings of this study are available from the corresponding author, upon reasonable request.

**Conflicts of Interest:** The authors declare no conflict of interest.

## References

1. Takahashi, R. The "SMAC" strong motion accelerograph and other latest instruments for measuring earthquakes and building vibrations. In Proceedings of the 1st World Conference on Earthquake Engineering, San Francisco, CA, USA, 12–15 June 1956; pp. 1–11.
2. Kanda, K.; Nakashima, M.; Suzuki, Y.; Ogasawara, S. "q-NAVI": A case of market-based implementation of structural health monitoring in Japan. *Earthq. Spectra* **2021**, *37*, 160–179. [CrossRef]
3. Japan National Committee on Earthquake Engineering. Niigata Earthquake of 1964. In Proceedings of the Third World Conference on Earthquake Engineering, Auckland and Wellington, New Zealand, 22 January–1 February 1965; pp. 78–109.
4. Available online: https://earthquake.usgs.gov/monitoring/nsmp/history/ (accessed on 12 March 2023).
5. Astorga, A.; Guéguen, P.; Ghimire, S.; Kashima, T. NDE1.0: A new database of earthquake data recordings from buildings for engineering applications. *Bull. Earthq. Eng.* **2020**, *18*, 1321–1344. [CrossRef]
6. Péquegnat, C.; Guéguen, P.; Hatzfeld, D.; Langlais, M. The French accelerometric network (RAP) and national data centre (RAP-NDC). *Seism. Res. Lett.* **2008**, *79*, 79–89. [CrossRef]
7. Dolce, M.; Nicoletti, M.; De Sortis, A.; Marchesini, S.; Spina, D.; Talanas, F. Osservatorio sismico delle strutture: The Italian structural seismic monitoring network. *Bull. Earthq. Eng.* **2017**, *15*, 621–641. [CrossRef]
8. Richardson, M. *Detection of Damage in Structures from Changes in Their Dynamic (Modal) Properties—A Survey (UCRL-15103)*; Structural Measurement Systems, Inc.: Santa Clara, CA, USA, 1979. [CrossRef]
9. Doebling, S.W.; Farrar, C.R.; Prime, M.B.; Shevitz, D.W. *Damage Identification and Health Monitoring of Structural and Mechanical Systems from Changes in Their Vibration Characteristics: A Literature Review*; Los Alamos National Laboratory report LA-13070-MS; Los Alamos National Laboratory: New Mexico, NM, USA, 1996.

10. Sivasuriyan, A.; Vijayan, D.S.; Górski, W.; Wodzyński, Ł.; Vaverková, M.D.; Koda, E. Practical implementation of structural health monitoring in multi-story buildings. *Buildings* **2021**, *11*, 263. [CrossRef]
11. Shokravi, H.; Shokravi, H.; Bakhary, N.; Rahimian Koloor, S.S.; Petru, M. Health monitoring of civil infrastructures by subspace system identification method: An overview. *Appl. Sci.* **2020**, *10*, 2786. [CrossRef]
12. Sohn, H.; Farrar, C.R.; Hemez, F.M.; Shunk, D.D.; Stinemates, D.W.; Nadler, B.R.; Czarnecki, J.J. *A Review of Structural Health Monitoring Literature: 1996–2001*; Los Alamos National Laboratory Report LA-UR-02-2095; Los Alamos National Laboratory: New Mexico, NM, USA, 2003.
13. Ko, J.M.; Ni, Y.Q. Technology developments in structural health monitoring of large-scale bridges. *Eng. Struct.* **2005**, *27*, 1715–1725. [CrossRef]
14. Farrar, C.R.; Worden, K. An introduction to structural health monitoring. *Philos. Trans. R. Soc. A* **2007**, *365*, 303–315. [CrossRef]
15. Kurka, P.R.G.; Cambraia, H.N. Application of a multivariable input–output subspace identification technique in structural analysis. *J. Sound Vib.* **2008**, *312*, 461–475. [CrossRef]
16. Li, H.N.; Ren, L.; Jia, Z.G.; Yi, T.H.; Li, D.S. State-of-the-art in structural health monitoring of large and complex civil infrastructures. *J. Civ. Struct. Health Monit.* **2016**, *6*, 3–16. [CrossRef]
17. Fan, W.; Qiao, P. Vibration-based damage identification methods: A review and comparative study. *Struct. Health Monit.* **2011**, *10*, 83–111. [CrossRef]
18. Artese, S.; Zinno, R. TLS for dynamic measurement of the elastic line of bridges. *Appl. Sci.* **2020**, *10*, 1182. [CrossRef]
19. Wu, B.; Wu, G.; Yang, C.; He, Y. Damage identification method for continuous girder bridges based on spatially-distributed long-gauge strain sensing under moving loads. *Mech. Syst. Signal Process.* **2018**, *104*, 415–435. [CrossRef]
20. Zhu, Y.; Ni, Y.Q.; Jin, H.; Inaudi, D.; Laory, I. A temperature-driven MPCA method for structural anomaly detection. *Eng. Struct.* **2019**, *190*, 447–458. [CrossRef]
21. Yu, Z.; Xia, H.; Goicolea, J.M.; Xia, C. Bridge damage identification from moving load induced deflection based on wavelet transform and Lipschitz exponent. *Int. J. Struct. Stab. Dyn.* **2016**, *16*, 1550003. [CrossRef]
22. Ozer, E.; Feng, M.Q. Structural reliability estimation with participatory sensing and mobile cyber-physical structural health monitoring systems. *Appl. Sci.* **2019**, *9*, 2840. [CrossRef]
23. Benz, H.; Buland, R.; Filson, J.; Frankel, A.; Shedlock, K. The advanced national seismic system. *Seism. Res. Lett.* **2001**, *72*, 70–75. [CrossRef]
24. Aoi, S.; Kunugi, T.; Fujiwara, H. Strong-motion seismograph network operated by NIED: K-NET and KiK-net. *J. Jpn. Assoc. Earthq. Eng.* **2004**, *4*, 65–74. [CrossRef]
25. Scislo, L. High activity earthquake swarm event monitoring and impact analysis on underground high energy physics research facilities. *Energies* **2022**, *15*, 3705. [CrossRef]
26. Scislo, L.; Guinchard, M. Source based measurements and monitoring of ground motion conditions during civil engineering works for high luminosity upgrade of the LHC. In Proceedings of the 26th International Congress on Sound and Vibration, Montreal, Canada, 7–11 July 2019.
27. Hsu, T.Y.; Yin, R.C.; Wu, Y.M. Evaluating post-earthquake building safety using economical MEMS seismometers. *Sensors* **2018**, *18*, 1437. [CrossRef]
28. Koide, E.; Fukuwa, N.; Masaki, K.; Hara, T.; Ohta, K.; Itoigawa, K. Development of low-cost seismograph for building response through internet. *J. Architect. Build. Sci. (AIJ)* **2006**, *23*, 453–458.
29. Albarbar, A.; Badri, A.; Sinha, J.K.; Starr, A. Performance evaluation of MEMS accelerometers. *Measurement* **2009**, *42*, 790–795. [CrossRef]
30. Cochran, E.S.; Lawrence, J.F.; Christensen, C.; Jakka, R.S. The quake-catcher network: Citizen science expanding seismic horizons. *Seismol. Res. Lett.* **2009**, *80*, 26–30. [CrossRef]
31. Bennett, V.; Abdoun, T.; Shantz, T.; Jang, D.; Thevanayagam, S. Design and characterization of a compact array of MEMS accelerometers for geotechnical instrumentation. *Smart Struct. Syst.* **2009**, *5*, 663–679. [CrossRef]
32. Lawrence, J.F.; Cochran, E.S.; Chung, A.; Kaiser, A.; Christensen, C.M.; Allen, R.; Baker, J.W.; Fry, B.; Heaton, T.; Kilb, D.; et al. Rapid earthquake characterization using MEMS accelerometers and volunteer hosts following the M 7.2 Darfield, New Zealand, earthquake. *Bull. Seismol. Soc. Am.* **2014**, *104*, 184–192. [CrossRef]
33. Milne, D.; Le Pen, L.; Watson, G.; Thompson, D.; Powrie, W.; Hayward, M.; Morley, S. Proving MEMS technologies for smarter railway infrastructure. *Procedia Eng.* **2016**, *143*, 1077–1084. [CrossRef]
34. Bedon, C.; Bergamo, E.; Izzi, M.; Noè, S. Prototyping and validation of MEMS accelerometers for structural health monitoring—The case study of the Pietratagliata cable-stayed bridge. *J. Sens. Actuator Netw.* **2018**, *7*, 30. [CrossRef]
35. Girolami, A.; Brunelli, D.; Benini, L. Low-cost and distributed health monitoring system for critical buildings. In Proceedings of the 2017 IEEE Workshop on Environmental, Energy, and Structural Monitoring Systems (EESMS), Milan, Italy, 24–25 July 2017.
36. Kong, Q.; Allen, R.M.; Schreier, L.; Kwon, Y.W. MyShake: A smartphone seismic network for earthquake early warning and beyond. *Sci. Adv.* **2016**, *2*, e1501055. [CrossRef]
37. Naito, S.; Azuma, H.; Senna, S.; Yoshizawa, M.; Nakamura, H.; Hao, K.X.; Fujiwara, H.; Hirayama, Y.; Yuki, N.; Yoshida, M. Development and testing of a mobile application for recording and analyzing seismic data. *J. Disaster Res.* **2013**, *8*, 990–1000. [CrossRef]

38. Shrestha, A.; Dang, J.; Wang, X. Development of a smart-device-based vibration-measurement system: Effectiveness examination and application cases to existing structure. *Struct. Control Health Monit.* **2018**, *25*, e2120. [CrossRef]
39. Jung, Y.S.; Yoon, S.W. The analysis in measurement performance MEMS sensor through the low-noise vibration measurement APP. *J. Korean Assoc. Spat. Struct.* **2017**, *17*, 93–100. [CrossRef]
40. Feng, M.; Fukuda, Y.; Mizuta, M.; Ozer, E. Citizen sensors for SHM: Use of accelerometer data from smartphones. *Sensors* **2015**, *15*, 2980–2998. [CrossRef] [PubMed]
41. Ozer, E.; Feng, M.Q. Synthesizing spatiotemporally sparse smartphone sensor data for bridge modal identification. *Smart Mater. Struct.* **2016**, *25*, 085007. [CrossRef]
42. Matarazzo, T.; Vazifeh, M.; Pakzad, S.; Santi, P.; Ratti, C. Smartphone data streams for bridge health monitoring. *Procedia Eng.* **2017**, *199*, 966–971. [CrossRef]
43. Guzman-Acevedo, G.M.; Vazquez-Becerra, G.E.; Millan-Almaraz, J.R.; Rodriguez-Lozoya, H.E.; Reyes-Salazar, A.; Gaxiola-Camacho, J.R.; Martinez-Felix, C.A. GPS, accelerometer, and smartphone fused smart sensor for SHM on real-scale bridges. *Adv. Civ. Eng.* **2019**, *2019*, 6429430. [CrossRef]
44. Shrestha, A.; Dang, J. Deep learning-based real-time auto classification of smartphone measured bridge vibration data. *Sensors* **2020**, *20*, 2710. [CrossRef]
45. Han, R.; Zhao, X. Shaking Table Tests and Validation of Multi-Modal Sensing and Damage Detection Using Smartphones. *Buildings* **2021**, *11*, 477. [CrossRef]
46. Roman-Stork, H.L.; Subrahmanyam, B.; Murty, V.S.N. Quasi-biweekly oscillations in the Bay of Bengal in observations and model simulations. *Deep Sea Res. Part II Top. Stud. Oceanogr.* **2019**, *168*, 104609. [CrossRef]
47. Nadarajah, S. Comments on "Approximation of statistical distribution of magnitude squared coherence estimated with segment overlapping". *Signal Process.* **2007**, *87*, 2834–2836. [CrossRef]
48. Pan, G.; Li, S.; Zhu, Y. A time-frequency correlation analysis method of time series decomposition derived from synchrosqueezed S transform. *Appl. Sci.* **2019**, *9*, 777. [CrossRef]

buildings

MDPI

*Article*

# Implementation of a Condition Monitoring Strategy for the Monastery of Salzedas, Portugal: Challenges and Optimisation

**Eduarda Vila-Chã, Alberto Barontini and Paulo B. Lourenço ***

Department of Civil Engineering, Institute for Sustainability and Innovation in Structural Engineering (ISISE), University of Minho, 4800-058 Guimarães, Portugal
* Correspondence: pbl@civil.uminho.pt

**Abstract:** The implementation of condition monitoring for damage identification and the generation of a reliable digital twin are essential elements of preventive conservation. The application of this promising approach to Cultural Heritage (CH) sites is deemed truly beneficial, constituting a minimally invasive mitigation strategy and a cost-effective decision-making tool. In this light, the present work focuses on establishing an informative virtual model as a platform for the conservation of the monastery of Santa Maria de Salzedas, a CH building located in the north of Portugal. The platform is the first step towards the generation of the digital twin and is populated with existing documentation as well as new information collected within the scope of an inspection and diagnosis programme. At this stage, the virtual model encompasses the main cloister, whose structural condition and safety raised concerns in the past and required the implementation of urgent remedial measures. In the definition of a vibration-based condition monitoring strategy for the south wing of the cloister, five modes were identified by carrying out an extensive dynamic identification. Nonetheless, significant challenges emerged due to the low amplitude of the ambient-induced vibrations and the intrusiveness of the activities. To this end, a data-driven Optimal Sensor Placement (OSP) approach was followed, testing and comparing five heuristic methods to define a good trade-off between the number of sensors and the quality of the collected information. The results showed that these algorithms for OSP allow the selection of sensor locations with good signal strength.

**Keywords:** masonry; built heritage conservation; foundation settlement; digital twin; dynamic identification; operational modal analysis; ambient vibration test; optimal sensor placement; vibration-based monitoring

check for updates

**Citation:** Vila-Chã, E.; Barontini, A.; Lourenço, P.B. Implementation of a Condition Monitoring Strategy for the Monastery of Salzedas, Portugal: Challenges and Optimisation. *Buildings* **2023**, *13*, 719. https://doi.org/10.3390/buildings13030719

Academic Editor: Giuseppe Quaranta

Received: 10 February 2023
Revised: 4 March 2023
Accepted: 7 March 2023
Published: 9 March 2023



## 1. Introduction

In the past decades, the increasing awareness of Cultural Heritage (CH) sites' social and economic impacts has led to the implementation of national and international policies and frameworks for their effective safeguarding and preservation. Particular attention has been given to the definition of a set of principles for conservation, formalised in well-known documents such as the Charter of Athens [1], in 1931, and the Charter of Venice [2], in 1964. These principles have been constantly updated with the aim of enforcing state-of-the-art strategies to address the unavoidable processes of damage and decay caused by growing human and man-made threats.

In this context, new instances, such as the significant cuts to the heritage sector budget, the recent financial crises [3], and the general demand for sustainable use of the resources, pose greater challenges and call for the development and validation of cost-effective practices [4]. To this end, institutions such as the International Council on Monuments and Sites (ICOMOS) have acknowledged preventive conservation as the best course of action [5].

### *1.1. Preventive Conservation Paradigm: Advantages and Open Challenges*

Accepting the underlying philosophy of preventive conservation requires a change of mindset that shifts the focus from remedying the damage once it has already spread to avoiding its causes and tracking its evolution in the earliest stage possible. Indeed, the deterioration process can be tolerated as long as it does not interfere with the ability of the structure and its components to perform as and when required in terms of safety, serviceability, durability, economic, and heritage values, among other criteria [6]. Therefore, preventive conservation encompasses a set of measures to identify possible hazards, mitigate their effects, and monitor the evolution of the system performance over time to prioritise and schedule its maintenance effectively. This can be achieved through the integration of two disciplines, namely risk assessment and condition survey [7].

On one hand, risk assessments allow for linking causes and consequences of damage and predicting the performance loss under given hazard scenarios. On the other hand, condition surveys assess the actual building performance and state through manual or automatic screening techniques. The effective integration of these two disciplines is fostered by the generation of a reliable model of the investigated system. This model, or digital twin, is expected to evolve together with its tangible counterpart, allowing [4,7,8]: (i) timely detection of anomalies in the system's behaviour; (ii) identification of the most probable causes of these anomalies; (iii) prediction of the anomaly evolution under expected scenarios; (iv) prioritisation and design of tailored remedial measures. Following a paradigm developed for Building Information Modelling (BIM), the digital twin can be seen as a federated model that combines geometrical data, alphanumerical data, and documentation from different disciplines and purposes to ensure interoperability, streamline information exchange, and continuously updating upon new acquisitions [9].

The implementation of the digital twin paradigm can rely on different damage identification (DI) methods. Indeed, DI techniques have emerged as strongly automated and robust tools to evaluate the structural health condition. These techniques employ periodic or continuous acquisitions of damage-sensitive features through sensing systems to ultimately support decision-making [10–12]. The identification of the damage itself consists of the following: (i) the generation of a model that, after processing these damage-sensitive features, is capable of simulating the system behaviour and (ii) the comparison of the predicted behaviour with the actual one, evaluated through the real-time interpretation of the monitoring data, to detect anomalous responses. To this end, it is necessary to define a baseline or reference condition and employ a strategy for model development, considering that two suitable approaches exist [13] as follows: (i) data-driven and (ii) model-based. In data-driven approaches, the generated model only depends on the experimental output data over time and aims at explaining the time-dependent variation of one or more of these damage-sensitive features [14–17]. In model-based approaches, instead, the physical characteristics of the system (i.e., geometry and mechanical properties) are considered to develop a detailed numerical model of the structure (e.g., employing finite element modelling strategies), calibrated by matching the numerical with the experimental response [18–21].

Lately among the damage-sensitive features, properties obtained from vibration monitoring proved to be suitable for DI, allowing a global structural assessment in nearly real-time through a few wired or wireless contact sensors (e.g., accelerometers, velocimeters, or strain transducers) [22–29] or even contactless systems [30]. These methods demonstrated are able to detect damage onset in the very early stage, outperforming traditional condition survey approaches based on visual inspection [31–33]. The rationale behind vibration-based DI is that the dynamic response of the system depends on its modal properties (i.e., natural frequencies, mode shapes, and modal damping ratios) which, in turn, depend on the physical and mechanical properties that are directly affected by the damage outbreak and evolution.

The advantages of preventive conservation for CH have been clearly recognised, and specific methods and tools for its implementation exist. Combinations of experimental data and advanced numerical techniques for risk assessment at the building level have

been developed and successfully employed for the diagnosis and prognosis of historical structures [20,21,34–37]. Similarly, in the last few years, the applications of automated vibration-based DI strategies to heritage buildings and monuments have increased [15,38–43]. However, the effective implementation of a preventive conservation strategy is still hindered by several open issues, especially those related to the dynamic nature of the digital twin and the quality of the collected data.

The documentation of CH is strongly multidisciplinary, addressing architectonic, artistic, material, structural, historic, and economic aspects among others, and encompasses several types of qualitative (e.g., pictures, drawings, oral stories, texts, etc.) and quantitative (e.g., values, ranges, dates, indexes, distances, etc.) information [9,44]. The nature of such information is cumulative, increasing with time and with source availability; it is often non-existent or outdated due to limited budget, time constraints, or a lack of an adequate platform/medium to contain and maintain it. Therefore, a proper digital twin must be flexible and adaptable to a level of information that is intended to grow and vary over time.

With respect to the evolution of damage, in presence of a federated digital twin composed of data-driven and/or physics-based models, updated according to vibration monitoring strategies with the peculiarities and specific issues of CH vibration testing properly addressed. To this end, two types of approaches can be followed: Forced Vibration Tests (FVTs) and Ambient Vibration Tests (AVTs). For FVT, an artificially controlled external force is used, whereas, for AVT, the structural response to naturally available sources (e.g., microtremors, wind, vehicles, and human activities) is acquired [45,46]. Although the use of predetermined artificial inputs in FVT provides a more accurate estimation of the modal properties, the application to large, massive, and complex structures is hardly possible with the existing excitation mechanisms [32], since the required instrumentation could be too heavy and expensive and/or the induced action could be detrimental due to the brittle behaviour and the poor conditions and structural capacity of many built heritages. Hence, in most cases, AVT is the only suitable approach. AVT is less expensive and prevents downtime, allowing testing during the normal operation of the buildings [45]. Nonetheless, large and massive structures may be hardly excitable by ambient vibrations, especially when they are located in areas restricted to traffic or with low traffic, such as historical city centres or the countryside [47]. This produces signals with low amplitude and high levels of noise, which affect the identification of higher modes, commonly local and more sensitive to damage, limiting the investigated bandwidth to a few hertz [45,47,48]. Moreover, the dynamic response of the built CH is commonly governed by its components and macro-elements, which are complex to identify through ambient vibration and could be evident only at specific measurement points [49,50]. Finally, it is worth noting that the intrusiveness of the sensing systems to the view and their obstructiveness for operation should be minimised, especially for long-term monitoring, as with any other measures affecting CH fruition, aesthetics, and heritage value [47,51,52].

All these factors should be considered in the sensor network design, namely in the definition of the most appropriate sensors, their number, and location [53]. An optimised sensor network design aims at reducing the number of sensors, consequently reducing the purchase, deployment, and maintenance costs, along with the extent of transmitted, processed, and stored data, and the intrusiveness, while ensuring an adequate quality of the information produced. The network design is often driven by engineering experience and intuition. Nonetheless, robust numerical methods have been developed and implemented to support decision-making within the Optimal Sensor Placement (OSP) field of research, further described in Section 2. Applications of OSP to CH are still very limited [54–58].

### 1.2. Objectives

The present work aims at generating a simple yet informative digital twin to support the preventive conservation of a relevant heritage building located in the north of Portugal, namely the monastery of Santa Maria de Salzedas, described in Section 3. The monastery underwent significant interventions and alterations, mainly due to partial demolition, aban-

donment, lack of maintenance, and geotechnical problems. To this end, the damage to the main cloister has been mapped through visual inspection, supported by photogrammetric and thermographic surveys. In Section 4, the implementation of the platform for the digital twin is presented. This is a navigable model obtained by interconnecting 360° panoramic views with hotspots linked to relevant information and documents collected during the documentary search and the on-site condition survey. This virtual environment will be enriched with models suited for DI, supporting maintenance, preservation, and structural assessment through vibration-based structural health monitoring techniques. A preliminary baseline for the development of such models is generated by carrying out an extensive dynamic identification of one of the most fragile components of the complex, namely the south wing, as described in Section 5. Due to the characteristics of the case study and its environment, several complications emerged during its dynamic identification; therefore, to improve the subsequent condition monitoring, suitable strategies for the optimisation of the placement of the sensors are investigated. Finally, in Section 6, the main conclusions of the work are drawn and future scopes are outlined.

## 2. Optimal Sensor Placement

The definition of the sensor locations for vibration monitoring and dynamic identification has traditionally been carried out according to individual expertise and engineering judgment. In the last few decades, automatic methods have been the object of increasing interest and development, first for aerospace applications [59,60]. Despite the different constraints and goals of vibration monitoring in the aerospace and civil engineering fields, these methods have been recently applied to structures and infrastructures [61–63].

The OSP is commonly formulated as a combinatorial, discrete constrained, black box optimisation problem, in which $p$ out of $n$ candidate degrees of freedom (DOFs), i.e., locations and directions for the sensors, are selected [62,64,65]. The quality of the placement is assessed according to one or more metrics that are common functions of the modal parameters, especially the mode shapes. Among the developed methods, a large class is composed of heuristic algorithms [59,61,63,66]. These are sub-optimal methods but, in most cases, provide a sufficiently good solution, with low time requirements and computational costs by assessing the contribution of each candidate DOF to the mode's identifiability according to one specific metric. These methods may rely on a single or an iterative assessment. In the latter, at each iteration, they can either add to or reject one or more candidates from the set of candidates from the previous iteration. The modal parameters used for the optimisation are estimated through numerical simulations on a preliminary model of the investigated system [53,67–69]. Indeed, most of the currently adopted methods have been developed to support the updating of such a preliminary model. This has led to the definition of probabilistic optimisation procedures to deal with the significant sources of uncertainty that commonly affect any numerical model of an existing structure [67,70–73].

In the present work, a rather different approach is followed, since generating and updating a numerical model of the monastery is not the main goal. The aim is to ensure a good signal-to-noise ratio and the experimental identifiability of the modes by selecting good candidate sensor locations among the points investigated in the preliminary dynamic identification. In order to provide a better insight into OSP, Figure 1 shows a flowchart of the main tasks according to the model-based approach and the data-driven alternative that is adopted in the present paper.

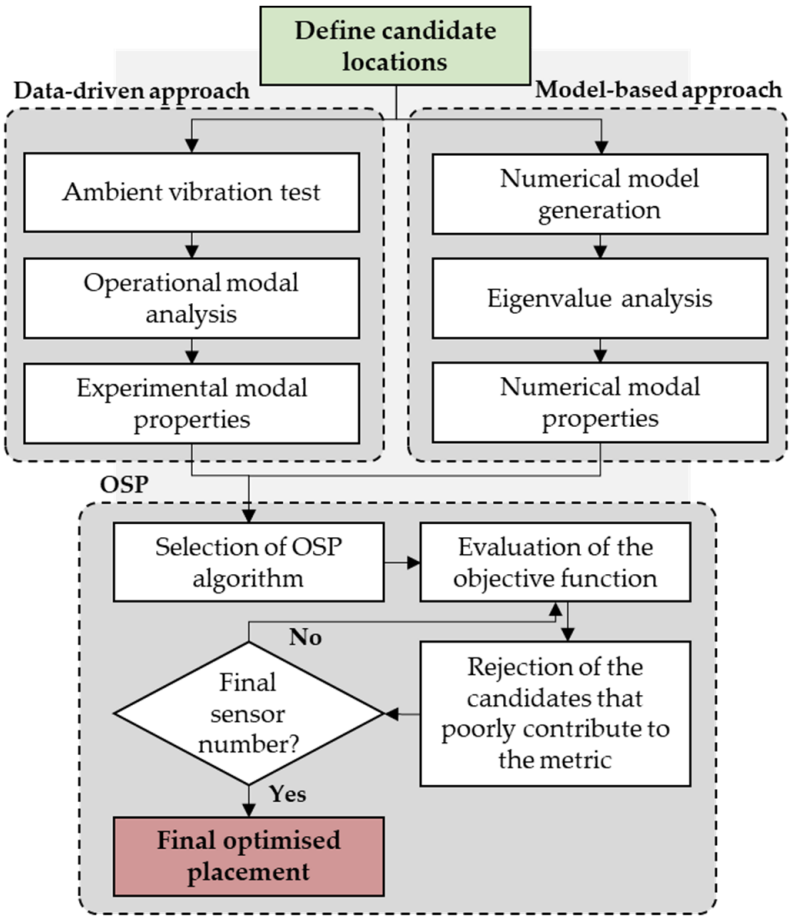


**Figure 1.** Data-driven and model-based optimal sensor placement framework.

To this end, the following simple OSP approaches are hereafter adopted and compared, in Section 5.3, to identify the reduced set of sensors by applying them directly to the experimentally estimated modal properties: (i) Eigenvector Component Product (ECP); (ii) Mode Shape Summation Plot (MSSP); (iii) Average Drive Point Residue (ADPR); (iv) Weighted Average Drive Point Residue (WADPR); and (v) QR Decomposition (QRD). These heuristic methods provide a sub-optimal combination of placements by ranking the candidates in a single iteration. The ECP method [74] maximises the following index:

$$ECP_i = \prod_{k=1}^{m} |\Phi_{ik}| \quad (1)$$

where, $ECP_i$ is the absolute product of the $i$-th row of the mode shape matrix ($i$-th sensor position) $\Phi$ and $m$ is the number of target mode shapes. Similarly, the MSSP [75] maximises the absolute summation of the row:

$$MSSP_i = \sum_{k=1}^{m} |\Phi_{ik}| \quad (2)$$

The ADPR metric consists of the average of the DPR computed across the rows, where the DPR is estimated as follows [76]:

$$DPR = \Phi \otimes \Phi \Lambda^{-1} \quad (3)$$

with $\Lambda^{-1}$ inverse of the diagonal matrix of the angular frequencies $\omega_i$ and $\Phi \otimes \Phi$ term-by-term multiplication of the mode shape matrix. The method aims at the larger ADPRs. For

the WADPR method, instead, the ADPR is weighted by the minimum of the DPR in absolute value across the rows [76]. Finally, the QRD relies on the following decomposition [77]:

$$\Phi^T P = QR \tag{4}$$

where $P$ is a permutation matrix with $P_{ij} \in [0, 1]$, $Q \in \mathbb{R}^{m \times m}$ and $R \in \mathbb{R}^{m \times n}$ is an upper triangular matrix. The QRD allows the definition of a number of sensors equal to or lower than the number of target modes, and the first $m$ columns of the permutation identify the best locations ranked by the method.

The distinct optimised placements that the methods provide are compared in terms of three relevant metrics [78]: (i) the Singular Value Decomposition Ratio ($SVD_r$); (ii) the determinant of the Fisher Information Matrix (detFIM); and (iii) the maximum off-diagonal value of the Auto-Modal Assurance Criterion matrix (maxoffMAC). The $SVD_r$, calculated as follows:

$$SVD_r = \frac{\sigma_1}{\sigma_m} \tag{5}$$

is the ratio of the largest to the smallest singular value of the mode shape matrix. The FIM is formulated as follows:

$$FIM = \Phi^T R^{-1} \Phi \tag{6}$$

where R is the sensor noise covariance intensity matrix. Finally, given the MAC, we calculated as follows:

$$MAC_{ij} = \frac{\left(\varphi_i^T \varphi_j\right)^2}{\left(\varphi_i^T \varphi_i\right)\left(\varphi_j^T \varphi_j\right)}, \; i, j = 1, \ldots, m \tag{7}$$

where $\varphi_i$ is the i-th mode, the maxoffMAC corresponds to the maximum value outside the diagonal. These metrics aim to ensure that the mode shapes are sufficiently distinguishable, estimating their linear dependency and orthogonality. In particular, for an orthogonal matrix, the MAC matrix is the identity matrix, and the $SVD_r$ is 1, therefore low values of these two metrics indicate a better placement [78]. Maximising the FIM determinant, instead, ensures the signal strength and the spatial independence of the mode shapes [79].

## 3. Description of the Case Study

The Monastery of Santa Maria de Salzedas, located in the heart of northern Portugal, was an important male monastery, initially Benedictine and later affiliated with the Cistercian Order. The monastic complex currently comprises a church with a Latin cross shape, 35 m long and 12.5 m wide, a transept with one nave, two side aisles, a chancel (indicated as 1 in Figure 2), a sacristy (indicated as 2), a chapter room (indicated as 3), two cloisters (indicated as 4 and 5, respectively), and an inn (indicated as 6). The construction of the primary church began in the 12th century and was greatly expanded over the years. Indeed, the current church is likely the third built within the complex. The first was possibly demolished. The second, begun in 1168 and consecrated in 1225 with a Burgundian Romanesque style, was taken as the foundation and partially included in the third and last church, completed in the 17th century. This presents strong features of a mannerist and baroque architectural style. Additionally, in the same century, a monumental cloister was built to partially replace the old one that was in ruins. Finally, the part of the tower that was completed was erected in the 19th century. In 1992, renovation works were carried out and some remains of the second church were identified (Figure 3). All the complex stands in a rural environment, with the church surrounded by a few buildings of the Salzedas village (Figure 4) [80].

In 1997, the church was classified as a National Monument due to the architectural importance of the place, and in 2009, the complex became part of the Vale do Varosa Project, along with two other monuments, the Monastery of São João de Tarouca and the Convent of Santo António de Ferreirim.

The current work focuses on the main cloister, as this area has been characterised by severe damage mechanisms and deterioration processes so several interventions have been necessary over time. The cloister is about 30 m long and 25 m wide and comprises two levels. The first level has round arches covered by cross vaults made of brick masonry with earth filling, whereas the second level has barrel vaults and consists of an enclosed gallery (Figure 5). As shown in Figure 2, the cloister is surrounded by contiguous structures. The north wing communicates with the church, the east wing with the chapter room, and the west wing with the little cloister.

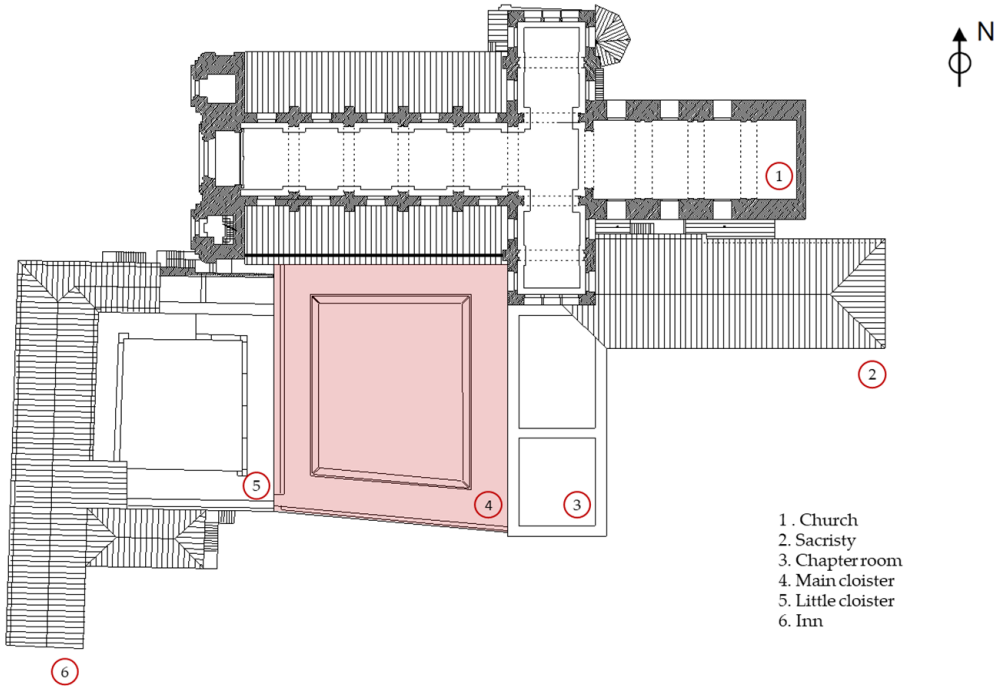


**Figure 2.** Spatial units of the Monastery of Santa Maria de Salzedas. Main cloister is marked in light red.

(**a**) (**b**)

**Figure 3.** Elements of the second church emerged during renovation works: (**a**) left aisle and (**b**) right aisle.

**Figure 4.** Aerial view of the Monastery of Santa Maria de Salzedas.

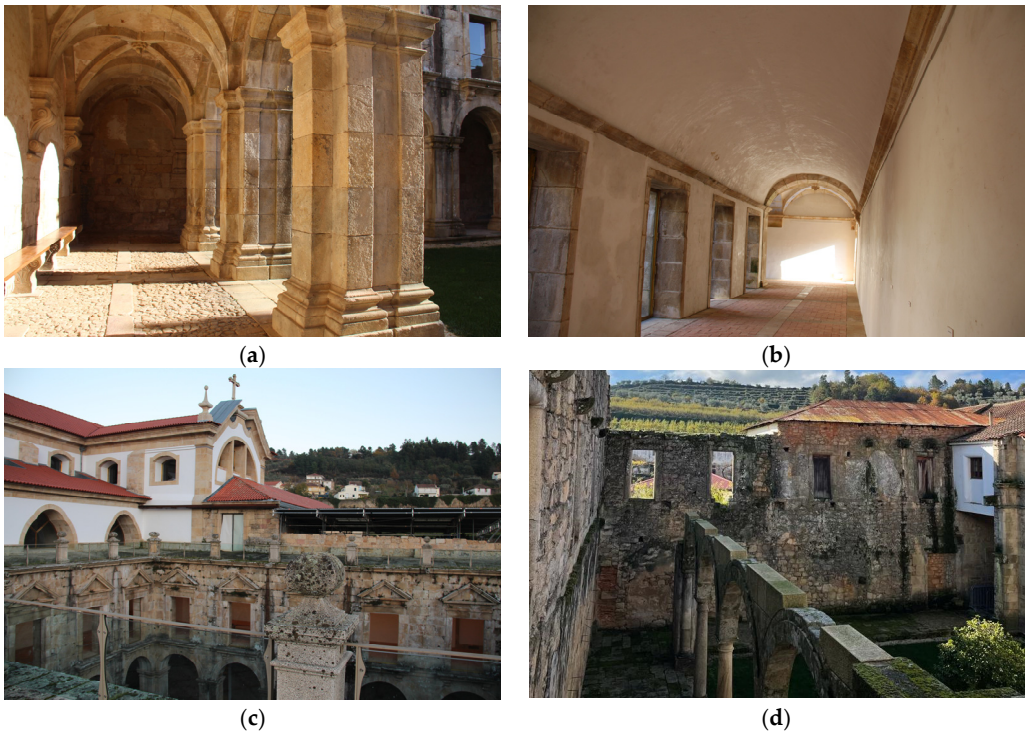

(**a**) (**b**)

(**c**) (**d**)

**Figure 5.** Cloister: (**a**) first level; (**b**) second level; (**c**) accessible roof; and (**d**) little cloister.

The first evidence of the urgent need for remedial measures in the large cloister dates back to 1963 when the collapse of the structure was feared. Repeated warnings were given over time. The first documented conservation works took place between 1980 and 1983 and involved quite invasive solutions such as [80]: (i) demolition of the vault on the second level of the west wing and its replacement with a new vault made of reinforced concrete; (ii) reconstruction of the wall between the two cloisters; and (iii) disassemble and reassemble of the second-floor roof in the west wing.

Despite the interventions, in early 2000, the concern about the significant deterioration state of the cloister rose again, especially regarding the south wing, leading to consolidation works, better described in [80], which included: (i) repositioning the walls

in plumb; (ii) elevation/re-centring vaults and arches; and (iii) additional strengthening by tying the walls. Within the scope of these conservation works, the soil was investigated, and the following stratification was identified [46]: (i) 0.00–1.10 m, fill material; (ii) 1.10–1.40 m, organic soil; (iii) 1.40–2.00 m and 2.00–2.50 m, alluvial soil with medium-sized stones and pebbles; (iv) 2.50–2.70 m, granular soil with some clay; and (v) below 2.70 m deep, large stones, measuring 0.30 m to 0.40 m in diameter. The cloister foundations were built on top of the remains of a previous pavement, settled between 1.00 m and 1.80 m, on an organic soil layer that offers moderate resistance with significant material heterogeneity [80]. Nevertheless, the foundation of the walls exhibits good quality, whereas the foundation of the columns seems unsuitable for the structural elements, strongly contributing to the damage mechanisms that emerged over time.

## 4. On-Site Inspection and Virtual Model Generation

In 2022, a comprehensive inspection and diagnosis campaign was carried out to map the state of damage, verify the recent interventions, and collect meaningful data to establish a simple yet informative digital twin of the main cloister, according to a methodology described in the flowchart reported in Figure 6. Prior to the on-site assessment, a documentary search was conducted to collect all available information. Most information was produced before and during the most recent conservation works and encompasses historical and geometrical surveys, structural and geotechnical reports, as well as the intervention design [80].

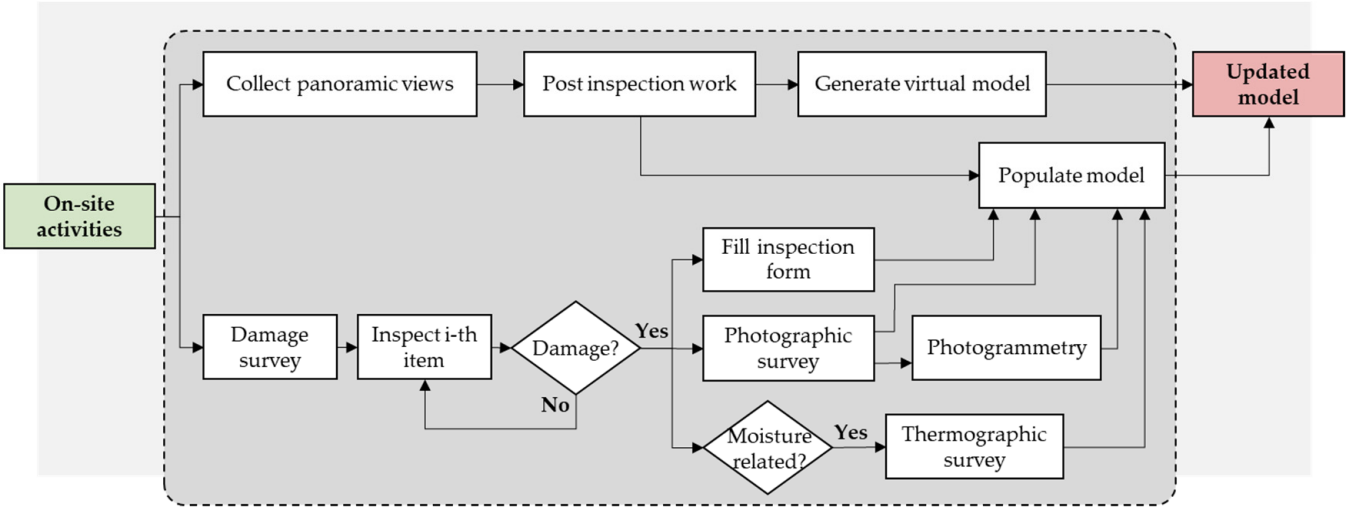


**Figure 6.** Flowchart of the on-site inspection and digital twin generation process.

The work carried out on-site, instead, comprised as follows: photographic survey, damage survey, thermographic inspection, and dynamic identification. For this purpose, around 375 photographs, 19 panoramic views (360°), and 45 thermographic images were taken. After the inspection, the virtual model was created as a reliable data collection system. This is the first step towards the implementation of the digital twin and a straightforward preventive conservation strategy for the cloister. The development of the virtual model follows and improves a replicable strategy that has already been validated and tested over other similar case studies [4]. This strategy presents three key advantages: (i) the possibility of navigating the model, even remotely, on different devices; (ii) the possibility of visualising each significant item of the cloister; and (iii) the possibility of consulting meaningful information by different stakeholders, easily and clearly. For this, a list of hotspots was defined, each one distinguishable by its icon and name and link to photos, documents, or online folders with additional data. This model constitutes an informative visual interface for the digital twin that is currently under development, allowing one to connect in real time to multidisciplinary sources of information and models for the

documentation, assessment, and conservation of the building, which will be continuously updated upon new acquisitions.

The nineteen 360° panoramic views were interlinked to create a virtual model through the Panoroo software. This model is composed of six pictures for each floor (i.e., one per corner plus two in the middle of the north and south wings) and one picture taken from the courtyard. The virtual model is navigable through the use of hotspots, characterised by arrows, that link distinct 360° pictures, as well as by clicking either on the picture locations, reported in the three plans of the three levels or on the icon of the picture itself (Figure 7). A first layer of linked information was added through dedicated hotspots to store the outcome of the documentary search, including architectural and historical evidence as well as previous technical reports and documents (Figure 8).

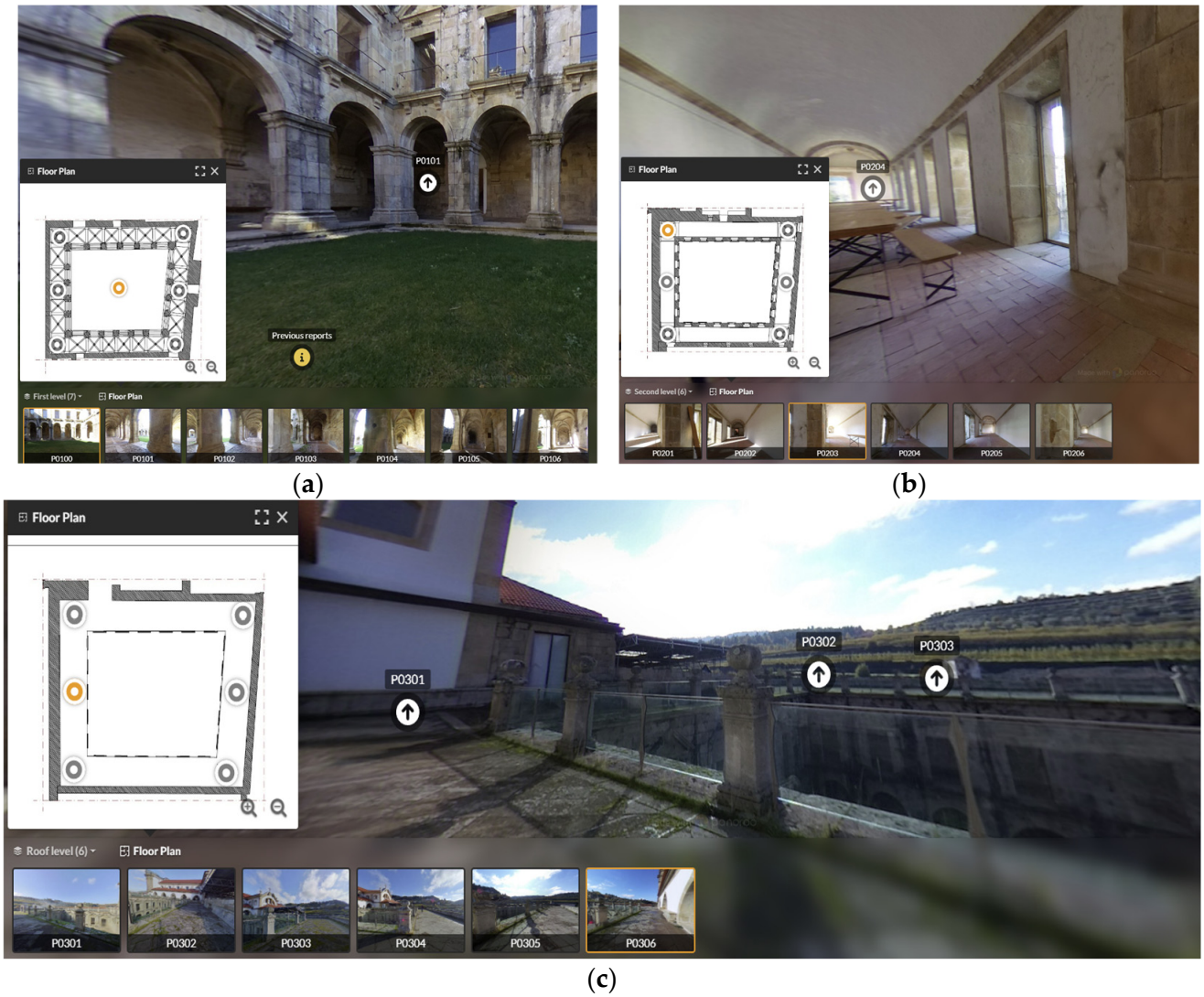


**Figure 7.** Virtual tour, with navigation options (arrow hotspots, floor plan, or image icon): (**a**) first level; (**b**) second level; and (**c**) accessible roof.

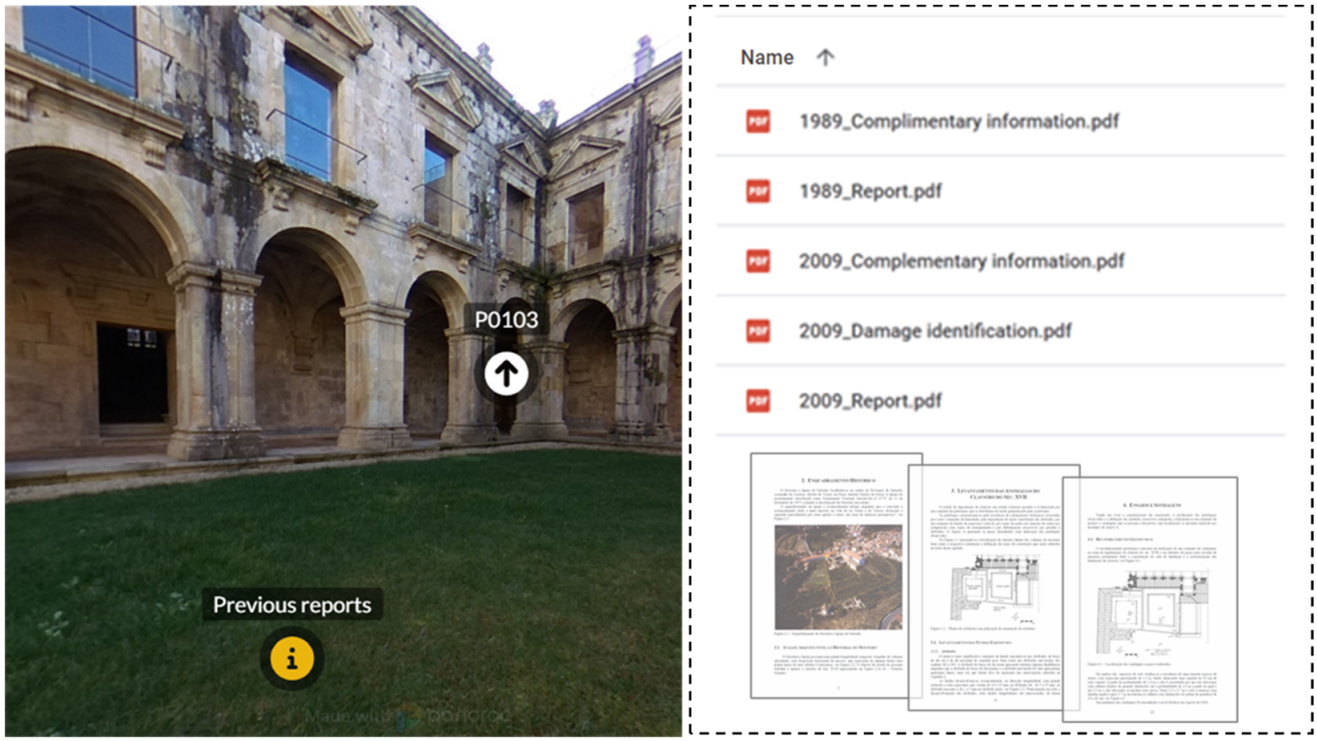


**Figure 8.** Information collection: the outcome of the documentary search linked in the model to an external online folder and previous reports.

During the fieldwork, the current state of the cloister was evaluated through a visual inspection to identify damage, alterations, and decay. These phenomena were classified according to the ICOMOS Guidelines [81] into five categories: (i) cracks and deformation; (ii) detachment; (iii) feature induced by material loss; (iv) discoloration and deposit; and (v) biological colonisation.

The cloister shows considerable evidence of water infiltration at the second level and moist areas associated with rainfall events (especially in the north Figure 9a and the south wing, Figure 9b). These phenomena are likely due to localised damages to the waterproof membrane and the degradation of the joints in the horizontal surfaces of the accessible roof, string course mouldings, and capping of the walls (Figure 9c). Indeed, the walls lack protection (Figure 9d) and are exposed to frequent rain and freeze-thaw cycles during the winter. A slow and inefficient water flow on the roof surface, further complicated by diffuse biological growth, contributes to the permanence of the water and its penetration through cracks, porosity, and capillarity of the material.

To record what was observed during the visual inspection, the survey results were entered into the digital twin, creating hotspots for the ICOMOS classes. These are linked to distinct online folders dedicated to each identified alteration, which collect the digital inspection form, relevant photographs, and any other associated documents (Figure 10).

For damage diagnosis purposes, photogrammetry models were developed as baseline data and mapping support (Figure 11). Indeed, the photogrammetric model allows both a future comparison of the point cloud obtained upon following acquisitions and a visual identification of alteration processes. To this end, in the digital twin, a specific hotspot was introduced and linked to an online repository of the photogrammetric survey, including orthophotos and models in interoperable file formats.

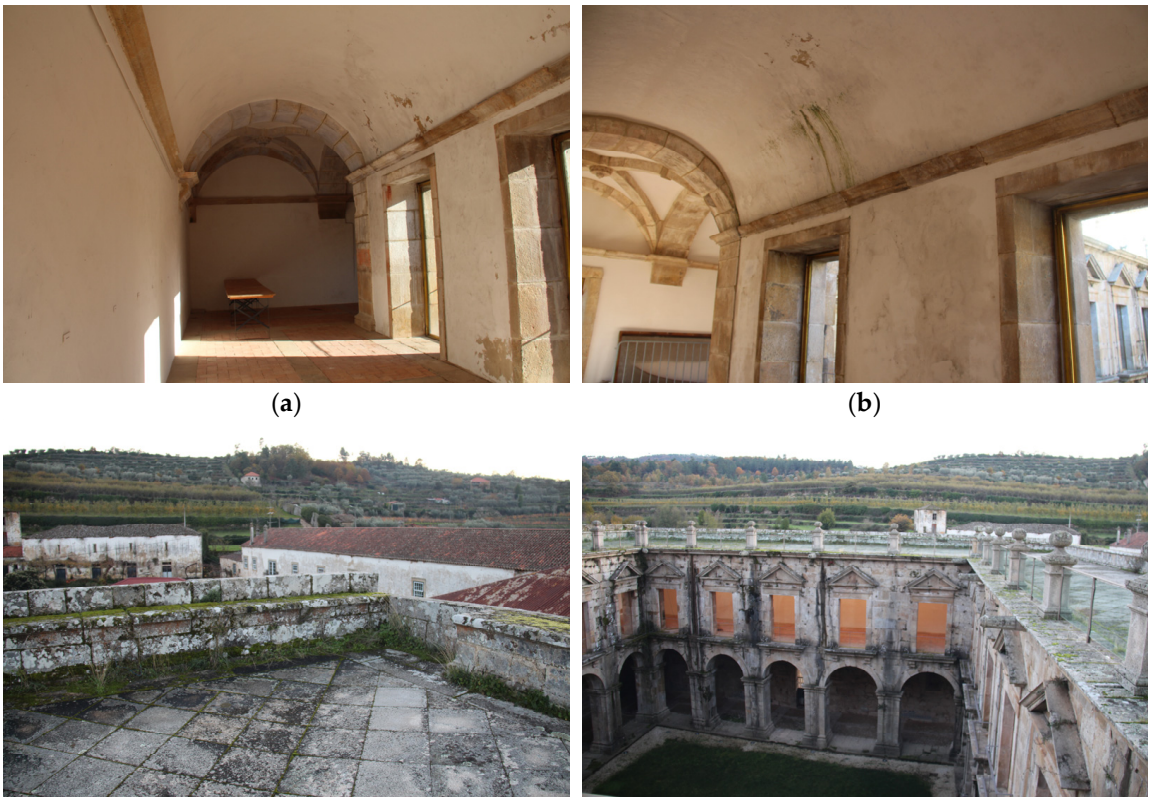

**Figure 9.** Water infiltration: (**a**) second-level north wing; (**b**) second-level east wing; (**c**) accessible roof; and (**d**) south facade.

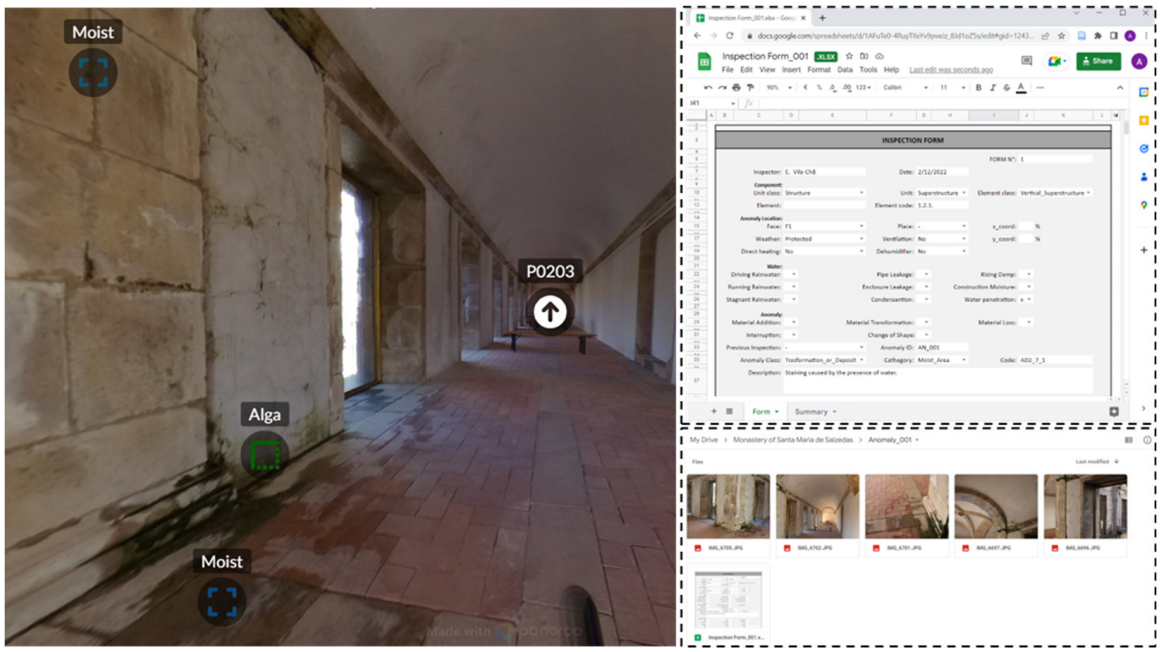


**Figure 10.** Damage survey: damage mapping through hotspots in the virtual model, digital inspection form, and online folder.

**Figure 11.** Photogrammetric model.

To support the visual inspection, non-destructive tests were carried out, and the outcomes were also stored within the digital model. Given the alterations observed on the two levels of the cloister and the fact that the second level is a close environment and shows spread water infiltration, an inspection with a thermographic camera was conducted in order to identify surface deterioration, hidden damage, humidity, and water penetration paths. Indeed, thermal images have become a reliable tool for damage inspection and diagnosis [82–87]. In Figure 12a,b, the measurement locations in the west and east wings, respectively, are identified together with representative examples of thermal imaging. The results of the inspection allowed us to identify colder spots, likely due to the presence of water within the walls and vaults, that, in some cases, were not evident by visual inspection. These areas largely correspond to the damaged portions of the cloister that were the subjects of recent interventions. Irrespective of that, the plaster is still in good condition, and no evidence of crack reopening was found.

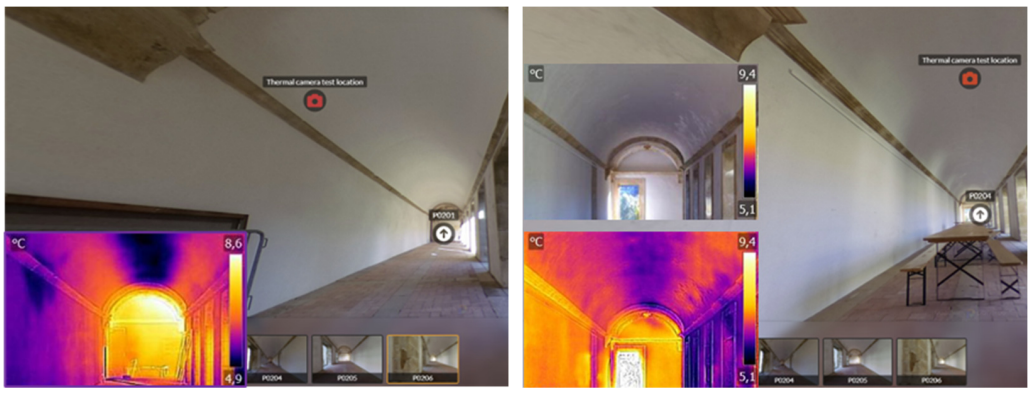


(**a**) (**b**)

**Figure 12.** Inspection with a thermographic camera and link through hotspots: (**a**) West wing and (**b**) East wing.

Finally, the feasibility of the virtual model to support on-site inspection and easy collection and updating of the data was tested by operating it remotely on a tablet (Figure 13a). The operator was enabled to navigate the virtual tour, identifying and querying on-site the relevant information stored within the model or in the linked folders. Among them, rapid access to the results of the previous damage mapping was obtained, and the anomaly inspection form was edited (Figure 13b).

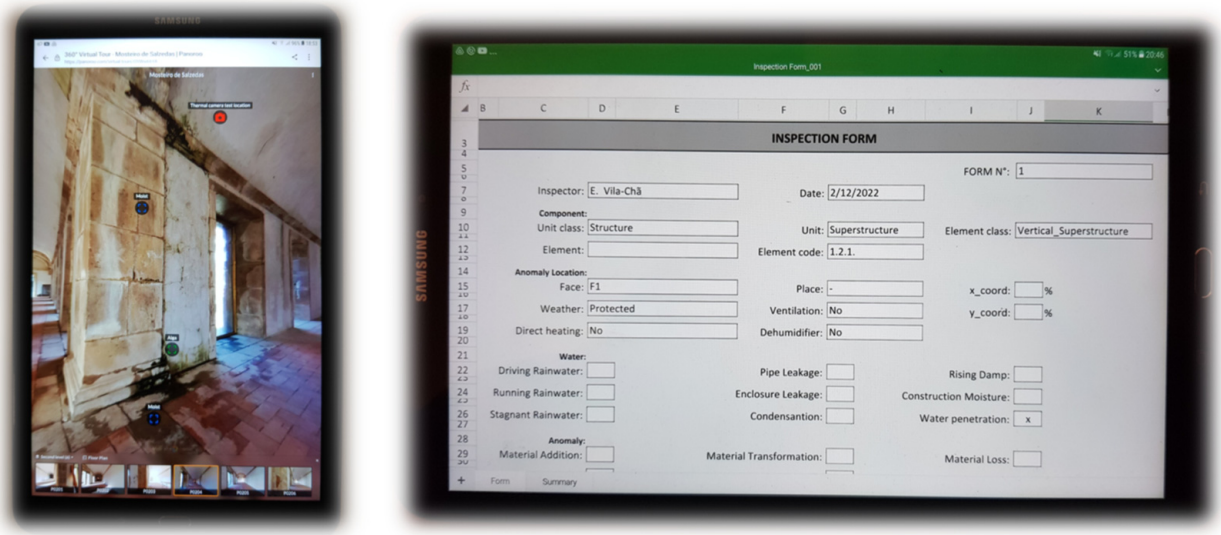


(**a**) (**b**)

**Figure 13.** On-site navigation, interrogation, and updating of the virtual model: (**a**) inspection of previously identified anomalies and (**b**) inspection form.

## 5. Dynamic Identification

### *5.1. Ambient Vibration Test and Limitations*

In order to create a baseline of dynamic characteristics for the implementation of a condition monitoring strategy, a dynamic identification was carried out. The AVT focused on the south wing of the cloister and employed 12 high-sensitivity piezoelectric uniaxial accelerometers (model PCB 393B12, 0.15 to 1000 Hz frequency range, 10 V/g sensitivity, ±0.5 g dynamic range, and 8 μg broadband resolution) in five consecutive setups. Each setup corresponds to a different spatial configuration of the accelerometers, always maintaining two of them as a reference and summing up to a total of 40 acquired degrees of freedom, evenly distributed over the top-most (Figure 14a) and intermediate floor (Figure 14b). Data were recorded through an acquisition system composed of a 4-slot USB chassis model cDAQ-9174 and three 4-channel data acquisition modules model NI 9234 (24-bit resolution, 102-dB dynamic range, anti-aliasing filters, signal conditioning, and 50 kS/s maximum sampling rate per channel).

The tests were conducted under low ambient vibration input, mainly due to a light or moderate wind, the limited presence of visitors in the museum, and the negligible traffic in the area. Sources of non-stationary vibration, such as the bells of the church, were avoided. Each acquisition was carried out at 200 Hz with a duration of 20 min to ensure that the records were longer than 2000 times the fundamental period of the system. The signals were acquired during the operation of the museum to prevent downtime. Nonetheless, the test itself interfered with the complete fruition of the cloister as access was partially interrupted during each recording. Moreover, the use of cabled sensors and extension cords to supply the laptop and the acquisition system resulted in a rather intrusive deployment of the monitoring network. Indeed, for some of the setups, the acquisition system was located about 40 m from the closest wall socket, and the accelerometers were distributed in an area of about a 30–40 m radius around the acquisition system itself, connecting the two investigated floors through the windows opened on the inner court (Figure 15a).

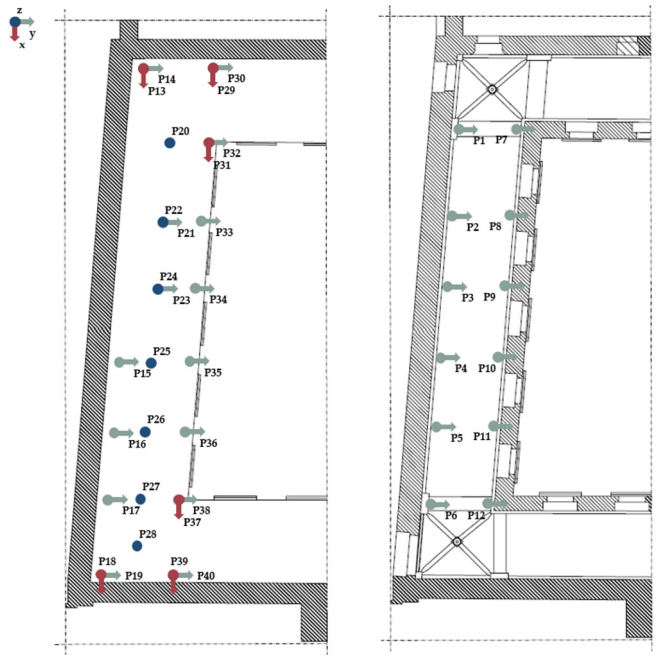


(**a**) (**b**)

**Figure 14.** Sensor deployment, locations, and directions: (**a**) accessible roof and (**b**) second level.

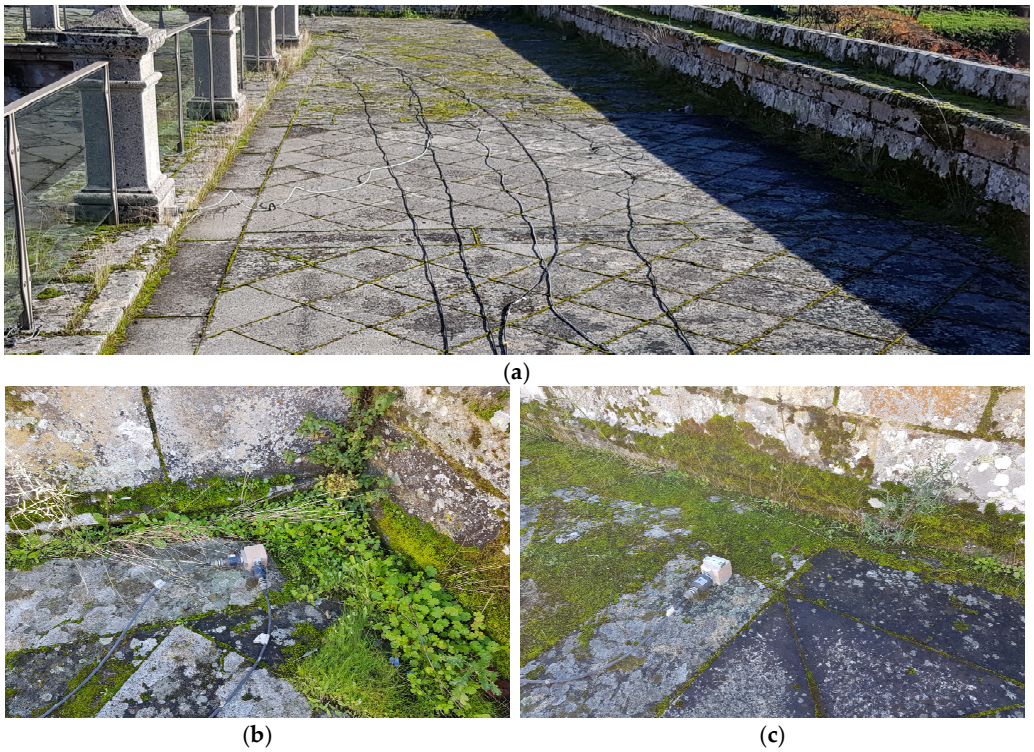

(**a**)

(**b**) (**c**)

**Figure 15.** Sensor deployment: (**a**) cable distribution; (**b**) reference sensors; and (**c**) biological growth, wet and frozen surfaces close to a sensor location.

On the topmost floor, the harsh open-air environment also affected the operations. In particular, to limit the invasiveness of the test for the required connection of the accelerometer with the system, mechanical joints as well as strong adhesives, which could have damaged the surface of the stone, were avoided. However, the diffuse presence of biological growth and a layer of ice on the stone during most of the day, in some cases,

prevented the correct functioning of the hot melt adhesive adopted, limiting the selection of the measurement points and forcing to repeat acquisitions (Figure 15b,c).

### *5.2. Data Processing*

Acquisition records were down-sampled to investigate the 0–50 Hz range and processed through a well-known modal estimator, implemented in the software ARTeMIS Modal, namely the Enhanced Frequency Domain Decomposition (EFDD). It is worth noting that the optimal sensor methodology adopted hereafter is independent of the software and algorithm used for the modal estimation.

The low extent of the ambient vibration affected the quality of the acquired data, providing a likely low signal-to-noise ratio, which is reflected in the small distance between the first and second singular values in the Singular Values Decomposition (SVD) diagram (Figure 16) [88]. In the same diagram, several candidate peaks appear, arguably caused by nuisances in the acquisitions or local modes of the building complex, which are not clearly distinguishable due to the focus on the south wing of the cloister only. These factors contribute to the difficulties in the estimation of the modes and the failure of automated detection through robust algorithms such as the EFDD or Stochastic Subspace Identification. Therefore, the data processing required a careful inspection of the diagrams, considering different subsets of signals, and five modes were identified with a sufficient degree of certainty. Among them, two couples of closely spaced modes were found. The presence of a peak, although unpronounced, in the second SVD line, helped distinguish them [88]. The natural frequencies, damping ratios, and mode shapes are shown in Table 1 and Figure 17. Finally, the most relevant information regarding this preliminary dynamic identification, including the different setups and sensor positions, acquisition records, and processed data, was collected in a dedicated drive folder linked to the virtual model through an ad-hoc hotspot (Figure 18).

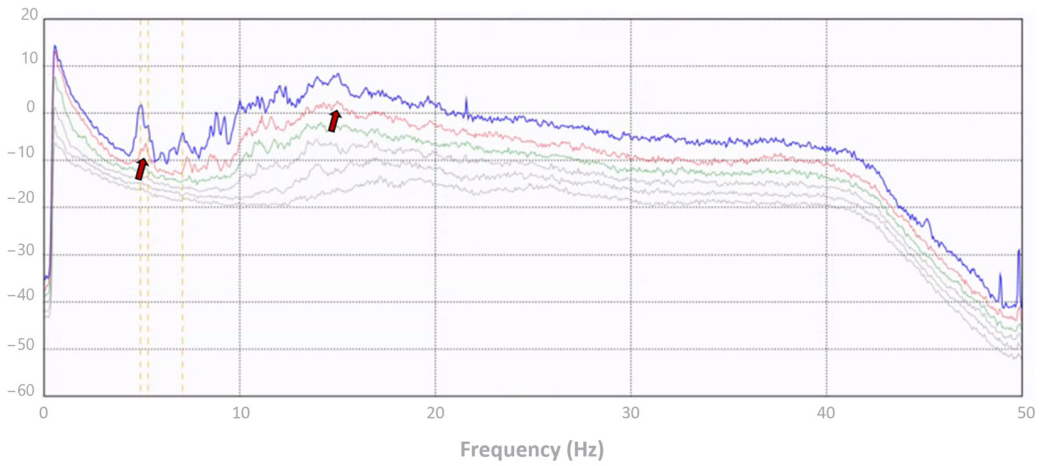


**Figure 16.** Frequency Domain Decomposition: Singular Value Decomposition diagram; red arrows indicate peaks in the second SVD line popping up to separate closely spaced modes.

**Table 1.** Identified modes: natural frequencies, damping ratios, and descriptions with respect to the axes of the south wing of the cloister.

| Mode | Natural Frequency [Hz] | Damping Ratio [%] | Description |
|---|---|---|---|
| 1 | 4.94 | 1.45 | Transversal |
| 2 | 5.32 | 2.56 | Longitudinal |
| 3 | 7.08 | 1.34 | Transversal |
| 4 | 14.65 | 0.64 | Vertical |
| 5 | 15.04 | - | Vertical |

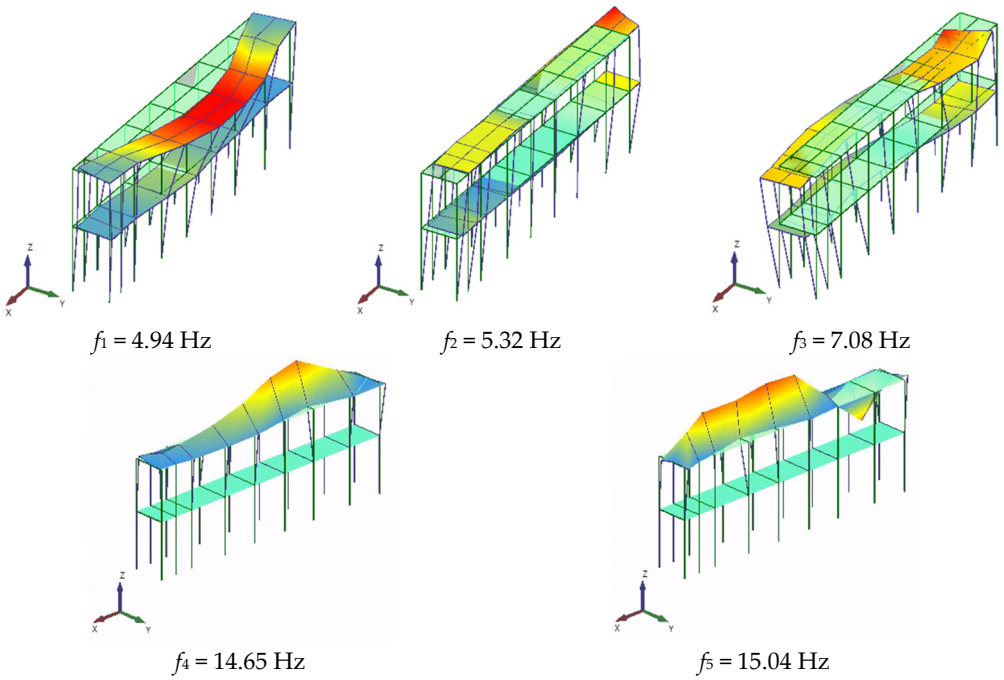


**Figure 17.** Mode shapes and natural frequencies of the five identified modes.

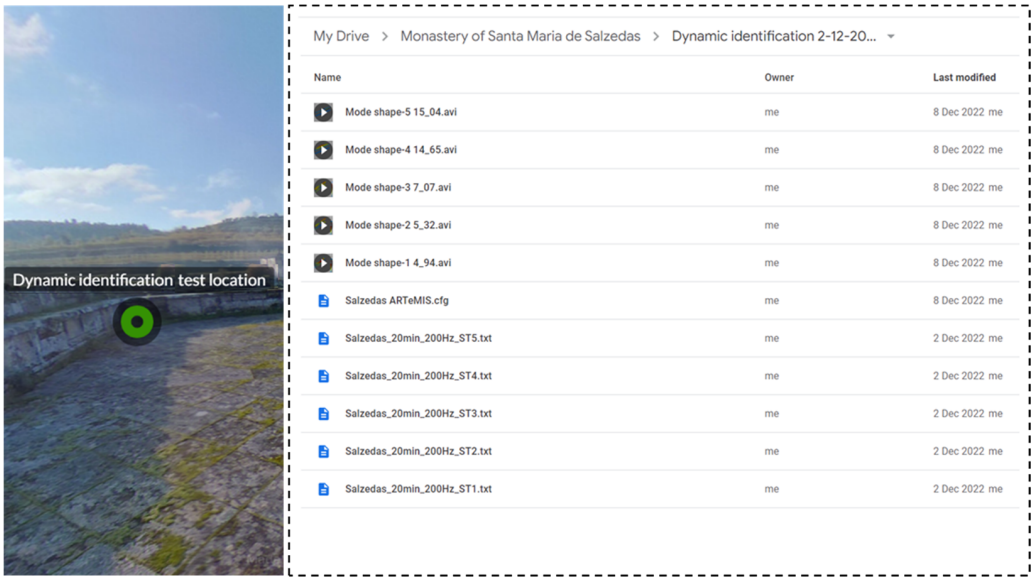


**Figure 18.** Dynamic identification test hotspot in the model and linked drive folder.

### *5.3. Optimisation of the Sensors' Location*

The aforementioned criticalities that affect the dynamic identification of historical buildings can be appropriately addressed by defining a reduced number of optimal sensor locations, either for long-term monitoring or for future repetitions of the test. Reducing the number of sensors is essential to minimise the invasiveness and duration of the activities, with beneficial effects in terms of costs and interaction with normal operations. The application of OSP methodologies directly to recorded signals and experimental modal properties is a rather new approach that is hereafter explored. Considering the peculiarities of the identified modes, the OSP is formulated to target both the complete set of modes (i.e., five) and a reduced set, excluding the two local modes of the roof. It is assumed that, among the forty candidate measurement points of the preliminary dynamic identification,

a minimum number of essential uniaxial sensors, equal to the number of target modes, is to be placed.

The results of the optimisation through four of the five investigated heuristic methods for five and three target modes are reported in Figures 19a and 19b, respectively. These consist of the value of the metrics to maximize and normalise to a unitary interval for comparison purposes. The results of the QRD are not reported in the plot as this method provides a metric value for a number of sensors equal to the target modes only. Especially when five modes are targeted, quite large variability in the estimation of the relevance of each candidate according to distinct metrics emerges. This is reflected in the final optimum sets, reported in Table 2. Among the tested methods, no one suggests the location of a sensor on the intermediate floor. According to most of the heuristics, the vertical component of the mode shapes plays a negligible role in the identification. This is reflected in the lack of sensors along this direction except for P20 and P27, as suggested by MSSP and QRD. In the longitudinal direction, the presence of position P13 is almost constant, whereas, in the transversal direction, P33 is always recommended together with at least another sensor (e.g., P32, P34, or P35) in any solution except for the ECP targeting three modes.

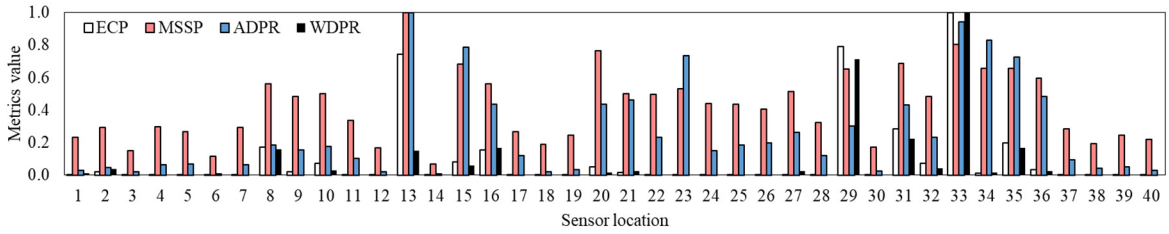


(**a**)

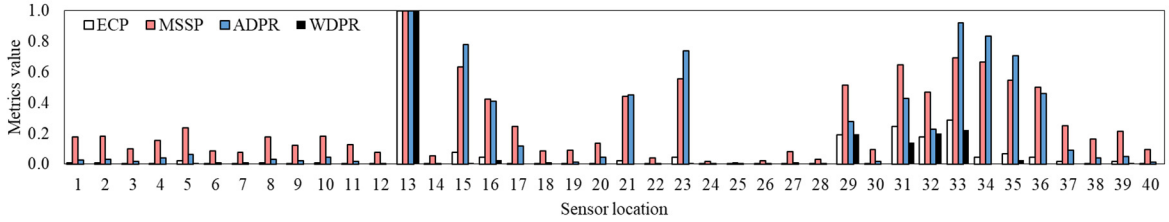


(**b**)

**Figure 19.** Results of the optimisation with different heuristics, according to the placement identification number presented in Figure 14: (**a**) normalised metrics for five target modes and (**b**) normalised metrics for three target modes.

**Table 2.** Recommended sensor placements, according to the placement identification number presented in Figure 14, for five target modes (five sensors) and three target modes (three sensors).

| ECP | MSSP | ADPR | WADPR | QRD | ECP | MSSP | ADPR | WADPR | QRD |
|---|---|---|---|---|---|---|---|---|---|
| P33 | P13 | P13 | P29 | P13 | P13 | P13 | P13 | P13 | P13 |
| P29 | P33 | P33 | P33 | P20 | P33 | P33 | P33 | P33 | P33 |
| P13 | P20 | P34 | P35 | P33 | P31 | P34 | P34 | P32 | P32 |
| P31 | P31 | P15 | P31 | P27 | – | – | – | – | – |
| P35 | P15 | P23 | P36 | P32 | – | – | – | – | – |

Figure 20 shows the values, normalised to a unitary interval, of the three metrics considered to assess and compare the performance of the five methods. Due to their characteristics, the values assumed by the $SVD_r$ and the moaxoffMAC vary within a limited range, whereas the detFIM obtained over the total number of sensors is extremely larger than the results over the reduced sets. Indeed, for the normalised detFIM metric, the total set scores 1, whereas all the reduced sets are less than 0.02. Nonetheless, the three metrics present the QRD as the best method. Therefore, the dynamic identification is carried out

again, but considering the five sensors recommended by this method and Figure 21, which reports the SVD diagram. Comparing it with the plot in Figure 16, the ability of the reduced set to ensure effective peak picking emerges, at least for the first three modes, which are even more clear, and for the fifth mode. The identification of the fourth mode is still possible, although affected by more nuisance, as reflected in several closely spaced peaks. A small relative error in the estimation, equal to 2.0%, affects the first natural frequency only (Table 3). It is, thus, confirmed that the heuristic algorithm for OSP ensures a good signal strength and can be successfully adopted to define sensor locations with larger modal displacement and, potentially, larger signal-to-noise ratios.

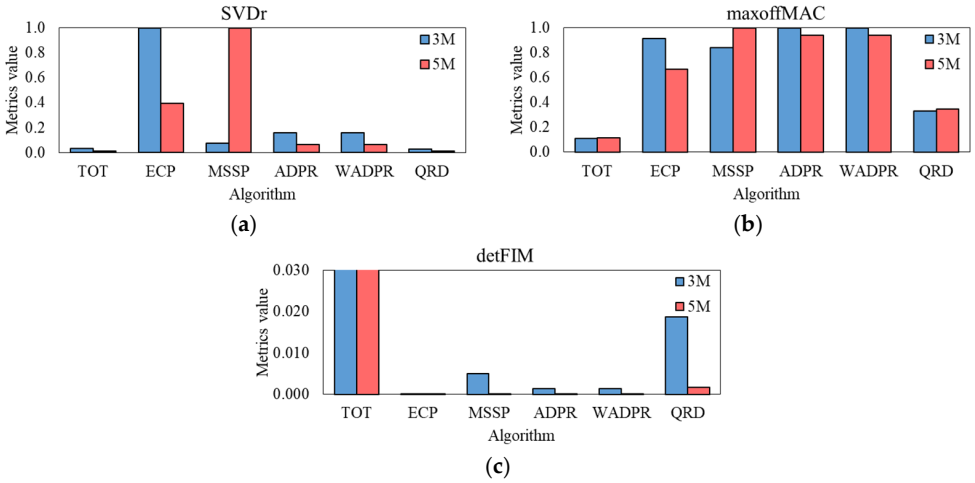


**Figure 20.** Normalised values of the three metrics used for comparison: (**a**) SVDr; (**b**) maxoffMAC; and (**c**) detFIM.

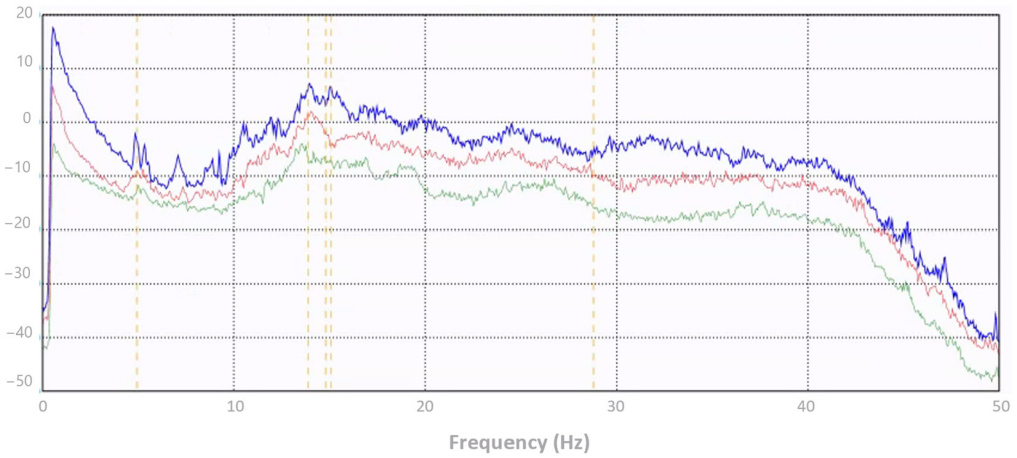


**Figure 21.** Frequency Domain Decomposition applied to five signals: Singular Value Decomposition diagram.

**Table 3.** Comparison between the frequencies identified considering the total (TOT) and the reduced (QRD) number of sensors.

| Mode | TOT $f$ [Hz] | QRD $f$ [Hz] | $\Delta f$ [%] |
|---|---|---|---|
| 1 | 4.94 | 4.83 | 2.0 |
| 2 | 5.32 | 5.32 | 0.0 |
| 3 | 7.08 | 7.08 | 0.0 |
| 4 | 14.65 | 14.65 | 0.0 |
| 5 | 15.04 | 15.04 | 0.0 |

As far as the interpretation of the mode shape is concerned, the recommended placements are questionable. Although the reduced number of final locations (i.e., three or five) is indisputably a limitation to a correct spatial interpretation of the mode shapes, a clear tendency to cluster the sensors emerges, together with a bias towards the maximum modal displacements. These issues have been confirmed in other studies [57,61,63] and are a significant drawback whenever complex structures and local modes are addressed, as some of these modes could be overlooked in the optimisation. For instance, the ECP, in the case of targeting five modes, groups three sensors in the longitudinal direction close together, providing no information in the vertical direction, thus making modes 4 and 5 unidentifiable. Quite the opposite, the ADPR gathers four sensors in a transversal direction, close to the middle of the roof, but provides no information along the vertical as well. The weighted version (WADPR) finally, despite the lack of vertical sensors, more effectively spreads the sensors over the rooftop. Comparing the performance metrics (Figure 20) and the final recommended deployments (Table 2), a metric based on the auto-MAC matrix seems to be the only one capable of providing information about the mode shape interpretation, considering the pairwise similarity of the identified modes. Nonetheless, it is worth noting that the maxoffMAC that is estimated during the optimisation process by reducing the original mode shape matrix to the rows of the recommended sensors, underestimates the actual maxoffMAC that is obtained by repeating the identification on the reduced set of sensors only. Moreover, as reported in Figure 22, the estimated MAC matrix itself, for some of the pairwise comparisons, fails to predict the similarity. This problem is likely due to the poor quality of the initial identification, affected by low signal strength, and proved by the significant complexity of the estimated modes. To this end, new OSP procedures and metrics that can consider the sources of uncertainty and nuisance that affect data acquisition and processing may be needed to improve the prediction.

| Mode | 1 | 2 | 3 | 4 | 5 |
|---|---|---|---|---|---|
| 1 | 1.00 | 0.04 | 0.19 | 0.00 | 0.02 |
| 2 | 0.04 | 1.00 | 0.51 | 0.02 | 0.02 |
| 3 | 0.19 | 0.51 | 1.00 | 0.00 | 0.02 |
| 4 | 0.00 | 0.02 | 0.00 | 1.00 | 0.23 |
| 5 | 0.02 | 0.02 | 0.02 | 0.23 | 1.00 |

(**a**)

| Mode | 1 | 2 | 3 | 4 | 5 |
|---|---|---|---|---|---|
| 1 | 1.00 | 0.39 | 0.39 | 0.02 | 0.06 |
| 2 | 0.39 | 1.00 | 0.60 | 0.02 | 0.01 |
| 3 | 0.39 | 0.60 | 1.00 | 0.00 | 0.01 |
| 4 | 0.02 | 0.02 | 0.00 | 1.00 | 0.42 |
| 5 | 0.06 | 0.01 | 0.01 | 0.42 | 1.00 |

(**b**)

**Figure 22.** QRD method, targeting five modes: (**a**) comparison between the estimated MAC matrix and the recommended set of sensors, reducing the mode shapes estimated with all the sensors (on the left) and (**b**) the actual MAC matrix conducting the identification with the reduced set of sensors only (on the right).

## 6. Conclusions

In the present work, a virtual model based on nineteen interlinked 360° panoramic views was created as a platform to store meaningful information for the preventive conservation of the Monastery of Santa Maria de Salzedas, located in the north of Portugal. This model mainly focuses on the large cloister, which has been characterised by severe damage mechanisms and has required urgent remedial measures since 2000, and it is a preliminary step towards the generation of a digital twin. The information collected on the virtual platform is organised through pre-defined and well-recognisable hotspots with links to embedded or external sources that encompass existing documents, in particular the ones produced during the last diagnosis and strengthening of the cloister, as well as new data produced during a recent condition survey of the monument. These on-site activities comprised a photographic survey, a damage survey, and a thermographic inspection. Aiming at the implementation, within the virtual platform, of a data-driven damage detection strategy, an extensive dynamic identification of the south wing, which had been particularly

affected by the latest interventions, was carried out. Subsequently, an optimisation of the sensor placement was studied in order to ensure a good trade-off between the number of sensors and the identifiability of the modes, supporting future condition monitoring. To this end, five simple heuristic methods were tested and compared using three performance metrics. The following main conclusions can be drawn:

- Although the cloister shows considerable evidence of water infiltration associated with rainfall events, likely due to a deterioration of the waterproof membrane and the joints, the area that was the object of the last interventions does not present signs of alterations or reopening of the cracks;
- The structure presents five modes in the range between 4.94 and 15.04 Hz: three global and two local vertical modes of the accessible roof;
- Environmental and operational conditions strongly affect the ambient vibration test. In particular, the negligible traffic, wind, and presence of visitors within the building limit the extent of the ambient vibration;
- The sensor placement was optimised through the tested algorithms to effectively identify the natural frequencies, reducing significantly the number of measurement points.

Despite the capability of estimating the natural frequencies, the methods failed to provide solutions that, by spreading the sensors, allowed a good interpretation of the mode shapes.

Indeed, this rather innovative application of optimal sensor placement strategies to ambient vibration experimental data instead of numerical simulations confirmed some limitations of the existing algorithms, which tend to cluster the sensors and select only points with larger modal displacements. Moreover, it emerged that a proper optimisation would benefit from the repetition of the modal identification with the reduced number of sensors, since the simple reduction of the initial mode shape matrix is likely to produce a poor estimation of the adopted metrics, especially with noisy signals. Nonetheless, the promising results call for the development and testing of new data-driven OSP procedures and performance metrics able to overcome such issues as a relevant future scope of the present work.

**Author Contributions:** Conceptualization, A.B.; methodology, E.V.-C., A.B. and P.B.L.; formal analysis, E.V.-C. and A.B.; investigation, E.V.-C. and A.B.; writing—original draft preparation, E.V.-C.; writing—review and editing, A.B. and P.B.L.; visualization, E.V.-C.; supervision, P.B.L. All authors have read and agreed to the published version of the manuscript.

**Funding:** This work was partly financed by FCT/MCTES through national funds (PIDDAC) under the R&D Unit Institute for Sustainability and Innovation in Structural Engineering (ISISE), under reference UIDB/04029/2020, and under the Associate Laboratory Advanced Production and Intelligent Systems ARISE, under reference LA/P/0112/2020.

**Institutional Review Board Statement:** Not applicable.

**Informed Consent Statement:** Not applicable.

**Data Availability Statement:** The data available in the study are available on request.

**Conflicts of Interest:** The authors declare no conflict of interest.

## References

1. The Athens Charter—The Athenas Charter for the Restoration of Historic Monuments. In Proceedings of the 1st International Congress of Architects and Technicians of Historic Monuments, Athens, Greece, 21–30 October 1931.
2. *The Venice Charter—International Charter for the Conservation and Restoration of Monuments and Sites*; ICOMOS: Venice, Italy, 1964.
3. Marjanović, V. *Europe's Endangered Heritage*; Parliamentary Assembly: Strasbourg, France, 2014.
4. Lourenço, P.B.; Barontini, A.; Oliveira, D.; Ortega, J. Rethinking preventive conservation: Recent examples. In *Geotechnical Engineering for the Preservation of Monuments and Historic Sites III*; CRC Press: Boca Raton, FL, USA, 2022; pp. 70–86. [CrossRef]
5. ICOMOS Charter—Principles for the analysis, conservation and Structural Restoration of Architectural Heritage. In Proceedings of the ICOMOS 14th General Assembly and Scientific Symposium, Victoria Falls, Zimbabwe, 27–31 October 2003; pp. 27–31.
6. *EN 13306*; Maintenance–Maintenance Terminology. European Committee for Standardization (CEN): Brussels, Belgium, 2010.
7. Taylor, J. An Integrated Approach to Risk Assessments and Condition Surveys. *J. Am. Inst. Conserv.* **2005**, *44*, 127–141. [CrossRef]

8. Wagg, D.J.; Worden, K.; Barthorpe, R.J.; Gardner, P. Digital twins: State-of-the-art future directions for modelling and simulation in engineering dynamics applications. *ASCE—ASME J. Risk Uncertain. Eng. Syst. B Mech. Eng.* **2020**, *6*, 030901. [CrossRef]
9. Barontini, A.; Alarcon, C.; Sousa, H.S.; Oliveira, D.V.; Masciotta, M.G.; Azenha, M. Development and Demonstration of an HBIM Framework for the Preventive Conservation of Cultural Heritage. *Int. J. Arch. Herit.* **2021**, *16*, 1451–1473. [CrossRef]
10. Adams, D.E. *Health Monitoring of Structural Materials and Components: Methods with Applications*; John Wiley & Sons: Hoboken, NJ, USA, 2007.
11. Sohn, H.; Farrar, C.R.; Hemez, F.; Czarnecki, J. *A Review of Structural Health Monitoring Literature: 1996–2001*; Los Alamos National Laboratory: Los Alamos, NM, USA, 2003; Volume 1, p. 16.
12. Masciotta, M.-G.; Barontini, A.; Ramos, F.; Amado-Mendes, P.; Lourenço, P.B. An Overview on Structural Health Moni-toring: From the Current State-of-the-Art to New Bio-inspired Sensing Paradigms. *Int. J. Bio-Inspired Comput.* **2019**, *14*, 1–26. [CrossRef]
13. Farrar, C.R.; Worden, K. An introduction to structural health monitoring. *Philos. Trans. R. Soc. A Math. Phys. Eng. Sci.* **2007**, *365*, 303–315. [CrossRef] [PubMed]
14. Worden, K.; Dulieu-Barton, J.M. An Overview of Intelligent Fault Detection in Systems and Structures. *Struct. Health Monit.* **2004**, *3*, 85–98. [CrossRef]
15. Gentile, C.; Guidobaldi, M.; Saisi, A. One-year dynamic monitoring of a historic tower: Damage detection under changing environment. *Meccanica* **2016**, *51*, 2873–2889. [CrossRef]
16. Peeters, B.; de Roeck, G. One-year monitoring of the Z24-bridge: Environmental effectsversus damage events. *Earthq. Eng. Struct. Dyn.* **2001**, *30*, 149–171. [CrossRef]
17. Barontini, A.; Masciotta, M.G.; Amado-Mendes, P.; Ramos, L.F.; Lourenço, P.B. Negative selection algorithm based methodology for online structural health monitoring. *Eng. Struct.* **2020**, *229*, 111662. [CrossRef]
18. I Friswell, M. Damage identification using inverse methods. *Philos. Trans. R. Soc. A Math. Phys. Eng. Sci.* **2006**, *365*, 393–410. [CrossRef]
19. Pellegrini, D.; Girardi, M.; Lourenço, P.B.; Masciotta, M.G.; Mendes, N.; Padovani, C.; Ramos, L.F. Modal analysis of historical masonry structures: Linear perturbation and software benchmarking. *Constr. Build. Mater.* **2018**, *189*, 1232–1250. [CrossRef]
20. Giordano, E.; Marcheggiani, L.; Formisano, A.; Clementi, F. Application of a Non-Invasive Technique for the Preservation of a Fortified Masonry Tower. *Infrastructures* **2022**, *7*, 30. [CrossRef]
21. Milani, G.; Clementi, F. Advanced Seismic Assessment of Four Masonry Bell Towers in Italy after Operational Modal Analysis (OMA) Identification. *Int. J. Arch. Herit.* **2019**, *15*, 157–186. [CrossRef]
22. Hou, R.; Xia, Y. Review on the new development of vibration-based damage identification for civil engineering structures: 2010–2019. *J. Sound Vib.* **2020**, *491*, 115741. [CrossRef]
23. Malekloo, A.; Ozer, E.; AlHamaydeh, M.; Girolami, M. Machine learning and structural health monitoring overview with emerging technology and high-dimensional data source highlights. *Struct. Health Monit.* **2021**, *21*, 1906–1955. [CrossRef]
24. An, Y.; Chatzi, E.; Sim, S.; Laflamme, S.; Blachowski, B.; Ou, J. Recent progress and future trends on damage identification methods for bridge structures. *Struct. Control. Health Monit.* **2019**, *26*, e2416. [CrossRef]
25. Avci, O.; Abdeljaber, O.; Kiranyaz, S.; Hussein, M.; Gabbouj, M.; Inman, D.J. A review of vibration-based damage detection in civil structures: From traditional methods to Machine Learning and Deep Learning applications. *Mech. Syst. Signal Process.* **2021**, *147*, 107077. [CrossRef]
26. Guzman-Acevedo, G.M.; Vazquez, E.; Millan-Almaraz, J.R.; Rodriguez-Lozoya, H.E.; Reyes-Salazar, A.; Gaxiola-Camacho, J.R.; Félix, C.A.M. GPS, Accelerometer, and Smartphone Fused Smart Sensor for SHM on Real-Scale Bridges. *Adv. Civ. Eng.* **2019**, *2019*, 1–15. [CrossRef]
27. dos Reis, J.; Costa, C.O.; da Costa, J.S. Strain gauges debonding fault detection for structural health monitoring. *Struct. Control Health Monit.* **2018**, *25*, e2264. [CrossRef]
28. Zhu, L.; Fu, Y.; Chow, R.; Spencer, B.F.; Park, J.W.; Mechitov, K. Development of a high-sensitivity wireless accelerometer for structural health monitoring. *Sensors* **2018**, *18*, 262. [CrossRef]
29. Preciado, A. Seismic vulnerability and failure modes simulation of ancient masonry towers by validated virtual finite element models. *Eng. Fail. Anal.* **2015**, *57*, 72–87. [CrossRef]
30. Khuc, T.; Catbas, F.N. Completely contactless structural health monitoring of real-life structures using cameras and computer vision. *Struct. Control Health Monit.* **2017**, *24*, e1852. [CrossRef]
31. Spina, D.; Lamonaca, B.G.; Nicoletti, M.; Dolce, M. Structural monitoring by the Italian Department of Civil Protection and the case of 2009 Abruzzo seismic sequence. *Bull. Earthq. Eng.* **2011**, *9*, 325–346. [CrossRef]
32. Saidin, S.S.; Jamadin, A.; Kudus, S.A.; Amin, N.M.; Anuar, M.A. An Overview: The Application of Vibration-Based Techniques in Bridge Structural Health Monitoring. *Int. J. Concr. Struct. Mater.* **2022**, *16*, 1–17. [CrossRef]
33. Cruz, P.J.S.; Salgado, R. Performance of Vibration-Based Damage Detection Methods in Bridges. *Comput. Civ. Infrastruct. Eng.* **2008**, *24*, 62–79. [CrossRef]
34. Vuoto, A.; Ortega, J.; Lourenço, P.B.; Suárez, F.J.; Núñez, A.C. Safety assessment of the Torre de la Vela in la Alhambra, Granada, Spain: The role of on site works. *Eng. Struct.* **2022**, *264*, 114443. [CrossRef]
35. Ramírez, R.; Mendes, N.; Lourenço, P.B. Diagnosis and seismic behavior evaluation of the church of são miguel de refojos (Portugal). *Buildings* **2019**, *9*, 138. [CrossRef]

36. Alejo, L.E.; Mendes, N.; Lourenço, P.B.; Martínez, G. Protecting the Historic Buildings of Mexico: The Barrel Vault of San Agustin Church in Morelia. *J. Perform. Constr. Facil.* **2021**, *35*, 04020146. [CrossRef]
37. Aşıkoğlu, A.; Avşar, Ö.; Lourenço, P.B.; Silva, L.C.; Kaplan, O.; Karanikoloudis, G. Finite element modeling and operational modal analysis of a historical masonry mosque. In *COMPDYN Proceedings*; National Technical University of Athens: Athens, Greece, 2019. [CrossRef]
38. Pallarés, F.J.; Betti, M.; Bartoli, G.; Pallarés, L. Structural health monitoring (SHM) and Nondestructive testing (NDT) of slender masonry structures: A practical review. *Constr. Build. Mater.* **2021**, *297*, 123768. [CrossRef]
39. Kaya, Y.; Safak, E. Real-time analysis and interpretation of continuous data from structural health monitoring (SHM) systems. *Bull. Earthq. Eng.* **2014**, *13*, 917–934. [CrossRef]
40. Masciotta, M.-G.; Ramos, L.F.; Lourenço, P.B. The importance of structural monitoring as a diagnosis and control tool in the restoration process of heritage structures: A case study in Portugal. *J. Cult. Herit.* **2017**, *27*, 36–47. [CrossRef]
41. Ceravolo, R.; Pistone, G.; Fragonara, L.Z.; Massetto, S.; Abbiati, G. Vibration-based monitoring and diagnosis of cultural heritage: A methodological discussion in three examples. *Int. J. Arch. Herit.* **2014**, *10*, 375–395. [CrossRef]
42. Ubertini, F.; Cavalagli, N.; Kita, A.; Comanducci, G. Assessment of a monumental masonry bell-tower after 2016 Central Italy seismic sequence by long-term SHM. *Bull. Earthq. Eng.* **2017**, *16*, 775–801. [CrossRef]
43. Zonno, G.; Aguilar, R.; Boroschek, R.; Lourenço, P.B. Analysis of the long and short-term effects of temperature and humidity on the structural properties of adobe buildings using continuous monitoring. *Eng. Struct.* **2019**, *196*, 109299. [CrossRef]
44. Lemaire, R.; Stovel, H. *Nara Document on Authenticity*; World Heritage Convention: Nara, Japan, 1994.
45. Koçak, A.; Toydemir, B.; Bulgur, M. Determination of characteristic Parameters of masonry Structures via Operational Modal Analysis. *Int. J. Eng. Sci.* **2019**, *12*, 120304. [CrossRef]
46. Vestroni, F.; Beolchini, G.C.; Antonacci, E.; Modena, C. Identification of dynamic characteristics of masonry buildings from forced vibration tests. In Proceedings of the 11th World Conference on Earthquake Engineering, Acapulco, Mexico, 23–28 June 1996.
47. Azzara, R.M.; Girardi, M.; Iafolla, V.; Lucchesi, D.M.; Padovani, C.; Pellegrini, D. Ambient Vibrations of Age-old Masonry Towers: Results of Long-term Dynamic Monitoring in the Historic Centre of Lucca. *Int. J. Arch. Herit.* **2019**, *15*, 5–21. [CrossRef]
48. Pau, A.; Vestroni, F. Dynamic Characterization of Ancient Masonry Structures. In *Advances in Vibration Analysis Research*; InTech: Osaka, Japan, 2011. [CrossRef]
49. Imposa, G.; Grassi, S.; Barontini, A.; Morreale, G.; Russo, S.; Lourenço, P.B.; Imposa, S. Extended Tromograph Surveys for a Full Experimental Characterisation of the San Giorgio Cathedral in Ragusa (Italy). *Sensors* **2023**, *23*, 889. [CrossRef]
50. Boscato, G.; Cin, A.D.; Ientile, S.; Russo, S. Optimized procedures and strategies for the dynamic monitoring of historical structures. *J. Civ. Struct. Health Monit.* **2016**, *6*, 265–289. [CrossRef]
51. Gentile, C.; Ruccolo, A.; Canali, F. Long-term monitoring for the condition-based structural maintenance of the Milan Cathedral. *Constr. Build. Mater.* **2019**, *228*, 117101. [CrossRef]
52. Hester, J.; Prabhu, S.; Atamturktur, S.; Sorber, J. Remote and Wireless Long-term Vibration Monitoring of Historic Monuments. *Procedia Eng.* **2017**, *199*, 3302–3307. [CrossRef]
53. Ostachowicz, W.; Soman, R.; Malinowski, P. Optimization of sensor placement for structural health monitoring: A review. *Struct. Health Monit.* **2019**, *18*, 963–988. [CrossRef]
54. Pachón, P.; Castro, R.; García-Macías, E.; Compan, V.; Puertas, E.E. Torroja's bridge: Tailored experimental setup for SHM of a historical bridge with a reduced number of sensors. *Eng. Struct.* **2018**, *162*, 11–21. [CrossRef]
55. Pachón, P.; Infantes, M.M.; Cámara, M.; Compán, V.; García-Macías, E.; Friswell, M.I.; Castro-Triguero, R. Evaluation of optimal sensor placement algorithms for the Structural Health Monitoring of architectural heritage. Application to the Monastery of San Jerónimo de Buenavista (Seville, Spain). *Eng. Struct.* **2019**, *202*, 109843. [CrossRef]
56. Prabhu, S.; Atamturktur, S. Selection of Optimal Sensor Locations Based on Modified Effective Independence Method: Case Study on a Gothic Revival Cathedral. *J. Arch. Eng.* **2013**, *19*, 288–301. [CrossRef]
57. Civera, M.; Pecorelli, M.L.; Ceravolo, R.; Surace, C.; Fragonara, L.Z. A multi-objective genetic algorithm strategy for robust optimal sensor placement. *Comput. Civ. Infrastruct. Eng.* **2021**, *36*, 1185–1202. [CrossRef]
58. Giordano, E.; Clementi, F.; Barontini, A.; Masciotta, M.G.; Chatzi, E. *Damage Detection and Optimal Sensor Placement in Health Monitoring of 'Collegiata di Santa Maria' in Visso (Central Italy)*; Pisa University Press: Pisa, Italy, 2019. [CrossRef]
59. Glassburn, R.S.; Student, G.; Weaver, S.; Assistant, S. *Evaluation of Sensor Placement Algorithms for on-Orbit Identification of Space Platforms*; NASA: Washington, DC, USA, 1994.
60. Padula, S.L.; Kincaid, R.K. Optimization Strategies Actuator Placement for Sensor and Actuator Placement. 1999. Available online: www.sti.nasa.gov (accessed on 26 January 2023).
61. Meo, M.; Zumpano, G. On the optimal sensor placement techniques for a bridge structure. *Eng. Struct.* **2005**, *27*, 1488–1497. [CrossRef]
62. Tan, Y.; Zhang, L. Computational methodologies for optimal sensor placement in structural health monitoring: A review. *Struct. Health Monit.* **2019**, *19*, 1287–1308. [CrossRef]
63. Leyder, C.; Dertimanis, V.; Frangi, A.; Chatzi, E.; Lombaert, G. Optimal sensor placement methods and metrics—Comparison and implementation on a timber frame structure. *Struct. Infrastruct. Eng.* **2018**, *14*, 997–1010. [CrossRef]
64. Yi, T.-H.; Li, H.-N. Methodology Developments in Sensor Placement for Health Monitoring of Civil Infrastructures. *Int. J. Distrib. Sens. Netw.* **2012**, *8*, 612726. [CrossRef]

65. Barontini, A.; Masciotta, M.-G.; Ramos, L.F.; Amado-Mendes, P.; Lourenço, P.B. An overview on nature-inspired optimization algorithms for Structural Health Monitoring of historical buildings. *Procedia Eng.* **2017**, *199*, 3320–3325. [CrossRef]
66. Papadopoulos, M.; Garcia, E. Sensor Placement Methodologies for Dynamic Testing. *AIAA J.* **1998**, *36*, 256–263. [CrossRef]
67. Capellari, G.; Chatzi, E.; Mariani, S. Structural Health Monitoring Sensor Network Optimization through Bayesian Experimental Design. *ASCE-ASME J. Risk Uncertain. Eng. Syst. Part A Civ. Eng.* **2018**, *4*, 04018016. [CrossRef]
68. Kammer, D. Effect of model error on sensor placement for on-orbit modal identification of Large Space Structures. *J. Guid. Control. Dyn.* **1991**, *15*, 334–341. [CrossRef]
69. Papadimitriou, C. Optimal sensor placement methodology for parametric identification of structural systems. *J. Sound Vib.* **2004**, *278*, 923–947. [CrossRef]
70. Castro-Triguero, R.; Murugan, S.; Gallego, R.; Friswell, M.I. Robustness of optimal sensor placement under parametric uncertainty. *Mech. Syst. Signal Process.* **2013**, *41*, 268–287. [CrossRef]
71. Guratzsch, R.F.; Mahadevan, S. Structural health monitoring sensor placement optimization under uncertainty. *AIAA J.* **2010**, *48*, 1281–1289. [CrossRef]
72. Liu, J.; Ouyang, H.; Han, X.; Liu, G. Optimal sensor placement for uncertain inverse problem of structural parameter estimation. *Mech. Syst. Signal Process.* **2021**, *160*, 107914. [CrossRef]
73. Kim, T.; Youn, B.D.; Oh, H. Development of a stochastic effective independence (SEFI) method for optimal sensor placement under uncertainty. *Mech. Syst. Signal Process.* **2018**, *111*, 615–627. [CrossRef]
74. Larson, C.C.; Zimmerman, D.C.; Marek, E.L. A Comparison of Modal Test Planning Techniques: Excitation and Sensor Placement Using the NASA 8-Bay Truss. In Proceedings of the 12th International Modal Analysis Conference, Honolulu, Hawaii, 31 January–3 February 1994; pp. 2005–2011.
75. de Clerck, J.P.; Avitable, P. Development of Several New Tools for Pre-Test Evaluation. In Proceedings of the 16th International Modal Analysis Conference, Santa Barabara, CA, USA, 2–5 February 1998; pp. 1272–1277.
76. Chung, Y.-T.; Moore, D. On-Orbit Sensor Placement and System Identification of Space Station with Limited Instru-mentations. In Proceedings of the 11th International Modal Analysis Conference, Kissimmee, FL, USA, 1–4 February 1993; pp. 41–46.
77. Schedlinski, C.; Link, M. An approach to optimal pick-up and exciter placement. In Proceedings of the 4th International Modal Analysis Conference, Los Angeles, CA, USA, 3–6 February 1996; pp. 376–382. [CrossRef]
78. Penny, J.E.T.; Friswell, M.I.; Garvey, S.D. Automatic choice of measurement locations for dynamic testing. *AIAA J.* **1994**, *32*, 407–414. [CrossRef]
79. Kammer, D.; Yao, L. Enhancement of On-Orbit Modal Identification of Large Space Structures Through Sensor Placement. *J. Sound Vib.* **1994**, *171*, 119–139. [CrossRef]
80. Lourenço, P.B.; Ramos, L.F.; Vasconcelos, G. Monastery of Salzedas (Portugal): Intervention in the Cloister Andinformation Management. CRC Press: Boca Raton, FL, USA, 2008.
81. Vergès-Belmin, V. *Illustrated Glossary on Stone Deterioration Patterns*; ICOMOS: Venice, Italy, 2008.
82. Seo, H. Infrared thermography for detecting cracks in pillar models with different reinforcing systems. *Tunn. Undergr. Space Technol.* **2021**, *116*, 104118. [CrossRef]
83. Glavaš, H.; Hadzima-Nyarko, M.; Haničar Buljan, I.; Barić, T. Locating hidden elements in walls of cultural heritage buildings by using infrared thermography. *Buildings* **2019**, *9*, 32. [CrossRef]
84. Lerma, C.; Mas, Á.; Gil, E.; Vercher, J.; Torner, M.E. Quantitative Analysis Procedure for Building Materials in Historic Buildings by Applying Infrared Thermography. *Russ. J. Nondestruct. Test.* **2018**, *54*, 601–609. [CrossRef]
85. Afshani, A.; Kawakami, K.; Konishi, S.; Akagi, H. Study of infrared thermal application for detecting defects within tunnel lining. *Tunn. Undergr. Space Technol.* **2019**, *86*, 186–197. [CrossRef]
86. Paoletti, D.; Ambrosini, D.; Sfarra, S.; Bisegna, F. Preventive thermographic diagnosis of historical buildings for consolidation. *J. Cult. Herit.* **2013**, *14*, 116–121. [CrossRef]
87. Avdan, U.; Kaplan, O.; Kaplan, G. Determination of building materials with ir-thermography in historical buildings. *Int. J. Eng. Geosci.* **2018**, *3*, 56–60. [CrossRef]
88. Cantieni, R. Experimental Modal Analysis Under Ambient Excitation: What We Can Learn from Experience. In Proceedings of the 5th International Operational Modal Analysis Conference, Guimaraes, Portugal, 13–15 May 2013; IOMAC 2013: Guimaraes, Portugal, 2013; pp. 13–15.